

**Investigations into the Relationship Between Surface
Activity and the Dynamical State of Asteroids**

by

Daniel N. Brack

BSc Aerospace Engineering, Technion - I.I.T 2013

MSc Aerospace Engineering, Technion - I.I.T 2016

A thesis submitted to the
Faculty of the Graduate School of the
University of Colorado in partial fulfillment
of the requirements for the degree of
Doctor of Philosophy
Department of Aerospace Engineering Sciences

2019

This thesis entitled:
Investigations into the Relationship Between Surface Activity and the Dynamical State of
Asteroids
written by Daniel N. Brack
has been approved for the Department of Aerospace Engineering Sciences

Prof. Jay W. McMahon

Dr. Paul Sanchez

Prof. Hanspeter Schaub

Prof. Daniel J. Scheeres

Dr. Kevin J. Walsh

Date _____

The final copy of this thesis has been examined by the signatories, and we find that both the content and the form meet acceptable presentation standards of scholarly work in the above mentioned discipline.

Brack, Daniel N. (Ph.D., Aerospace Engineering)

Investigations into the Relationship Between Surface Activity and the Dynamical State of Asteroids

Thesis directed by Prof. Jay W. McMahon

Asteroids undergo processes that change their orbit, spin state, and structure, and the relationship between these properties. This evolution usually occurs slowly, changing the asteroid's behavior over millennia, reaching an equilibrium between rotational state and shape. But no equilibrium lasts forever, and asteroids' states change and are redefined by the relationship between orbit, spin, and structure, sometimes in cascading series of events in short time frames. The work presented in this dissertation derives a model which links asteroid rotation with small scale structural changes on asteroid surfaces. The model allows for boulders placed on asteroid surfaces to move on and off these surfaces in accordance with the geopotential environment and surface material properties. In turn, boulder motion and other surface phenomena affect asteroid rotational states, at times further perturbing the asteroid system. Results are presented for fast rotating asteroids, showing the tendency of boulders to move towards the equator and in doing so reduce asteroid spin rates. However, boulder launches to orbit and variables in surface conditions add chaos to these systems, leading to random walk behavior which affects the system and its relationship with the solar system itself. Small particle events can also affect asteroid states, but in an extent smaller than is detectable with state-of-the-art spacecraft and observation capabilities. Examinations of human induced activity with the model show the extent that human activity such as momentum transfer deflection or material launch to space can have on asteroid rotational states and, in turn, how the shape-spin relationship affects the success of human activity. Mainly, the results demonstrate the importance of understanding an asteroid's shape and rotation prior to planning a deflection mission. Additionally, the dynamics of mass driver deflection derived show that optimized material launch schemes can be found which reduce the side effects on asteroid rotation. Mass launches can be used for deflection in several year time scales through a variety of operational schemes.

Dedication

“Regardez le ciel. Demandez-vous: le mouton oui ou non a-t-il mangé la fleur? Et vous verrez
comme tout change...

Et aucune grande personne ne comprendra jamais que ça a tellement d'importance!”

Le Petit Prince, Antoine de Saint-Exupéry

”שאו נא עיניכם אל השמים ושאלו את עצמכם: האם אכלה הכבשה את השושנה, כן או לא?”

שאלו נא שאלה זו וראיתם מיד כיצד הכל משתנה מעקרו...

שום אדם מבוגר לא יבין לעולם כי לענין זה נועדת חשיבות כה רבה!”

אנטואן דה סנט-אכזיפרי, הנסיך הקטן

“Look up at the sky. Ask yourselves: is it yes or no? Has the sheep eaten the flower? And you
will see how everything changes . . .

And no grown-up will ever understand that this is a matter of so much importance!”

The Little Prince, Antoine de Saint-Exupery

To my mother and father, Marcia and Robert.

As beautiful as this quote is, you are why I disagree with the second part of it. Thank you for seeing the importance of change, for being there through all my changes, and for helping me grow
by visiting as many little planets as possible.

Acknowledgements

I owe a lot of gratitude to my advisor Jay McMahon, for bringing me in to work at CU Boulder, for supporting my wacky endeavors into modeling asteroid related phenomena and activities, for providing guidance with a bird's eye view of everything I was doing, and for, at times, being more excited about my work than me. So thank you Jay! I would also like to thank my loving partner Evan. Babe, thanks for getting excited with me when things were good and for reminding me that there is a light at the end of the tunnel when needed. My family's support on this journey and before it was crucial in so many aspects, emotional as well as material, thank you Marcia, Robert, Yoni, and Gidon. I could not have completed my research without many hours of brainstorming, deriving and rederiving dynamical models, discussing coding best practices, and of course many many complaint sessions. Thanks to members of the ORCCA lab for that, Ben, Andrew, Don, Luke, and Mark. Thanks also to our close cousins at CSML, Alex, Marielle, CK, Stef, and Nicola. My PhD work would not have been able to be done without the financial support of NASA's OSIRIS-Rex mission. I would also like to thank the mission and its PIs at CU Boulder, Dan Scheeres and Jay McMahon, for providing me with opportunities experience work on real life asteroid data in a real life asteroid mission.

Contents

Chapter	
1	Background and motivation 1
1.1	Rubble pile asteroids 1
1.2	Driving forces of asteroid evolution 3
1.3	Artificial manipulation of asteroids 7
1.4	State-of-the-art of Rubble-pile modeling 9
1.5	Thesis statement 12
1.6	Thesis overview 12
1.6.1	Contributions 12
1.6.2	Dissertation outline 14
1.6.3	Publications 14
2	Dynamical model and numerical implementation 17
2.1	The Surface phenomena Effect on Asteroid Rotational And Translational State model 17
2.2	Assumptions and definitions 17
2.2.1	The modeled system 17
2.2.2	Rotational dynamics 20
2.2.3	Modeled events 22
2.3	Surface phenomena effect on model asteroid rotation 23
2.3.1	Boulder surface movement 23

2.3.2	Boulder launch	24
2.3.3	Boulder crash	26
2.3.4	Boulder escape	27
2.4	Boulder motion	27
2.4.1	Surface geophysical environment	27
2.4.2	Cohesion forces	33
2.4.3	Boulder motion mechanics	36
2.4.4	Threshold angular velocities	41
2.5	Fission event	43
2.6	Code structure	47
2.7	SEA RATS applications	50
3	Modeled natural behavior	51
3.1	Fast rotating bodies	51
3.1.1	Single boulder motion on a asteroid Bennu model	52
3.1.2	Multiple boulder motion on an asteroid Bennu model	75
3.1.3	Multiple boulder motion on an Itokawa-shaped asteroid model	104
3.1.4	Trends in fast rotating small bodies	114
3.2	Particle events and the YORP effect	115
3.2.1	The effects of a fast particle events	117
3.2.2	Slow moving particles' fate	126
4	Artificial manipulation of small bodies	133
4.1	Momentum transfer deflection relationship with small body rotation	133
4.1.1	Background	133
4.1.2	Dynamics of kinetic interception	135
4.1.3	Impact effects on rotating ellipsoids	137
4.1.4	Considerations of asteroid shape	146

4.1.5	Nuclear detonation deflection	149
4.1.6	Deflection effect on rotational dynamics using polyhedrons	149
4.1.7	Implications of the rotation - surface activity relationship on momentum transfer deflection	177
4.2	Mass driver deflection and additional applications	178
4.2.1	Background	178
4.2.2	Small deviations near principal axis rotation	180
4.2.3	Asteroid rotation manipulation	186
4.2.4	Boulder removal without precession	189
4.2.5	Boulder launch to affect asteroid orbits	199
4.2.6	Mass driver deflection launch campaign	209
4.2.7	Mass driver deflection effects on Yarkovsky and YORP	222
4.2.8	Insights into engineering mass driver deflection	225
5	Future work	227
5.1	The SEA RATS model	227
5.1.1	Modeling landslides and regolith motion	227
5.1.2	Modeling long term processes	227
5.1.3	Expanding analysis tools	228
5.2	Further investigations of momentum transfer deflection	228
5.3	Expanding the orbital dynamics guidance of mass driver deflection	229
	Bibliography	230

Tables

Table

3.1	Bennu asteroid model parameters	54
3.2	Surface motion parameters	69
3.3	Multiple boulder simulation parameters	75
3.4	Itokawa-shaped asteroid model parameters	105
3.5	Itokawa-shaped asteroid model boulder escape ΔV s	108
3.6	Bennu asteroid model parameters	116
4.1	Minimum launch velocities for boulders in different locations	193
4.2	MOID orbital states	210
4.3	Launch scenario deflection results	217
4.4	MOID orbital state for eccentric asteroid	222

Figures

Figure

1.1	Images of asteroids Bennu, Ryugu and, Itokawa as captured by the OSIRIS-REx, Hayabusa-2, and Hayabusa missions, respectively	2
2.1	Bennu ~6000 facet polyhedral shape model with 50 boulders distributed on its surface	19
2.2	Bennu geopotential parameter maps	30
2.3	Bennu-shaped tumbling asteroid surface slope evolution map	31
2.4	Bennu surface slope magnitudes and directions	32
2.5	Bennu surface escape velocities	33
2.6	Cohesion induced acceleration magnitudes for boulders of varying sizes, aspect ratio, and buried portion. Surface strength is 25 Pascal and boulder density is $2000 \text{ kg}\cdot\text{m}^{-3}$.	34
2.7	Cohesion induced acceleration compared to geopotential accelerations (gravity, rotation, and combination) for nominally rotating Bennu and a fast spinning Bennu .	35
2.8	Ratio between on-surface and surface acceleration and slope for identical boulders placed on Bennu's surface	37
2.9	SEA RATS boulder state flow chart	42
2.10	Threshold angular velocity compared to Bennu nominal for boulder motion. The heatmaps indicate surface (facet) properties, and the diamonds indicate boulders placed on the surface.	44
3.1	Boulder polyhedron in single boulder simulation	53

3.2	Boulder initial motion on Bennu model in single boulder simulation	56
3.3	Boulder motion surface projection in single boulder simulation. The heatmaps indicate surface slopes, boulder initial position indicated by white dot, surface motion indicated by white line, boulder launch and crash events indicated by triangles, and orbit projection on surface indicated by dashed yellow line	57
3.4	Boulder surface motion characteristics (latitude, surface slope, surface velocity) in single boulder simulation, the grayed areas indicate boulder off surface	58
3.5	Boulder orbit motion in single boulder simulation	58
3.6	Modeled asteroid mass in single boulder simulation. The parameters presented include system mass, parent body mass, asteroid mass, and control case mass.	59
3.7	Modeled asteroid inertia tensor elements in single boulder simulation. The parameters presented include parent body inertia tensor, asteroid inertia tensor, and control case inertia tensor.	60
3.8	Modeled asteroid principal maximum moment of inertia ratio with median and minimum principal moments of inertia in single boulder simulation. The parameters presented include parent body inertia ratio, asteroid inertia ratio, and control case inertia ratio.	61
3.9	Modeled asteroid and control case angular velocity evolution in single boulder simulation (asteroid body frame)	63
3.10	Modeled asteroid angular velocity vector projection on the equatorial plane in single boulder simulation (asteroid body frame)	63
3.11	Modeled asteroid and control case angle between angular velocity vector and initial axis of maximum inertia in single boulder simulation (asteroid body frame)	64
3.12	Modeled asteroid angular velocity vector projection on inertial x-y plane and angle between angular velocity vector and initial axis of maximum inertia in single boulder simulation (inertial frame)	64
3.13	Boulder position for varying time step sizes (inertial frame)	66

3.14 Boulder velocity for varying time step sizes (inertial frame)	66
3.15 Boulder position difference from $\delta t = 5$ [s] for varying time step sizes	67
3.16 Boulder velocity difference from $\delta t = 5$ [s] for varying time step sizes	67
3.17 Boulder position difference magnitude from $\delta t = 5$ [s] for varying time step sizes during surface motion	68
3.18 Boulder velocity difference magnitude from $\delta t = 5$ [s] for varying time step sizes during surface motion	68
3.19 Varying surface motion parameter simulation results. Left subfigures show surface characteristics (latitude, surface slope, surface velocity) and right subfigures show boulder trajectory projection on the surface	71
3.20 Boulder orbit motion in single boulder simulation for varying surface motion parameters	72
3.21 Modeled asteroid principal maximum moment of inertia ratio with median and min- imum principal moments of inertia in single boulder simulation for varying surface motion parameters. The parameters presented include parent body inertia ratio, asteroid cases inertia ratio, and control case inertia ratio.	73
3.22 Modeled asteroid and control case angular velocity evolution in single boulder sim- ulation for varying surface motion parameters (asteroid body frame)	74
3.23 Initial boulder placement for Bennu multiple boulder case	76
3.24 Examples of asteroid model surface boulders	77
3.25 Boulder motion surface projection in Bennu multiple boulder simulation. The heatmaps indicate surface slopes, boulder initial position indicated by white dot, surface mo- tion indicated by white line, boulder launch and crash events indicated by triangles, orbit projection on surface indicated by dashed yellow line, and boulder final position indicated by blue star.	79
3.26 Boulders #11 and #22 motion characteristics and trajectories. Left subfigures show surface characteristics (latitude, surface slope, surface velocity) and right subfigures show boulder trajectory projection on the surface.	80

3.27	Boulder orbit motion in Bennu multiple boulder simulation	81
3.28	Modeled asteroid mass in Bennu multiple boulder simulation. The parameters presented include system mass, parent body mass, asteroid mass, and control case mass.	83
3.29	Modeled asteroid inertia tensor elements in Bennu multiple boulder simulation. The parameters presented include parent body inertia tensor, asteroid inertia tensor, and control case inertia tensor.	83
3.30	Modeled asteroid principal maximum moment of inertia ratio with median and minimum principal moments of inertia in Bennu multiple boulder simulation. The parameters presented include parent body inertia ratio, asteroid inertia ratio, and control case inertia ratio.	84
3.31	Modeled asteroid and control case angular velocity evolution in Bennu multiple boulder simulation (asteroid body frame)	84
3.32	Modeled asteroid angular velocity vector projection on the equatorial plane and angle between angular velocity vector and initial axis of maximum inertia in Bennu multiple boulder simulation (asteroid body frame)	85
3.33	Modeled asteroid angular velocity vector projection on inertial x-y plane and angle between angular velocity vector and initial axis of maximum inertia in Bennu multiple boulder simulation (inertial frame)	86
3.34	Modeled asteroid final mass in Bennu multiple boulder Monte Carlo simulation. Histogram includes distribution mean and 1σ bounds as well as control value.	88
3.35	Modeled asteroid final inertia tensor elements in Bennu multiple boulder Monte Carlo simulation. Histograms include distribution means and 1σ bounds as well as control values.	88
3.36	Modeled asteroid final principal maximum moment of inertia over median and minimum moments of inertia in Bennu multiple boulder Monte Carlo simulation. Distribution maps includes distribution mean and 1σ ellipsoid as well as control value.	89

3.37 Modeled asteroid angular velocity final magnitude in Bennu multiple boulder Monte Carlo simulation. Histogram includes distribution mean and 1σ bounds as well as control value.	91
3.38 Modeled asteroid angular velocity projection of final precession center on the on inertial x-y plane and maximum angle between angular velocity vector and initial axis of maximum inertia in Bennu multiple boulder simulation (inertial frame). Histograms include distribution means and 1σ bounds as well as control values.	91
3.39 Boulders #11 motion characteristics and trajectories in Bennu multiple boulder Monte Carlo simulation	92
3.40 Boulders #22 motion characteristics and trajectories in Bennu multiple boulder Monte Carlo simulation	93
3.41 Modeled asteroid distribution of orbit outcomes in Bennu multiple boulder Monte Carlo simulation. Histograms include distribution means and 1σ bounds.	94
3.42 Bennu-shaped accelerated tumbling asteroid surface slope evolution. The heatmaps indicate surface slopes, the red pentagon represents body frame projection of angular velocity vector, the dashed white line represents bounds for slopes over 40 degrees.	96
3.43 Boulder motion surface projection in tumbling Bennu multiple boulder simulation. The heatmaps indicate surface slopes at simulation start, boulder initial position indicated by white dot, surface motion indicated by white line, boulder launch and crash events indicated by triangles, orbit projection on surface indicated by dashed yellow line, and boulder final position indicated by blue star.	98
3.44 Boulder surface motion characteristics (latitude, surface slope, surface velocity) tumbling Bennu multiple boulder simulation	99
3.45 Modeled asteroid mass in tumbling Bennu multiple boulder simulation. The parameters presented include system mass, parent body mass, asteroid mass, and control case mass.	100

3.46	Modeled asteroid inertia tensor elements in tumbling Bennu multiple boulder simulation. The parameters presented include parent body inertia tensor, asteroid inertia tensor, and control case inertia tensor.	100
3.47	Modeled asteroid principal maximum moment of inertia ratio with median and minimum principal moments of inertia in tumbling Bennu multiple boulder simulation. The parameters presented include parent body inertia ratio, asteroid inertia ratio, and control case inertia ratio.	101
3.48	Modeled asteroid and control case angular velocity evolution in tumbling Bennu multiple boulder simulation (asteroid body frame)	102
3.49	Modeled asteroid angle between simulation and control cases angular velocity vectors in tumbling Bennu multiple boulder simulation	103
3.50	Itokawa \sim 3000 facet polyhedron with 50 boulders distributed on its surface	106
3.51	Threshold angular velocity compared to Itokawa nominal for boulder motion. The heatmaps indicate surface (facet) properties, and the diamonds indicate boulders placed on the surface.	107
3.52	Boulder motion surface projection in Itokawa-like multiple boulder simulation. The heatmap indicates surface slopes, boulder initial position indicated by white dot, surface motion indicated by white line, boulder escape indicated by yellow diamonds, and boulder final position indicated by blue star.	109
3.53	Boulder orbit motion in Itokawa-like multiple boulder simulation	109
3.54	Modeled asteroid inertia tensor elements in Itokawa-like multiple boulder simulation. The parameters presented include parent body inertia tensor, asteroid inertia tensor, and control case inertia tensor.	111
3.55	Modeled asteroid principal maximum moment of inertia ratio with median and minimum principal moments of inertia in Itokawa-like multiple boulder simulation. The parameters presented include parent body inertia ratio, asteroid inertia ratio, and control case inertia ratio.	111

3.56	Modeled asteroid and control case angular velocity evolution in Itokawa-like multiple boulder simulation (asteroid body frame)	112
3.57	Modeled asteroid angular velocity vector projection on the equatorial plane and angle between angular velocity vector and initial axis of maximum inertia in Itokawa-like multiple boulder simulation (asteroid body frame)	112
3.58	Modeled asteroid angular velocity vector projection on inertial x-y plane and angle between angular velocity vector and initial axis of maximum inertia in Itokawa-like multiple boulder simulation (inertial frame)	113
3.59	Modeled asteroid and control case angular velocity evolution due to 10 kg particle launched at $37.4 \text{ m}\cdot\text{s}^{-1}$ from longitude and latitude [4.3 24.3] degrees (asteroid body frame)	119
3.60	Modeled asteroid angular velocity vector direction change due to 10 kg particle launched at $37.4 \text{ m}\cdot\text{s}^{-1}$ from longitude and latitude [4.3 24.3] degrees	119
3.61	Modeled asteroid and control case angular velocity evolution due to 1 kg particle launched at $1 \text{ m}\cdot\text{s}^{-1}$ from longitude and latitude [4.3 24.3] degrees (asteroid body frame)	120
3.62	Modeled asteroid angular velocity vector direction change due to 1 kg particle launched at $1 \text{ m}\cdot\text{s}^{-1}$ from longitude and latitude [4.3 24.3] degrees	120
3.63	Change to angular velocity due to 10 kg particle launched at $37.4 \text{ m}\cdot\text{s}^{-1}$ from longitude and latitude [4.3 24.3] degrees in various directions with respect to surface normal	121
3.64	Change to angular velocity due to 1 kg particle launched at $1 \text{ m}\cdot\text{s}^{-1}$ from longitude and latitude [4.3 24.3] degrees in various directions with respect to surface normal	122
3.65	Change in angular velocity due 10 kg particle launched at $37.4 \text{ m}\cdot\text{s}^{-1}$ from any point on surface in normal direction	124
3.66	Change in angular velocity due 1 kg particle launched at $1 \text{ m}\cdot\text{s}^{-1}$ from any point on surface in normal direction	125

3.67 Boulder motion surface projection for a 2.3 kg particle launch at $0.1 \text{ m}\cdot\text{s}^{-1}$ launched from longitude and latitude [4.3 24.3] degrees. The heatmap indicates surface slopes, particle initial position indicated by white dot, surface motion indicated by white line, particle launch and crash events indicated by triangles, orbit projection on surface indicated by dashed yellow line, and particle final position indicated by blue star.	127
3.68 Boulder orbit motion for a 2.3 kg particle launch at $0.1 \text{ m}\cdot\text{s}^{-1}$ launched from longitude and latitude [4.3 24.3] degrees	127
3.69 Modeled asteroid and control case angular velocity evolution due to 2.3 kg particle launched at $0.1 \text{ m}\cdot\text{s}^{-1}$ from longitude and latitude [4.3 24.3] degrees (asteroid body frame)	128
3.70 Modeled asteroid angular velocity vector direction change due to 2.3 kg particle launched at $0.1 \text{ m}\cdot\text{s}^{-1}$ from longitude and latitude [4.3 24.3] degrees	128
3.71 Boulder motion 500 case Monte Carlo surface projection for a 2.3 kg particle launch at $0.1 \text{ m}\cdot\text{s}^{-1}$ launched from longitude and latitude [4.3 24.3] degrees. The heatmaps indicate surface slopes, particle initial position indicated by white dot, surface motion indicated by white lines, particle launch and crash events indicated by triangles, orbit projection on surface indicated by dashed yellow lines, particle final positions indicated by gray stars, and yellow diamond indicates escaped particle.	130
3.72 Modeled asteroid angular velocity change due to 2.3 kg particle launched at $0.1 \text{ m}\cdot\text{s}^{-1}$ from longitude and latitude [4.3 24.3] degrees. Histograms include distribution means and 1σ bounds as well as control values.	131
3.73 Modeled asteroid angular velocity change due to 2.3 kg particle launched at $0.1 \text{ m}\cdot\text{s}^{-1}$ from longitude and latitude [-4.2 40.1] degrees. Histograms include distribution means and 1σ bounds as well as control values.	131

3.74	Modeled asteroid angular velocity change due to 2.3 kg particle launched at $0.1 \text{ m}\cdot\text{s}^{-1}$ from longitude and latitude $[-2.4 \text{ } 2.6]$ degrees. Histograms include distribution means and 1σ bounds as well as control values.	132
4.1	Precession reached for impacts on Bennu-like ellipsoid for $\hat{\mathbf{V}}_i = [0, -1, 0]$, the dot indicates the impactor direction parallel to the surface normal	140
4.2	Change in angular velocity magnitude reached for impacts on Bennu-like ellipsoid for $\hat{\mathbf{V}}_i = [-1, 0, 0]$, the dot indicates the impactor direction parallel to the surface normal, the dashed line indicates equal values between $ \omega _{max}$ and $ \omega_0 $	140
4.3	ΔV reached for impacts on Bennu-like ellipsoid for $\hat{\mathbf{V}}_i = [0, -1, 0]$, the dot indicates the impactor direction parallel to the surface normal	141
4.4	Precession reached for impacts located at $[25, 25]$ degrees on a Bennu-like ellipsoid, the star indicates the impactor direction parallel to the surface position	143
4.5	Change in angular velocity magnitude reached for impacts located at $[25, 25]$ degrees on a Bennu-like ellipsoid, the star indicates the impactor direction parallel to the surface position, the dashed line indicates equal values between $ \omega _{max}$ and $ \omega_0 $	143
4.6	ΔV reached for impacts located at $[25, 25]$ degrees on a Bennu-like ellipsoid, the star indicates the impactor direction parallel to the surface position	144
4.7	Precession reached for impacts on Itokawa-like ellipsoid for $\hat{\mathbf{V}}_i = [0, -1, 0]$, the dot indicates the impactor direction parallel to the surface normal	144
4.8	Change in angular velocity magnitude reached for impacts on Itokawa-like ellipsoid for $\hat{\mathbf{V}}_i = [0, -1, 0]$, the dot indicates the impactor direction parallel to the surface normal, the dashed line indicates equal values between $ \omega _{max}$ and $ \omega_0 $	145
4.9	Lever arm due to angle between surface position and surface normal for a Bennu-like ellipsoid	147
4.10	Lever arm due to angle between surface position and surface normal for a Itokawa-like ellipsoid	147

4.11 Lever arm due to angle between facet position and facet normal for Bennu polyhedral shape	148
4.12 Lever arm due to angle between facet position and facet normal for Itokawa polyhedral shape	148
4.13 Ejecta mass and velocity due to above surface nuclear detonation deflection from Sanchez et al. 2009	150
4.14 Asteroid polyhedra, impact locations, and ejecta mass	152
4.15 Deviation angle between launch velocity and velocity at Hill radius	154
4.16 Bennu angular velocity vector after kinetic interceptor impact	157
4.17 Bennu angle between angular velocity after kinetic interceptor impact and angular velocity prior to impact	157
4.18 Surface slopes on Bennu prior to deflection effort	158
4.19 Itokawa angular velocity vector after kinetic interceptor impact along x-axis	158
4.20 Itokawa angle between angular velocity after kinetic interceptor impact along x-axis and angular velocity prior to impact	159
4.21 Itokawa angular velocity vector after kinetic interceptor impact along y-axis	161
4.22 Itokawa angle between angular velocity after kinetic interceptor impact along y-axis and angular velocity prior to impact	161
4.23 Bennu angular velocity vector after nuclear detonation	162
4.24 Bennu angle between angular velocity after nuclear detonation and angular velocity prior to impact	162
4.25 Surface slopes on Bennu in a precession cycle after nuclear detonation	163
4.26 Precession reached for impacts located at [-84.4, 5.9] degrees on a polyhedral Bennu, the star indicates the impactor direction parallel to the surface position	166
4.27 Change in angular velocity magnitude reached for impacts located at [-84.4, 5.9] degrees on a polyhedral Bennu, the star indicates the impactor direction parallel to the surface position, the dashed line indicates equal values between $ \omega _{max}$ and $ \omega_0 $.	166

4.28	Δv reached for impacts located at $[-84.4, 5.9]$ degrees on a polyhedral Bennu, the star indicates the impactor direction parallel to the surface position	167
4.29	Precession reached for impacts located at $[25.0, 25.0]$ degrees on a polyhedral Bennu, the star indicates the impactor direction parallel to the surface position	167
4.30	Precession reached for impacts located at $[1.0, -0.9]$ degrees on a polyhedral Itokawa, the star indicates the impactor direction parallel to the surface position	168
4.31	Change in angular velocity magnitude reached for impacts located at $[1.0, -0.9]$ degrees on a polyhedral Itokawa, the star indicates the impactor direction parallel to the surface position, the dashed line indicates equal values between $ \omega _{max}$ and $ \omega_0 $.	168
4.32	Precession reached for nuclear detonations located above $[-84.4, 5.9]$ degrees on a polyhedral Bennu, the star indicates the impactor direction parallel to the surface position, the white areas indicate directions in which the rotation has reached LAM and thus ψ cycles through $[0, 360]$ degrees	169
4.33	Change in angular velocity magnitude reached for nuclear detonations located above $[-84.4, 5.9]$ degrees on a polyhedral Bennu, the star indicates the impactor direction parallel to the surface position, the dashed line indicates equal values between $ \omega _{max}$ and $ \omega_0 $	170
4.34	Δv reached for nuclear detonations located above $[-84.4, 5.9]$ degrees on a polyhedral Bennu, the star indicates the impactor direction parallel to the surface position . . .	170
4.35	Precession reached for impacts in direction of facet position on all surface locations on a polyhedral Bennu	172
4.36	Change in angular velocity magnitude reached for impacts in direction of facet position on all surface locations on a polyhedral Bennu	172
4.37	Δv efficiency reached for impacts in direction of facet position on all surface locations on a polyhedral Bennu	173
4.38	Precession reached for impacts in direction of facet position on all surface locations on a polyhedral Itokawa	174

4.39	Change in angular velocity magnitude reached for impacts in direction of facet position on all surface locations on a polyhedral Itokawa	175
4.40	Δv efficiency reached for impacts in direction of facet position on all surface locations on a polyhedral Itokawa	175
4.41	Precession reached for nuclear detonations in direction of facet position on all surface locations on a polyhedral Bennu	176
4.42	Change in angular velocity magnitude reached for nuclear detonations in direction of facet position on all surface locations on a polyhedral Bennu	176
4.43	Propagation comparison of true and linearized states	183
4.44	Deviation error between propagated and linearized solutions	185
4.45	Corrected rotation state of slightly precessing spacecraft	187
4.46	Single boulder launch results	191
4.47	Multiple boulder launch results	195
4.48	Tumble angular velocity change for different κ ratios	197
4.49	Single boulder tumble launch results	198
4.50	Boulder launch performance for launch direction and $\Delta v_{B,z}$ magnitude	203
4.51	Boulder launch performance for the asteroid Bennu	204
4.52	Bennu change in rotation rate due to boulder launch	205
4.53	Bennu change in rotation rate due to boulder launch	206
4.54	Bennu precession angle caused by directed boulder launch	206
4.55	Boulder launch performance for the asteroid Bennu for polar launch	206
4.56	Boulder launch performance for the asteroid Itokawa	207
4.57	Boulder launch performance on asteroid Bennu equatorial region	208
4.58	Bennu change in rotation rate due to boulder launch from equatorial region	208
4.59	Earth-Asteroid distance in 10 years prior to MOID	209
4.60	Deflection reached for single launch	213
4.61	Reached deflection in 10 year scenario	215

4.62 Orbit element evolution in 10 year scenario	215
4.63 Reached deflection in 10 year scenario with varying launch intervals	218
4.64 Orbit element evolution in 10 year scenario with varying launch intervals	218
4.65 Reached deflection in 10 year scenario with varying launch ΔV s	219
4.66 Orbit element evolution in 10 year scenario with varying launch ΔV s	219
4.67 Reached deflection in 10 year scenario with 5 degree $\Delta \hat{V}$ bias	220
4.68 Orbit element evolution in 10 year scenario with 5 degree $\Delta \hat{V}$ bias	220
4.69 Reached deflection in 10 year scenario of eccentric orbit	221
4.70 Orbit element evolution in 10 year scenario of eccentric orbit	221
4.71 Deflection reached for single launch with local minima presented	223
4.72 Reached deflection in 10 year scenario with maximum efficiency launch scheme . . .	223
4.73 Orbit element evolution in 10 year scenario with maximum efficiency launch scheme	224

Chapter 1

Background and motivation

1.1 Rubble pile asteroids

Asteroids are relics from the formation of the solar system. Seemingly having no active geological processes occurring on them, their compositions are thought to be mostly static since their formation. However, research and observations have shown evidence of dynamical processes that asteroids undergo, constantly reshaping them over long time spans. Two missions have been operating in the vicinity of asteroids in recent years: NASA’s Origins, Spectral Interpretation, Resource Identification, Security, Regolith Explorer (OSIRIS-REx) mission has orbited its target asteroid 101955 Bennu [1] for long periods in 2019 and JAXA’s Hayabusa-2 mission has been operating on and near its target, asteroid 162173 Ryugu [2], since mid 2018. Figures 1.1a and 1.1b present images taken by both missions of their prospective targets. Figure 1.1c shows an image of the asteroid 25143 Itokawa which was visited by the JAXA’s Hayabusa mission in 2005. All asteroids are small in size: about 0.5 km in mean diameter for Bennu, 1 km mean diameter for Ryugu [3], and 0.3 km for Itokawa [4], and are considered “rubble-pile” asteroids. The asteroid surfaces are inhomogeneous, presenting distinguishable areas rich and poor of large boulders, rough gravel, fine regolith as well as topographical features such as craters, ridges, and ponds. These are evidence of the slew of surface processes that asteroids experience in their lifetimes. The asteroids’ shapes themselves can also tell stories about the processes these small bodies have been through in their history, whether is be the spinning-top shape of Bennu and Ryugu, or the bi-lobe shape of Itokawa. The asteroid “rubble-pile” model was first suggested by Chapman [8] after comparing the esti-

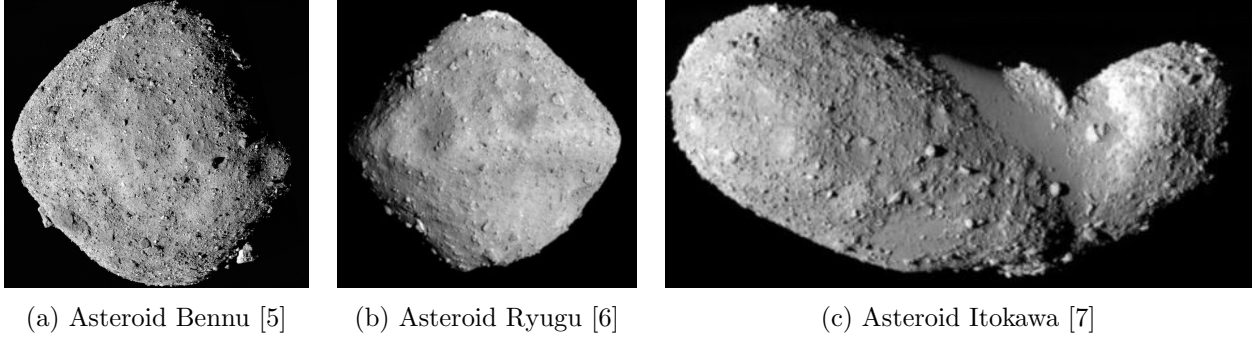


Figure 1.1: Images of asteroids Bennu, Ryugu and, Itokawa as captured by the OSIRIS-REx, Hayabusa-2, and Hayabusa missions, respectively

mated rate of asteroid collisions to the lifetime of the Solar System. This comparison led to the conclusion that large asteroids have gone through several cycles of breakup events and gravitational re-aggregation. Thus, rendering their structures aggregates of smaller boulders, gravel, and regolith, rather than single monolithic bodies. The “rubble-pile” model is supported by observations of asteroid sizes, shapes and spin states, which show a balance between the gravitational force that holds the aggregate together and the inertia of the rotating components pushing them outwards [9, 10]. These asteroids were more recently referred to as gravitational aggregates [9], or granular asteroids [11], in an attempt to better describe the range of internal structures they have. Gravitational aggregates range in diameter between 0.2 and 100 km and in spin periods between 2.2 and 12 hours [12]. Most objects rotating faster than the 2.2 hour lower limit are thought to be small (<0.2 km) monolithic bodies that have not been broken apart by collision events and are held together by the structural tensile forces in the single rock. This, in contrast to the gravitational force that holds larger bodies together. Slower rotating asteroids do exist, but they are a smaller share of the population. Bodies larger than 100 km are also present in the asteroid population, and are also held together by gravity. However, the magnitude of their gravity means that some of the forces and phenomena smaller asteroids are subject to are negligible for them.

Gravitational aggregates’ shapes are governed by the balance between their own gravity and rotation rate, the gravitational force pulling the asteroid material inward while the inertial centrifugal

force pushes it outwards. Recent research has found that cohesion also plays a substantial role in keeping an asteroid’s subcomponents together, at times presenting stabilizing forces that are orders of magnitude larger than the overall gravitational force [13, 14, 15, 16]. The balance between these forces can be quite delicate, as seen with asteroid Bennu [17], which presents significantly lower inward acceleration magnitudes on the equatorial ridge compared to the poles, demonstrating how the shape of the asteroid itself is in some type of equilibrium between gravity, rotation, and cohesion. When the balance between the forces is broken the total acceleration that a boulder or regolith deposit experiences can change enough in magnitude or direction to move it towards a new, lower, geopotential state. This new acceleration vector can point “downwards” to the lower geopotential or, if the rotational acceleration is larger in magnitude than the gravitational one, it can point “upwards” causing the boulder or material to be held to the surface by cohesion. If the cohesion forces are not sufficiently strong the boulder or material can launch into orbit or a hyperbolic trajectory. This process, in which mass is shed from the surface, is defined as rotational fission and it can happen to an asteroid in either local or global scales [7, 18, 19].

An asteroid is denoted as a Principal-Axis Rotator (PAR) when its angular velocity vector is aligned with one of its principal inertia axes, most commonly the maximum moment of inertia axis at the minimum energy state. The PAR characteristic leads to a time-constant angular velocity vector, which is fixed both in inertial space and in the rotating asteroid frame. This leads the surface geopotential to be constant as well. Observational data [20] has shown that a majority of asteroids are PARs. A small subset of non-PAR asteroids has been reported as well [21, 22], the gravitational aggregates among them appear to tumble slowly, providing a steady environment which is far from structural instabilities [23].

1.2 Driving forces of asteroid evolution

Although usually very slow changing, asteroid rotation rates do not remain constant throughout their life spans. Different types of processes and events can accelerate, decelerate or even reverse

asteroid spins. These could also shift the angular velocity vector to different directions, with respect to the asteroid body itself and or inertial space, potentially leading to changes in the geopotential. The Yarkovsky-O'Keefe-Radzievskii-Paddack (YORP) [24] effect was first coined by Rubincam [25] in 2000 as a rotational complementary to the orbital Yarkovsky effect. In these phenomena sunlight scattering and thermal re-radiation from an asteroid surface slowly torque and thrust an asteroid. These effects are small in magnitude, but their secular contribution accumulates and changes the asteroid's dynamical state over many years. The Yarkovsky and YORP effects have been pointed out as leading contributors in asteroid orbital and spin state evolution, especially for the Near-Earth Asteroid (NEA) population. Depending on an asteroid's shape, obliquity, and spin rate the YORP effect can accelerate or decelerate the angular velocity of an asteroid [26, 27], leading to changes in the balance between its gravity and rotation. In the case of an accelerating angular velocity a breach in the balance can lead to change in local accelerations that will cause boulder movement, landslides or even fission events. A decelerating asteroid can reach low rotation rates that are more susceptible to tumbling torques. YORP itself can induce non-PAR movement for a highly irregular shaped asteroid. However, a tumbling asteroid is less susceptible to YORP because of the complex motion of the torque's direction. YORP also leads asteroids to align their spin axes with their orbit plane, reaching obliquities of 0 or 180 degrees [28]. Being a radiative effect fueled by the Sun, YORP is more substantial for asteroids with smaller Semi-Major Axes (SMA), such as NEAs. It is also more effective on asteroids with oblate and elongated shapes due to the large lever arms it can apply.

Other, faster, mechanisms of changing an asteroid's angular velocity are collisions and planetary flybys. Collision [29] occurrence for a specific asteroid is in the realm of statistical probability over a given time span and is more likely for larger asteroids and bodies in the main asteroid belt. In addition to the possibility of such an event changing an asteroid's rotational and orbital state it can also directly disrupt the asteroid's surface or completely disaggregate it. Such disruptions, even local in nature, could cause movement of ejecta near the crash site or could cause global vibrations [30, 31] (seismic activity) that can induce motion of material anywhere on or in the asteroid. Some

of the ejecta created by collisions has been shown to drain angular momentum from an asteroid in a mechanism that cumulatively reduces an asteroid's spin rate [32].

Flyby events [33, 34], especially near planets, are easier to foresee, and their effect is also simpler to model. Most flybys do not directly affect the asteroid structure but can change its rotational and orbital states and lead to real time disruption [35] or set an asteroid in such a state that would lead to some event in the future. Asteroid 99942 Apophis is expected to change its orbit and rotation after its flyby of Earth in 2029 [36, 37], no immediate changes to its structure are expected.

The external mechanisms that affect an asteroid's rotation are counteracted by internal dissipation. Burns [38] has explained the small subset of that non-PAR asteroids by showing that asteroids dissipate any off-axis rotation during their lifetime. Thus, even if an event or a secular effect cause an asteroid to tumble, as observed for several asteroids [21], the PAR characteristic will return due to internal energy dissipation in the asteroid. The dissipation rate is proportional to r^{-2} , thus, expected to be slower for smaller asteroids.

Active asteroids [39] are a newly distinguished group of small bodies discussed by the scientific community. They present characteristics that place them on the spectrum between asteroids and comets. Mainly a combination of mass loss similar to comets and the orbital parameters of asteroids. As portrayed by their name active asteroids have, by nature, more activity on their surface. Water sublimation is suggested as the main mechanism of mass loss in these bodies, but several other phenomena, such as surface motion [40], have been proposed to explain some of the observed activities by these bodies. Surface motion has also been pointed out as a source of mass loss in tumbling asteroids [41], where ejections can be instigated by the irregular acceleration cycles that material on the surface might experience. Asteroid 311P/(2013 P5) PANSTARRS [42, 43] is thought to be a binary active asteroid and has been observed to have several discrete ejection events in 2013. These could be explained by motion of material on and off the surface of the primary. These events might have occurred as a result of the initial breakup of the asteroid which left the primary (and secondary) in some rotational instability or have left debris around the primary in orbital instability that led to crash events. Thermal fatigue [44] could cause fractures in surface

boulders, allowing boulder fragments to be freed to move on the surface, such as thought to have happened on asteroid (3200) Phaethon [40]. In 2013 asteroid P/2013 R3 [45] was observed to fragment into several components, possibly due to rotational fission. For several months the continued break-up of the asteroid was observed, with an initial component seen far away from the major cluster at the first observation. This object might have been the first to eject from the asteroid causing a cascade effect that led to the asteroid break-up. During its short time at its target, the OSIRIS-REx mission has observed several particle ejection events of asteroid Bennu [1]. The source of these events have yet to be identified, but thermal fracturing or meteoroid impacts have been pointed out as possible causes. The observed particles are cm in size and a singular event seems to have little to no effect on the asteroid itself. However, their accumulative effect could be part of the observed trends in asteroid state evolution.

Evidence of the phenomena that change asteroid states and the surface motion they induce has been observed on various seemingly dormant asteroids [46]. Examples of the relationship between asteroid rotation and shape were observed for asteroids Ryugu and Bennu [47, 17]. Evidence of surface movement of boulders was seen on asteroid 433 Eros [48, 49, 50]. These surface movement events seem to include boulder surface bounces and subsequent rolling/sliding motion, seen by displaced regolith in the boulder paths. Boulders on Eros have also been pointed out as possible precursors for ponds observed on the surface [51]. Cases of regolith, gravel, and boulder migration were seen on asteroids Bennu, Ryugu, and Itokawa [52, 53, 4]. Additionally, evidence of small scale collision events and their effects on Itokawa's surface have been observed [54]. More generally, the size distribution of boulders observed on asteroid Itokawa was linked to its surface geopotential [55]. Boulder distribution seen near an impact crater on asteroid 21 Lutetia was linked to the crater formation and is thought to be ejecta from the impact that created it [56]. Lastly, the mechanism for regolith migration observed on Mars' satellite Phobos has been suggested to stem from the dynamic geopotential surface environment caused by Mars' tidal forces [57].

1.3 Artificial manipulation of asteroids

The concept of asteroid manipulation is almost as old as the first discoveries of asteroids; From the 1898 "War of the Worlds" spin-off "Edison's Conquest of Mars" [58] which describes Martians mining gold from an asteroid to NASA's Asteroid Redirect Mission [59] that was planned to collect a boulder from the surface of an asteroid and retrieve it in to an orbit around the moon. There are many reasons to manipulate an asteroid's state. These include deflection of an asteroid that poses a threat to Earth, removal of materials off an asteroid for mining purposes, or rearrangement of surface areas for In-Situ Resource Utilization (ISRU) and research.

The discussion on the threat of a catastrophic asteroid collision with Earth is a question of when, not if, such an event will occur. Governments, space agencies, and the scientific community have been addressing this threat on several avenues: Potentially Hazardous Object (PHO) detection, global readiness for a possible collision, and research and development of collision prevention methods. Collision prevention by complete removal of a PHO is highly unlikely due to the size and momentum of such objects. Thus, the swath of solutions discussed to date refers to collision prevention by deflection. In PHO deflection an object's orbit is slightly perturbed in such a way that enlarges the body's Earth flyby Minimum Orbit Intersection Distance (MOID), leading it to miss our planet by a safe margin.

The population of PHOs includes both asteroids and comets. Although comets are at times larger than asteroids and have more eccentric orbits with potentially higher relative velocities, the Earth orbit crossing comet population is substantially smaller than that of asteroids [60]. In particular the NEA population, which crosses the Earth's orbit regularly, has been of interest when discussing PHOs to be addressed by deflection. Many methods of asteroid deflection have been and continue to be researched, some of which are applicable to asteroids and comets alike. All deflection methods require some kind of momentum transfer mechanism from the deflecting measure to the asteroid being deflected [61]. The predominant methods discussed include: nuclear detonation, kinetic interception, gravity tractor, the ion shepherd, high energy beams, and asteroid thrusting. Deflection

by nuclear detonation requires use of a nuclear device on or near the surface of a PHO while focusing the detonation radiation to the body's surface [62]. In the stand-off variation of this method the focused radiation leads to high surface temperatures causing ablation and, in turn, material ejection. If enough material is ejected at high velocities it will carry with it some of the PHO's orbital momentum, leading to the desired deflection. A kinetic interceptor brings the deflection momentum with it when it directly impacts the PHO. The momentum transfer reached due to a high relative velocity between intercepting spacecraft and target PHO [63, 64]. In addition to the spacecraft-PHO momentum exchange, this method is also expected to lead to some debris ejection, enhancing the deflection effort by hundreds of percents. Gravity tractor deflection is done by flying a heavy spacecraft near an asteroid in a defined orbital direction, gravitationally perturbing the asteroid's orbit over a long period [65]. The momentum transfer in this method is less obvious, originating from the spacecraft's propulsion system as it keeps its relative position with respect to the asteroid. Similarly to the gravity tractor method, the ion-beam shepherd concept would perturb an asteroid's orbit from a nearby spacecraft by bombarding the PHO with high velocity ions which will gently push it [66]. This method reduces the mass needed for a gravity tractor, but in turn requires a thruster to counter the ion cannon. Applying high energy beams on the surface of a PHO, usually from a nearby spacecraft, is meant to reach a similar effect as a nuclear device, causing surface ablation and momentum transfer through ejecta [67]. Unlike the nuclear device, this method applies the radiation over a long period of time, requiring less energy at any given time and enabling course corrections. Asteroid thrusting with a landed device essentially turns an asteroid into a spacecraft, applying continuous or impulsive thrust on the asteroid [68, 69]. Similarly to the tractor concepts, this method transfers momentum from some propulsion system, whether it be chemical, electric, kinetic, or solar radiation pressure based.

Asteroid orbit manipulation does not necessarily have to be applied for PHO deflection purposes. Advanced research studies [70, 71, 72] have described concepts which could enable asteroid maneuvering in the distant future. Some of these concepts even require manipulation of the asteroid's rotation as part of their operational scheme.

Similarly to the variety of deflection methods, several asteroid mining and ISRU concepts are being discussed and researched [73]. Amongst them are complete boulder removal, water extraction and regolith collection. These methods do not necessarily call for transferring momentum to or from the asteroid, but the movement of material on or off an asteroid surface will change the mass distribution of the asteroid and in turn affect its rotational state.

1.4 State-of-the-art of Rubble-pile modeling

Since the first asteroid missions were proposed and executed many models of the processes and mechanisms that occur on asteroids have been developed and described. These models examine the balance between gravitational aggregates' gravity, rotation, and cohesion forces inside asteroid structures and in their environments. Usually these research efforts are based on one of three gravity models used for astrodynamics research: the basic point mass, or masses, model, the spherical harmonics expansion, or the polyhedral gravity model.

In the context of gravitational aggregate modeling the point mass model has two variations to it: simple shape analyses of a limited number of bodies or complete N-body simulations which examine hundreds or thousands of point masses. Past research using simplified shapes to represent gravitational aggregates was conducted by Scheeres and Jacobson [7, 74, 75, 76, 77]. These research efforts examine the relative motion between two spheres or ellipsoids under YORP induced torque to map possible stability states, fission events, and the types of systems that result from these processes: disaggregated asteroids, binary, and contact binary systems. Additional work on simplified shapes examined the surface motion dynamics in geopotential environment of rotating ellipsoids [78] or cubes [79]. This type of work allows for simple analytical understanding and a low computational burden on the systems examined. However, this simplicity can lack in properly representing an asteroid system: forcing symmetry where it does not exist and overlooking phenomena that appears on complex shapes.

N-body simulation tools use multiple point masses or simplified shapes and examine their inter-

action to model the behavior gravitational aggregates' subcomponents with respect to each other. The point masses' interactions usually include gravitational attraction, pulling masses together, and normal forces, modeling the volume of material and keeping the modeled body from collapsing to a single point. Additional forces such as cohesion or friction can be applied to model Van der Waals attraction between the subcomponents. These tools have been used to examine the formation processes of asteroids [80, 81] and asteroid families [82, 83, 84]. More specifically N-body simulations of rapidly rotating gravitational aggregates have been used by Richardson, Walsh, and Hirabayashi to show the relationships between asteroid systems' shapes and rotation states [85, 86, 87, 88], some under the influence of cohesion forces [89, 90]. Research by Scheeres, Sanchez, and others using N-body and granular simulations has also been done to understand the magnitude of internal stresses and cohesion forces inside gravitational aggregates, on their surface, and between specific types of subcomponents [13, 91, 92, 93, 94, 95]. This type of simulations has also been used to understand the landing dynamics of small rovers in small body environments [96]. N-body simulation tools provide significantly higher resolution of the granular nature of gravitational aggregates, but they do that at the cost of computational complexity.

Spherical harmonics expansion is a common method used to efficiently and precisely model the gravity around celestial bodies. It is commonly used to model the motion of spacecraft operating near a small body, and it has been used to map the gravitational regime around small bodies [97]. However, it can fail to correctly model the gravity inside the Brillouin sphere, the sphere that encompass the entire shape of a small body [98]. An adaptation to the spherical harmonics gravity expansion for points inside the Brillouin sphere, the interior spherical harmonics gravity field, was developed and proven [99]. This method can be used to examine the geopotential on small body surfaces, but when discussing objects that can transition in and out of the Brillouin sphere a transition between the models is required as well, adding complexity to the modeling process.

The polyhedral gravity model was first presented by Werner and Scheeres [100]. It uses a polyhedral shape represented by a list of vertices their correlation in the form a list of facets to provide an exact solution for the gravity above, on, and below the surface of a uniform density polyhedron.

Using the polyhedral gravity model allows the connection of the gravity field to other geometric characteristics of a small body, such as surface normals and facet locations. This allows for a good representation of the geopotential environment of asteroids [101, 17, 102, 103]. Past research done by Tardivel and Van Wal [104, 105, 106] has used the polyhedral model together with other geometric models to simulate the motion of small landers and rovers on and around asteroid surfaces. However, due to the large mass ratio between asteroid and lander the effect the lander's motion might have had on the asteroid was not modeled. Tardivel has used the polyhedral and N-body models to examine cavities observed on asteroids 2008 EV5 and 2000 DP107 and their possible origin from fission events [107]. This work linked the rotational state to be the cause of the cavities, but it did not close the loop by examining the cavity formations' affects on the asteroids rotation. A well known downside for the polyhedral gravity model is its enforcement of a uniform density distribution. This assumption is usually sufficient in examining asteroid environments, especially far from the surface, but it can misrepresent gravitational aggregates' internal structures. Takahashi developed an expansion for the polyhedral gravity model that applies non-uniform densities [108]. This model allows a better comparison between possible polyhedral gravity models and the spherical harmonics observed by asteroid missions. However, it requires an a-priori internal mass geometry to be defined and constrains the density distribution to that geometry.

A different approach to research of gravitational aggregates' structures uses structural analysis of the stresses and strains inside the bodies' shapes that result from their own rotations. This research has been done on simplified shapes [109, 110] and known small body shapes [111, 112]. It has also been expanded to more complex numerical methods such as finite elements [113, 114] and a hybrid finite elements N-body simulations [115]. Using finite elements allows the modeled small body to deform and expanding the model with N-body simulation allows it to break apart, but it does it at a computational burden cost.

Additional research that should be mentioned in the context of gravitational aggregates is experimental studies into ejecta from an impact. These experiments, reported by Housen and Holsapple [116, 117, 118] shot projectiles into asteroid simulant to study the process of crater formation, ex-

aming the ejecta mass, velocity, and overall trajectories. The results were then scaled to asteroid scales for insight into observed natural impact craters and implications for asteroid deflection.

The research in to the dynamics of gravitational aggregates is expansive both in methods and in applications. This research has mostly focused on how changes in asteroid rotation might affect asteroid structures and surface geopotential. Some research into the effect asteroid shapes have on their rotation has been preformed, but it did so in a global context, studying asteroid shape analogs in aggregation, disaggregation, or reaggregation processes. The following observation summarizing the identified gap can thus be made:

There exists no model to examine small scale processes on small bodies in general, and asteroids in particular, and their effect on, and relationship with, the bodies' rotation states.

Addressing the identified gap would provide the small body community with tools to examine localized surface processes and their relationship with small body rotations.

1.5 Thesis statement

The work carried out in this thesis can be summarized under the following statement

Processes that occur on asteroid surfaces influence the dynamical state of asteroid rotational and orbital motion, and vice versa. Quantifying how natural and artificial surface processes affect asteroids is necessary to understanding how asteroids evolve and is crucial for human activities on or near asteroids.

1.6 Thesis overview

1.6.1 Contributions

This dissertation

- (1) Develops and describes a hybrid model for small scales activity and phenomena on asteroid surfaces and their relationship with asteroid rotational and orbital states

- (2) Shows that material on asteroid surfaces under various motion and dynamical conditions nominally trends towards the equator even in the presence of chaotic influences such as variables in movement path and orbital motion in small body environments
- (3) Demonstrates how surface motion leads to reduced rotation rates and introduction of precession of the angular velocity
- (4) Introduces a mechanism for small scale random walk behavior of asteroid angular momentum direction in inertial space
- (5) Presents the effect of small scale particle events on asteroid surfaces and the, lower than currently observable, magnitudes of changes expected from these events
- (6) Develops a model for small body momentum transfer deflection which accounts for asteroid rotation and demonstrates the rotational outcomes of momentum transfer deflection: near-spherical asteroids have negligible consequences due to impactor misalignments with required deflection direction, but elongated asteroids or powerful nuclear detonation deflection efforts have the potential to disrupt asteroid rotation in a way which is potentially catastrophic to the asteroid structure
- (7) Derives a linearized model for small scale inertia tensor and angular velocity changes in principal axis rotating bodies
- (8) Examines the dynamics of mass driver deflection and develops guidance laws for material launch from asteroid surfaces while minimizing effect on asteroid rotation, the biggest factor in mass driver deflection design is the latitudinal surface position the mass driver deflection is preformed from
- (9) Analyses orbit dynamics variables in mass driver deflection and shows that an 'earlier is better' approach in mass driver deflection reduces the required deflection efforts

1.6.2 Dissertation outline

This dissertation is organized as follows:

Chapter 2 presents the dynamical model used in this work together with the assumptions it is based on. Additionally, Chapter 2 describes the numerical implementation of the model and presents the logical flow in its core.

Chapter 3 implements the model presented in naturally induced dynamical behavior of asteroids. The chapter consists of two sections: Section 3.1 presents dynamical behavior of fast rotating asteroids with multiple examples and analysis, and Section 3.2 presents an analysis of the effects small particle events potentially have on small rubble-pile asteroids.

Chapter 4 implements the model on human induced activity on asteroids. First, Section 4.1, utilizes the model to examine the effects of momentum transfer deflection on asteroid states, and vice versa. Section 4.2 further expands the dynamics from Chapter 2 to develop the dynamics of material removal from asteroid surfaces in the context of asteroid rotation. These dynamics are then implemented on asteroid manipulation scenarios.

Lastly, Chapter 5 presents avenues for future development of the model presented and additional analysis that can be performed with it.

1.6.3 Publications

1.6.3.1 Journal papers

Accepted

- Brack, D.N., & McMahon, J.W. (2019). Active Mass Ejection for Asteroid Manipulation and Deflection (accepted). *Journal of Spacecraft and Rockets*.
- Brack, D.N., & McMahon, J.W. (2019). Modeling the Coupled Dynamics of an Asteroid with Surface Boulder Motion (In print). *Icarus*.
- Scheeres, D.J., McMahon, J.W., French, A.S., Brack, D.N., Chesley, S.R., Farnocchia,

D., Takahashi, Y., Leonard, J.M., Geeraert, J., Page, B. & Antreasian, P. (2019). The dynamic geophysical environment of (101955) Bennu based on OSIRIS-REx measurements (In print). *Nature Astronomy*.

- Venigalla, C., Baresi, N., Aziz, J.D., Bercovici, B., Brack, D.N., Dahir, A., De Smet, S., Fulton, J., Pellegrino, M.M. & Van wal, S. (2019). Near-Earth Asteroid Characterization and Observation (NEACO) Mission to Asteroid (469219) 2016 HO3 (In print). *Journal of Spacecraft and Rockets*.

Submitted

- Brack, D.N., & McMahon, J.W. Effects of Momentum Transfer Deflection Efforts on Small Body Rotational State. *Journal of Guidance, Control and Dynamics*.
- Scheeres, D.J., McMahon, J.W., Brack, D.N., French, A.S., Chesley, S.R., Farnocchia, D., Vokrounhlicky, D., Ballouz, R.L., Emery, J.P., Rozitis, B., Nolan, M.C., Hergenrother, C.W., Lauretta, D.S. Particle ejection contributions to the rotational acceleration and orbit evolution of Asteroid (101955) Bennu. *Journal of Geophysical Research*.

1.6.3.2 Conference proceedings

- Brack, D.N., & McMahon, J.W. (2019). Effects of Momentum Transfer Deflection Efforts on Small Body Rotational State. 70th International Astronautical Congress (IAC).
- Brack, D.N., & McMahon, J.W. (2019). Asteroid Deflection With Active Boulder Removal. 2019 AAS/AIAA Astrodynamics Specialist Conference.
- Brack, D.N., & McMahon, J.W. (2019). The Dynamical Surface Environment of Tumbling Asteroids. 50th AAS/Division of Dynamical Astronomy Meeting.
- Brack, D.N., & McMahon, J.W. (2019). Asteroid Manipulation With Active Boulder Removal. 2019 AAS/AIAA Space Flight Mechanics Meeting.

- Brack, D.N., & McMahon, J.W. (2018). Natural Dynamical Processes on Fast Rotating Asteroids. 69th International Astronautical Congress (IAC).
- Brack, D.N., McMahon, J.W., Scheeres, D.J. & French, A.S. (2018). Estimation Evaluation of the Radio Science Phase of the OSIRIS-REx Mission. 69th International Astronautical Congress (IAC).
- Brack, D.N., McMahon, J.W. (2018). An Investigation of Natural Dynamical Processes on Asteroid Surfaces Using a Combined Asteroid Surface-Boulders Model. 2018 AAS/AIAA Astrodynamics Specialist Conference.
- Brack, D.N., McMahon, J.W. (2018). Dynamical Behavior of an Asteroid Undergoing Material Removal. 2018 AIAA/AAS Space Flight Mechanics Meeting.

1.6.3.3 Posters

- Brack, D.N., McMahon, J.W., Scheeres, D.J. & French, A.S. (2018). Estimation Evaluation of the Radio Science Phase of the OSIRIS-REx Mission. 15th International Planetary Probe Workshop (IPPW).

Chapter 2

Dynamical model and numerical implementation

2.1 The Surface phenomena Effect on Asteroid Rotational And Translational State model

To investigate the dynamics of small scale events on asteroid surfaces and their relationship with rotational states the Surface phenomena Effect on Asteroid Rotational And Translational State (SEA RATS) model uses rigid body dynamics to model an asteroid and boulders on its surface. This hybrid model combines the relatively simple polyhedral gravity model with multi-body dynamic interaction model to examine the processes that lead to small perturbations on an asteroid's state. Specifically, the model examines the balance between gravitational pull, rotational acceleration, and cohesion forces on asteroid surfaces. The boulder motion scheme presented in the following sections is integrated into the SEA RATS model to determine when and how boulders should move on the surface. The model also allows for fission to occur by launching boulders or parts of the monolithic asteroid itself off the surface. Launched material is then propagated in orbit with the ability to crash back to the surface or escape the asteroid system completely.

2.2 Assumptions and definitions

2.2.1 The modeled system

The system is modeled as the combination of one large monolithic polyhedral body with N smaller polyhedrons in its vicinity, either resting on its surface or in orbit around it. The large monolithic polyhedron is defined as the parent body and denoted with the letter P . The small

polyhedrons are defined as boulders and denoted with the letter B . All bodies are assumed to be rigid bodies with constant density distributions (which may vary from body to body). Although the parent body is of uniform density, it is assumed to have harder core, so that the modeled asteroid structural failure is on its surface, leading to surface boulder motion or surface fission, rather than the structural failure happening underneath the surface, as proposed in [88]. The asteroid model is defined as the combination of the parent body and all boulders on its surface at any given time, it is denoted with the letter A . Boulders that are not on the surface but have negative orbital energy with respect to the asteroid model are considered orbiting boulders. Boulders with positive orbital energy with respect to the asteroid model are considered escaped boulders. Escaped boulders are no longer considered part of the asteroid system. Additionally, the model can allow sections of the parent body polyhedron to be sliced out of the original geometry to create two polyhedra at each slicing event. This, while preserving the overall shape and volume of the original parent body. This application of the model simulates a fission event in which material is ejected from the parent body. The larger of the newly created polyhedral shapes is defined as the parent body, while the smaller shape is denoted as fissioned material and treated dynamically like a boulder. The overall number of boulders gravitationally bound to the asteroid system is N , the subsets of boulders on the surface and in orbit are denoted as N_S and N_O , respectively. The number of escaped boulders is denoted as N_E , the number of fissioned aggregates (that have not escaped) is N_F , and the initial number of boulders in the system is N_I . The total number of boulders in the system at any given time is

$$N = N_S + N_O = N_I - N_E + N_F \quad (2.1)$$

Including the parent body a model begins with $N_I + 1$ bodies in the system (assuming fission has not occurred at $t \leq 0$). The asteroid model mass is the sum of the parent body mass and all the masses of boulders on it's surface at any given time. The overall system mass is the sum of the

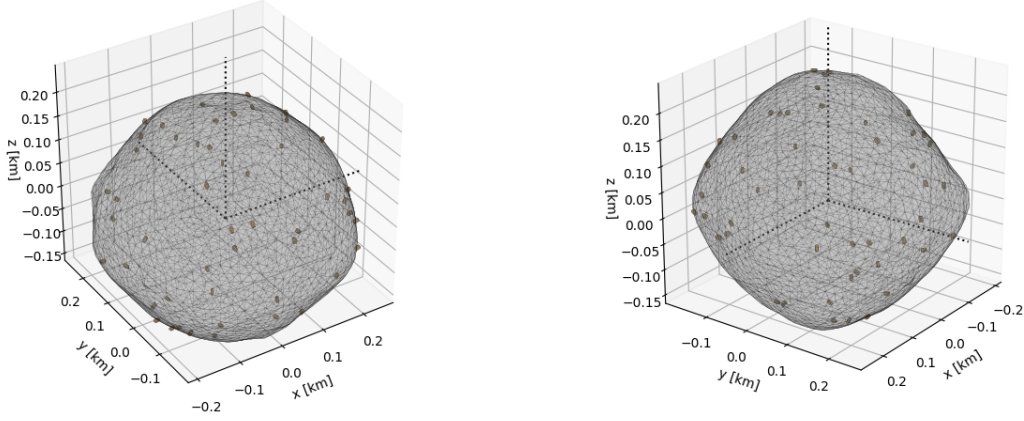


Figure 2.1: Bennu ~ 6000 facet polyhedral shape model with 50 boulders distributed on its surface

parent body mass and the masses of all boulders captured in the system's gravity well

$$M_A = M_P + \sum_{j=1}^{N_S} M_{B,j} \quad (2.2)$$

$$M = M_P + \sum_{j=1}^{N_S} M_{B,j} + \sum_{j=1}^{N_O} M_{B,j} = M_A + \sum_{j=1}^{N_O} M_{B,j} \quad (2.3)$$

Each boulder mass is assumed to be much smaller than the parent body ($M_{B,j} \ll M_P$).

An example of a SEA RATS initial model asteroid setup can be seen in Figure 2.1 which shows two views of a ~ 6000 facet polyhedron representing the asteroid Bennu with 50 boulders distributed on its surface. In this case the boulders are identical in shape and size, and are distributed evenly for the analysis presented in Figures 2.8 and 2.10.

Two types of reference frames are defined for the system, a single inertial frame, \mathcal{I} , and multiple body frames, \mathfrak{B} , that correspond with each polyhedron. The inertial frame's directions are fixed and its origin is set to the Center of Mass (CM) of the system as it orbits the Sun. Due to the mass ratio between parent body and boulders the changes in the asteroid model's CM position due to boulder motion are assumed negligible. For example, moving a 500 ton boulder from Bennu's pole to its equator would move the asteroid CM by ~ 2.5 mm. When examining this change in the context of Bennu's $\sim 30 \text{ km}\cdot\text{s}^{-1}$ orbital velocity around the Sun six orders of magnitude difference is seen. Thus, the CM of the asteroid model is set to coincide with the parent body's CM and the inertial frame origin, $\mathbf{r}_A = \mathbf{r}_P = \mathbf{0}$, $\dot{\mathbf{r}}_A = \dot{\mathbf{r}}_P = \mathbf{0}$. In addition, the asteroid model body frame and

the parent body frame are set to coincide, $\mathfrak{B}_A = \mathfrak{B}_P$. A boulder's CM position and velocity with respect to the origin in a general frame \mathfrak{G} are denoted as $\mathbf{r}_{B,j}^{\mathfrak{G}}$ and $\dot{\mathbf{r}}_{B,j}^{\mathfrak{G}}$, respectively. In the inertial frame they are denoted using upper case letters, $\mathbf{R}_{B,j}$ and $\dot{\mathbf{R}}_{B,j}$, respectively.

The inertia tensor of the asteroid model is the sum of the inertia tensor of the parent body and all boulder's on its surface

$$[I_A]^{\mathfrak{B}_A} = [I_P]^{\mathfrak{B}_A} + \sum_{j=1}^{N_S} \left([T]_{\mathfrak{B}_{B,j}}^{\mathfrak{B}_A} [I_{B,j}]^{\mathfrak{B}_{B,j}} + M_{B,j} [\tilde{\mathbf{r}}_{B,j}]^{\mathfrak{B}_A} [\tilde{\mathbf{r}}_{B,j}]^{\mathfrak{B}_A T} \right) \quad (2.4)$$

Here the $[T]_{\mathfrak{B}_{B,j}}^{\mathfrak{B}_A}$ term is the rotation matrix between the j th boulder body frame and the asteroid model body frame and is a function of the boulder's attitude, $[T] = [T](\boldsymbol{\sigma})$. The $M_{B,j} [\tilde{\mathbf{r}}_{B,j}]^{\mathfrak{B}_A} [\tilde{\mathbf{r}}_{B,j}]^{\mathfrak{B}_A T}$ element is the parallel axis contribution of each boulder's position on the surface where the cross-product operator is denoted as $[\tilde{\mathbf{a}}] = \mathbf{a} \times$.

The system's angular momentum is the sum of the asteroid model's and orbiting boulders' angular momenta with respect to the origin

$$\mathbf{H}^{\mathfrak{J}} = \mathbf{H}_A^{\mathfrak{J}} + \sum_{j=1}^{N_O} \mathbf{H}_{B,j}^{\mathfrak{J}} = [T]_{\mathfrak{B}_A}^{\mathfrak{J}} [I_A]^{\mathfrak{B}_A} \boldsymbol{\omega}_A^{\mathfrak{B}_A} + \sum_{j=1}^{N_O} \left([T]_{\mathfrak{B}_{B,j}}^{\mathfrak{J}} [I_{B,j}]^{\mathfrak{B}_{B,j}} \boldsymbol{\omega}_{B,j}^{\mathfrak{B}_{B,j}} + M_{B,j} [\tilde{\mathbf{r}}_{B,j}]^{\mathfrak{J}} [\tilde{\mathbf{r}}_{B,j}]^{\mathfrak{J}} \right) \quad (2.5)$$

Here the angular momentum is presented in the inertial frame because in this frame, nominally, no external torques are applied and thus the system's angular momentum is constant. When there are no orbiting or ejected boulders the angular momentum of the system is the asteroid model angular momentum $\mathbf{H}^{\mathfrak{J}} = \mathbf{H}_A^{\mathfrak{J}}$.

2.2.2 Rotational dynamics

The asteroid model and orbiting boulders are modeled as rotating rigid bodies where the angular velocity dynamics without torques are governed by Euler's equation for rigid body dynamics

$$[I]\dot{\boldsymbol{\omega}} = -[\tilde{\boldsymbol{\omega}}][I]\boldsymbol{\omega} \quad (2.6)$$

In case of a PAR body this differential equation is degraded to $\dot{\boldsymbol{\omega}} = \mathbf{0}$ and the time constant nature of the system is seen mathematically. However, the dynamics of non-PARs are more complex

and lead to a time varying system that requires mathematical manipulations to solve analytically. An example for a solution of torque free rotation in the context of small bodies was presented by Samarasinha and A'Hearn [119]. As part of the solution several definitions are made: first, a distinction between two modes of non-PAR behavior is provided - Short-Axis Mode (SAM) and Long-Axis Mode (LAM), then the evolving Euler angles between the body's principal axes and angular momentum are defined, and lastly the cycle periods (or averaged periods) of these angles are derived. SAM and LAM are non-PAR regimes near the two extreme principal axes, in SAM the angular momentum vector in the body frame rotates about the maximum inertia axis (the shortest of the three principal axes) and in LAM the angular momentum vector rotates about the minimum inertia axis (the longest of the principal axes). Perfect alignment of the angular momentum with one of these axes is PAR. Alignment with the median inertia axis is the boundary between SAM and LAM and is an unstable state. The majority of asteroids are PAR around the maximum inertia axis, the minimum energy state [38], or in SAM near it. When analytically solving Euler's equation an understating of the rotation mode is required in order to apply the solution correctly. The model presented in this work solves Euler's equation using numerical integration and thus it does not need to account for the rotation mode in the solution process. However, the motion simulated in this work is initiated at or near maximum inertia axis PAR, and thus unless mentioned otherwise the motion is assumed to be SAM and treated accordingly.

In SAM the angle between the body frame angular velocity vector and the maximum inertia axis can be described by [119]

$$\psi = \tan^{-1} \left(\frac{I_{pa,y}\omega_{pa,y}}{I_{pa,z}\omega_{pa,z}} \right) \quad (2.7)$$

where $I_{pa,y}$ and $\omega_{pa,y}$ are the median principal axis moment of inertia and angular velocity components, respectively, and $I_{pa,z}$ and $\omega_{pa,z}$ are their maximum principal axis equivalents. For the purpose of this work this angle will be defined as the angle of precession. In SAM rotation this angle is always acute ($\psi \leq \pi/2$). The angle's cycle period is

$$P_\psi = 4\sqrt{\frac{I_{pa,x}I_{pa,y}I_{pa,z}}{2E(I_{pa,z} - I_{pa,y})(M^2/(2E) - I_{pa,x})}}K(k^2) \quad (2.8)$$

where $I_{pa,x}$ and $\omega_{pa,x}$ are the minimum principal axis moment of inertia and angular velocity components, respectively, $E = 1/2(I_{pa,x}\omega_{pa,x}^2 + I_{pa,y}\omega_{pa,y}^2 + I_{pa,z}\omega_{pa,z}^2)$, $M^2 = (I_{pa,x}^2\omega_{pa,x}^2 + I_{pa,y}^2\omega_{pa,y}^2 + I_{pa,z}^2\omega_{pa,z}^2)$, $k^2 = ((I_{pa,y} - I_{pa,x})(I_{pa,z} - M^2/(2E)))/((I_{pa,z} - I_{pa,y})(M^2/(2E) - I_{pa,x}))$, and $K(k^2)$ is the complete elliptic integral of the first kind. This period represents an oscillatory roll around the body's long axis as it rotates with respect to the angular momentum. The maximum value of this angle can also be found analytically

$$\psi_{max} = \tan^{-1} \left(\sqrt{\frac{I_{pa,y}(I_{pa,z} - M^2/(2E))}{I_{pa,z}(M^2/(2E) - I_{pa,y})}} \right) \quad (2.9)$$

For the purpose of this work an additional angle is defined:

$$\tilde{\psi} = |\cos^{-1}(\hat{\omega} \cdot \hat{z})| \quad (2.10)$$

This angle is the magnitude angle between the evolving angular velocity and initial maximum inertia axis (which for the modeled asteroid coincides with the z-axis). This angle encompasses in it the precession angle in addition to other manipulations that are inflicted on the angular velocity. It can be defined either in the asteroid body frame or in the inertial frame, depicting changes in the rotational state depending on the observer.

The attitude dynamics are described using the Modified Rodrigues Parameters (MRP), denoted as σ . The MRP's relation to the angular velocity is

$$\dot{\sigma} = \frac{1}{4}[(1 - \sigma^T \sigma)[I_{3 \times 3}] + 2[\tilde{\sigma}] + 2\sigma\sigma^T]\omega \quad (2.11)$$

Each boulder is modeled as a rigid body itself; however, while resting on the parent body surface the boulders' motion is linked to the parent body's. Their angular velocities are matched to the parent body's and their attitudes are propagated accordingly.

2.2.3 Modeled events

Several types of surface phenomena are defined for the model -

- (1) Boulder movement on the surface. Referred to as “boulder surface movement”.
- (2) Boulder separation from the surface. Referred to as “boulder launch”.
- (3) Boulder return to the surface. Referred to as “boulder crash”.
- (4) Boulder launch or transition to a hyperbolic trajectory. Referred to as “boulder escape”.
- (5) Polyhedral slice from the parent body. Referred to as “fission event”.

2.3 Surface phenomena effect on model asteroid rotation

The model allows for boulder motion on and off the surface of the asteroid model to be simulated. The mechanism of boulder motion is described in Sections 2.4-2.5, as a local process that has to do with a single boulder or material deposit at a time. When discussing the global effects of a moving boulder two contributions to the overall system dynamics can be described: the direct transfer of momentum and the change in overall mass properties.

2.3.1 Boulder surface movement

In the case of boulder surface movement the j th surface boulder ($j \subset N_S$) moves on the parent body, either on a single facet or between two facets, with a change in its attitude with respect to the parent body. This means there is some rearrangement of the asteroid model mass distribution while the overall asteroid model mass remains constant ($M_A = M_A^+ = M_A^-$)¹. The change in inertia tensor reflects the movement and reorientation of the boulder

$$[I_A^+]^{\mathfrak{B}_A} = [I_A^-]^{\mathfrak{B}_A} + ([T^+]_{\mathfrak{B}_{B,j}}^{\mathfrak{B}_A} - [T^-]_{\mathfrak{B}_{B,j}}^{\mathfrak{B}_A})[I_{B,j}]^{\mathfrak{B}_{B,j}} + M_{B,j}([\tilde{\mathbf{r}}_{B,j}^+]^{\mathfrak{B}_A}[\tilde{\mathbf{r}}_{B,j}^+]^{\mathfrak{B}_A T} - [\tilde{\mathbf{r}}_{B,j}^-]^{\mathfrak{B}_A}[\tilde{\mathbf{r}}_{B,j}^-]^{\mathfrak{B}_A T}) \quad (2.12)$$

Assuming that the angular momentum of the asteroid model remains constant ($\mathbf{H}_A = \mathbf{H}_A^+ = \mathbf{H}_A^-$) the angular velocity changes proportionally to the change in inertia tensor

$$\boldsymbol{\omega}_A^{+, \mathfrak{B}_A} = [I_A^+]^{\mathfrak{B}_A}{}^{-1}([T]_{\mathfrak{J}}^{\mathfrak{B}_A} \mathbf{H}_A^{\mathfrak{J}}) = [I_A^+]^{\mathfrak{B}_A}{}^{-1}([I_A^-]^{\mathfrak{B}_A} \boldsymbol{\omega}_A^{-, \mathfrak{B}_A}) \quad (2.13)$$

¹ The $(\cdot)^+$ and $(\cdot)^-$ indices indicate the variable state before and after an event, respectively.

For continuity reasons the surface movement event does not change the asteroid attitude

$$\boldsymbol{\sigma}_A = \boldsymbol{\sigma}_A^- = \boldsymbol{\sigma}_A^+ \quad (2.14)$$

2.3.2 Boulder launch

The boulder launch case models some type of separation of the j th boulder ($j \in N_S$) from the surface. After separation the boulder's orbital state and attitude are evaluated separately from the asteroid model. The boulder CM orbital position is propagated around the asteroid model using the polyhedral gravity model described in [100]. The parent body shape is used in the model to compute the gravity around the asteroid. Other orbital perturbations such as the Solar Radiation Pressure (SRP) can be added to the orbit propagation. The asteroid model mass is assumed to be too small to substantially torque the boulder's rotation and thus the boulder's attitude is propagated using the Euler equation for a rigid body with no external torques (Eq. 2.6). For continuity reasons, the asteroid model and boulder attitudes and the boulder's inertial position do not change at the moment of separation

$$\boldsymbol{\sigma}_A = \boldsymbol{\sigma}_A^- = \boldsymbol{\sigma}_A^+ \quad (2.15)$$

$$\boldsymbol{\sigma}_{B,j} = \boldsymbol{\sigma}_{B,j}^- = \boldsymbol{\sigma}_{B,j}^+ \quad (2.16)$$

$$\mathbf{R}_{B,j} = \mathbf{r}_{B,j}^{-,\mathcal{J}} = \mathbf{r}_{B,j}^{+,\mathcal{J}} = [T]_{\mathfrak{B}_A}^{\mathcal{J}} \mathbf{r}_{B,j}^{\mathfrak{B}_A} \quad (2.17)$$

The asteroid model mass and inertia tensor after launch are

$$M_A^+ = M_A^- - M_{B,j} \quad (2.18)$$

$$[I_A^+]^{\mathfrak{B}_A} = [I_A^-]^{\mathfrak{B}_A} - [T]_{\mathfrak{B}_{B,j}}^{\mathfrak{B}_A} [I_{B,j}]^{\mathfrak{B}_{B,j}} - M_{B,j} [\tilde{\mathbf{r}}_{B,j}^-]^{\mathfrak{B}_A} [\tilde{\mathbf{r}}_{B,j}^-]^{\mathfrak{B}_A T} \quad (2.19)$$

The boulder's orbital velocity after separation is

$$\dot{\mathbf{R}}_{B,j}^+ = [T]_{\mathfrak{B}_A}^{\mathcal{J}} (\boldsymbol{\omega}_A^{-,\mathfrak{B}_A} \times \mathbf{r}_{B,j}^{\mathfrak{B}_A} + \dot{\mathbf{r}}_{B,j}^{\mathfrak{B}_A}) \quad (2.20)$$

This velocity is the combination of the linear velocity of the boulder's surface position as the asteroid model rotates (right before separation) and any additional velocity it may have relative to

the parent body's surface. An added velocity that can be a result of boulder movement or some type of event such as an artificial removal or outgassing.

Assuming that the boulder's angular velocity at the moment of separation is equal to the asteroid model's angular velocity before separation, $\boldsymbol{\omega}_{B,j}^+ = \boldsymbol{\omega}_A^-$, the angular momentum of the boulder about its CM is

$$\mathbf{H}_{B,j}^{+,\mathfrak{B}_{B,j}} = [I_{B,j}]^{\mathfrak{B}_{B,j}} \boldsymbol{\omega}_A^{-,\mathfrak{B}_{B,j}} \quad (2.21)$$

and its angular momentum about the system origin after separation is

$$\mathbf{H}_{B,j}^{+,\mathfrak{J}} = [T]_{\mathfrak{B}_{B,j}}^{\mathfrak{J}} [I_{B,j}]^{\mathfrak{B}_{B,j}} \boldsymbol{\omega}_A^{-,\mathfrak{B}_{B,j}} + M_{B,j} \mathbf{R}_{B,j} \times \dot{\mathbf{R}}_{B,j}^+ \quad (2.22)$$

Given that the system's angular momentum is constant at all times the asteroid model's angular momentum after separation is

$$\mathbf{H}_A^{+,\mathfrak{J}} = \mathbf{H}_A^{-,\mathfrak{J}} - \mathbf{H}_{B,j}^{+,\mathfrak{J}} \quad (2.23)$$

Assuming the change in angular momentum of a boulder after separation is negligible, the boulder's angular momentum after separation is recorded in case it returns to the asteroid

$$\mathbf{H}_{B,j}^{\mathfrak{J}}(t > t_{j \text{ separation}}^+) = \mathbf{H}_{B,j}^{+,\mathfrak{J}} \quad (2.24)$$

This leads to an overall angular momentum of the system always being the sum of the asteroid model's angular momentum and all of the orbiting boulders' angular momenta at the moments of separation

$$\mathbf{H}^{\mathfrak{J}} = \mathbf{H}_A^{\mathfrak{J}} + \sum_{j=1}^{N_O} \mathbf{H}_{B,j}^{\mathfrak{J}} \quad (2.25)$$

which means that the system's angular momentum $\mathbf{H}^{\mathfrak{J}}$ remains constant and only changes in case of a boulder escape from the system.

The asteroid model's angular velocity after separation is then

$$\boldsymbol{\omega}_A^{+,\mathfrak{B}_A} = [I_A^+]^{\mathfrak{B}_A}{}^{-1} ([T]_{\mathfrak{J}}^{\mathfrak{B}_A} \mathbf{H}_A^{+,\mathfrak{J}}) = [I_A^+]^{\mathfrak{B}_A}{}^{-1} [T]_{\mathfrak{J}}^{\mathfrak{B}_A} (\mathbf{H}_A^{-,\mathfrak{J}} - [T]_{\mathfrak{B}_{B,j}}^{\mathfrak{J}} [I_{B,j}]^{\mathfrak{B}_{B,j}} \boldsymbol{\omega}_A^{-,\mathfrak{B}_{B,j}} - M_{B,j} \mathbf{R}_{B,j} \times \dot{\mathbf{R}}_{B,j}^+) \quad (2.26)$$

Although fission events are initiated differently than boulder launches the dynamics of their departure from the parent body is the same. Once the fissioned polyhedron is created it is added to the roster of boulders and then treated like a launched boulder.

2.3.3 Boulder crash

In the boulder crash case, a return of the separated j th boulder ($j \in N_O$) to the surface is modeled. When an orbiting boulder CM enters the parent body a crash event is initiated ². The boulder's position on the parent body is decided by placing the boulder on the closest facet to it at the moment of the crash. Thus, there is some added $\delta\mathbf{r}$ to the boulder's position on the surface

$$\mathbf{r}_{B,j}^{+,\mathfrak{B}_A} = [T]_j^{\mathfrak{B}_A} \mathbf{R}_{B,j}^- + \delta\mathbf{r}^{\mathfrak{B}_A} \quad (2.27)$$

This added $\delta\mathbf{r}$ ensures the boulder CM is placed on the surface of the parent body, and not deep inside it. The added facet placement element can also be randomized to simulate different local conditions, such as other boulders present, that would perturb the final reseting place. The asteroid model mass and inertia tensor after the crash are

$$M_A^+ = M_A^- + M_{B,j} \quad (2.28)$$

$$[I_A^+]^{\mathfrak{B}_A} = [I_A^-]^{\mathfrak{B}_A} + [T]_{\mathfrak{B}_{B,j}}^{\mathfrak{B}_A} [I_{B,j}]^{\mathfrak{B}_{B,j}} + M_{B,j} [\tilde{\mathbf{r}}_{B,j}^+]^{\mathfrak{B}_A} [\tilde{\mathbf{r}}_{B,j}^+]^{\mathfrak{B}_A T} \quad (2.29)$$

Because the boulder angular momentum at separation is logged, when the boulder returns to the surface (as described in Eq. 2.24), the value at separation is added to the asteroid model's angular momentum after the crash

$$\mathbf{H}_A^{+,\mathcal{J}} = \mathbf{H}_A^{-,\mathcal{J}} + \mathbf{H}_{B,j}^{\mathcal{J}} \quad (2.30)$$

The asteroid model's angular velocity is then

$$\boldsymbol{\omega}_A^{+,\mathfrak{B}_A} = [I_A^+]^{\mathfrak{B}_A}{}^{-1} ([T]_j^{\mathfrak{B}_A} \mathbf{H}_A^{+,\mathcal{J}}) = [I_A^+]^{\mathfrak{B}_A}{}^{-1} [T]_j^{\mathfrak{B}_A} (\mathbf{H}_A^{-,\mathcal{J}} + \mathbf{H}_{B,j}^{\mathcal{J}}) \quad (2.31)$$

² Conditions for deciding when a CM enters the parent body are presented in a later section.

The boulder's surface velocity is the difference between its orbital velocity and the linear velocity of the boulder crash location on the surface

$$\dot{\mathbf{r}}_{B,j}^{+,\mathfrak{B}^A} = [T]_{\mathfrak{J}^A}^{\mathfrak{B}^A} \dot{\mathbf{R}}_{B,j}^- - \boldsymbol{\omega}_A^{+,\mathfrak{B}^A} \times \mathbf{r}_{B,j}^{+,\mathfrak{B}^A} \quad (2.32)$$

2.3.4 Boulder escape

As described, in the boulder escape event a boulder's orbital energy ($\xi = \dot{\mathbf{R}}_{B,j}^2/2 - U$) reaches positive values with respect to the asteroid system. This means the boulder has enough energy to escape the system's gravitational pull and is on a hyperbolic trajectory with respect to the asteroid system. In this case the boulder's mass is redacted from the system

$$M^+ = M^- - M_{B,j} \quad (2.33)$$

Assuming Keplerian dynamics for the hyperbolic escape and that the change in velocity the system is subject to is proportional to the boulder's velocity after leaving the system the change in the system's velocity is

$$\Delta \mathbf{V} = -\frac{M_{B,j}}{M^+} \sqrt{|\dot{\mathbf{R}}_{B,j}|^2 - \frac{2GM^+}{|\mathbf{R}_{B,j}|}} \hat{\mathbf{R}}_{B,j,\infty} \quad (2.34)$$

where GM^+ is the model asteroid gravitational parameter after separation. The escape direction, $\hat{\mathbf{R}}_{B,j,\infty}$, is found using classical orbital elements by setting the true anomaly far away from the system's origin, at the edge of its Hill sphere, and computing the corresponding inertial Cartesian position and velocity. The escape $\Delta \mathbf{V}$ s are logged to examine their possible contribution in the system's orbital dynamics around the Sun.

2.4 Boulder motion

2.4.1 Surface geophysical environment

The geopotential on the surface of a rotating asteroid is governed by the balance between two forces: the gravitational pull of the body and the accelerations experienced in a rotating frame. A common method to describe the gravity on or near the surface of small bodies is by using the

constant-density polyhedral gravity model. This model uses a triangular-faced polyhedron with a constant density to provide the gravitational potential $U(\mathbf{r})$, gravitational attraction $\nabla U(\mathbf{r})$, and gravity gradient $\nabla\nabla U(\mathbf{r})$ at any position \mathbf{r} ³ below, on, or above the surface of a body. The geopotential of any point on the surface in the rotating frame is [120]

$$V(\mathbf{r}) = \frac{1}{2}(\mathbf{r} \times \boldsymbol{\omega}) \cdot (\boldsymbol{\omega} \times \mathbf{r}) + U(\mathbf{r}) \quad (2.35)$$

The combined acceleration a particle in the rotating frame experiences is then

$$\ddot{\mathbf{r}} = -\boldsymbol{\omega} \times (\boldsymbol{\omega} \times \mathbf{r}) - \dot{\boldsymbol{\omega}} \times \mathbf{r} - 2\boldsymbol{\omega} \times \dot{\mathbf{r}} + \nabla U(\mathbf{r}) \quad (2.36)$$

When discussing the surface environment itself without of a specific particle the $\dot{\mathbf{r}}$ element can be nullified. In this case Eq. 2.36 describes the surface acceleration [101] in position \mathbf{r} on the surface. It is common to use facet centers as indicator points for the surface acceleration. Surface accelerations and their magnitudes are used as indicators of the likelihood of a stationary particle in point \mathbf{r} or on facet f on the surface to remain at that point. However, surface accelerations disregard the local topography in the point's or facet's vicinity and thus cannot indicate the particles tendency to move on the surface without examining nearby points and their geopotential. Surface slope angles, on the other hand, combine the local acceleration vector with local facet normal $\hat{\mathbf{n}}_f$ to give an indicator of the degree a particle is pulled to lower geopotential regions. Surface slope angles are defined as the supplement angles between the acceleration vectors and surface normals at point \mathbf{r}

$$\alpha_s = \pi - \cos^{-1} \left(\frac{\ddot{\mathbf{r}}^T \hat{\mathbf{n}}_f}{|\ddot{\mathbf{r}}|} \right) \quad (2.37)$$

The plots in Figure 2.2 present Mollweide projections of the surface geopotential, surface accelerations, and surface slope angles of the asteroid Bennu as a PAR with a rotation period of 4.29 hours and density of $1190 \text{ kg}\cdot\text{m}^{-3}$. These values, presented in [17], are initial values determined from the OSIRIS-REx spacecraft measurements at the asteroid. The asteroid's shape model is a degraded $\sim 6,000$ facet version of the $\sim 200,000$ facet shape model⁴ constructed from OSIRIS-REx

³ In this section all vectors are in the rotating asteroid model frame, $\mathbf{a} = \mathbf{a}^{\text{B}A}$.

⁴ The shape model was degraded to reach ~ 10 meter long facets that are comparable with the boulder sizes in the simulations presented in later sections.

measurements and available in [121]. Due to the asteroid's constant angular velocity the surface geopotential presented in the figure remains constant as well.

As can be seen in Eq. 2.36, a steady geopotential environment is not the case for a non-PAR. For example, Figure 2.3 presents the surface slope angles for an asteroid with Bennu's shape and density with the presented nominal angular velocity vector initially skewed at the $[\frac{1}{4}, \frac{1}{4}, \sqrt{\frac{7}{8}}]$ direction (an initial angle of ~ 34 degrees between the axis of maximum inertia and angular velocity) in the body frame. The figure shows the slopes at a time t_0 and half a precession cycle period later, as well as the difference in slope angles between the two phases. It is noticeable that although the change in the maximum slope angle is around 2 degrees between the phases, some areas are subject to slope angle changes that reach up to 35 degrees in magnitude. For example the equatorial region near coordinates $[-90, 0]$ degrees shows an increase from a near zero degree slope to a 20 degree slope angle. These changes are linked to the degree of precession an asteroid experiences, leading to bigger slope angle shifts for asteroids with larger magnitudes of off-principal-axis motion.

The acceleration vector at each point can be divided to its facet tangential and facet normal components. The facet tangential component is defined as the slope acceleration, denoted as $\ddot{\mathbf{r}}_s$. The facet normal component is defined as the normal acceleration, denoted $\ddot{\mathbf{r}}_n$. These components' values are:

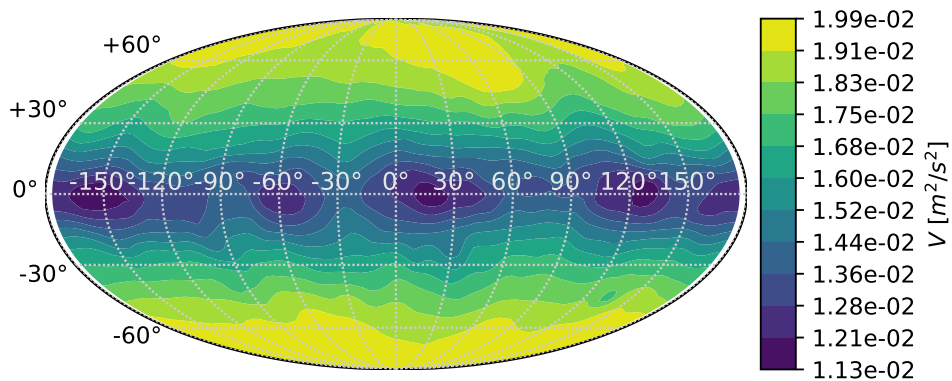
$$\ddot{\mathbf{r}}_n = (\ddot{\mathbf{r}}^T \hat{\mathbf{n}}_f) \hat{\mathbf{n}}_f \quad (2.38)$$

$$\ddot{\mathbf{r}}_s = \ddot{\mathbf{r}} - \ddot{\mathbf{r}}_n \quad (2.39)$$

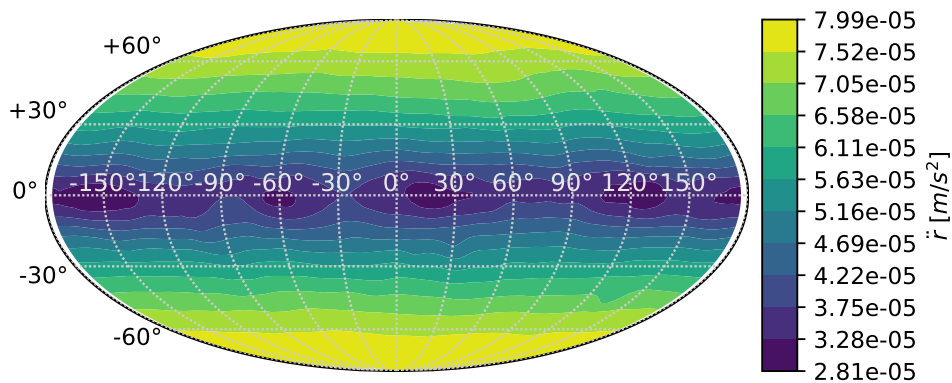
The slope vectors are the slope acceleration unit vectors

$$\hat{\mathbf{s}} = \frac{\ddot{\mathbf{r}}_s}{|\ddot{\mathbf{r}}_s|} \quad (2.40)$$

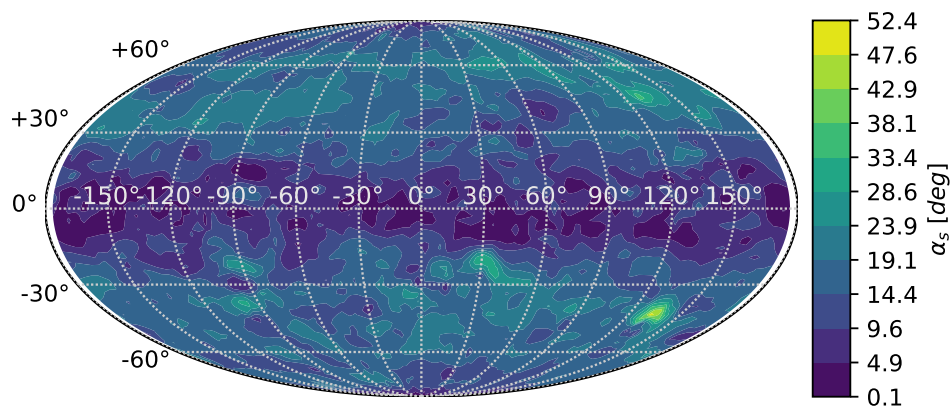
Figure 2.4 presents a map Bennu's surface slope vector directions, a clear tendency towards the equator can be seen for all longitudes and latitudes.



(a) Surface geopotential

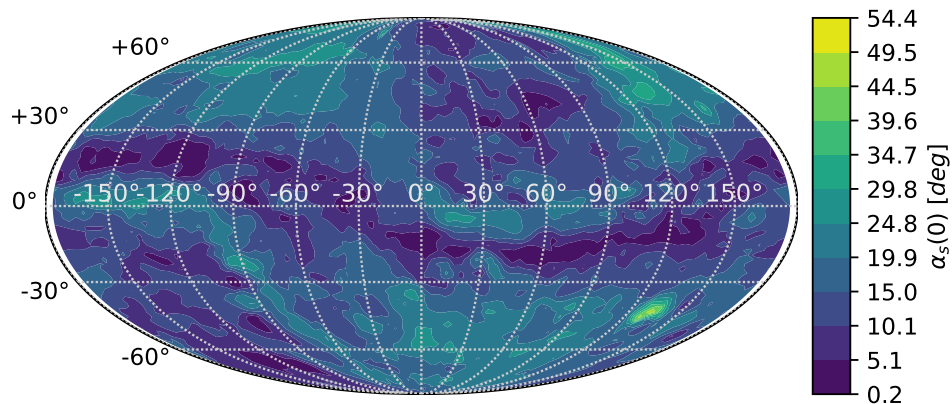
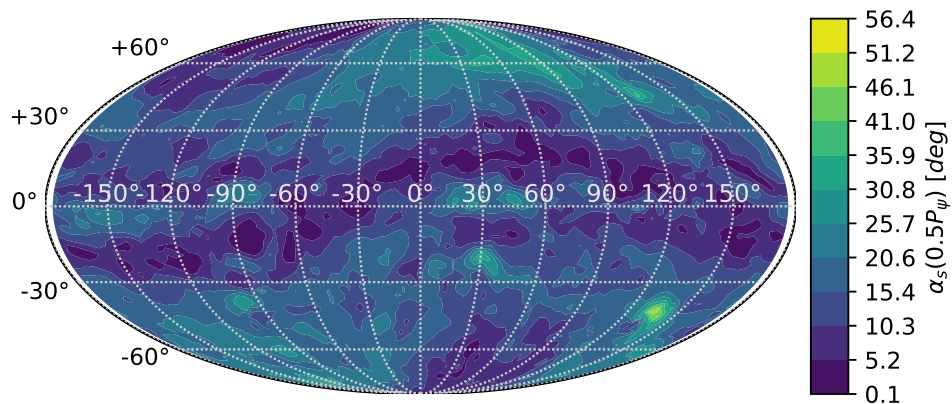
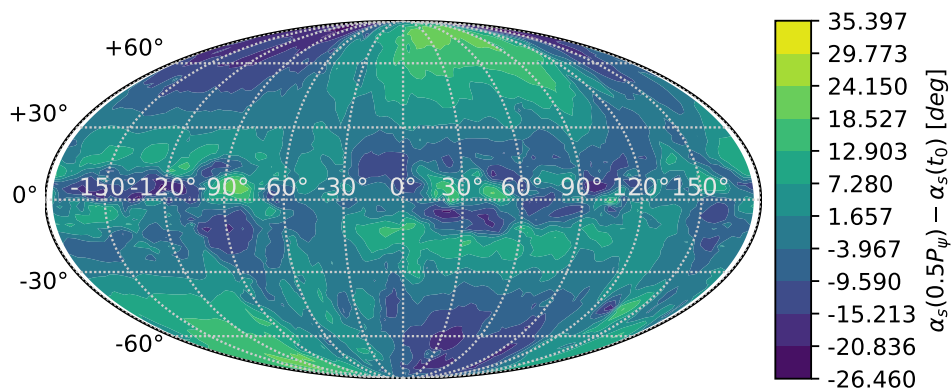


(b) Surface acceleration magnitudes



(c) Surface slopes

Figure 2.2: Benu geopotential parameter maps

(a) Slope angles at t_0 (b) Slope angles at $t_0 + \frac{1}{2}P_\psi$ 

(c) Slope angle differences

Figure 2.3: Bennu-shaped tumbling asteroid surface slope evolution map

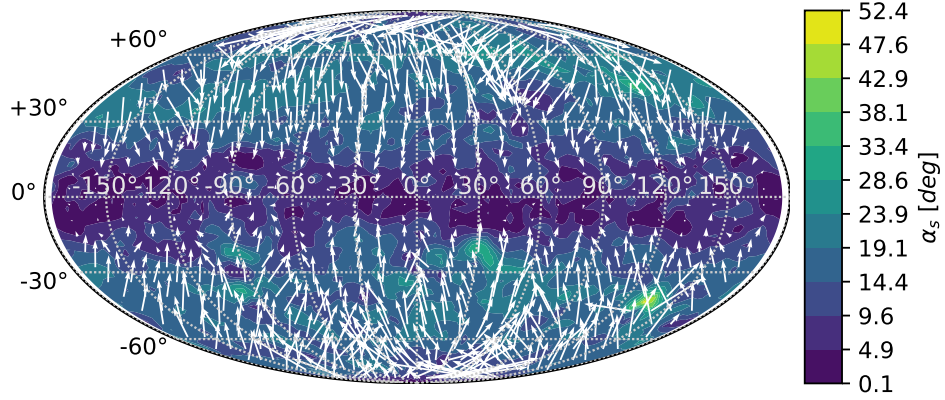


Figure 2.4: Benu surface slope magnitudes and directions

An additional surface dynamical parameter that is used in this work is the surface escape velocity. This parameter is the velocity a particle on the surface needs to have (with respect to the rotating frame) in order of having sufficient energy to escape the asteroid system [122]. The escape velocity is:

$$v_{esc} = -\hat{\mathbf{n}}_f \cdot (\boldsymbol{\omega} \times \mathbf{r}) + \sqrt{(\hat{\mathbf{n}}_f \cdot (\boldsymbol{\omega} \times \mathbf{r}))^2 + 2U_{max}(\mathbf{r}) - (\boldsymbol{\omega} \times \mathbf{r})^T (\boldsymbol{\omega} \times \mathbf{r})} \quad (2.41)$$

where $U_{max}(\mathbf{r}) = \max(U(\mathbf{r}), GM/|\mathbf{r}|)$. Figure 2.5 presents a map of of Benu's surface escape velocities. The values in the map range from just under 0.15 to 0.25 $\text{m}\cdot\text{s}^{-1}$ providing a scale of velocity magnitude expected to exist around such a body. The low escape velocity regions are highly correlated with the low geopotential areas, as expected from Eq. 2.41.

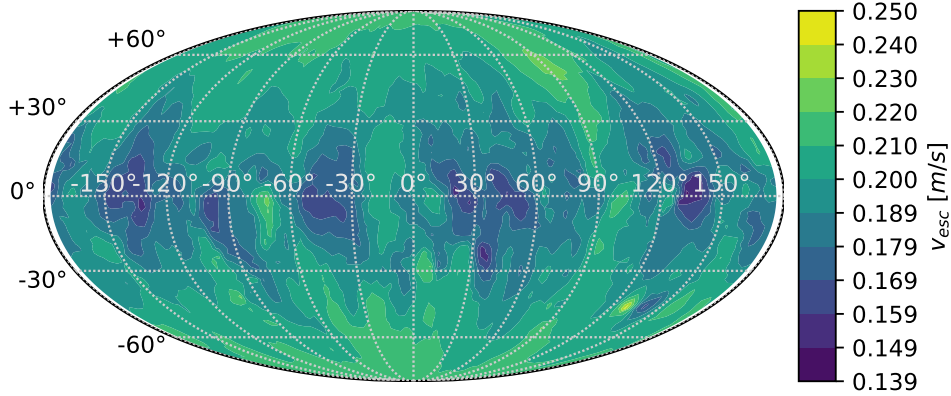


Figure 2.5: Benu surface escape velocities

2.4.2 Cohesion forces

In addition to the geopotential environment, the bodies and material that comprise an asteroid experience cohesion forces. For kilometer size asteroids these forces can be significant in governing material motion, or lack thereof [16, 13]. An analytical expression for the cohesion force of a boulder under a constant upwards acceleration is developed by Kulchitsky [92]. Its formula is

$$F_c = 0.62p_cS \quad (2.42)$$

where p_c is the cohesion strength and S is the boulder surface area in contact with regolith. In [13] an order of magnitude for p_c on asteroid surface is concluded to be around 25 Pascal. The surface area in contact with regolith is a function of the degree a boulder is buried in the regolith. Figure 2.6a presents the cohesion induced accelerations (F_c/M_B) for rectangular boulders with long axes of 5, 10, and 15 meters, axes aspect ratios of b-a-a, and different regolith horizontal burial levels, from zero (only bottom facet on surface) to 60% of boulder sides in regolith⁵. The surface strength used is 25 Pascal and the boulder density is set to $2000 \text{ kg}\cdot\text{m}^{-3}$. This density value is in the range of densities presented for the asteroid Benu in [52]. Figure 2.7 presents a comparison of the cohesion

⁵ The use of rectangular boulders for this examination is based on images of Benu [52] and Itokawa [4], which present meter-size boulders with wide planer faces and distinguishable angles between them.

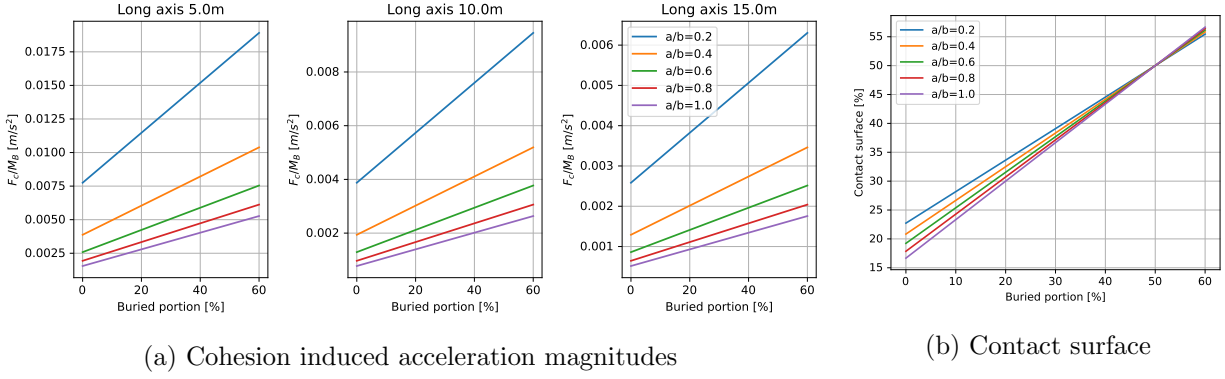


Figure 2.6: Cohesion induced acceleration magnitudes for boulders of varying sizes, aspect ratio, and buried portion. Surface strength is 25 Pascal and boulder density is $2000 \text{ kg}\cdot\text{m}^{-3}$.

induced acceleration a 5×5 meter boulder experiences in different burial levels and the geopotential acceleration it would experience on the equator of the asteroid Bennu. The geopotential presented shows the gravitational acceleration, the rotational acceleration, and a combination of both. The figure indicates downwards (of stationary) accelerations with down-pointing triangles, and upwards accelerations with up-pointing triangles. In addition to the nominal geopotential state of Bennu (indicated by solid lines) an accelerated Bennu is presented (indicated by dashed lines), the gravity is identical for both cases. The figure shows that in the accelerated case the overall geopotential acceleration experienced by the boulder on the equator is upwards pointing, meaning that it should be ejected to space. However, this upwards acceleration is more than two orders of magnitude smaller than the cohesion induced acceleration for the boulder. For that reason it is important to account for cohesion when examining surface motion in sub-kilometer and kilometer size asteroids. Figure 2.6b presents the percentage of contact surface area for the different horizontal burial levels, in a scenario where all buried surface area is in contact with regolith. Based on the results presented in this figure area percentages for cohesion are decided for the later simulations.

The behavior of cohesion forces on gravitational aggregates' surfaces has many unknowns. An in-situ examination of the forces has yet to be performed and the results seen in [92, 13] are based on theoretical models that are not yet fully validated. The extent of regolith-boulder surface area

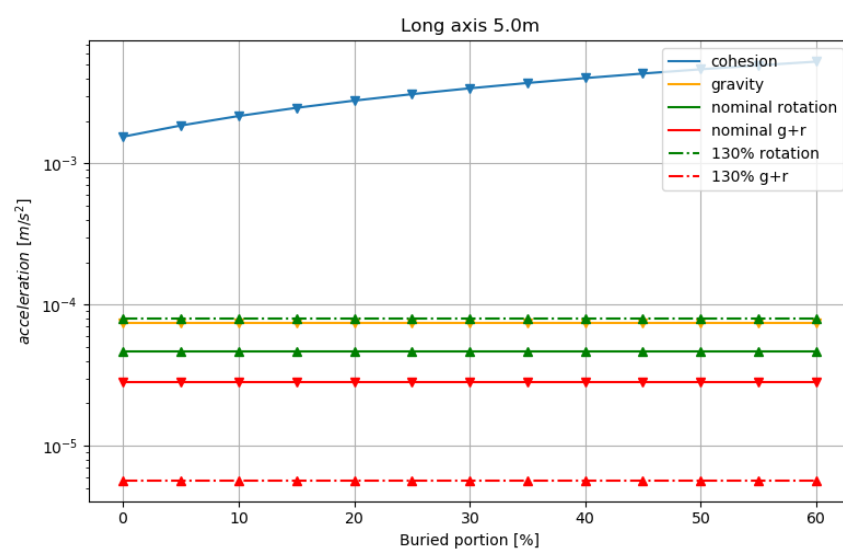


Figure 2.7: Cohesion induced acceleration compared to geopotential accelerations (gravity, rotation, and combination) for nominally rotating Bennu and a fast spinning Bennu

contact is unknown as well. For this work the model takes a conservative approach, assuming maximum regolith contact. An argument for lower contact area percentages in porous asteroid structures can be made. However, in the cases presented here, the cohesion induced acceleration is two orders of magnitude larger than the rotating asteroid geopotential. Changing the balance between cohesion and outwards acceleration would require a reduction in contact area in the same order of magnitude.

The relationship between cohesion forces and the geopotential comes into play when looking at surface slopes. Research into critical slopes on asteroids has shown that there is a maximum angle in which cohesion forces hold material together [10, 114]. Above such an angle motion is induced. The range for these critical slope angles has been found to be between 35 to 45 degrees.

2.4.3 Boulder motion mechanics

The dynamical mechanism of boulder motion has many factors that influence it. These include the regolith grain size and composition, the existence of other rocks or boulders in the movement path, the cohesive forces between boulder and regolith, and the shape of the moving boulder. The extent of influence of these factors, and how they correlate with each-other, is not fully solved for asteroid surface environments. For that reason the SEA RATS model does not seek to fully model the boulder motion dynamics, but rather enable motion in the direction and conditions governed by the geopotential. This, while giving a generalized consideration to cohesion forces. In the model, boulders on the surface of the parent body are set to remain fixed to the body as it rotates. At every time step, the boulders' CMs on-surface accelerations (as described by the full Eq. 2.36) and slopes are examined for motion conditions.

A distinction between surface and on-surface properties should be made. Where surface properties refer to accelerations and slope angles of facets' center positions and on-surface properties refer to accelerations and slope angles experienced by boulder centers of mass. The difference between a facet center and a boulder CM comes from the boulder being placed on the facet, with its periphery

in contact with the facet. Figure 2.8 presents a comparison of fifty identical ~ 8 meter boulders placed on the surface of the Bennu shape model⁶, dividing the on-surface boulder property (notated as a_b and s_b for acceleration and slope, respectively) by the corresponding facet surface property (similarly notated as a_f and s_f). The s_b/s_f ratio shows substantial differences between on-surface and surface slope angles presenting, for the most part, higher ratios experienced by the boulder CMs. The a_b/a_f ratios show slightly lower accelerations experienced by the boulders. This corresponds with their CMs being farther away from the asteroid center, and thus less gravitationally bound to the asteroid. Thus, due to the variance between the two types of properties the on-surface accelerations and slope angles are used to determine boulder motion thresholds.

The boulder motion scheme begins with computing the gravity and rotational components of the

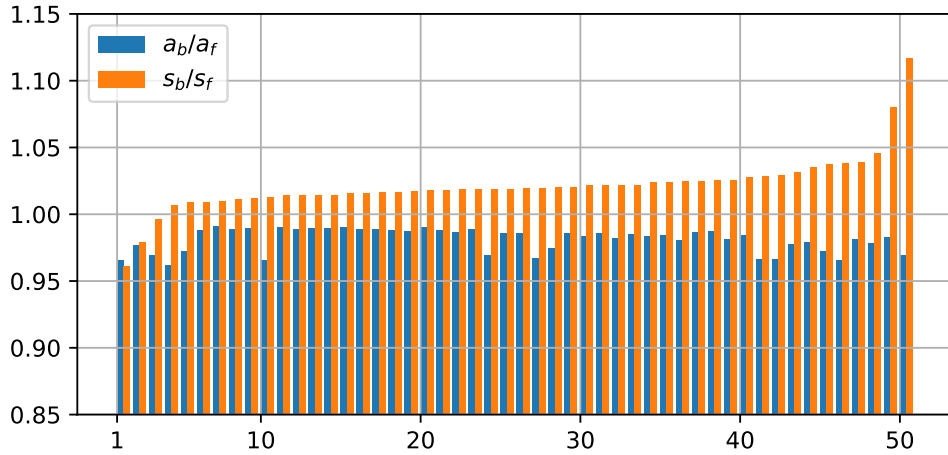


Figure 2.8: Ratio between on-surface and surface acceleration and slope for identical boulders placed on Bennu's surface

on-surface acceleration (including boulder surface velocity, as described in the full Eq. 2.36), as well as the boulder's on-surface slope. If the outwards rotational acceleration magnitude is greater than the inwards gravitational acceleration, or the slope angle is greater than the defined launch angle⁷ the cohesion force acting on the boulder is examined (as described in the previous section).

If the overall acceleration magnitude is larger than the cohesion hold on the boulder ($|\ddot{\mathbf{R}}| > \frac{F_c}{M_B}$) a

⁶ The boulder placement can be seen in Figures 2.1 and 2.10.

⁷ Usually defined as 90 degrees [101].

launch scenario is initiated. If these conditions are not met and the boulder is already in motion, a third launch condition is examined: if the facet normal component of a boulder’s surface movement velocity points upwards and is greater than the downward (facet normal) acceleration integrated over a characteristic time period ($\dot{\mathbf{r}}_n^{\mathfrak{B}A} \uparrow$ and $|\dot{\mathbf{r}}_n^{\mathfrak{B}A}| > |\int \ddot{\mathbf{r}}_n^{\mathfrak{B}A} d\tau_B|$), boulder launch is initiated. This condition links the surface topography and the surface movement velocity in order of modeling a scenario in which a boulder flies off a geopotential “cliff”. The characteristic time period is defined as the time the boulder CM travels half of its long axis at its current velocity ($d\tau_B = \frac{L_B}{2|\dot{\mathbf{r}}_n|}$).

If the launch conditions described are not met the slope is examined for surface motion conditions: a slope angle condition for surface movement from a surface-stationary state (static condition), and a lower threshold slope angle condition for surface movement continuation (kinetic condition). If the slope is greater than the static condition angle surface movement is initiated. If the slope angle is greater than the kinetic condition and the boulder is already in motion on the surface ($|\dot{\mathbf{r}}^{\mathfrak{B}A}| > 0$) the movement continues. If none of the launch or surface movement conditions are met the boulder will remain fixed at its position. In case the kinetic movement condition is not met but the boulder has been previously in motion the surface velocity is nullified ($\dot{\mathbf{r}}^{\mathfrak{B}A} = \mathbf{0}$). If a boulder in surface motion is launched its orbital launch velocity is the sum of its surface movement velocity, $\dot{\mathbf{r}}_{B,j}^{\mathfrak{B}A}$, and facet linear velocity, as described in Eq. 2.20. The surface movement velocity component can also be used to “artificially” instigate surface movement or a launch at a defined time or asteroid state by inputting

$$\dot{\mathbf{r}}_{B,j}^{\mathfrak{B}A} = \Delta \mathbf{v}_{B,j}^{\mathfrak{B}A} \quad (2.43)$$

Research into the specific mechanics of asteroid surface motion has been conducted in [104, 98, 123]. This research has focused on small lander activity on asteroids and distinguished between sliding and rolling motion. The SEA RATS model does not seek to reach such granular accuracy, but rather enable boulder motion as governed by the geopotential and cohesion forces. For that reason, surface movement is defined as some linear combination of rolling and sliding. Whenever a boulder surface movement occurs the slope acceleration and previous movement velocity are used to determine the

movement direction and magnitude. Using equations of motion from classical mechanics, while factoring for friction, a boulder's nominal position and velocity after surface movement are defined as

$$\mathbf{r}^{+,\mathfrak{B}_A} = \left(\ddot{\mathbf{r}}_s^{\mathfrak{B}_A} - \mu_k |\ddot{\mathbf{r}}_n^{\mathfrak{B}_A}| \hat{\mathbf{s}}^{\mathfrak{B}_A} \right) \frac{\delta t^2}{2} + \dot{\mathbf{r}}^{-,\mathfrak{B}_A} \delta t + \mathbf{r}^{-,\mathfrak{B}_A} \quad (2.44)$$

$$\dot{\mathbf{r}}^{+,\mathfrak{B}_A} = \left(\ddot{\mathbf{r}}_s^{\mathfrak{B}_A} - \mu_k |\ddot{\mathbf{r}}_n^{\mathfrak{B}_A}| \hat{\mathbf{s}}^{\mathfrak{B}_A} \right) \delta t + \dot{\mathbf{r}}^{-,\mathfrak{B}_A} \quad (2.45)$$

where μ_k is the combined roll and slide kinetic friction coefficient and δt is some incremental time element in which the motion on the surface is assumed linear. The kinetic friction coefficient is modeled to be the linear combination of both slide and roll friction with some ratio factor κ

$$\mu_k = \kappa \mu_s + (1 - \kappa) \mu_r \quad (2.46)$$

This ratio factor can be kept fixed throughout the asteroid model surface and the propagation time, or be made adjustable according to location on the surface, simulation run time, or boulder surface velocity. For example, if some area on the asteroid surface presents fine regolith the sliding friction might be more dominant and if another area is more rocky the rolling friction might be more dominant.

Because the motion dynamics presented in Eq. 2.44 are simplified and do not consider changing surface conditioning along the boulder path, an additional randomized positioning and velocity vectors can be added

$$\mathbf{r}^{+,\mathfrak{B}_A} = \mathbf{r}_{nominal}^{+,\mathfrak{B}_A} + \delta \mathbf{r}^{\mathfrak{B}_A} \quad (2.47)$$

$$\dot{\mathbf{r}}^{+,\mathfrak{B}_A} = \dot{\mathbf{r}}_{nominal}^{+,\mathfrak{B}_A} + \delta \dot{\mathbf{r}}^{\mathfrak{B}_A} \quad (2.48)$$

this $\delta \mathbf{r}$ is proportional to the distance traveled and not necessarily in the nominal direction traveled, allowing for some random motion related to interference along the path of the boulder:

$$\delta \mathbf{r}^{\mathfrak{B}_A} = 0.1 a_0 |\mathbf{r}_{nominal}^{+,\mathfrak{B}_A} - \mathbf{r}^{-,\mathfrak{B}_A}| \frac{\hat{\mathbf{n}}_f \times ((1-a_1)(1-a_2)\mathbf{v}_{1,f} + (1-a_1)a_2\mathbf{v}_{2,f} + a_1\mathbf{v}_{3,f})}{|\hat{\mathbf{n}}_f \times ((1-a_1)(1-a_2)\mathbf{v}_{1,f} + (1-a_1)a_2\mathbf{v}_{2,f} + a_1\mathbf{v}_{3,f})|} \quad (2.49)$$

$$\delta \dot{\mathbf{r}}^{\mathfrak{B}_A} = 0.1 a_3 |\dot{\mathbf{r}}_{nominal}^{+,\mathfrak{B}_A}| \frac{\delta \mathbf{r}^{\mathfrak{B}_A}}{|\delta \mathbf{r}^{\mathfrak{B}_A}|} \quad (2.50)$$

where $a_0, a_3 \sim U(-1, 1)$ and $a_1, a_2 \sim N(0, 0.5)$ are random variables, and $\mathbf{v}_{1,f}, \mathbf{v}_{2,f}, \mathbf{v}_{3,f}$ are the three vertices of the facet the boulder is placed on. In the case a boulder moves from facet to facet the added $\delta\mathbf{r}$ also assures the boulder is secured to the new facet. Similarly to its new location, the boulder's attitude is randomly perturbed from the previous attitude. Once the boulder's new surface state is determined its CM position, relative velocity, and attitude are propagated fixed to the parent body. The asteroid model rotation is then propagated with the new mass properties.

When a boulder is launched to orbit its orbital energy with respect to the asteroid model is examined. If its value is negative the boulder is added to the orbital propagation roster. If the energy is positive the boulder is considered to have escaped the system, it is removed from the system total boulder roster, and the asteroid model's orbital velocity change is logged.

For the case of an orbiting boulder, three types of orbital states are defined: near-surface orbit, mid-altitude orbit, and high-altitude orbit. The border separating between near-surface and mid-altitude orbits being the Brillouin sphere. And the border separating between mid- and high-altitude orbits being the asteroid model's Hill sphere radius. A boulder orbiting in the near-surface region is checked at every time step for a possible transition to mid-altitude orbit, or for a possible crash on the surface. The orbit region transition check is simply done by examining the boulder's orbital radius. A boulder crash is defined as the movement of the boulder CM into the parent body shape. This is checked by computing the boulder's CM position's (\mathbf{r}) Laplacian of the polyhedron's potential, $\nabla^2 U(\mathbf{r})$. If the Laplacian value is zero the point \mathbf{r} is outside the polyhedron, and if it is $4\pi/G\rho$ ⁸ the point is inside the polyhedron [100], and thus, the boulder crashed on the surface. In a crash case, the facet closest to the crashed boulder CM position is defined as the boulder's new surface facet. To promise boulder CM placement on the surface (and not below it), and to account for local deviations during the crash, the boulder is randomly placed on the facet, adding some $\delta\mathbf{r}$ to the boulder's position. The boulder's angular velocity is fixed to the asteroid model's and its attitude is perturbed from its attitude at the moment of the crash. As described in Eq. 2.32, a surface movement velocity is added to the boulder to be propagated after the crash. In the

⁸ Here G is the universal gravitational constant and ρ is the polyhedron's density.

case of a boulder orbiting in the mid-altitude region the boulder is checked for region transition at every time step before its orbit is propagated to the next time step. A boulder orbiting in the high-altitude region is checked for region transition and also for a possible escape scenario. This could occur as the result of non-Keplerian forces, such as SRP, that can introduce energy to the boulder's orbit, turning a high-altitude orbit into a hyperbolic trajectory. Similarly to a surface launch escape, the boulder's orbital energy sign is examined to determine such an event. This type of orbital escape is also recorded in the boulder roster with the orbital velocity change for the asteroid model logged as well.

Figure 2.9 summarizes the boulder motion scenarios presented in this section.

2.4.4 Threshold angular velocities

The analysis of surface and on-surface properties can be reversed to find threshold angular velocities that will lead to boulder motion. By defining desired acceleration magnitudes and slope angles Eqs. 2.36 and 2.37 can be used to find corresponding angular velocities that will initiate a boulder's (cohesionless) launch or surface movement. In order to reach definitive ω values for fission (launch) the asteroid is assumed to be principal-axis rotating ($\dot{\omega} = \mathbf{0}$) and the surface movement velocity is set to be zero ($\dot{\mathbf{r}}^{\mathcal{B}^A} = \mathbf{0}$). The total acceleration at the point \mathbf{r} is nullified and the angular velocity is then computed from Eq. 2.36. For the slope surface movement angle correlating angular velocity an assumption that the rotation axis is aligned with the $\hat{\mathbf{z}}$ axis is added to simplify computation. Eq. 2.37 is then used to find ω that leads to a certain slope angle. Threshold angular velocities can be found for the asteroid surface and used to map areas that are more susceptible to be active in different rotation regimes. Similarly, surface boulders that are at higher risk of moving can be pointed out. The values found in such an analysis will differ from actual values in the case of a precessing asteroid or a boulder moving on the surface, but they provide an additional input to the fission characteristics discussed in past research. Figure 2.10 presents the angular velocity values required for fission (Figure 2.10a) or surface motion at a 40 degree slope (Figure 2.10b⁹) on

⁹ The heatmap in Figure 2.10b is limited in range as to show the relevant values in a differentiable manner.

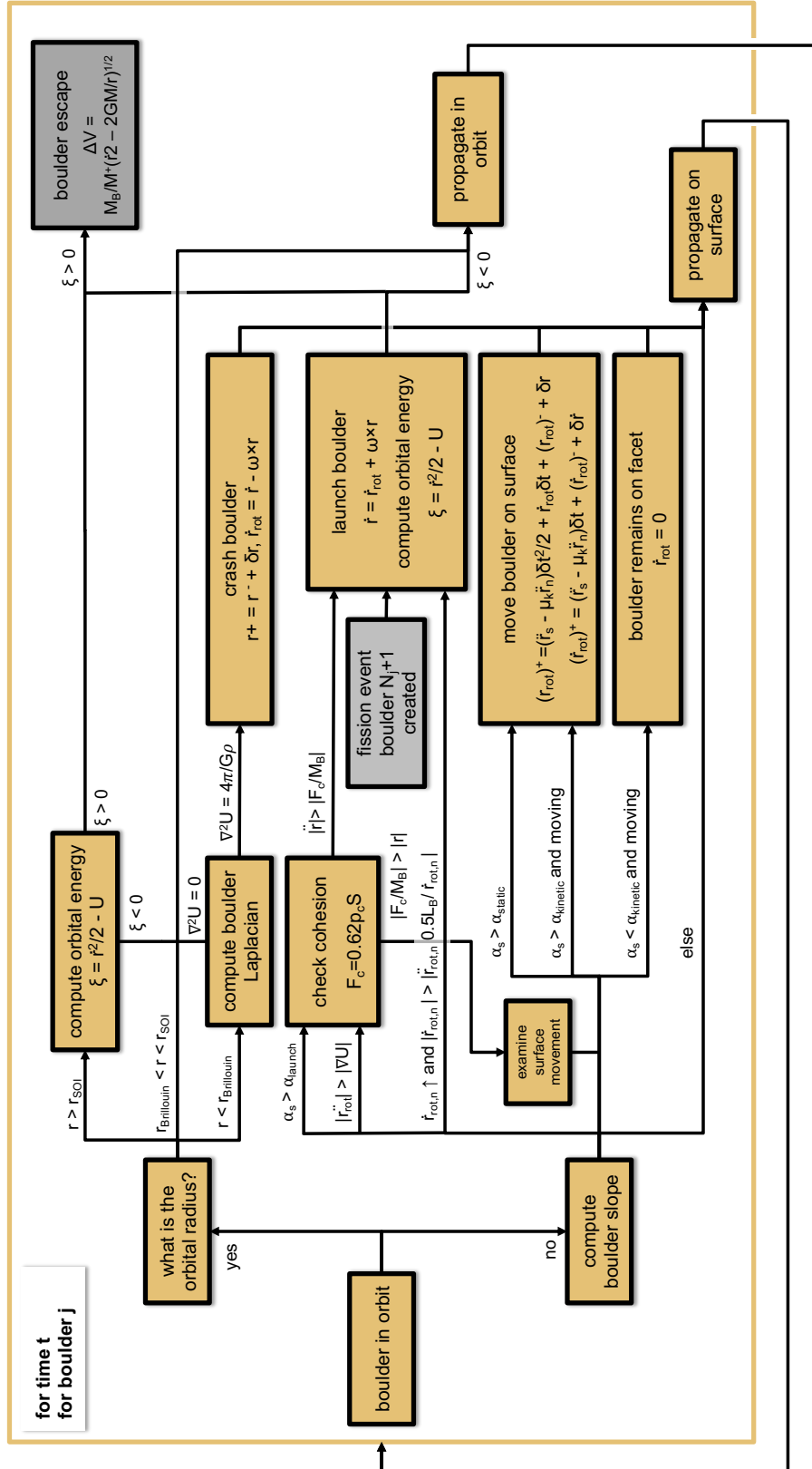


Figure 2.9: SEA RATS boulder state flow chart

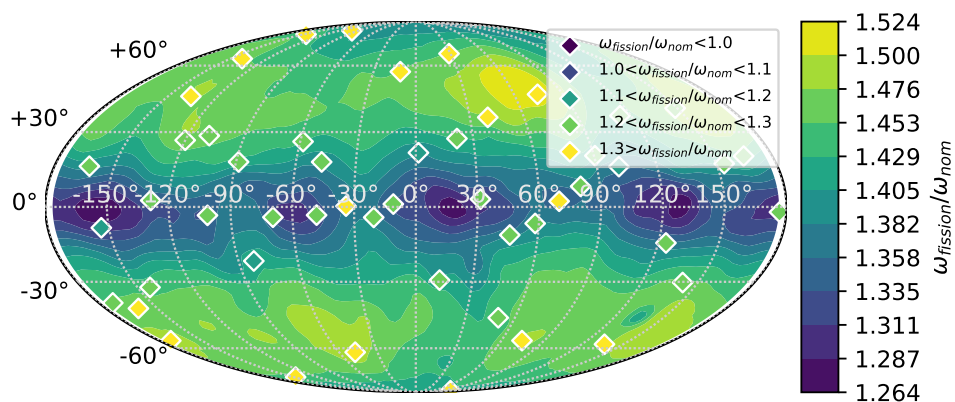
the asteroid Bennu¹⁰. The figures also show ranges of motion angular velocity magnitudes for the 50 boulders presented in Figure 2.8. These are marked as colored diamonds on the maps, each color corresponding to a range of angular velocity magnitudes that would cause those boulders to launch or move. The ranges presented are relative to the nominal Bennu angular velocity. Figure 2.10a shows an outwards boulder CM acceleration at angular velocity rates of $1.1\omega_{nom}$, and higher and Figure 2.10b shows the 40 degree slopes at angular velocity rates of $1.2\omega_{nom}$ and higher. In general low to mid latitudes show the lowest angular velocity rates needed for motion conditions, while high latitudes and some equatorial regions show higher angular velocity rates needed for motion conditions.

When comparing the values presented in the figure to Bennu’s actual angular velocity at a value of $4.06e^{-4} \text{ s}^{-1}$ [17] it is noticeable that there is a very fine balance between Bennu’s shape and its rotation rate. Faster rotation or bigger equator radius (assuming same overall mass) would probably lead to areas in which the total accelerations point outwards, or areas where slopes reach critical values. When comparing the fission thresholds in Figure 2.10a to the fission condition presented in the literature [7] ($\omega > \sqrt{4\pi G\rho/3}$), which for Bennu is at a value of $5.76e^{-4} \text{ s}^{-1}$, it is noted that extensive areas of the asteroid surface require lower angular velocity to lead to boulder motion than in the simpler model.

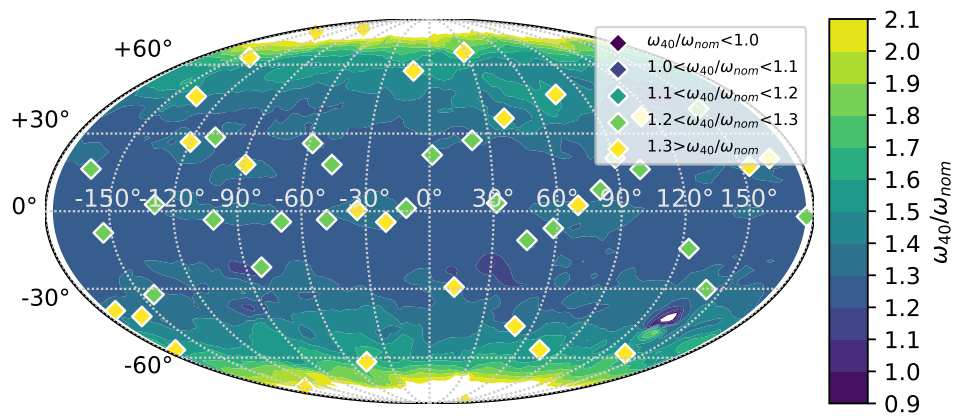
2.5 Fission event

The mechanics of initiating a fission event in the SEA RATS model are different than those of a boulder launch. Mostly because boulder geometry is predefined in the model setup process and the geometry of fission slicing are defined while the event is processed. The fission event model allows more drastic changes to the asteroid shape than boulder motion and for other types of gravitational aggregates components to be removed from the model asteroid’s surface. Currently the model code only allows for a fission event to be initiated “artificially” to model a detonation or impact event on an asteroid surface. The model can allow for “inspection points” to be defined inside the parent

¹⁰ Using the shape model and parameters presented in Section 2.4.1.



(a) Fission (cohesionless)



(b) Slopes at 40 [deg]

Figure 2.10: Threshold angular velocity compared to Benu nominal for boulder motion. The heatmaps indicate surface (facet) properties, and the diamonds indicate boulders placed on the surface.

body and observed throughout a simulation run to initiate a fission event according to predefined geopotential conditions.

In the fission event model the polyhedral shape which represents the ejected mass is found in an iterative process which begins with a single surface interface location on the polyhedral asteroid surface. For simplicity this location is selected as a facet center, but other facet locations, vertices, or even points above or below the surface can be used as surface interface locations. The fission polyhedron generation process includes a top iterative loop which matches the new polyhedral mass with the required fissioned mass for a given density (nominally the asteroid bulk density) and three inner algorithms which find the vertices and facets to be altered, reshape the polyhedral asteroid, and create a new polyhedral body which simulates the fissioned mass. The fission polyhedron can be created in two ways: a vertex shifting option, which carves a crater in the surface, simulating an impact or surface detonation, and a vertex scaling option, which carves a shell off the surface, simulating some surface ablation event. The shifting option receives a crater radius to depth ratio as an input, and the scaling option receives an affected area radius as an input.

The polyhedron shape modification algorithm has three stages in it, nested in a iterative loop which seeks to match the removed polyhedron mass to a required mass. Once in the loop, the algorithm recognizes the vertices that need to be adjusted and lists the correlating facets. The algorithm then reshapes the original body according to specified geometry. This geometry can either be scaling of a vertex radius, while maintaining the original direction, or shifting the vertex location by a defined vector. It should be mentioned, that in vertex shift, intersection of facet edges could occur, and thus the defined shift should account for neighboring vertices and their shift. Lastly, the algorithm creates a new body from the removed material. The overall shape at the moment of separation (both bodies attached together) is equal to the original shape.

- **Iterate to required mass** - *iterate()*

- (1) receive deflection interface location \mathbf{p}
- (2) initiate input radius

if *shift*: guess initial crater radius r based on average facet length

else if *scale*: receive affected area radius r

(3) **while** $\left|1 - \frac{M_{e,calc}}{M_{e,req}}\right| > \epsilon$:

(a) vertex change list, facet change list = *list*(\mathbf{p}, r)

(b) modified body geometry = *reshape*(reshape type, vertex change list, facet change list)

(c) new body geometry = *new*(vertex change list, facet change list, density)

(d) $M_{e,calc}$ = new body mass

• **List vertices and facets** - *list*()

(1) receive deflection interface location \mathbf{p} radius r

(2) **for** \mathbf{v} **in** vertex list:

if $|\mathbf{v} - \mathbf{p}| \leq r$:

add \mathbf{v} **to** vertex change list

for f **in** facet list:

if \mathbf{v} **in** f :

add f **to** facet change list

• **Body reshape** - *reshape*()

(1) receive reshape type, vertex change list, facet change list

(2) clone vertex change list

(3) **for** \mathbf{v} **in** cloned vertex change list:

if *scale*:

$\mathbf{v} = \textit{scale} \times \mathbf{v}$

if shift:

$$\mathbf{v} = \mathit{shift} + \mathbf{v}$$

- **New body** - *new()*

(1) clone facet change list

(2) **for** f **in** cloned facet change list:

for v **in** cloned vertex change list:

if original v **in** original f:

assign v **to** f

(3) **merge**(original facet list,cloned facet list)

(4) **merge**(original vertex list,cloned vertex list)

2.6 Code structure

The SEA RATS model utilizes a Python based code for simulation and analysis. Python's class and object oriented environment provides the ability to fully define and propagate the state of each modeled object, from the parent body, to the boulders and fissioned masses.

The code includes a **Body** class with which each body is initiated. This class lists provided features such as polyhedral geometry and bulk density and their derived characteristics: volume, mass, gravitational parameter, polyhedral gravity model constants, inertia tensor, Brillouin and Hill sphere radii. In addition, the **Body** class logs the dynamical state and event flags. For all bodies dynamical state is defined as

$$\mathbf{X} = [\boldsymbol{\omega}^T, \boldsymbol{\sigma}^T, \dot{\mathbf{R}}^T, \mathbf{R}^T]^T \quad (2.51)$$

where all state elements are in the inertial frame. The events flagged include any type of boulder surface moment, the boulder dynamical environment (surface, orbit, or escape), the boulder placement facet, on-surface slope, and surface velocity. It is important to note that some properties are irrelevant for the parent body (CM position and velocity, surface motion parameters) and other are

irrelevant for boulder (gravity constants and parameters) but the **Body** class still includes them for all bodies, either nullifying or not including an entry for them (using nan, not a number). This setup simplifies the objects' propagation by using a single function thread for all types of bodies. The simulation runs for a predefined time vector which can have varying time step sizes but cannot be altered once it has begun. The length of the time vector is used to create state vector elements which are then populated as the simulation is propagated.

A second class used in the code is **Delta**, which allows for the boulder motion characteristics to be defined. Whether those be natural characteristics: launch threshold, static and kinetic surface movement thresholds, friction coefficients, and cohesion factors, or artificial ones: boulder launch and fission event timing, launch direction and magnitude, selected boulder, region, or fission event geometry.

The code runs several preprocessing functions which upload the asteroid geometry from a wavefront file (.obj), this geometry, together with the other characteristics and an initial dynamical state are then used to populate the parent body **Body** class as $j = 0$, boulders $j = 1, 2, 3, \dots$ are then added and placed on the surface according to predefined parameters (number of boulders, characteristic size, placement location/area, boulder density). The **Delta** class is populated with boulder movement conditions and/or artificial launch criteria. Once all bodies and predefined events are populated a propagation function initiates the simulation. This function calls an integrator loop which iterates over the time vector elements and an internal loop iterates over all bodies. For time t and body j a classical Runge-Kutta method [124] step is run with an internal dynamics function. This internal function selects between parent body propagation (full rigid body dynamics and nullified CM linear dynamics), orbiting/escaping boulder propagation (full rigid body dynamics and CM orbit propagation based on polyhedral gravity model and added perturbations), or boulder surface placement (rigid body linked to parent body and CM propagation as the asteroid rotates). It is important to note that the surface motion dynamics is not propagated at this step but rather performed at a later step once surface motion thresholds have been examined. In case of an escaped boulder an option for simplified CM linear dynamics with no acceleration source can

be implemented to reduce computational burden. Once the dynamics for body j at time t have been propagated a condition function is run to examine if any threshold is met. This function examines the time t with the predefined **Delta** class movements to initiate any artificial events (boulder launch or fission). If none are initiated and the body is a boulder the event thresholds are examined, depending on the boulder environment, surface or orbit, different parameters are checked, on-surface geopotential and cohesion factors for a surface boulder, or Laplacian for an orbiting boulder. Escaped boulders are not examined as their environment is defined as outside the asteroid system. For a surface boulder the threshold hierarchy presented in Figure 2.9 is used: launch acceleration and slope are examined, followed by cohesion check, if those are not met, the static surface movement is checked, if that is not met and the boulder is moving the kinetic slope is checked, if none of these conditions are met the boulder is left in its propagated location. If any of these conditions are met the boulder and asteroid propagations are updated according to the type of event that has occurred. Similarly an orbiting boulder that meets the crash or escape conditions leads to an update in the boulder and asteroids states.

The code is able to run several case propagations sequentially or in parallel, thus allowing to run a control case with the same initial conditions but different event thresholds, or allowing for a Monte Carlo analysis of multiple cases that differ by the random factors in the boulder surface motion.

Following each simulation completion overall system properties such as mass and angular momentum are computed for every time step and packaged together with the **Body** class objects in a single run Python list.

The following list describes the code in algorithmic form:

- (1) **load**(asteroid.obj)
- (2) initiate **Body**(asteroid, $j = 0$)
- (3) **for** j **in** $1, \dots, N_I$:
 - initiate **Body**(boulder, $j = j$)
- (4) initiate **Delta**

```

(5) for run in 0,1,..., $N_{runs}$ :
    for  $t_i$  in  $t$ :
        for  $j$  in 0,1,..., $N_{Body}$ :
             $\mathbf{X}_{j,i+1} = \mathbf{RK4}(\mathbf{Dynamics}(\mathbf{X}_{j,i}))$ 
            if  $\mathbf{conditions}(\mathbf{X}_{j,i+1}, \mathbf{Body}, \mathbf{Delta}) == \mathbf{True}$ :
                 $\mathbf{X}_{j,i+1}, \mathbf{Body}(j = j) = \mathbf{events}(\mathbf{X}_{j,i+1}, \mathbf{Body}, \mathbf{Delta})$ 
                update  $\mathbf{X}_{0,i+1}, \mathbf{Body}(j = 0)$ 

(6) pack( $\mathbf{X}_{j=0,1,\dots,N_{Body}}, \mathbf{Body}(j = 0, 1, \dots, N_{Body})$ )

```

2.7 SEA RATS applications

The following chapters present results from the SEA RATS model and code in a variety of scenarios, both naturally caused and human induced. These results provide insights into how small movements on and off of small body surfaces affect rotation in an efficient manner which accounts for small body overall shapes as well as small scale geometry. The application of the SEA RATS model lays between simple analytical examinations and complex numerical investigations. It can present motion trends related to events occurring on a local scale of an asteroid while still accounting for global reproductions.

Chapter 3

Modeled natural behavior

This chapter explores the dynamical changes asteroid undergo when material motion is induced naturally, either in fast rotating body environments, or in small scale particle events.

3.1 Fast rotating bodies

The following sections present results for simulations of fast rotating model asteroids. These simulated bodies are based on known asteroid shapes and bulk densities with adjusted angular velocity vectors selected to induce motion. The new a-priori angular velocity magnitudes are larger than the known nominal values for these asteroids to an extent higher than expected to be induced by the YORP effect in short time scales. Thus, the harder core assumption presented in Section 2.2 is important to “maintain” the modeled asteroid in its shape until reaching the simulation initial conditions. Alternatively, the increased angular velocity magnitudes presented could be caused by a faster torque inducing effect such as a planetary flyby or a small impact.

The simulation results presented in this section are based on asteroids Bennu and Itokawa as two examples of shapes for small rubble pile asteroids. First, a Bennu model single boulder example is described and presented. This case serves as a benchmark to other simulations and, unless mentioned otherwise, the following cases use the same parameters. The single boulder example is also used to present a time step analysis for the simulations as well as a comparison of different modeled surface conditions. The cases that follow present multiple boulder simulations for both the Bennu and Itokawa shapes at varies angular velocity states.

3.1.1 Single boulder motion on a asteroid Bennu model

This section demonstrates the changes that occur in a fast rotating asteroid state due a the motion of a single boulder. Additionally, the boulder motion model is analyzed through modeling variable comparisons.

3.1.1.1 Simulation setup

The following section presents the motion results from a SEA RATS simulation of a single boulder on the surface of a Bennu-like asteroid model. The simulation is propagated for a period of 48 hours at a fixed time step of 50 seconds, Section 3.1.1.3 presents an analysis of time step sizes. The asteroid model parameters are presented in Table 3.1. The asteroid model is set as a PAR with a rotation rate 30% faster than that of asteroid Bennu, a value selected to induce boulder motion according to the thresholds seen in Figure 2.10b. The asteroid model and boulder density values are based on [17, 52]. The parent body shape model is the one presented in Figure 2.1. No external perturbations are applied to the simulation. The modeled boulder, seen in Figure 3.1, is a perturbed 84 facet box with meter scale principal axes. The boulder size is selected to represent the boulder population described in [52]. The boulder is placed on a mid latitude in the northern hemisphere. The slopes conditions are selected based on [10, 101]. The cohesion strength is as described in [13], and boulder-regolith contact area is selected for a boulder at 15-20% burial, as seen in Figure 2.6b. The surface motion friction coefficients are based on experiments presented in [125, 126]. Due to lack of information of slide to roll ratio a fixed 1-1 ratio between the movements is selected. This leads to an overall constant friction factor of 0.625. The simulation is preformed with the randomness capabilities enabled ($\delta\mathbf{r}^{\mathfrak{B}_A}, \delta\dot{\mathbf{r}}^{\mathfrak{B}_A} \neq \mathbf{0}$).

In addition to the simulation of the modeled asteroid, a control case is run using the same asteroid parameters (parent body and boulder), but with motion conditions disabled. Throughout this chapter the control case is used to compare the results from the simulated asteroid state to those

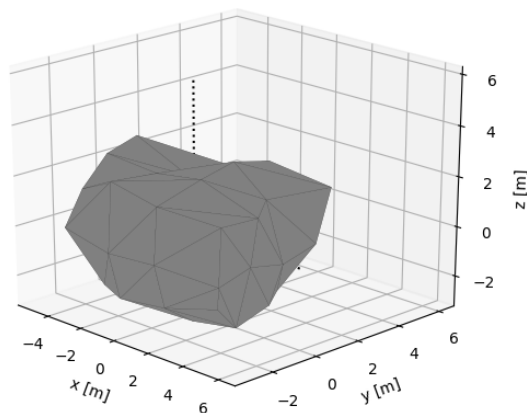


Figure 3.1: Boulder polyhedron in single boulder simulation

in which surface activity does not occur.

3.1.1.2 Results

Figure 3.2 presents the boulder motion in the first ~ 3 hours of the simulation as observed in the asteroid body frame. The boulder can be seen moving towards the asteroid's equator and slightly to the east (Figures 3.2a-3.2c), in the time between Figures 3.2c and 3.2d the boulder is launched to an equatorial orbit, which can be seen to continue in Figures 3.2e and 3.2f. Figure 3.3 presents the complete boulder trajectory during the simulation run projected on the model asteroid surface (in the asteroid body frame). The figure shows a global view (3.3), a local view presenting the first ~ 3 hour time frame (3.3b), and a close-up view of the surface motion of the boulder (3.3c). The figure presents all types of boulder motion: surface movement (notated as roll), launch events, crash events, and orbital motion. The boulder can be seen bouncing (crashing and launching immediately) several times in its path to the equator. Once it reaches near the equator (latitude ~ 12 degrees) it is launched to orbit for several revolutions. At around hour 10 of the simulation the boulder crashes and is immediately launched to orbit as seen in the near longitude -180 degrees in Figure 3.3a. Figure 3.4 presents the boulder's surface motion characteristics, its

Parameter	Values
Rotation period	3.3 [h]
Parent body density	1190 [kg·m ⁻³]
Boulder density	2000 [kg·m ⁻³]
Parent body principal radii	261, 254, 221 [m]
Boulder principal radii	5.25, 3.38, 2.95 [m]
Boulder mass	410 [ton]
Boulder location [lon,lat]	-16.6, 30.3 [deg]
Launch slope condition	90 [deg]
Static slope condition	40 [deg]
Kinetic slope condition	35 [deg]
Cohesion strength (p_c)	25 [Pa]
Boulder-regolith contact area (S)	30 [% of boulder surface area]
Sliding friction (μ_s)	0.5
Rolling friction (μ_r)	0.75
Friction ratio (κ)	0.5
Total kinetic friction (μ_k)	0.625

Table 3.1: Bennu asteroid model parameters

latitude, on-surface slope, and surface velocity magnitude. The boulder’s time in orbit is indicated by a gray background in the plot. A correlation between all three characteristics can be seen as the boulder travels towards the equator and accelerates its surface velocity, increasing its on-surface slopes. The boulder’s orbital trajectory can be seen in Figure 3.5, the orbit presents chaotic behavior (as described in [23]), with an evolving semi-major axis, eccentricity, and argument of periapsis. Behavior that is caused by the close proximity to the irregularly shaped model asteroid.

The model asteroid’s global characteristics of mass distribution and angular velocity best represent the change in asteroid state due to boulder activity. The model asteroid mass is seen in Figure 3.6 with four mass calculations presented in the figure: the overall system mass (M), the mass of the parent body, the simulated asteroid mass (M_A), and the control case asteroid mass. The mass evolution is shown both in an absolute kg value and as a fraction of the asteroid system mass. The results show the overall system mass remaining constant as the boulder is kept bound to the asteroid system. The modeled asteroid mass is seen to switch between the initial value and that of the parent body as the boulder moves from surface to orbit and vice versa. Figure 3.7 presents the asteroid’s inertia tensor evolution for the simulated case compared to the parent body and control case. The control case (and simulation initial values) are aligned with the asteroid’s principal axes of inertia (cross axis elements are zero). The simulated case inertia tensor values (in the original body frame) veers away from these initial values, reaching none zero cross axis inertia elements. A result that means the modeled asteroid’s principal axis have shifted. Figure 3.8 presents a relative comparison between the modeled asteroid’s principal axes throughout the simulation, the presented values are of the maximum inertia z-axis divided by the minimum and median inertia axes, x and y, respectively. This type of variable presentation allows for some analysis of the evolving model asteroid shape. The figure presents the values for the simulated case, the control case, and the parent body. Figure 3.8a presents the entire simulation run time, which shows, similarly to the mass, the inertia values (relative and absolute in Figure 3.7) alternating between the initial values and those of the parent body. The ratio between these two values are governed by the initial boulder placement and a-priori parent body shape. Figure 3.8b presents principal axis changes

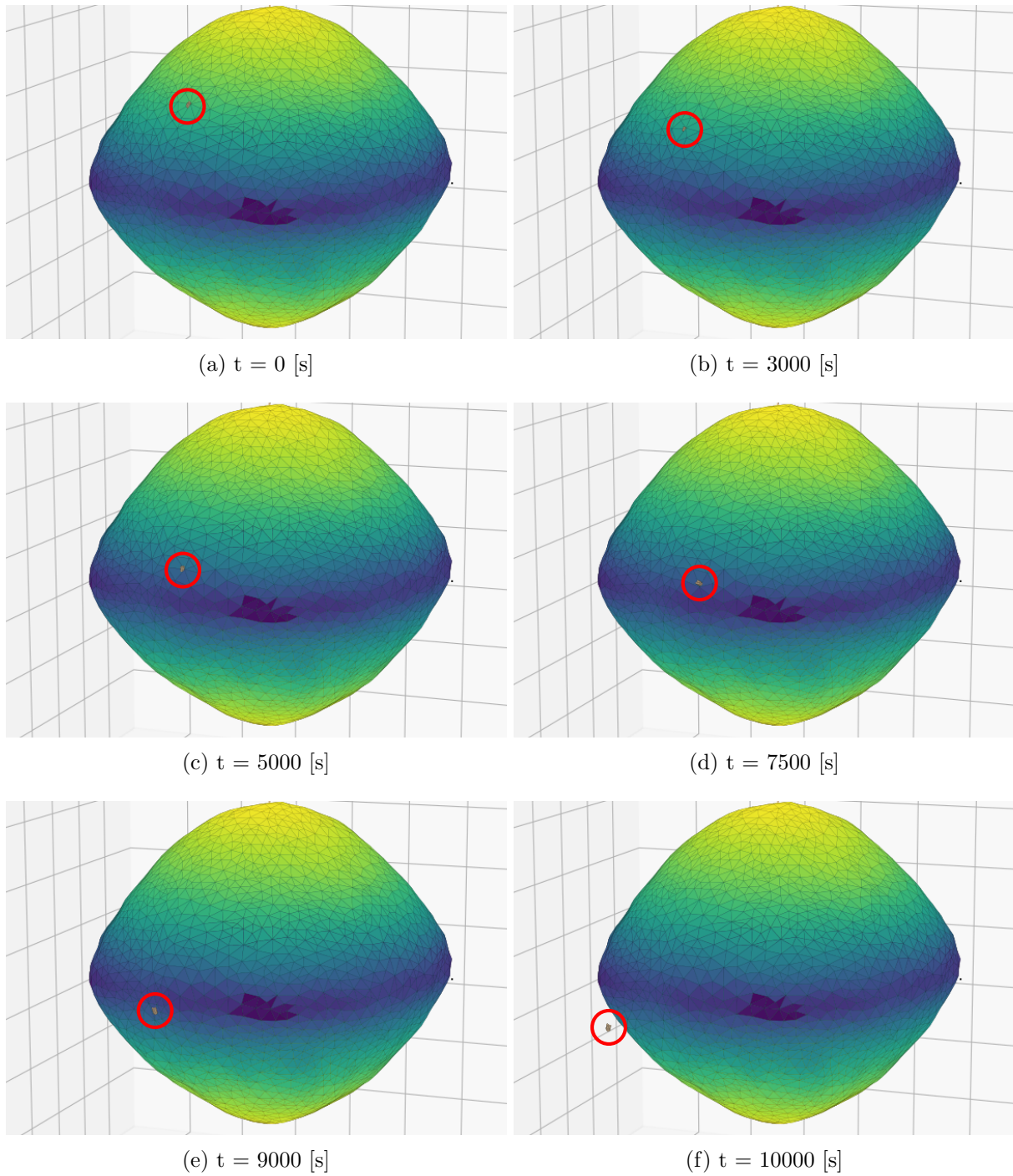
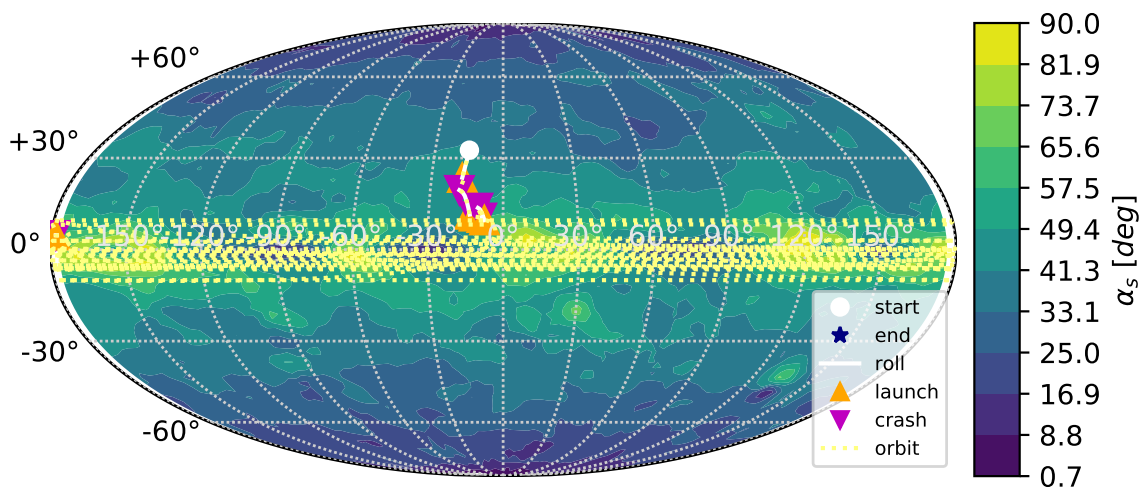
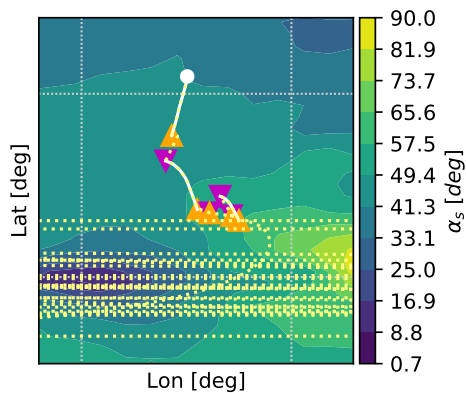


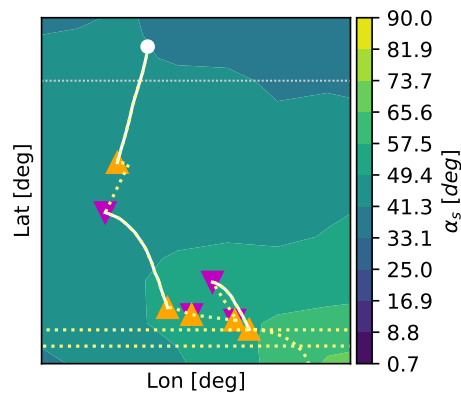
Figure 3.2: Boulder initial motion on Benu model in single boulder simulation



(a) Global view



(b) Local view



(c) Surface view

Figure 3.3: Boulder motion surface projection in single boulder simulation. The heatmaps indicate surface slopes, boulder initial position indicated by white dot, surface motion indicated by white line, boulder launch and crash events indicated by triangles, and orbit projection on surface indicated by dashed yellow line

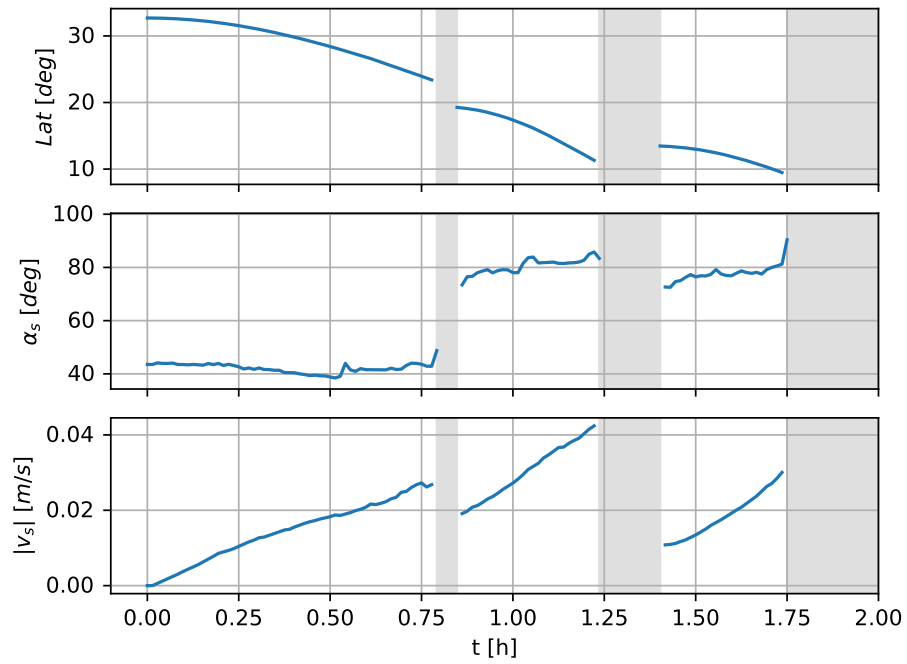


Figure 3.4: Boulder surface motion characteristics (latitude, surface slope, surface velocity) in single boulder simulation, the grayed areas indicate boulder off surface

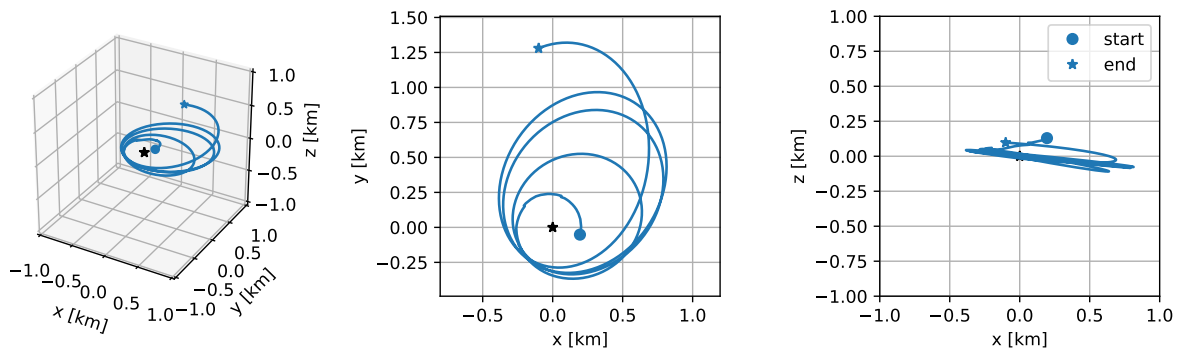


Figure 3.5: Boulder orbit motion in single boulder simulation

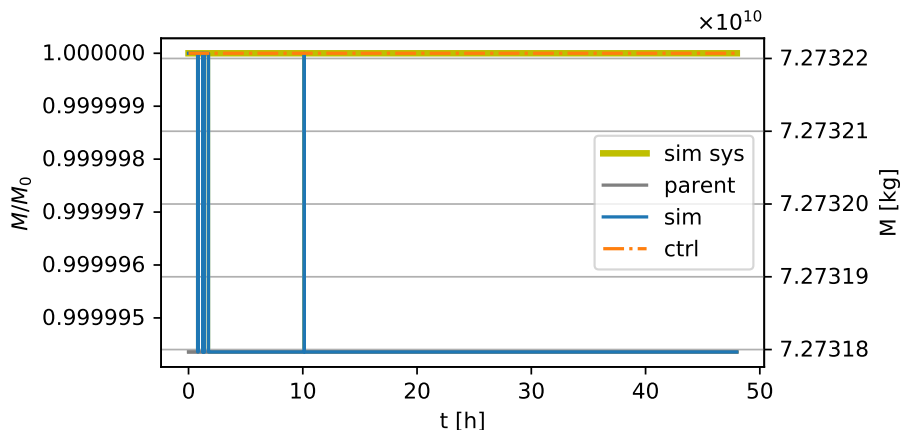


Figure 3.6: Modeled asteroid mass in single boulder simulation. The parameters presented include system mass, parent body mass, asteroid mass, and control case mass.

in the initial 2 hours of the simulation run, when the boulder is moving on the model asteroid’s surface. The figure shows an increase in the maximum inertia axis with respect to the other two axes, indicating a tendency of material to move towards the equator.

The modeled asteroid angular velocity vector evolution is presented in Figure 3.9. The figure shows both the simulated and control case values. A decrease of the angular velocity can be seen in the figure, this change in angular velocity amounts to an increase of 0.12 seconds in the model asteroid instantaneous (at the end of simulation) rotation period. The majority of angular velocity reduction can be seen in the first two hour of the simulation, when the boulder travels on the asteroid surface towards the equator. Additionally, an introduction of out-of-axis motion can be seen for the simulated case, this result, together with the change in inertia tensor elements leads to the loss of the PAR characteristic and the introduction of precession. For that reason the rotation period mentioned is an instantaneous one that is computed using one value of the changing angular velocity magnitude. The precession reached can also be seen in Figures 3.10-3.12 which show how the direction of the angular velocity vector evolves. Figure 3.10 presents the projection of the body frame angular velocity direction vector (normalized to magnitude) on the model asteroid equatorial plane (the body frame x-y plane). The out-of-axis motion is clearly seen in the figure, with the angular velocity circling around a point other than the original maximum inertia axis direction.

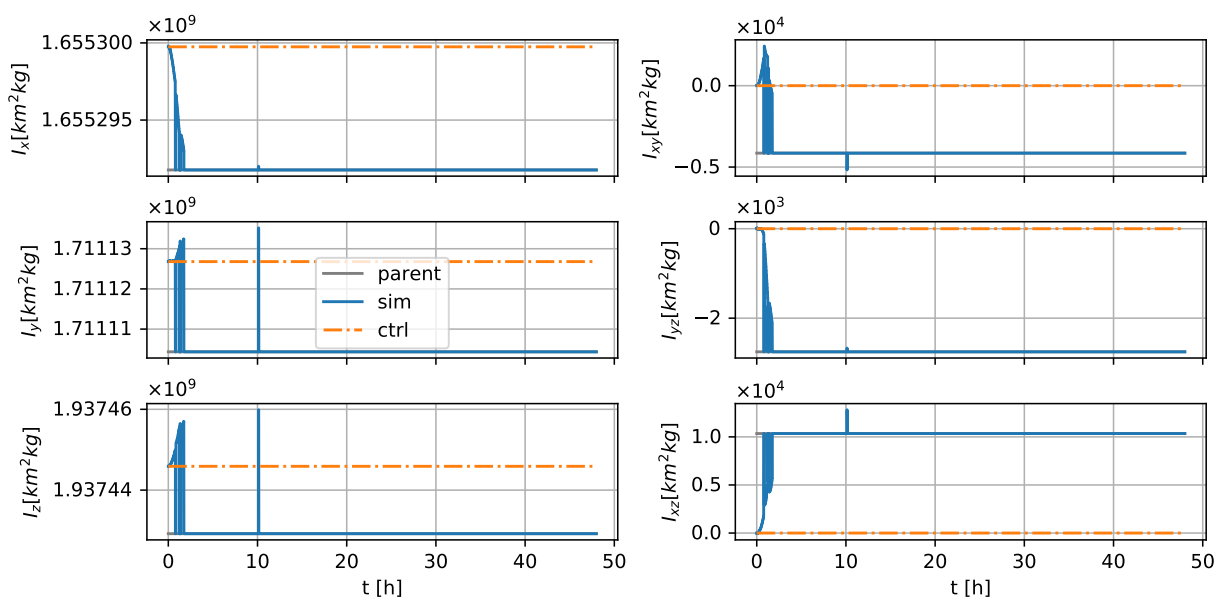
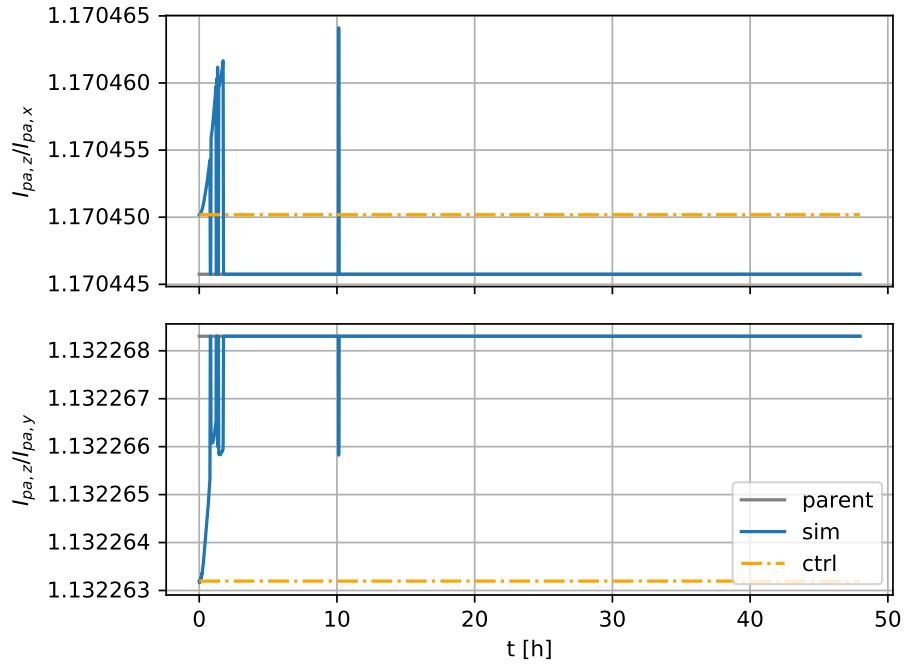
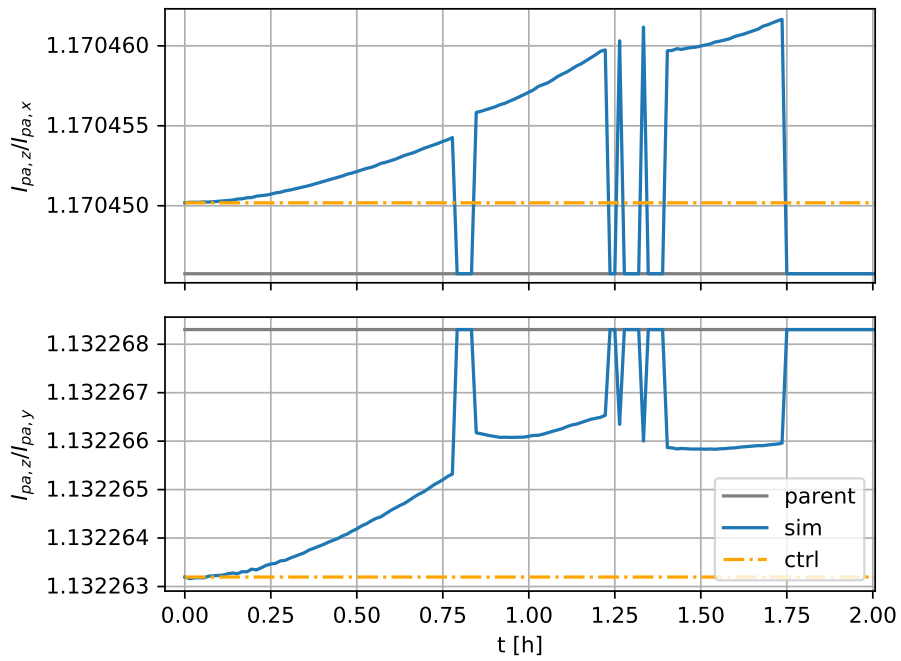


Figure 3.7: Modeled asteroid inertia tensor elements in single boulder simulation. The parameters presented include parent body inertia tensor, asteroid inertia tensor, and control case inertia tensor.



(a) Complete simulation



(b) Surface motion phase

Figure 3.8: Modeled asteroid principal maximum moment of inertia ratio with median and minimum principal moments of inertia in single boulder simulation. The parameters presented include parent body inertia ratio, asteroid inertia ratio, and control case inertia ratio.

Figure 3.11 presents the angle created between the original maximum inertia axis (seen by the control case) and the evolving angular velocity vector, as defined in Eq. 2.10. The angle includes both the shift in angular velocity direction due to boulder activity (predominantly seen as the shift in the initial hour of simulation as well the jump in hour 10) and the precession motion caused by the newly created misalignment between angular velocity and maximum inertia axis. Overall this angle reaches a magnitude of almost 0.005 degrees for a single boulder motion sequence. Figure 3.12 presents the angular velocity vector projection on the x-y plane in inertial frame as well as the angle between initial and evolving angular velocity directions in the inertial frame. These values show that for an external observer the angular velocity precesses in a smaller magnitude (~ 1 order of magnitude less), and in a higher frequency due to the model asteroid's rotation itself. The center of the angular velocity precession is shifted from the original direction due to the initial angular velocity changes, which means that the averaged angular velocity direction has changed as well.

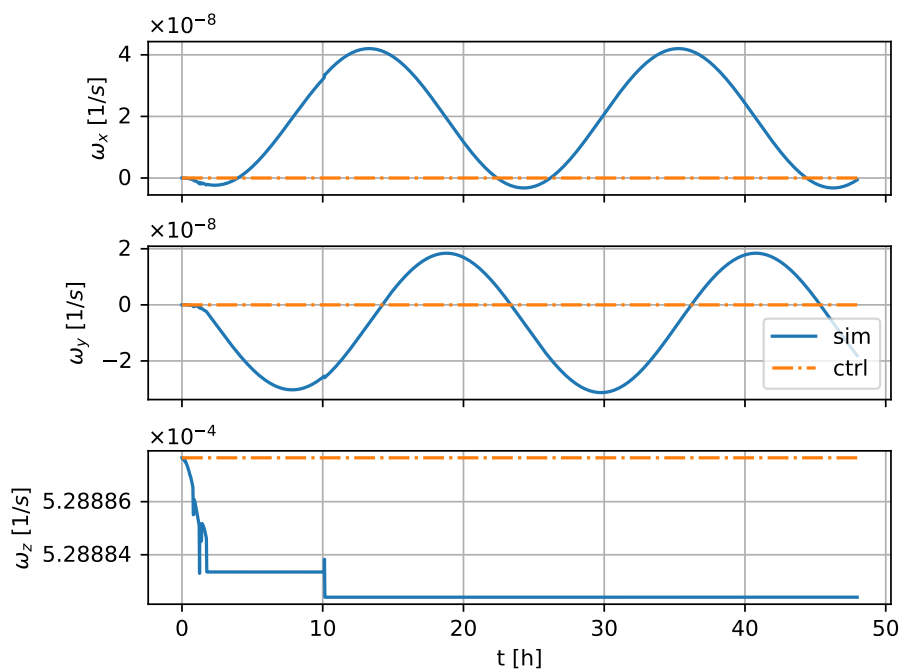


Figure 3.9: Modeled asteroid and control case angular velocity evolution in single boulder simulation (asteroid body frame)

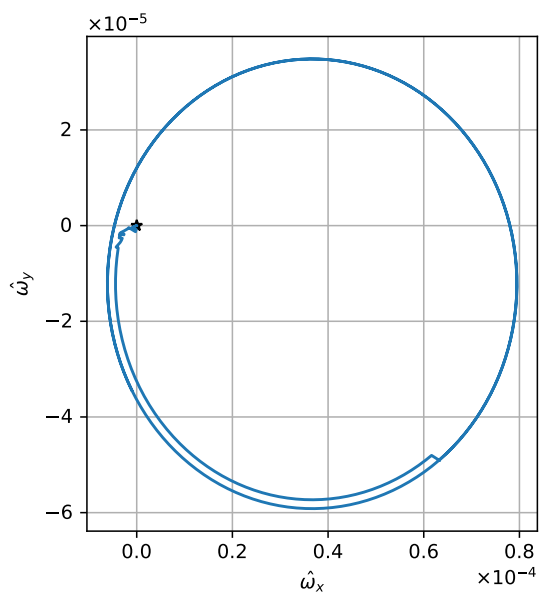


Figure 3.10: Modeled asteroid angular velocity vector projection on the equatorial plane in single boulder simulation (asteroid body frame)

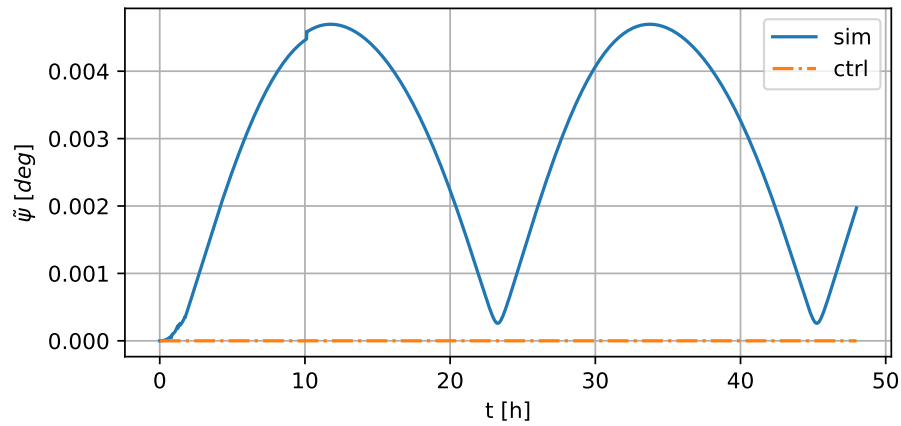


Figure 3.11: Modeled asteroid and control case angle between angular velocity vector and initial axis of maximum inertia in single boulder simulation (asteroid body frame)

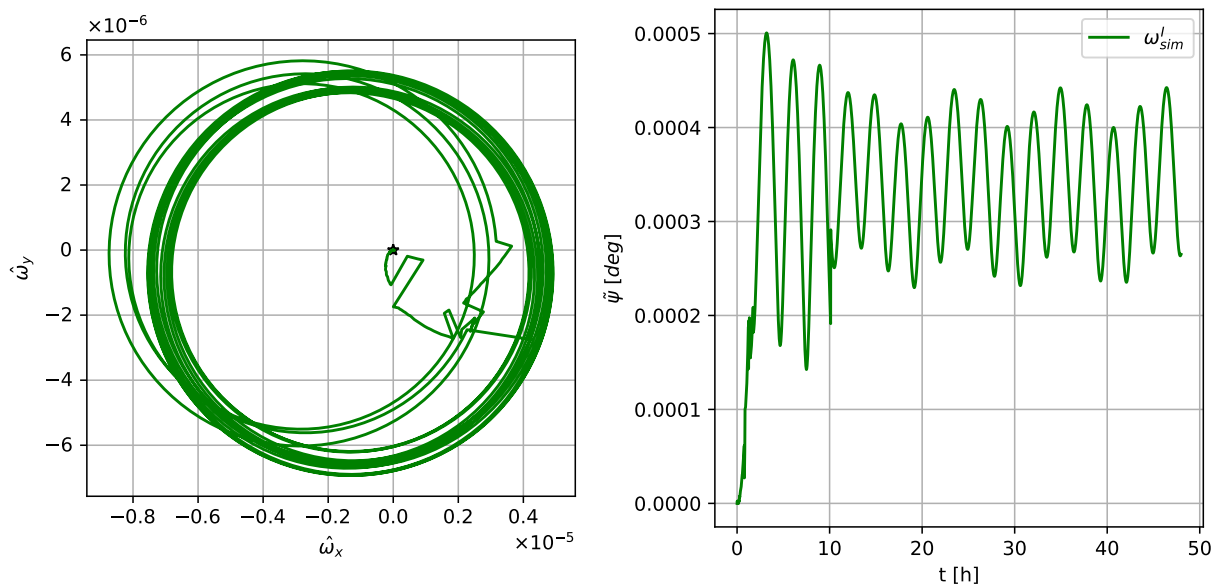


Figure 3.12: Modeled asteroid angular velocity vector projection on inertial x-y plane and angle between angular velocity vector and initial axis of maximum inertia in single boulder simulation (inertial frame)

3.1.1.3 Time step analysis

The following section presents an analysis of the simulation time step size performed to determine which time step is adequate for use in the simulations presented in this work. Figures 3.13-3.18 present results from seven simulations which differ only in the time step size. All the initial conditions are identically set to those presented in the previous section (Table 3.1) and the simulation randomness capabilities are disabled ($\delta\mathbf{r}^{\mathfrak{B}_A}, \delta\dot{\mathbf{r}}^{\mathfrak{B}_A} = \mathbf{0}$). The step sizes examined are 5, 10, 25, 50, 100, 200, and 400 seconds. These step sizes are 2 to 4 orders of magnitude smaller than the orbit period of a low altitude orbit around asteroid Bennu (which is ~ 12 hours for a 600 meter semi-major axis orbit) and are 1 to 3 orders of magnitude smaller than the modeled asteroid rotation period. Previous research has shown that this dynamic period to time step ratio is sufficient for orbit propagation [127]. Thus the analysis here seeks to examine the surface motion behavior for different time steps.

Figures 3.13-3.14 present the boulder position and velocity in the inertial frame for 6 hours. The boulder can be seen moving on the surface and then launching to orbit after almost 1 simulation hour (orbit indicated by the gray background). The overall motion behavior is the same with slight phase differences in the orbital motion. Figures 3.15-3.18 present the difference between all simulation results and the smallest time step results ($\mathbf{e}_{R,B,j} = \mathbf{R}_{B,j,\delta t} - \mathbf{R}_{B,j,\delta t=5s}$, $\mathbf{e}_{\dot{R},B,j} = \dot{\mathbf{R}}_{B,j,\delta t} - \dot{\mathbf{R}}_{B,j,\delta t=5s}$). Here the difference between orbit phases can be seen reaching hundred meter and $\text{cm}\cdot\text{s}^{-1}$ scale for the large time step simulations. However, a convergence in results can be seen as the time steps decrease. When looking specifically at the surface motion significantly smaller differences can be observed, with the largest differences between cases seen in the interface between surface and orbit. The 50 second time step shows a position difference of less than a meter and a velocity difference of less than $0.5 \text{ mm}\cdot\text{s}^{-1}$ at the end of the surface motion. These values are smaller than other sources of disturbance in asteroid environments, such as obstacles in a boulder's path on an asteroid surface. Thus, a 50 second time step is used for the simulations presented in this research.

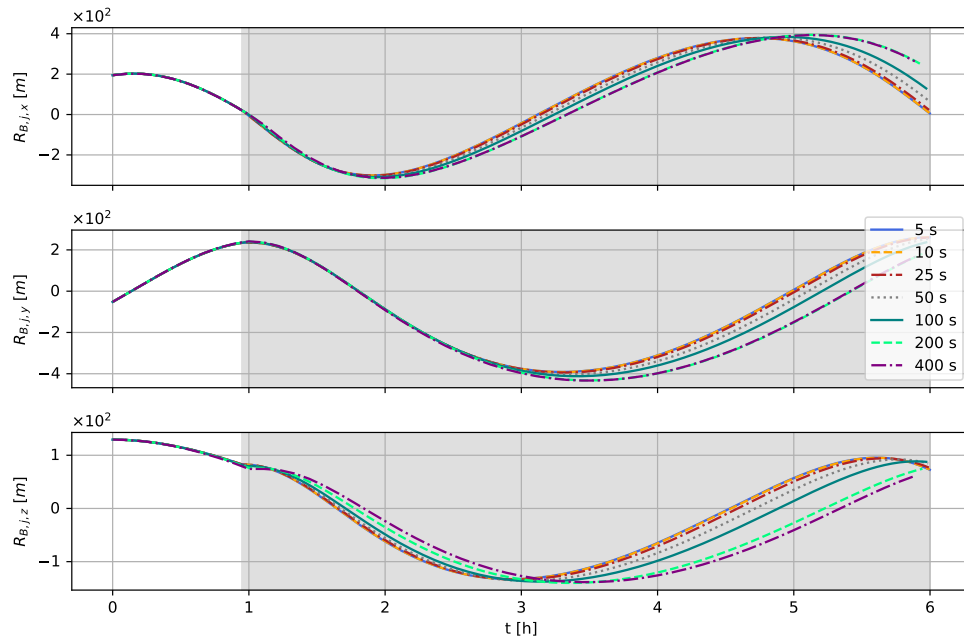


Figure 3.13: Boulder position for varying time step sizes (inertial frame)

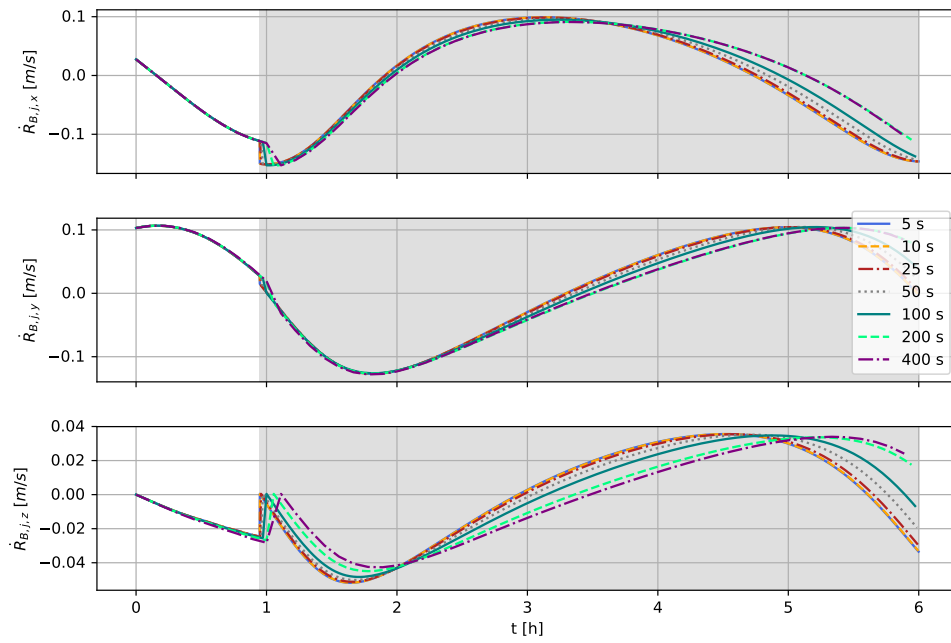


Figure 3.14: Boulder velocity for varying time step sizes (inertial frame)

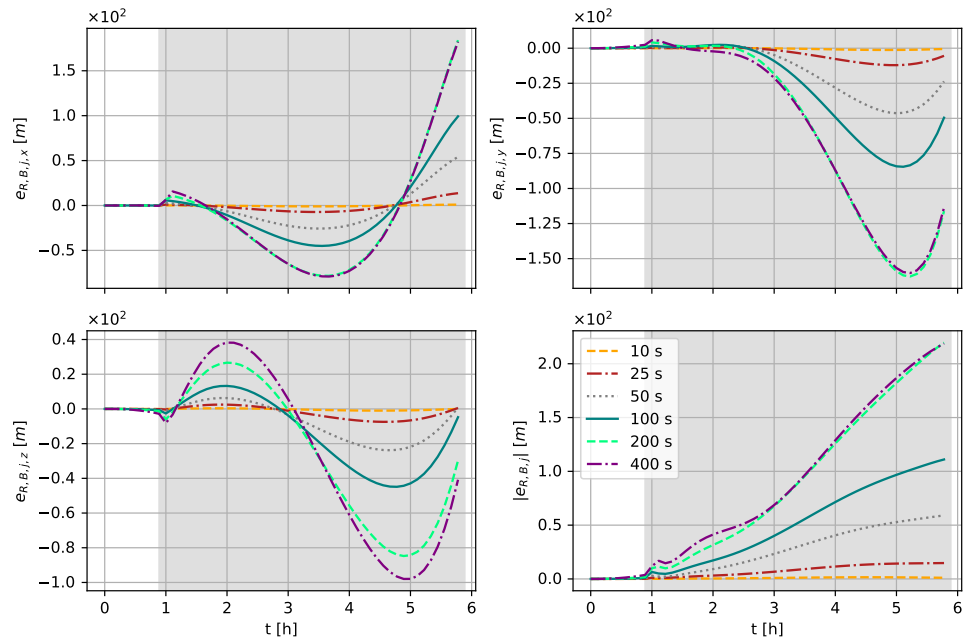


Figure 3.15: Boulder position difference from $\delta t = 5 [s]$ for varying time step sizes

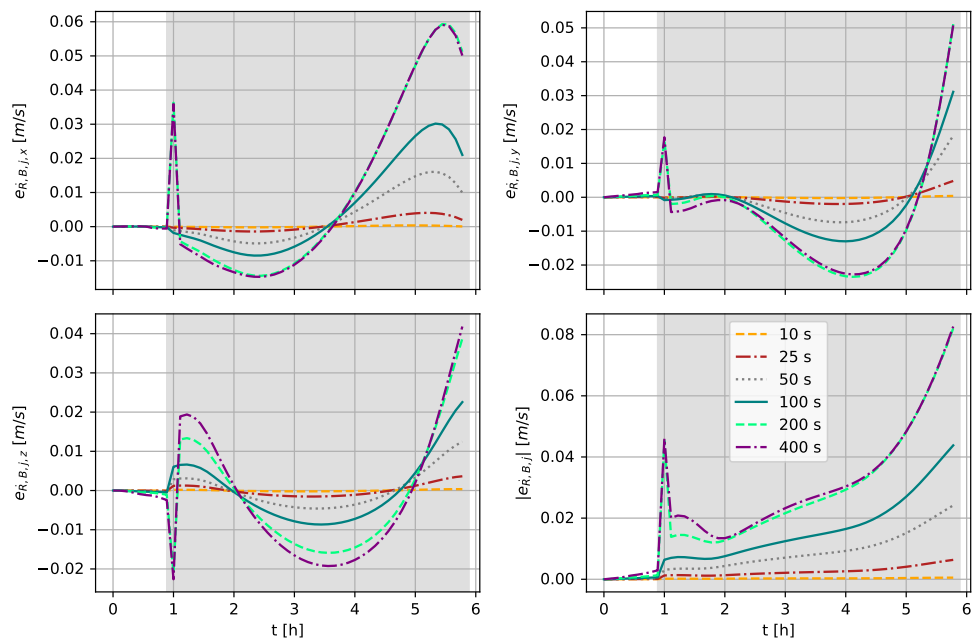


Figure 3.16: Boulder velocity difference from $\delta t = 5 [s]$ for varying time step sizes

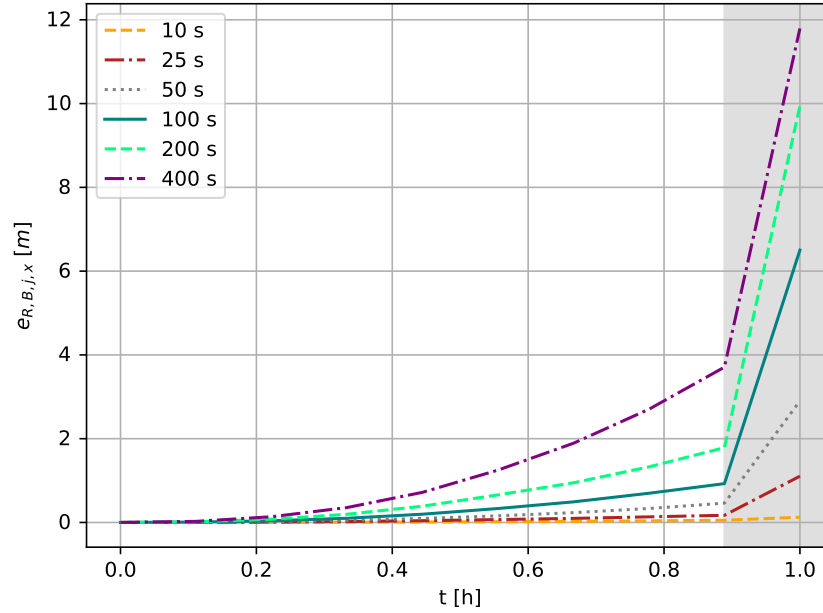


Figure 3.17: Boulder position difference magnitude from $\delta t = 5$ [s] for varying time step sizes during surface motion

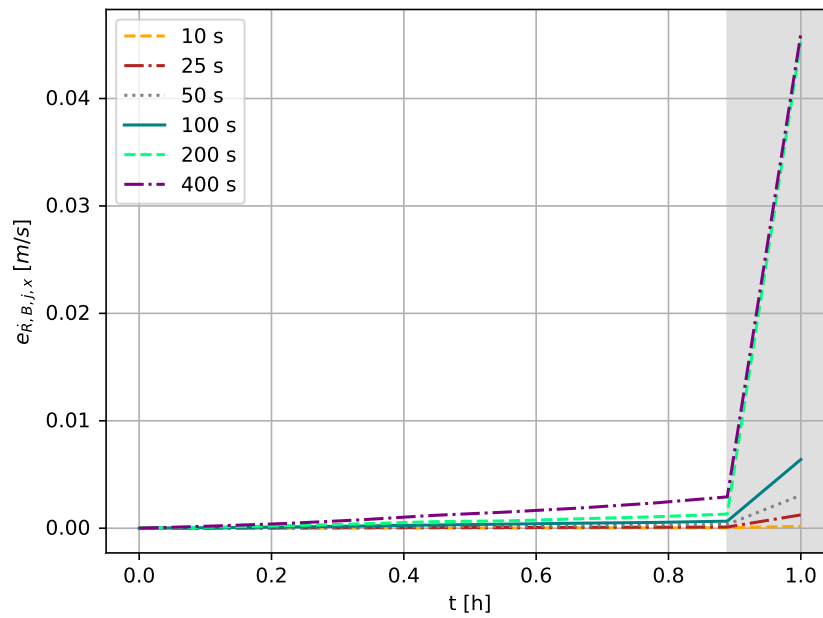


Figure 3.18: Boulder velocity difference magnitude from $\delta t = 5$ [s] for varying time step sizes during surface motion

3.1.1.4 Surface condition effects on boulder motion

A significant unknown in asteroid environments is the conditions and behavior of the surface with respect to motion of objects and material. For that reason the SEA RATS model has the capability to adjust key surface motion parameters. The following figures present results for three 12 hour simulations of the boulder presented previously differing only in the surface motion parameters, presented in Table 3.2. The parameters in the three cases are set to represent three levels of cohesion strength. These are defined by the motion slope conditions and the friction coefficient ratio. The static slope conditions are set by the range of values described in the literature [10]. And the kinetic slope condition is set to be 5 degrees lower than the static one. Higher static slope conditions were examined as well, but they did not reach motion initiation, and thus resulted in a static simulation. The friction ratio was used to determine the magnitude of friction coefficient in order to minimize the number of variables checked. The nominal surface motion parameters used throughout this research are those of case 2. For the purpose of comparison the simulation randomness capabilities are disabled.

Parameter	Case 1	Case 2	Case 3
Static slope condition	35 [deg]	40 [deg]	42 [deg]
Kinetic slope condition	30 [deg]	35 [deg]	37 [deg]
Friction ratio (κ)	1.0	0.5	0.0
Total kinetic friction (μ_k)	0.5	0.625	0.75

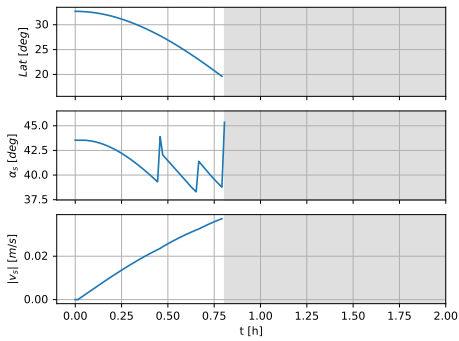
Table 3.2: Surface motion parameters

Figure 3.19 presents the boulder surface motion characteristics and trajectories for all three cases. When comparing the initial surface motion, all three cases present a similar surface trajectory but with different scales in time to launch, maximum velocity reached, lowest latitude reached, and

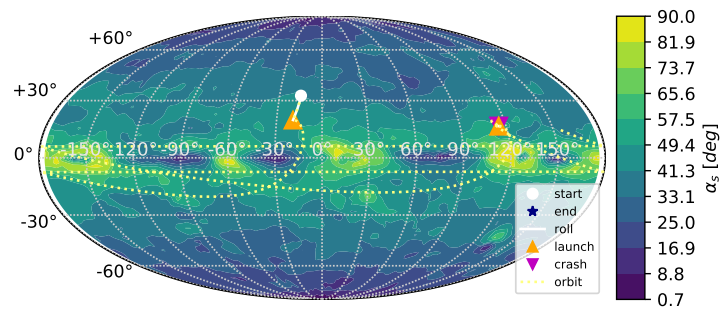
on-surface slope at time of launch. These differences can all be explained by the different friction coefficient used to model the motion, leading to a range of velocity loss magnitudes, which lead to longer duration on the surface and more surface traveled. The orbital trajectories that follow (also presented in Figure 3.20) are similarly of low altitude and chaotic, presenting a different orientation due to the difference in location in inertial space at time of launch. However, these orbits lead to the same eastern region for the boulder's first crash. A crash that for cases 1 and 3 leads to an immediate launch back into orbit. For case 2 the crash leads to surface motion towards the equator, a short bounce, and then stopped motion on the equator. This difference in results serves as evidence to the chaotic nature of orbits around small bodies and the resulting redistribution of material.

The global model asteroid characteristics are presented in Figures 3.21 and 3.22 which compare the simulations' principal axis inertia tensor element ratio and angular velocity evolution. The inertia tensor element ratio in Figure 3.21 shows, similarly to the previous section results, the maximum principal axis inertia element growing with respect to the other two for the duration of the boulder movement towards the equator. The growth in the ratio differs in duration (later launch time for more friction) and magnitude (lower latitude reached for more friction). The effect of the difference in motion on the modeled asteroid seen in Figure 3.22 shows the same trend as the inertia element ratio, larger difference in angular velocity for higher friction cases, especially for the duration of the surface motion seen in Figure 3.22b. The figure also shows the change in angular velocity that results from the boulder launch to correlate to the surface velocity at launch, largest change for case 1, and lowest for case 3. However, the overall change to angular velocity (surface motion and launch) is highest in case 3, presenting a higher contribution to the surface motion over the boulder launch. The end results of the angular velocity magnitudes correlate to an instantaneous rotational period increase of 0.09 seconds for case 1, 0.08 seconds for case 2, and 0.1 seconds for case 3. These results do not adhere with the surface motion trend due to the chaotic nature of the orbital motion and return of the boulder in case 2 to the surface.

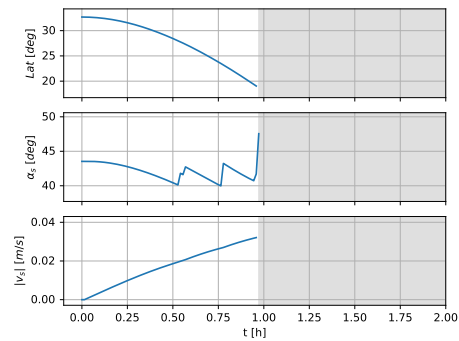
In general, the results presented here show an overall consistent boulder behavior and motion trend



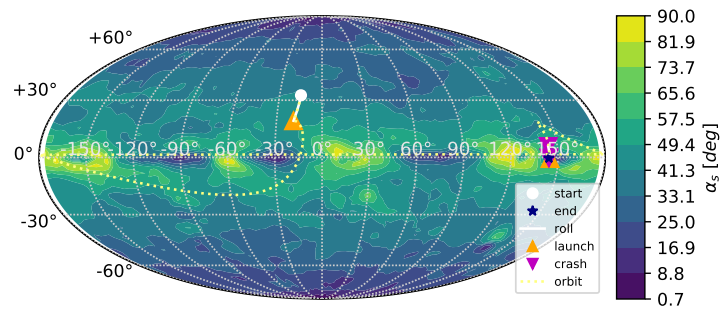
(a) Case 1 boulder surface motion characteristics



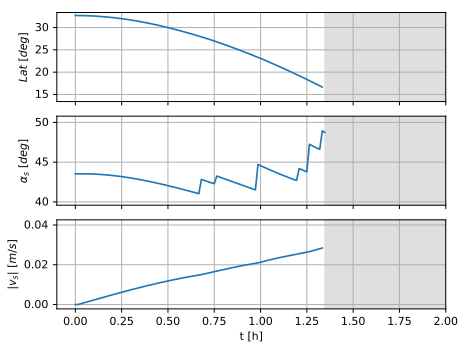
(b) Case 1 boulder trajectory



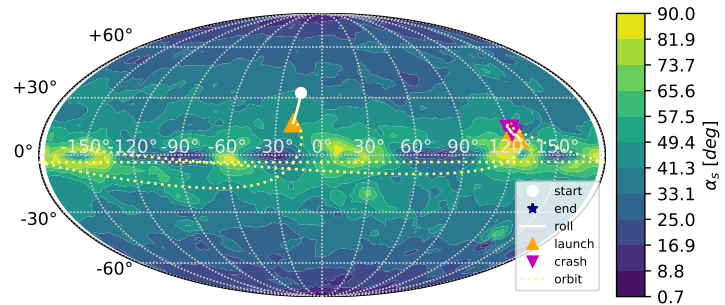
(c) Case 2 boulder surface motion characteristics



(d) Case 2 boulder trajectory



(e) Case 3 boulder surface motion characteristics



(f) Case 3 boulder trajectory

Figure 3.19: Varying surface motion parameter simulation results. Left subfigures show surface characteristics (latitude, surface slope, surface velocity) and right subfigures show boulder trajectory projection on the surface

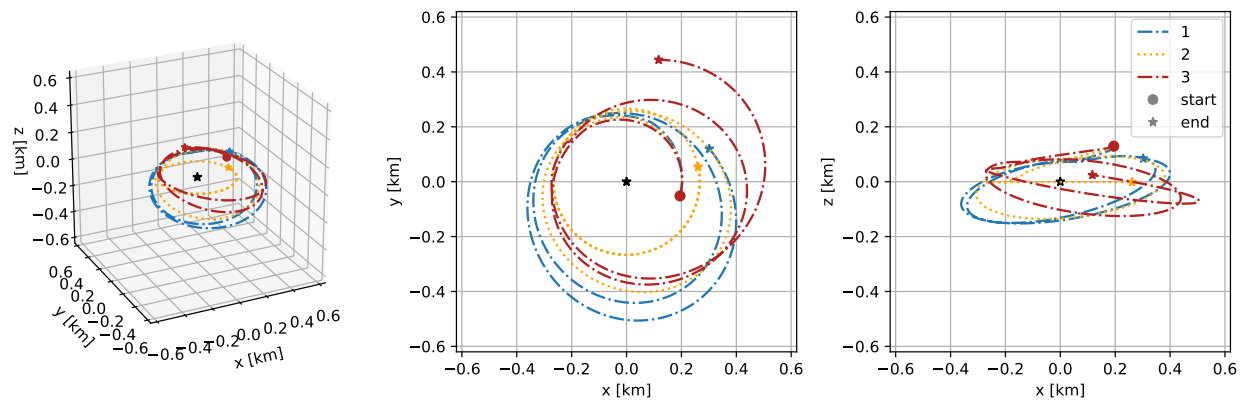


Figure 3.20: Boulder orbit motion in single boulder simulation for varying surface motion parameters

(motion toward equator and launch once critical velocity is reached) within the range of surface motion characteristics described in past research. When comparing the case 2 results to those of the previous section, which differ only in the simulation randomness capability being disabled, the trends are similar, but the added random factors (best seen in the on-surface slopes and surface velocity in Figures 3.4 and 3.19c) leads to an earlier launch in the randomness enabled case which “fails” to become orbital. That in turn leads to additional time on the surface for the boulder, which results in lower latitude and higher on-surface slopes and surface velocity reached, providing an overall larger change in the angular velocity vector magnitude.

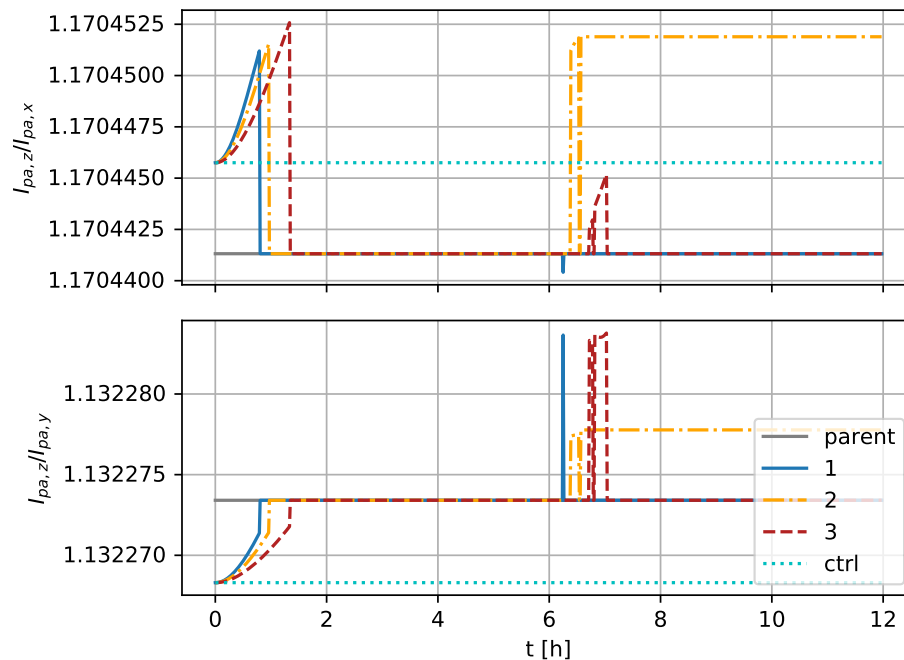
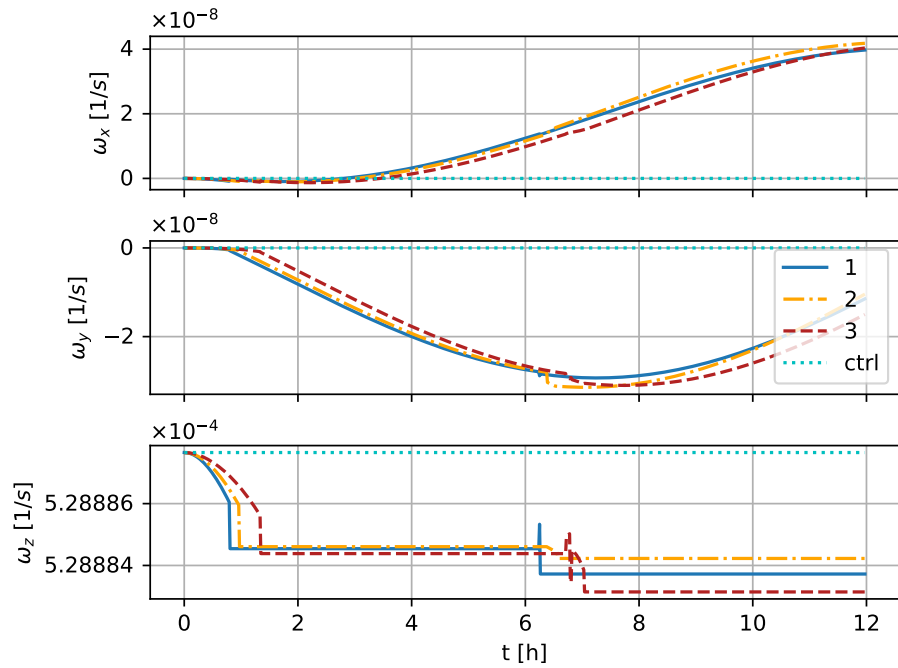
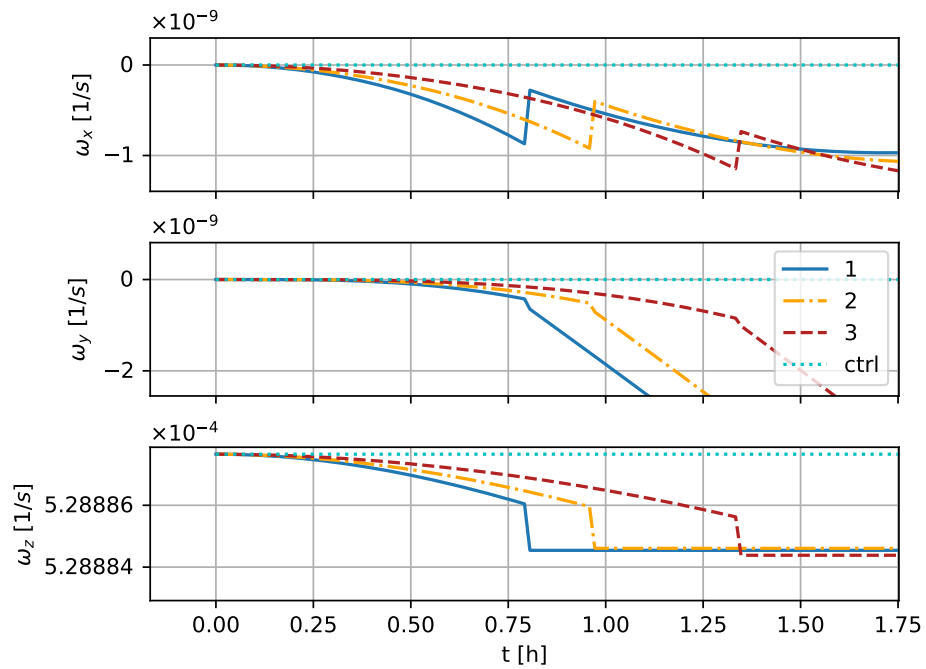


Figure 3.21: Modeled asteroid principal maximum moment of inertia ratio with median and minimum principal moments of inertia in single boulder simulation for varying surface motion parameters. The parameters presented include parent body inertia ratio, asteroid cases inertia ratio, and control case inertia ratio.



(a) Complete simulation



(b) Surface motion phase

Figure 3.22: Modeled asteroid and control case angular velocity evolution in single boulder simulation for varying surface motion parameters (asteroid body frame)

3.1.2 Multiple boulder motion on an asteroid Bennu model

The following section presents simulation results of twenty five boulders randomly distributed on the surface of the model asteroid Bennu.

3.1.2.1 Simulation setup

The simulation setups used are an accelerated PAR modeled Bennu identical to that presented in Section 3.1.1 (30% faster than nominal rotation) and a tumbling modeled Bennu, accelerated to the same angular velocity magnitude as in Section 3.1.1 but with the angular velocity vector direction presented in Figure 2.3. Table 3.3 presents the simulation setup condition differences.

Parameter	PAR modeled Bennu	Tumbling modeled Bennu
Initial angular velocity magnitude	$5.28887 \times 10^{-4} \text{ [s}^{-1}\text{]}$	$5.28887 \times 10^{-4} \text{ [s}^{-1}\text{]}$
Initial angular velocity direction	[0,0,1]	$[\frac{1}{4}, \frac{1}{4}, \sqrt{\frac{7}{8}}]$
Simulated period	48 hours	24 hours

Table 3.3: Multiple boulder simulation parameters

The twenty five boulders randomly placed on the parent body surface are presented in Figure 3.23a. The boulders are again perturbed 84 facet boxes differing in mean radii between 3 and 12 meters and overall axis ratio around 4-3-2. Each boulder is randomly perturbed such that their shape and placement orientation differ. An example of the largest and smallest boulders are presented in Figure 3.24. The boulder presented in Section 3.1.1 is included in the simulated boulders in this section as boulder #11.

In addition to the single simulation results presented in Sections 3.1.2.2 and 3.1.2.4, Section 3.1.2.3 presents results from a Monte Carlo simulation of 250 runs of the PAR modeled Bennu. These simulations are identical in all parameters and initial conditions and only differ by the boulder

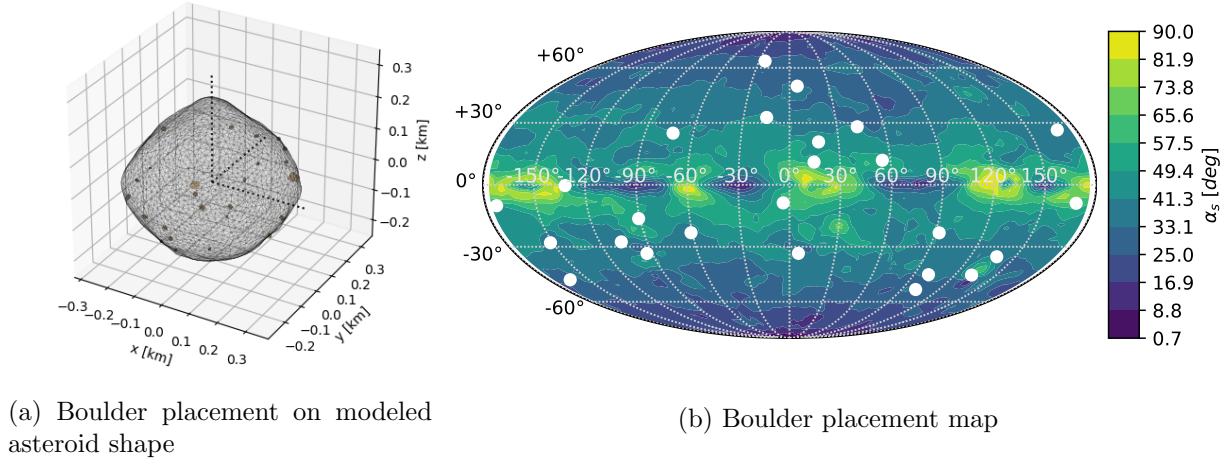
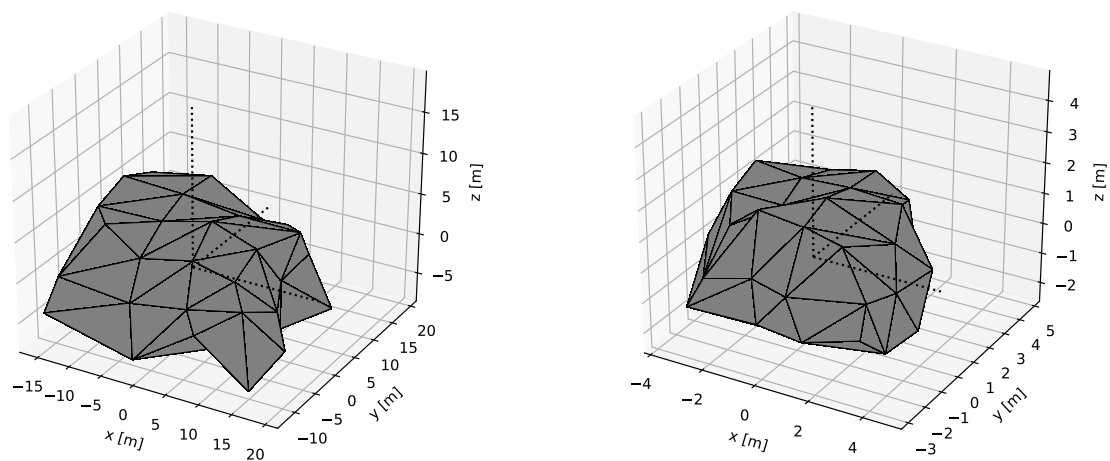


Figure 3.23: Initial boulder placement for Bennu multiple boulder case

motion randomness ($\delta \mathbf{r}^{\mathcal{B}_A}, \delta \dot{\mathbf{r}}^{\mathcal{B}_A} \neq \mathbf{0}$).

3.1.2.2 Results for principal axis rotator

Figure 3.25 presents a summary of the boulder motion on and off the surface of the asteroid model, projected on the its surface. Figure 3.25a shows boulders' initial positions, final positions, and surface motion trajectories. In Figure 3.25b the boulders' orbits are added to present their complete paths with respect to the surface. An overall trend towards the equator is observed, with a slight tilt due west caused by the Coriolis Effect. Boulders do not seem to cross the equator, but rather travel towards it, stop in mid latitudes, or reach near-equatorial regions and launch to orbit. All launched boulders have some amount of surface motion before launching to orbit. This result correlates with the magnitude of cohesion forces a static boulder on the surface experiences, forces that are reduced once a boulder is in motion. All launches, but that of Boulder #11, occur within latitude ± 15 degrees and lead to low inclination orbits. The equatorial region presents several crash-launch events in which a boulder touches down and immediately launches back to orbit. The boulder initially located in coordinates $[\sim 55, \sim 12]$ degrees travels to the equator, launches into



(a) Largest boulder (principal radii 16.5, 12.1, 8.0 [m]) (b) smallest boulder (principal radii 4.0, 2.8, 2.4 [m])

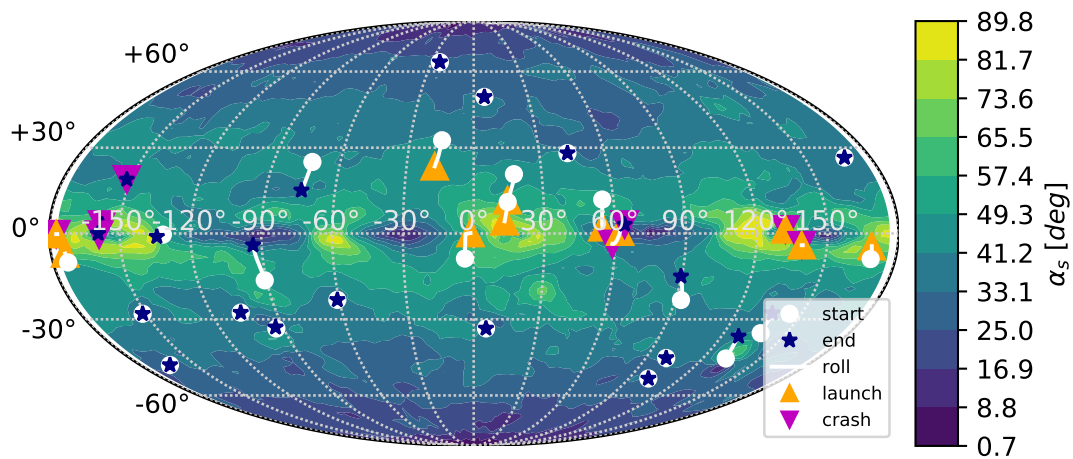
Figure 3.24: Examples of asteroid model surface boulders

a ballistic trajectory, crashes, travels back to the equator and hops again before stopping on the surface, all occurring in the same equatorial region around longitude 60 degrees.

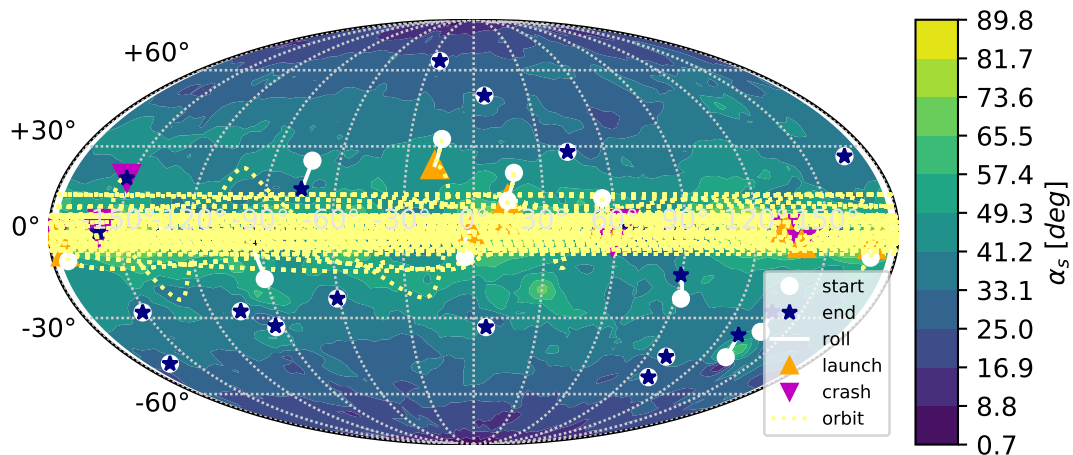
The trajectories of Boulder #11 and an additional boulder, #22, are seen in Figure 3.26. Boulder #22 is a 1291 ton boulder (principal radii 8.8, 5.7, 3.3 meters) originally placed in longitude and latitude $[-4,-9]$ degrees. Boulder #11 is the most extreme latitude boulder to reach launch conditions. It moves from latitude 33 degrees due south, launches around latitude 23 degrees, orbits the asteroid model for two revolutions within 100 meters from the surface before crashing on the surface at the highest latitude crash (~ 20 degrees). Boulder #22 also travels towards the equator, reaches it, lingers at the equator in a state of instability for more than 3 hours before reaching a critical state and then launches into a ~ 0 degree inclination orbit. The boulder orbits the asteroid model for several revolutions before touching down on the surface and launching back to orbit at longitude and latitude $[160,0]$ degrees. Boulder #22 eventually crashes on the surface near longitude and latitude $[-160,0]$ degrees. As seen in Figure 3.25, other boulders also exhibit this crash-launch behavior, some even more than once during the simulation run time. The maximum surface speed reached are 0.039 and $0.023 \text{ m}\cdot\text{s}^{-1}$ for boulder #11 and boulder #22, respectively. The highest surface speed reached is of boulder #12, initially located at latitude and longitude $[132,-45]$ degrees, making it the highest latitude boulder to move, which reaches a surface speed of $0.041 \text{ m}\cdot\text{s}^{-1}$. The speeds are a testament to the slow pace of dynamics in asteroid environments and the low velocities required for launching material off of asteroids.

All boulders' overall trajectories in inertial space can be seen in Figure 3.27. Again, the low inclination of the orbits resulting from the equatorial launches can be seen. All the orbits also present chaotic behavior due to the close proximity to the irregular shaped asteroid model. Most boulders in orbit crash back into the asteroid model by the simulation cut-off and none of them reach an escape trajectory sending them away from the asteroid system.

In the scenario presented here a total of 14 out of 25 boulders moved on the surface, out of which 7 boulders launched to orbit or a sub-orbital trajectory. Three boulders remained in orbit by the end of the simulation. As seen before, this surface activity had an effect on the asteroid model

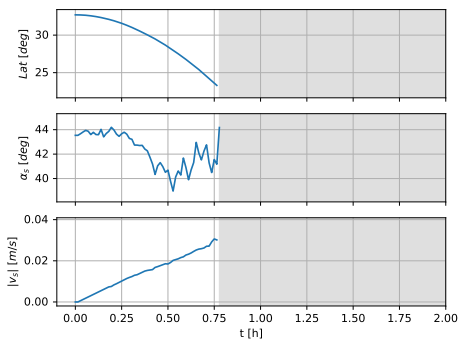


(a) Surface motion

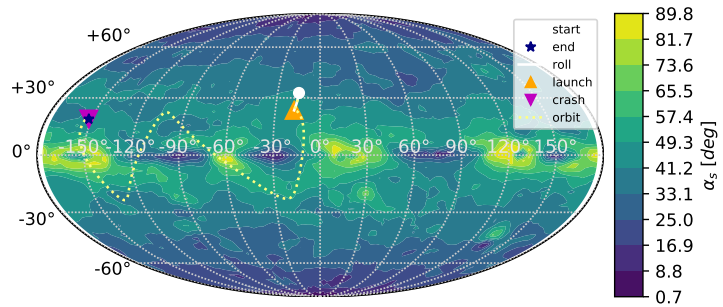


(b) Surface and orbital motion

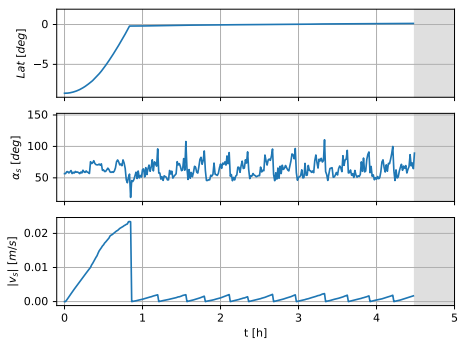
Figure 3.25: Boulder motion surface projection in Benu multiple boulder simulation. The heatmaps indicate surface slopes, boulder initial position indicated by white dot, surface motion indicated by white line, boulder launch and crash events indicated by triangles, orbit projection on surface indicated by dashed yellow line, and boulder final position indicated by blue star.



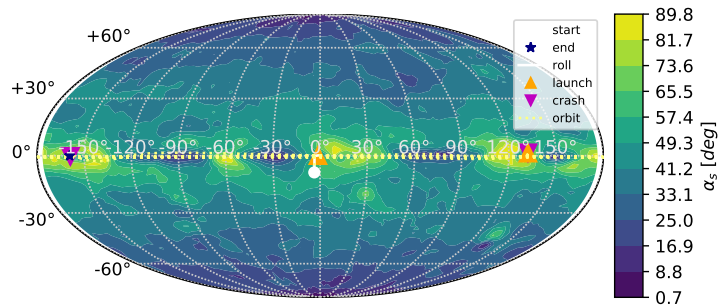
(a) Boulder #11 initial surface motion characteristics



(b) Boulder #11 trajectory



(c) Boulder #22 initial surface motion characteristics



(d) Boulder #22 trajectory

Figure 3.26: Boulders #11 and #22 motion characteristics and trajectories. Left subfigures show surface characteristics (latitude, surface slope, surface velocity) and right subfigures show boulder trajectory projection on the surface.

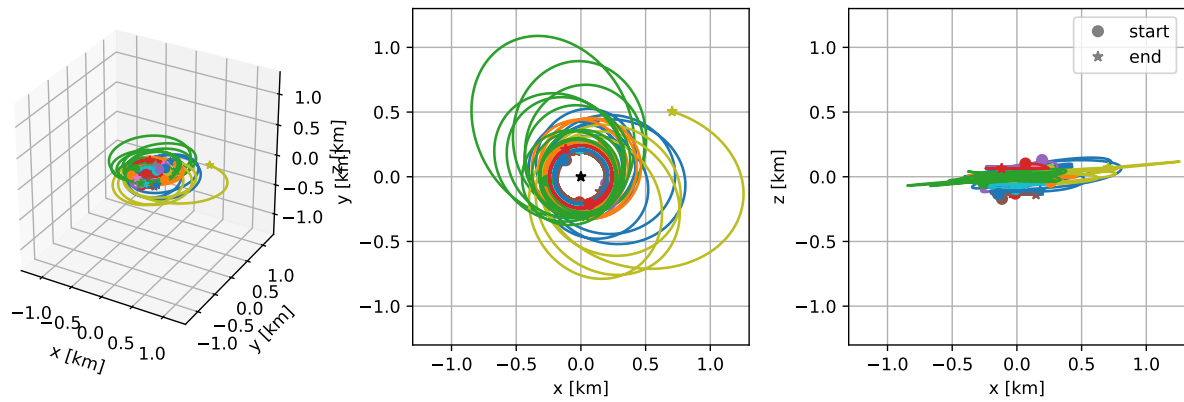


Figure 3.27: Boulder orbit motion in Benu multiple boulder simulation

itself, leading to changes in the mass properties as well as system dynamics. Figure 3.28 presents the evolution of the asteroid model and asteroid system masses. The figure shows a substantial amount of activity in the beginning of the simulation. This can be explained by the introduction of the new, higher, rotation rate compared to the asteroid Bennu whose shape is used as the basis of the asteroid model. The figure also shows that the maximum amount of lost mass is around 0.021% of the total mass (or ~ 15240 tons), this is only about a third of the sum of the surface boulder masses. The mass that remains in orbit by the simulation cut-off is about 0.018% of the initial mass (~ 13240 tons). The crash-launch events can be seen in the figure as spikes around hours 17,40 and 45. The majority of mass loss is attributed to boulder #18, with a mass of 11640 tons, which launches from near its original location at $[15,11]$ degrees and remains in orbit by the end of the simulation. Figure 3.29 presents the inertia tensor evolution of the asteroid model, this is a better indicator of the change in mass properties due to boulder surface motion (which will not be shown in the system mass change). Again, most activity is seen in the initial hours of the propagation. The deviation from the initial principal axis and introduction of non-zero off-diagonal elements is seen in the figure. The continuous growth in maximum principal axis ratio with respect to the median and minimum axis is seen during the first 0.75 hours in Figure 3.30. However, once boulders launch off the surface the moments of inertia principal axes ratios break, leading the maximum-minimum ratio at lower values and the maximum-median ratio at higher values.

The evolution of the angular velocity vector is seen in Figure 3.31. The loss of the PAR characteristic is seen as well as an overall reduction in the angular velocity magnitude. This reduction constitutes an added 2.52 seconds in asteroid model's instantaneous rotation period (at the simulation end). When comparing Figure 3.31 to Figures 3.28 and 3.29, it can be seen that the significant changes in angular velocity correlate to the pure surface motion, rather than launch and crash events. Meaning the changing inertia tensor has a more substantial effect on the asteroid model angular velocity than the momentum transfer due to boulder launch.

Figure 3.32 presents the asteroid body frame angular velocity vector projection on the asteroid equatorial plane as well as the angle between initial body frame maximum inertia axis and evolving

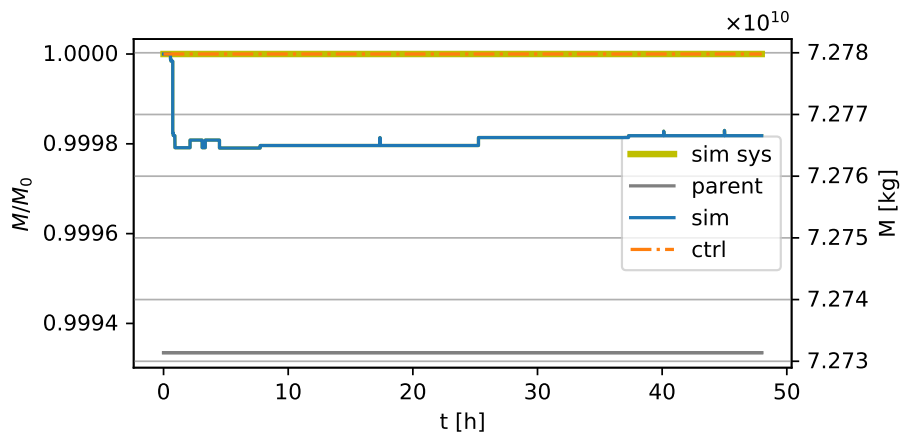


Figure 3.28: Modeled asteroid mass in Bennu multiple boulder simulation. The parameters presented include system mass, parent body mass, asteroid mass, and control case mass.

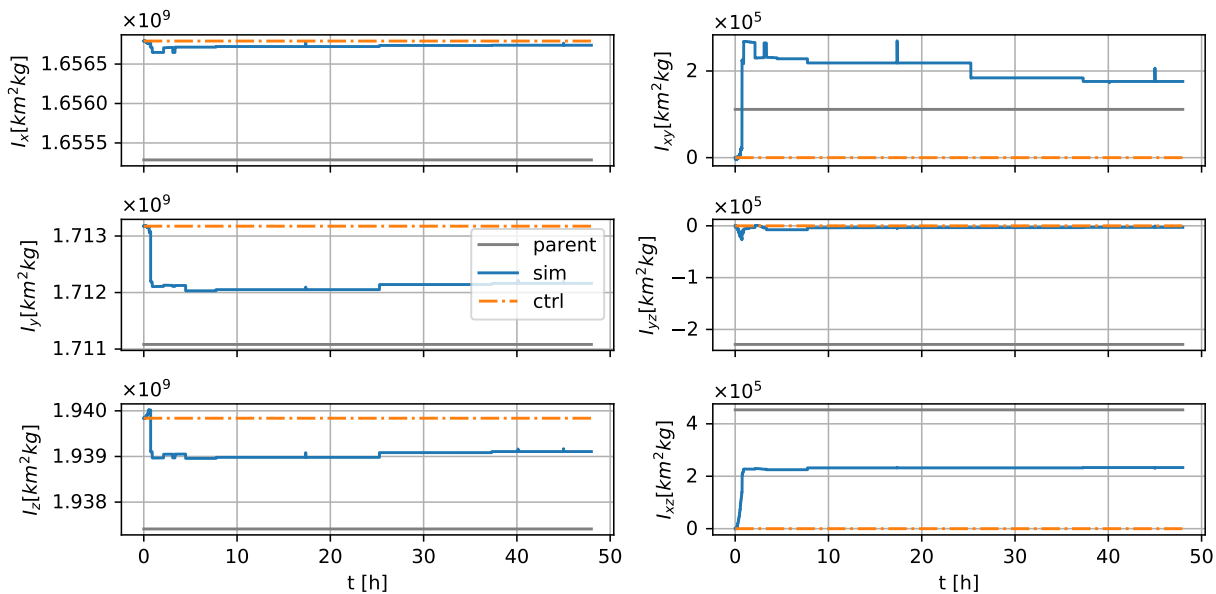


Figure 3.29: Modeled asteroid inertia tensor elements in Bennu multiple boulder simulation. The parameters presented include parent body inertia tensor, asteroid inertia tensor, and control case inertia tensor.

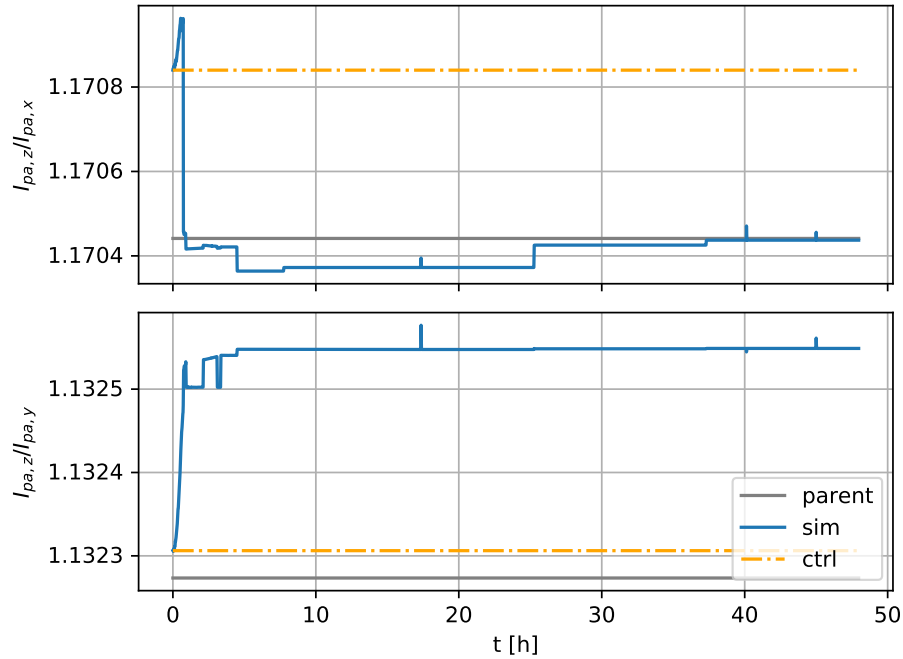


Figure 3.30: Modeled asteroid principal maximum moment of inertia ratio with median and minimum principal moments of inertia in Bennu multiple boulder simulation. The parameters presented include parent body inertia ratio, asteroid inertia ratio, and control case inertia ratio.

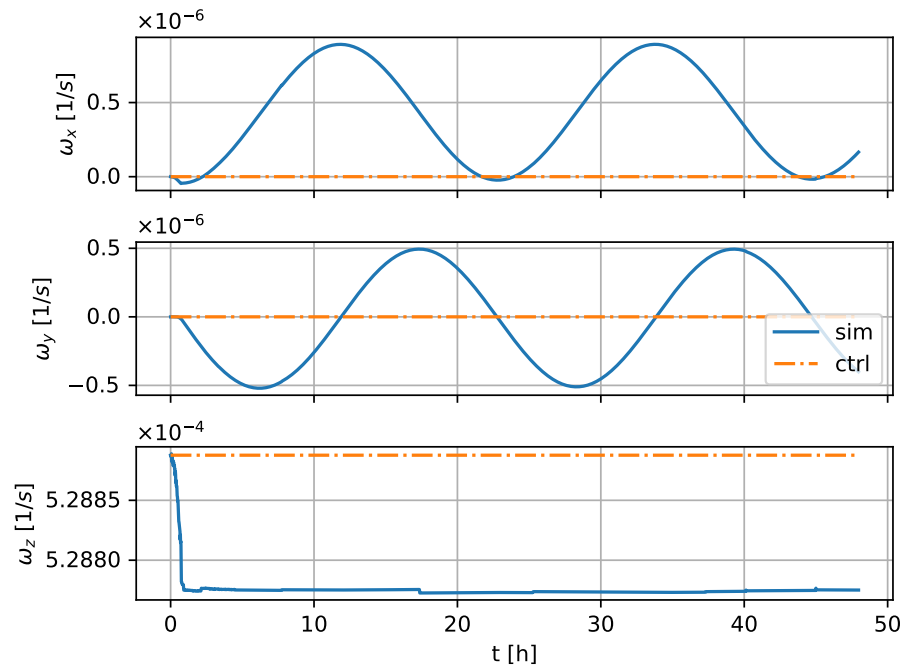


Figure 3.31: Modeled asteroid and control case angular velocity evolution in Bennu multiple boulder simulation (asteroid body frame)

angular velocity vector. Here the modeled asteroid precession is seen to reach a maximum angle of almost 0.1 degrees. However, because of the gradual initial boulder motion the precessing angular velocity returns close to its initial orientation once in a precession cycle. The precession as observed in inertial space is seen in Figure 3.33, similarly to the previous results the magnitude of precession is about 10 times smaller and at a higher frequency than the in the asteroid body frame. The precession in inertial space also show a different center of rotation due to boulder motion, this new center is likely to become the the new inertial direction of angular velocity as dissipation sets in and the precession is damped back to a PAR.

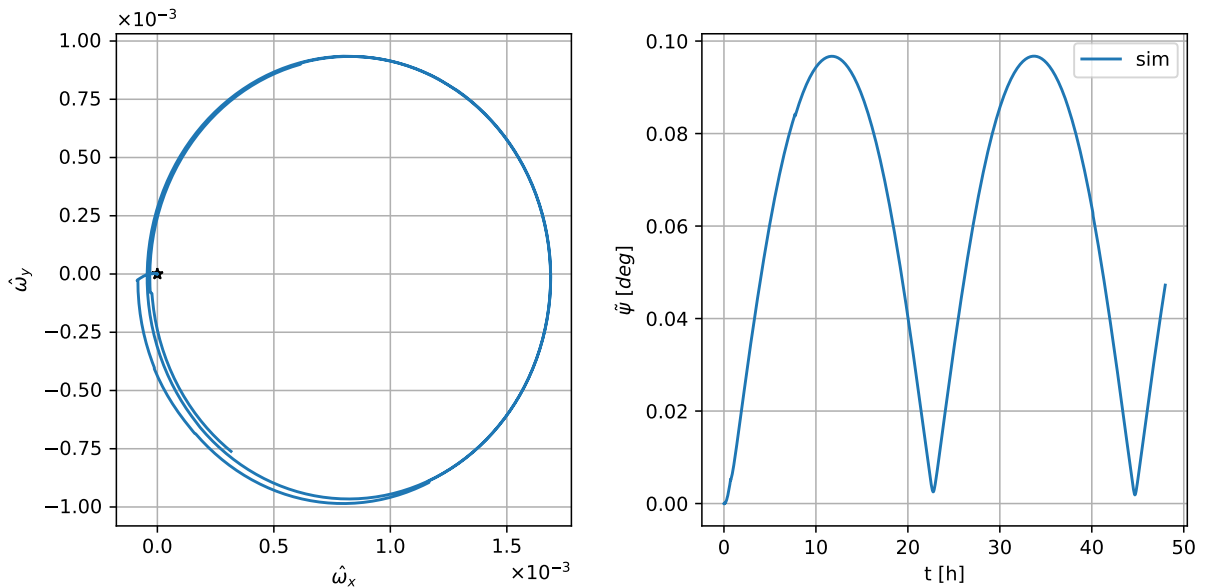


Figure 3.32: Modeled asteroid angular velocity vector projection on the equatorial plane and angle between angular velocity vector and initial axis of maximum inertia in Bennu multiple boulder simulation (asteroid body frame)

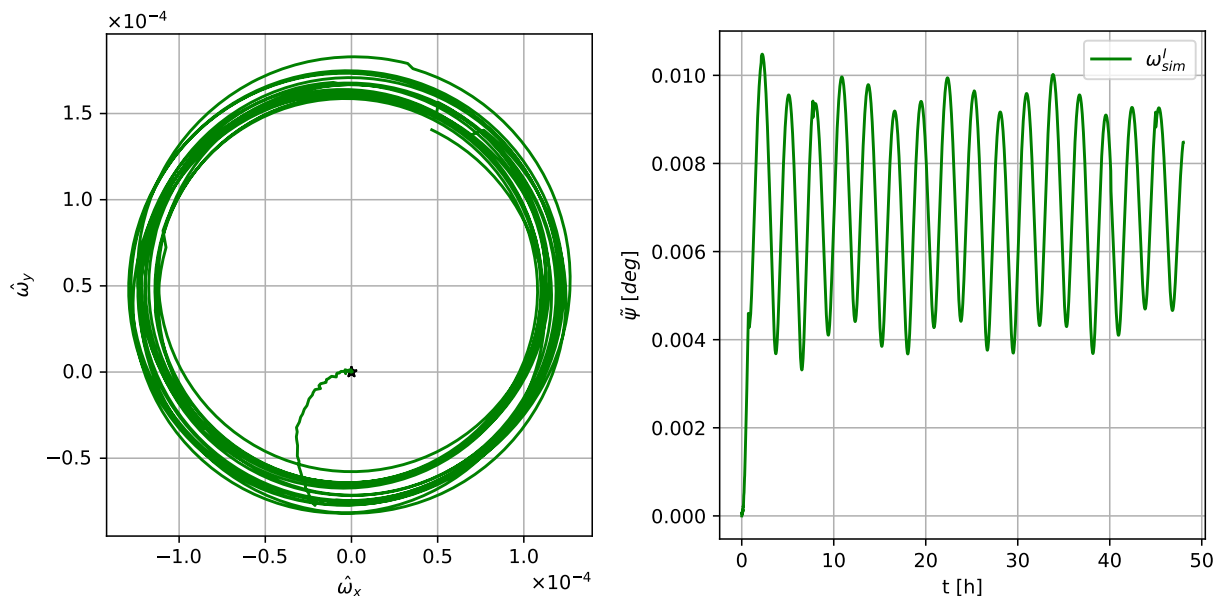


Figure 3.33: Modeled asteroid angular velocity vector projection on inertial x-y plane and angle between angular velocity vector and initial axis of maximum inertia in Bennu multiple boulder simulation (inertial frame)

3.1.2.3 Principal axis rotator Monte Carlo results

As mentioned in Section 2.4, boulder placement during surface movement has both deterministic and random elements to it. These leads to some random walk behavior in boulder motion, as seen when comparing Section 3.1.1's results to Boulder #11 in the previous section. This setup means that a single case does not necessarily represent the definitive outcome of a given boulder placement. For that reason multiple simulations are propagated differing only by the added $\delta\mathbf{r}$ and $\delta\dot{\mathbf{r}}$ perturbing vectors at each step of surface movement. By using a Monte Carlo (MC) simulation setup trends in the asteroid model dynamics can be studied and overall behaviors can be examined. The following figures present the end distributions of 250 cases, identical in initial state to the case presented in Section 3.1.2.2. These cases are propagated for 24 hours. The histograms also present the control case values, the end value means, and the end value 1σ standard deviation.

Figure 3.34 presents the distribution of final asteroid model masses. All but one of the cases show

some mass loss, with one large distribution peak ($\sim 65\%$ of cases) around 0.02% mass loss. Another, smaller peak is noticed around 0.033% mass loss, and a third peak presents $\sim 0.003\%$ mass loss. This type of distribution is the result of the discrete nature of boulder masses as part of the asteroid model, leading to similar changes as the same masses end up in orbit.

Figure 3.35 presents the ratio between the initial and final values of the inertia tensor elements. The off-diagonal ratios in the figure are computed with respect to the initial minimum inertia x axis because their initial, aligned with principal axes, values are zero. The figure shows that all cases gain off-diagonal elements, showing that all cases lose the PAR characteristic of the asteroid model. Most cases show the final diagonal elements smaller than the initial values with small off-diagonal elements, evidence of the asteroid model mass loss. The maximum inertia z axis does present about 20% of results reaching higher values. Results that relate to mass migration to the equator, either by pure surface movement or by launch and crash events. Figure 3.36 presents the principal-axis moments of inertia ratios between the maximum axis and the median and minimum axes. The results show three major clusters of new ratios between the asteroid model principal axes. The largest cluster is similar to the results presented in Figure 3.30, with an increase (up to 0.031%) in the z - y ratio, and a decrease (up to 0.035%) in the z - x ratio. The two other results either show an increase, or a decrease in both ratios. Results that can be explained by boulder redistribution from orbital motion.

The changes in asteroid model average rotation rates and periods are seen in Figure 3.37. Here the rotation rate is averaged over the final hours of the simulation once the boulder motion's effect on rotation has stopped. All cases show a decrease in rotation rate, with the average instantaneous rotation period increasing around 3 seconds and a maximum instantaneous rotation period increasing about 4.5 seconds. The end averaged rotation rate results present a close-to-Gaussian distribution which correlates to the different paths the boulders have taken. Figure 3.38 presents the distribution of rotation direction parameters in the inertial frame. The distribution map on the left shows the center of the equatorial plane projection of the precession ellipse reached at the end of each propagation. The histogram on the right shows the distribution of maximum cone angles

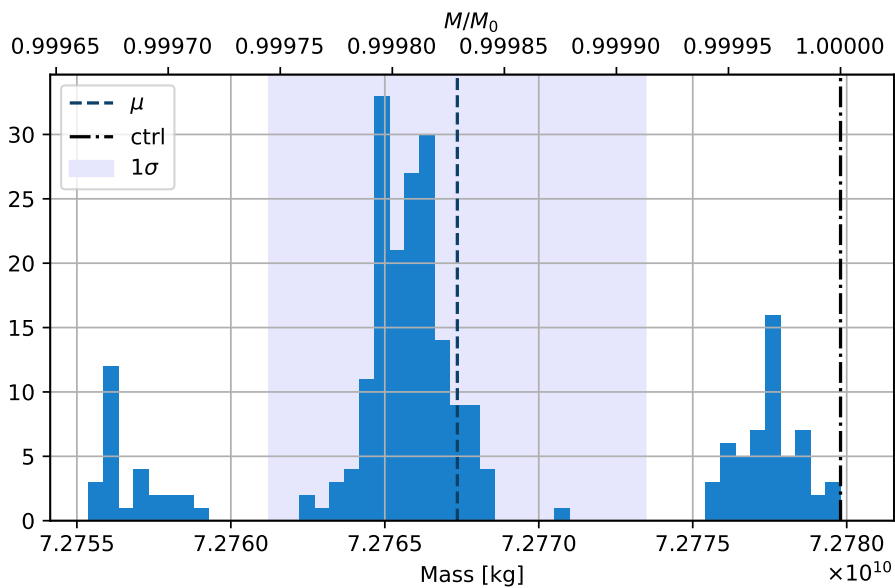


Figure 3.34: Modeled asteroid final mass in Benu multiple boulder Monte Carlo simulation. Histogram includes distribution mean and 1σ bounds as well as control value.

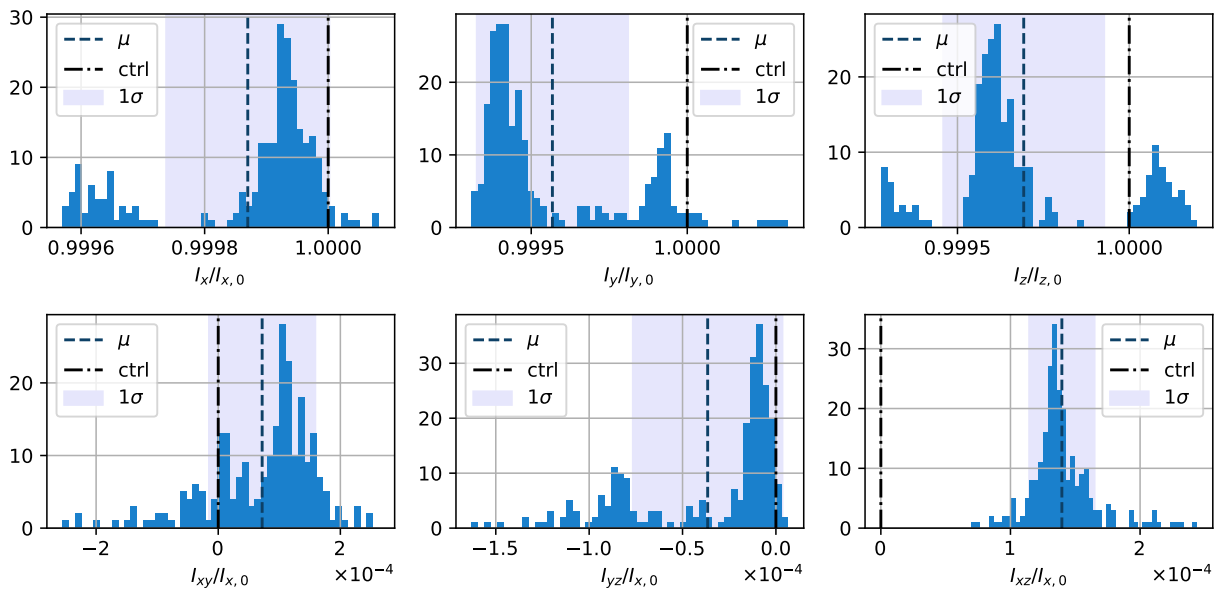


Figure 3.35: Modeled asteroid final inertia tensor elements in Benu multiple boulder Monte Carlo simulation. Histograms include distribution means and 1σ bounds as well as control values.

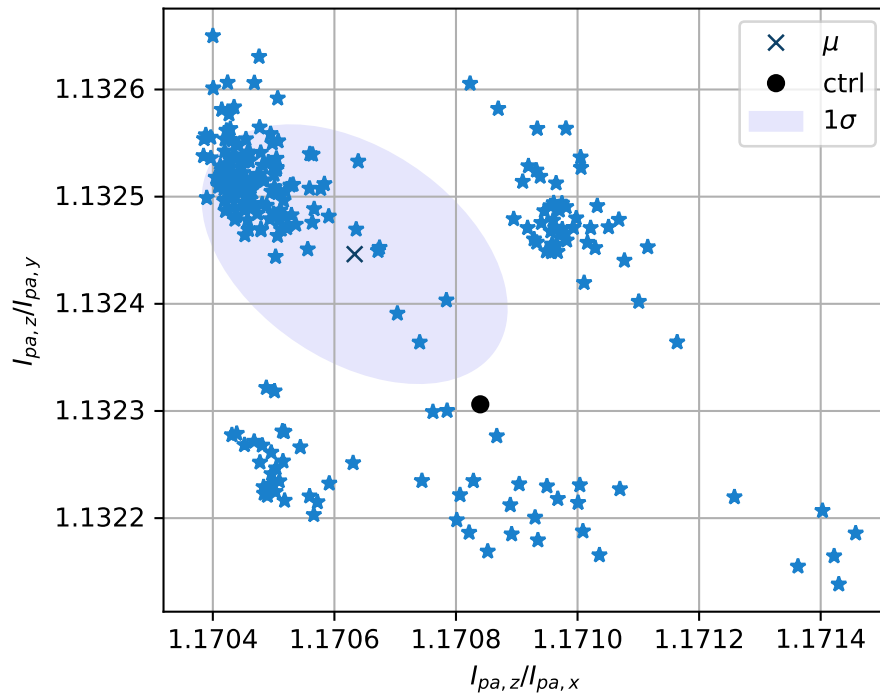


Figure 3.36: Modeled asteroid final principal maximum moment of inertia over median and minimum moments of inertia in Bennu multiple boulder Monte Carlo simulation. Distribution maps includes distribution mean and 1σ ellipsoid as well as control value.

created by the shift of the angular velocity and precession motion.

The MC path results for boulders #11 and #22, presented in Figure 3.26, are presented in Figures 3.39 and 3.40. Boulder #11 presents a wide variety of outcomes leading it to launch from different latitudes between its initial location and the equator. This leads to different orbits, varying in inclination. Three wide crash-launch sites can be seen, together they span about 60% of the equatorial regions between latitudes ± 20 degrees. By the end of the 24 hour simulation runs $\sim 80\%$ of boulder #11 cases have crashed back to the surface, while $\sim 20\%$ remain in orbit (all cases presented some orbital motion). Boulder #22 shows more consistent behavior, presenting mostly equatorial orbits at inclinations of up to ± 10 degrees. Boulder #22 also presents three crash-launch areas, but they span $\sim 40\%$ of the equatorial region between latitudes ± 10 degrees. By the end of the simulation $\sim 60\%$ of boulder #22 cases end in orbit, while $\sim 40\%$ are on the surface (again, all cases reached some orbital motion). Other boulders that reach orbit present behaviors between #11 and #22 showing some correlation between the span of orbits reached by a boulder and its initial latitude. Overall, orbiting boulders show low inclination, low altitude, chaotic orbits. Figure 3.41 presents the MC distributions of two orbit outcomes, the maximum distance reached by any orbiting boulder in a specific case (Figure 3.41a), and the percentage of crashed boulders by the end of each simulation run (Figure 3.41b). Figure 3.41a shows an average maximum distance reached of 1.1 km and an extreme case of maximum distance at 2.76 km, which represents 10% of the Hill Sphere radius of an asteroid at the asteroid model mass and semi major axis [128]. As seen in Figure 3.41b, an average of 40% of orbiting boulders return to the surface by the end of the simulation run time, with several cases showing as much as 80% returned boulders, or as little as 0%. These close maximum distances and high return rates are evidence of the low orbital energies orbiting boulders reach.

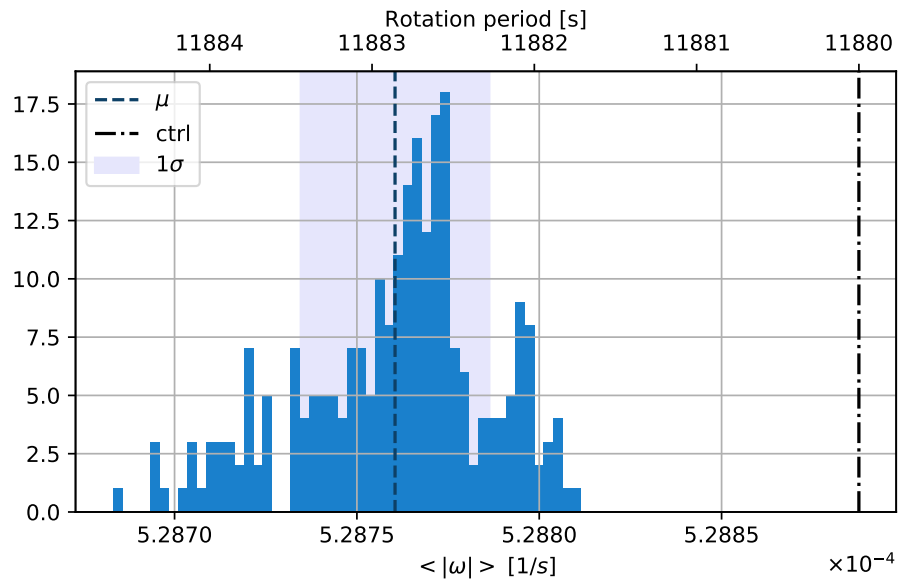


Figure 3.37: Modeled asteroid angular velocity final magnitude in Benu multiple boulder Monte Carlo simulation. Histogram includes distribution mean and 1σ bounds as well as control value.

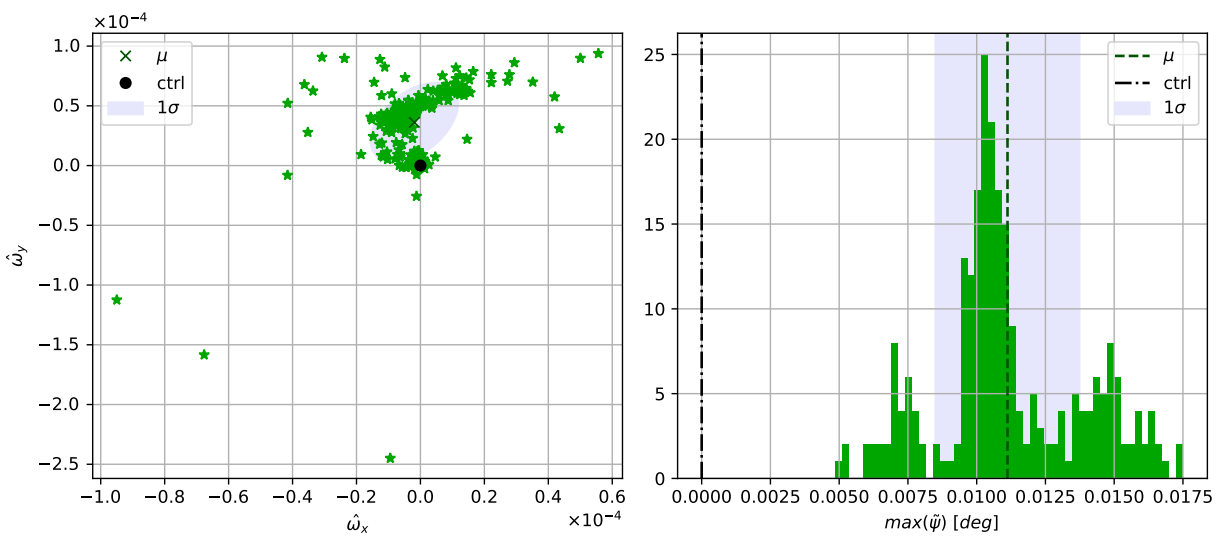
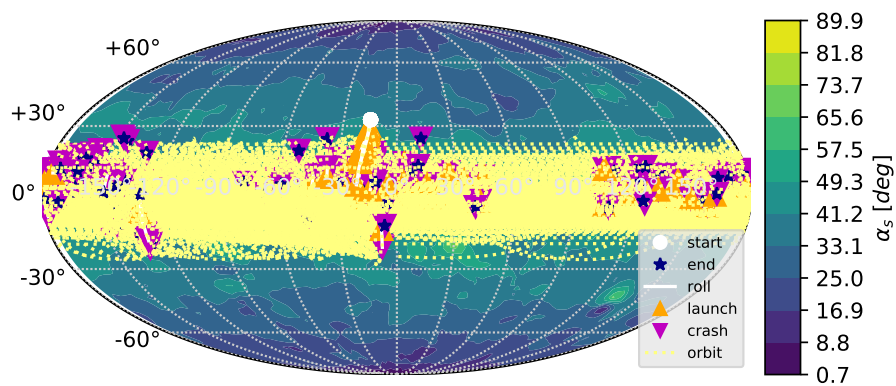
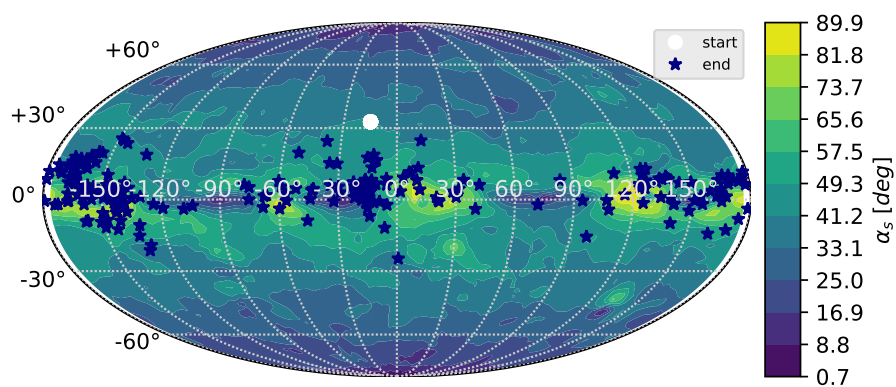


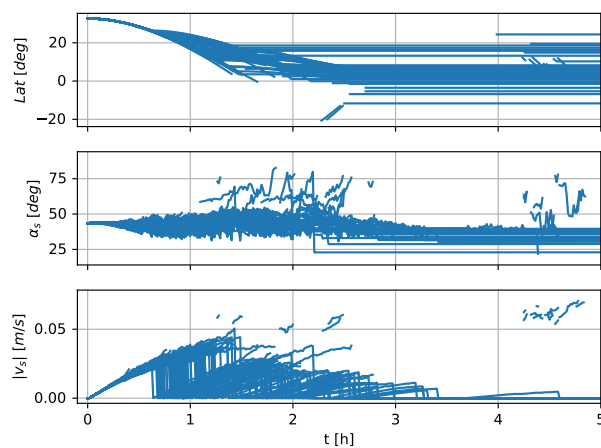
Figure 3.38: Modeled asteroid angular velocity projection of final precession center on the on inertial x-y plane and maximum angle between angular velocity vector and initial axis of maximum inertia in Benu multiple boulder simulation (inertial frame). Histograms include distribution means and 1σ bounds as well as control values.



(a) Surface and orbital motion

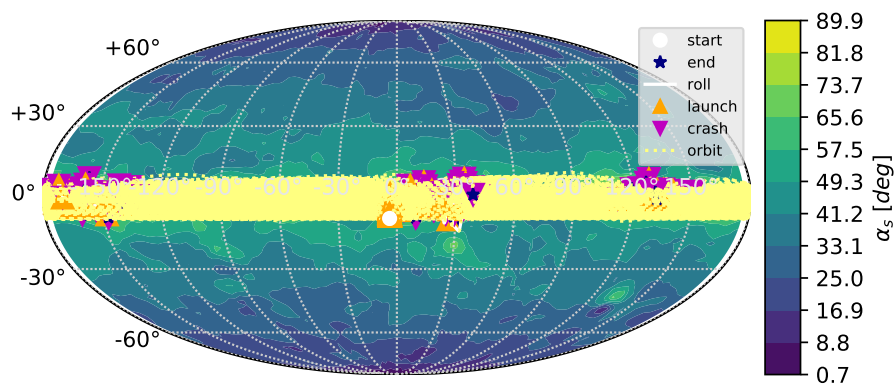


(b) Initial and final surface locations

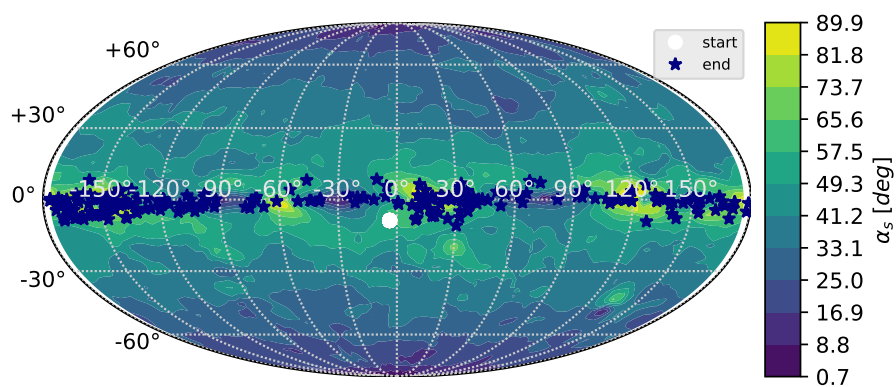


(c) Initial surface motion characteristics (latitude, surface slope, surface velocity)

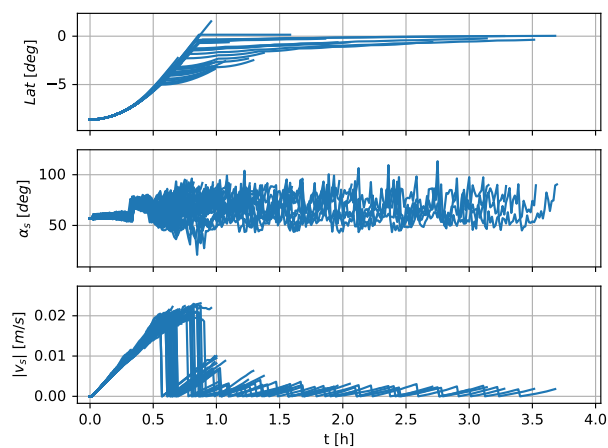
Figure 3.39: Boulders #11 motion characteristics and trajectories in Bennu multiple boulder Monte Carlo simulation



(a) Surface and orbital motion

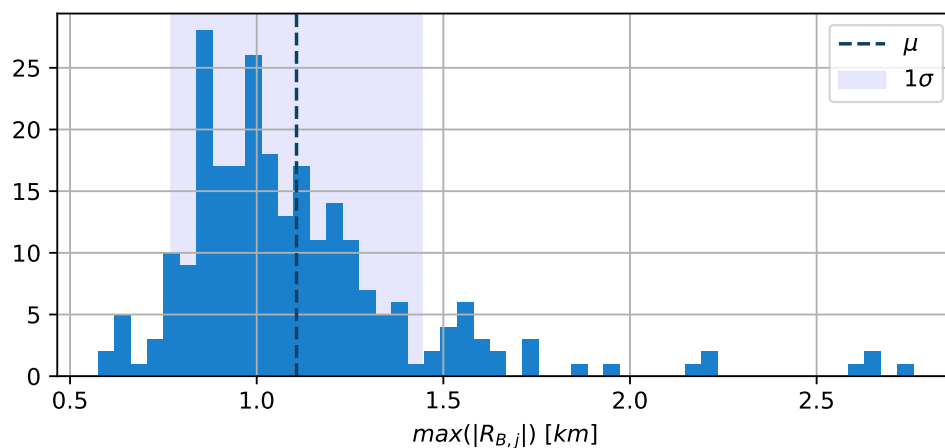


(b) Initial and final surface locations

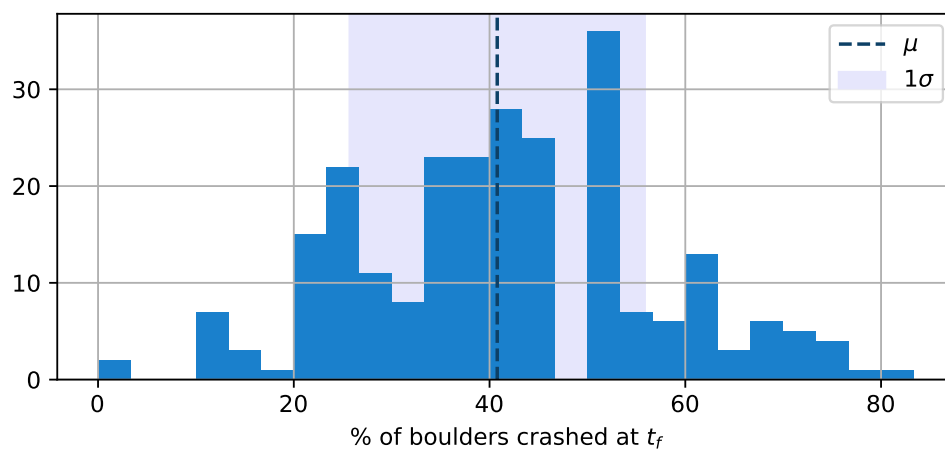


(c) Initial surface motion characteristics (latitude, surface slope, surface velocity)

Figure 3.40: Boulders #22 motion characteristics and trajectories in Bennu multiple boulder Monte Carlo simulation



(a) Maximum distance reached



(b) % of crashed boulders at end of simulation

Figure 3.41: Modeled asteroid distribution of orbit outcomes in Bennu multiple boulder Monte Carlo simulation. Histograms include distribution means and 1σ bounds.

3.1.2.4 Results for a tumbling body

A fast rotation accelerating event such as an impact or flyby will probably torque the angular velocity direction of an asteroid in addition to its magnitude. This section presents results for an accelerated and directionally perturbed Bennu asteroid model in order of examining the motion of boulders on its surface and the motion's effects on asteroid rotation.

Figure 3.42 presents the model asteroid slope angles at four snapshots throughout a precession cycle, beginning at the simulation initiation. In addition to the slope angle heatmaps each plot indicates the projection of the angular velocity vector on the modeled asteroid surface as well as a dashed line indicating areas with slopes higher than the motion inducing 40 degrees. Throughout the precession cycle about 89% of the modeled asteroid surface reaches this slope magnitude leading a volatile surface as seen in the following results.

The simulated boulders' surface and orbit trajectory projection on the surface are presented in Figure 3.43 and their surface motion characteristics are presented in Figure 3.44. Additionally, Figure 3.44 specifically presents the surface motion characteristics prior to first launch of boulders #11 and #22. Both boulders show a trend towards the equator with some period of time where the slopes do not reach motion thresholds. For boulder #22 this period is between hour 0 and 0.75 of the simulation and then again a quick stop near hour 2. Boulder #11 stops and starts moving five times prior to launching to orbit, with an extended stationary period between hour 2.5 and 11. When comparing this motion behavior to the PAR cases the "temporariness" of a boulder's resting place in a tumbling system is seen. All boulders in the tumbling case experience some motion with five boulders only moving on the surface during the simulation and the remaining twenty reaching orbit. A motion rate of 100%, which when compared with the 56% seen in the PAR case demonstrates the volatility of material placement in a fast tumbling system. By the simulation's end (24 hours) thirteen boulders remain orbiting the modeled asteroid. Figures 3.43 and 3.44 show that all boulders' motion trend toward the equator where they either launch to orbit or rest for the remainder of the simulation.

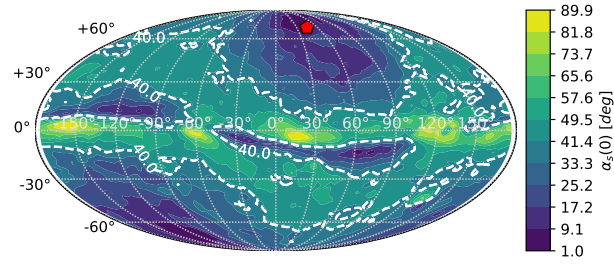
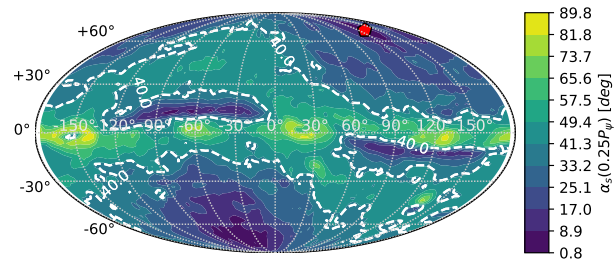
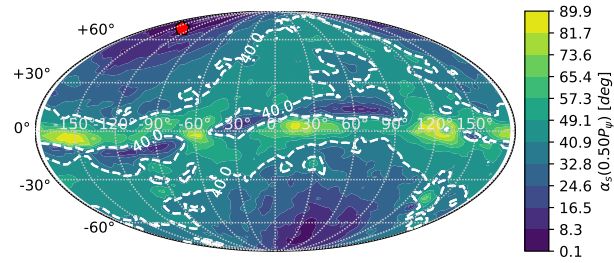
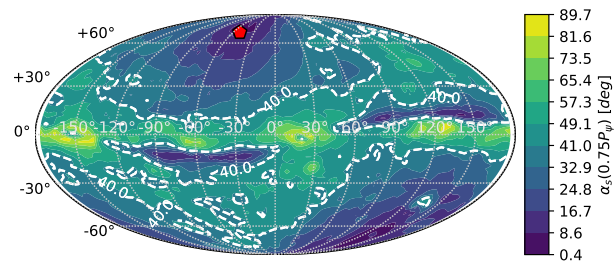
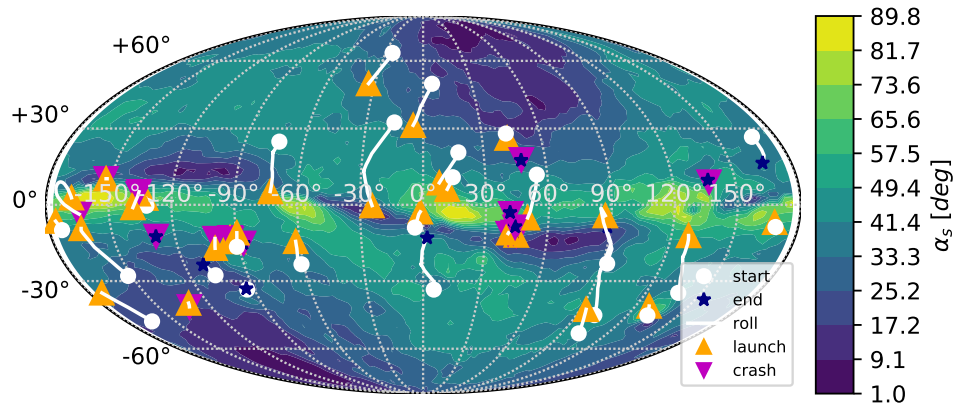
(a) Slope angles at t_0 (b) Slope angles at $t_0 + \frac{1}{4}P_{rotation}$ (c) Slope angles at $t_0 + \frac{1}{2}P_{rotation}$ (d) Slope angles at $t_0 + \frac{3}{4}P_{rotation}$

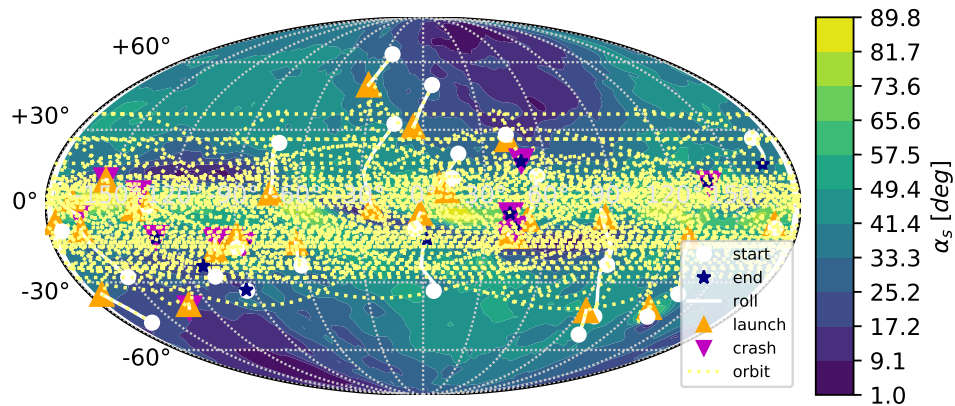
Figure 3.42: Bennu-shaped accelerated tumbling asteroid surface slope evolution. The heatmaps indicate surface slopes, the red pentagon represents body frame projection of angular velocity vector, the dashed white line represents bounds for slopes over 40 degrees.

The modeled asteroid mass distribution characteristics are presented in Figures 3.45-3.47 which show the higher percentage (2.5 times more) of mass lost in the tumbling case compared to the PAR. The material trend towards the equator is seen in Figure 3.47 whenever material is moving on the surface and not abruptly launching to orbit.

The modeled angular velocity evolution is seen in Figure 3.48, here the control case is seen tumbling as well as the simulated case for comparison purposes. Figure 3.48a presents the absolute angular velocity vector and Figure 3.48b presents the difference vector between the simulation and control case. A divergence trend can be seen in all three tumbling elements, a result that is different from the PAR case where the x and y elements only appear to be oscillating around the 0 values. Additionally, the tumbling case shows a larger change in angular velocity magnitude, probably due to the higher mass loss in the tumbling case. This result can also be seen in Figure 3.49 which presents the growing angle between the simulation and control tumbling angular velocity vectors.

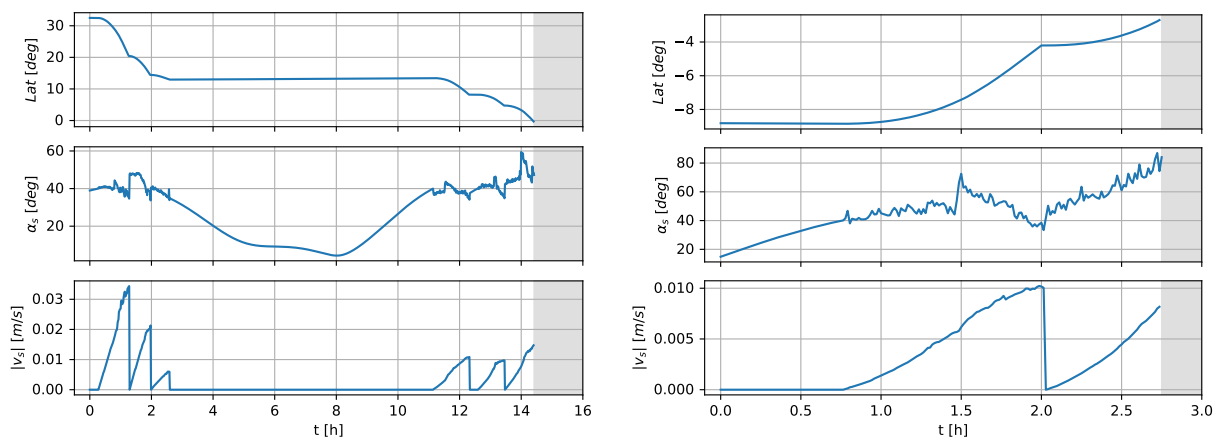


(a) Surface motion



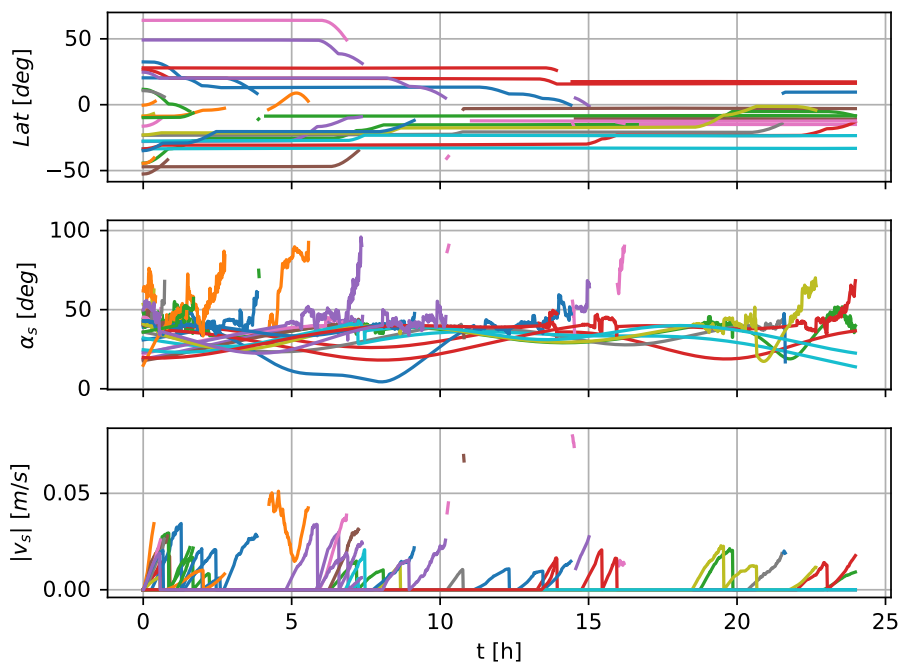
(b) Surface and orbital motion

Figure 3.43: Boulder motion surface projection in tumbling Bennu multiple boulder simulation. The heatmaps indicate surface slopes at simulation start, boulder initial position indicated by white dot, surface motion indicated by white line, boulder launch and crash events indicated by triangles, orbit projection on surface indicated by dashed yellow line, and boulder final position indicated by blue star.



(a) Boulder #11

(b) Boulder #22



(c) All boulders

Figure 3.44: Boulder surface motion characteristics (latitude, surface slope, surface velocity) tumbling Bennu multiple boulder simulation

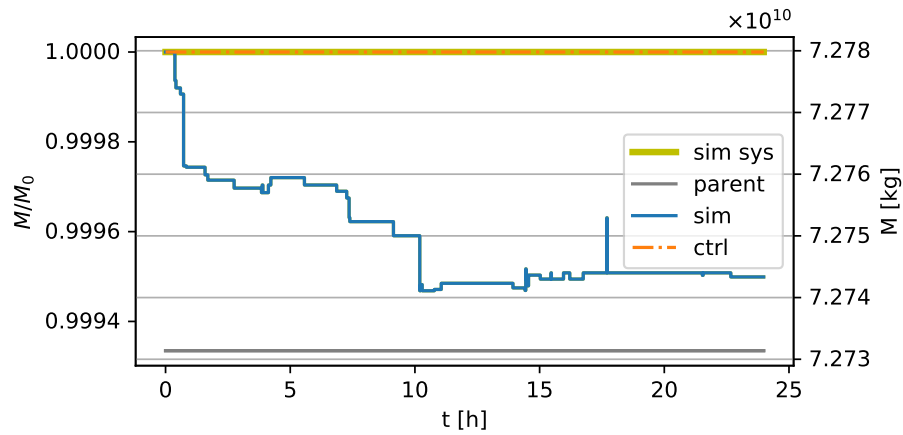


Figure 3.45: Modeled asteroid mass in tumbling Bennu multiple boulder simulation. The parameters presented include system mass, parent body mass, asteroid mass, and control case mass.

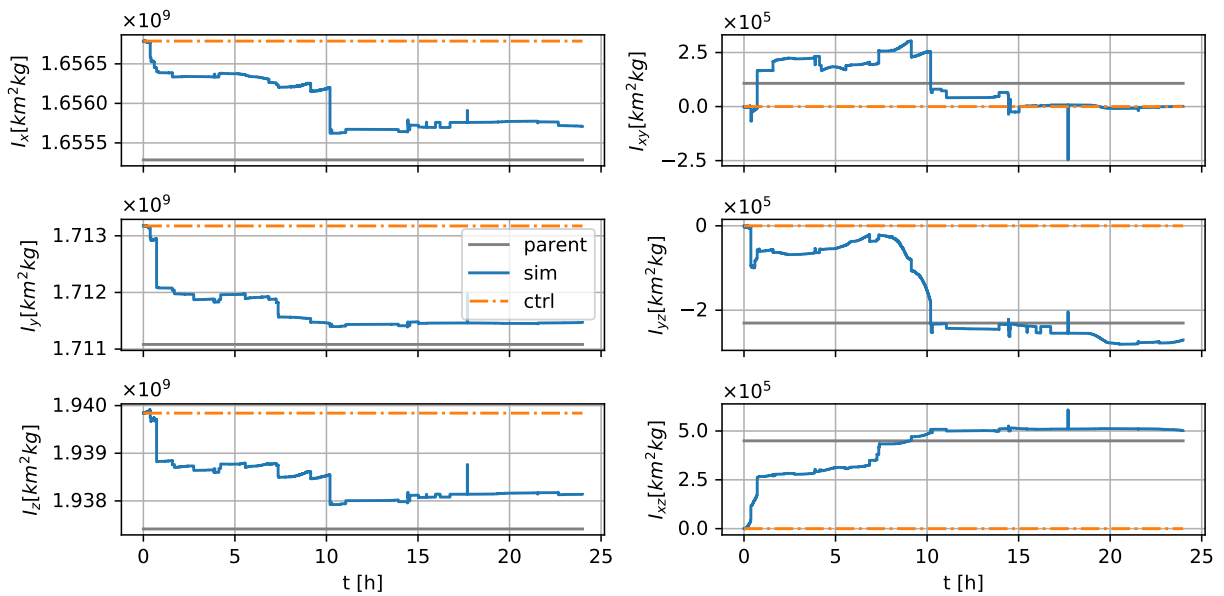


Figure 3.46: Modeled asteroid inertia tensor elements in tumbling Bennu multiple boulder simulation. The parameters presented include parent body inertia tensor, asteroid inertia tensor, and control case inertia tensor.

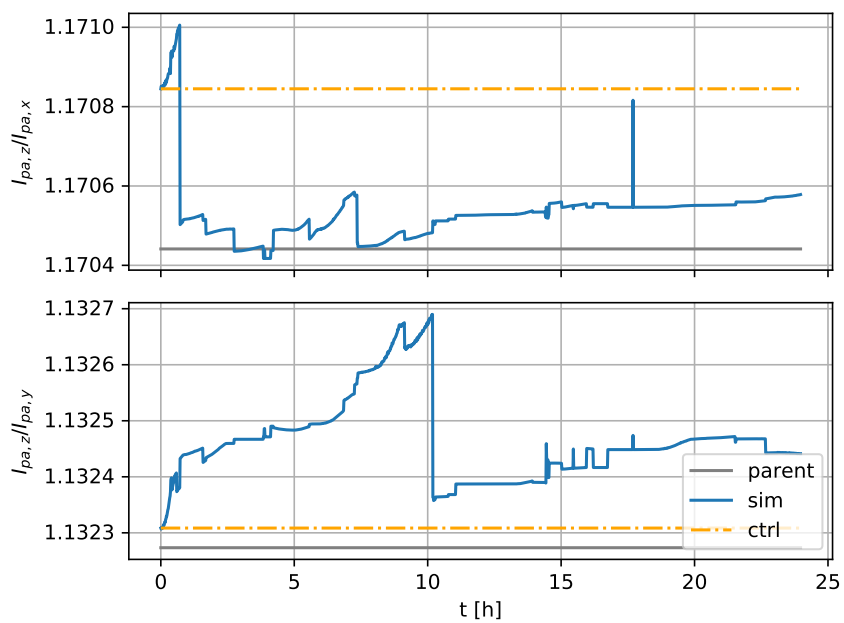
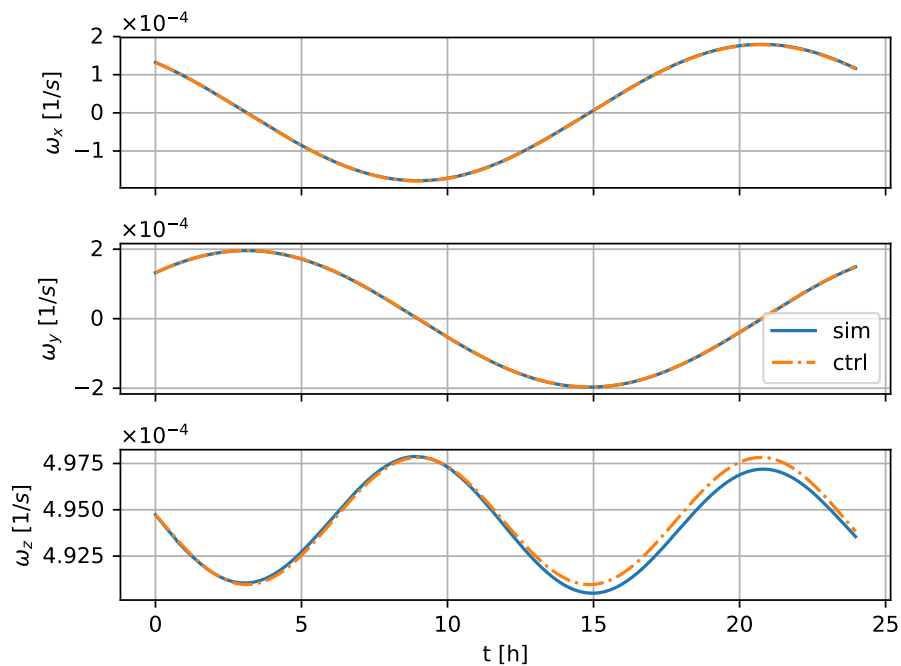
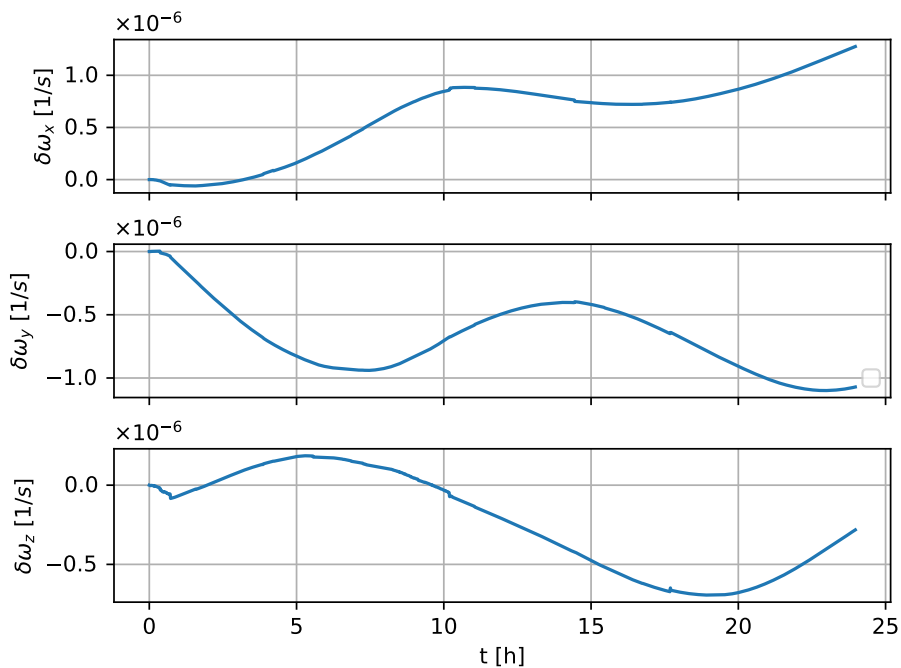


Figure 3.47: Modeled asteroid principal maximum moment of inertia ratio with median and minimum principal moments of inertia in tumbling Bennu multiple boulder simulation. The parameters presented include parent body inertia ratio, asteroid inertia ratio, and control case inertia ratio.



(a) Absolute values



(b) Difference between simulation and control cases

Figure 3.48: Modeled asteroid and control case angular velocity evolution in tumbling Benu multiple boulder simulation (asteroid body frame)

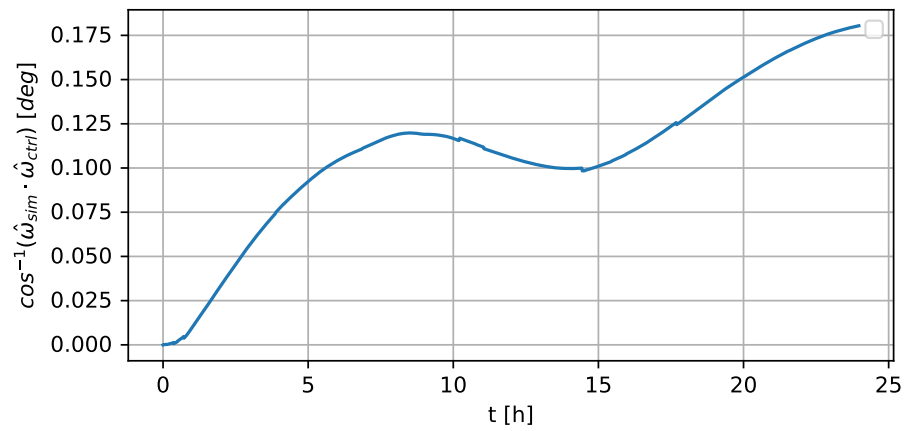


Figure 3.49: Modeled asteroid angle between simulation and control cases angular velocity vectors in tumbling Bennu multiple boulder simulation

3.1.3 Multiple boulder motion on an Itokawa-shaped asteroid model

The following section presents simulation results for an Itokawa-shaped asteroid model propagated for a period of 24 hours.

3.1.3.1 Simulation setup

The asteroid model parameters are presented in Table 3.4 and the asteroid shape, together with 50 boulders distributed on its surface is presented in Figure 3.50. The asteroid model is set as a PAR with a rotation period 3.5 times faster than the asteroid Itokawa. This value is selected to induce boulder motion according to the thresholds seen in Figure 3.51. Here the harder core assumption is crucial for the feasibility of an elongated asteroid system reaching high rotation rates. While this assumption is aggressive is it meant to provide an example of an elongated asteroid being disturbed to the extent of structural failure on the surface. The asteroid model and boulder density values are based on [129, 4]. The boulder setup is similar to that presented in Section 3.1.2, with the exception in boulder placement, which for the case presented here was intended to be primarily in the edges of the long axis of the model asteroid. No external perturbations are applied and the simulation is preformed with the randomness capabilities enabled.

Parameter	Values
Rotation period	3.45 [h]
Parent body density	1900 [kg·m ⁻³]
Boulder density	2000 [kg·m ⁻³]
Parent body principal radii	267, 147, and 105 [m]
Launch slope condition	90 [deg]
Static slope condition	40 [deg]
Kinetic slope condition	35 [deg]
Cohesion strength (p_c)	25 [Pa]
Boulder-regolith contact area (S)	30 [% of boulder surface area]
Sliding friction (μ_s)	0.5
Rolling friction (μ_r)	0.75
Friction ratio (κ)	0.5
Total kinetic friction (μ_k)	0.625

Table 3.4: Itokawa-shaped asteroid model parameters

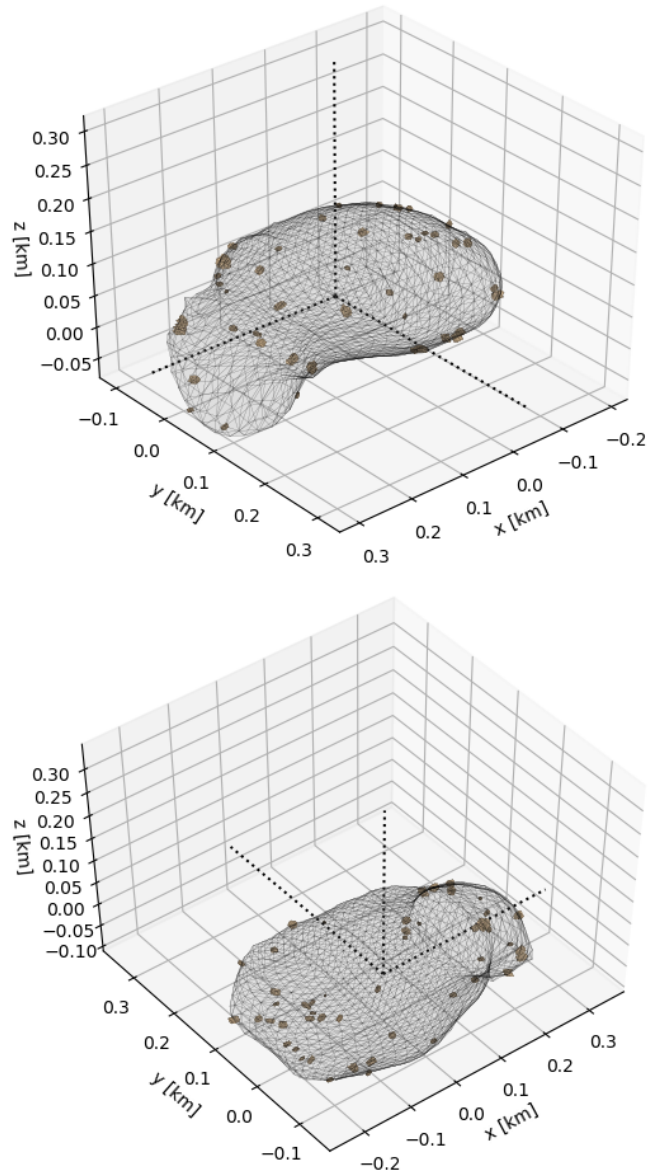
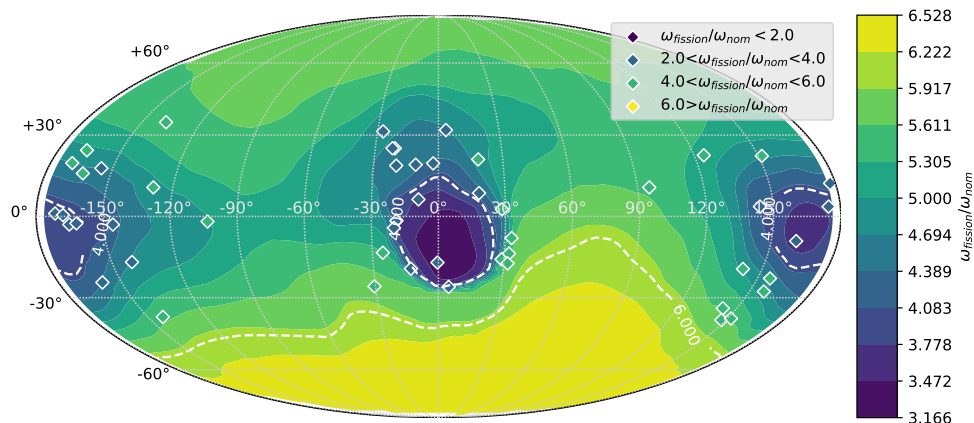
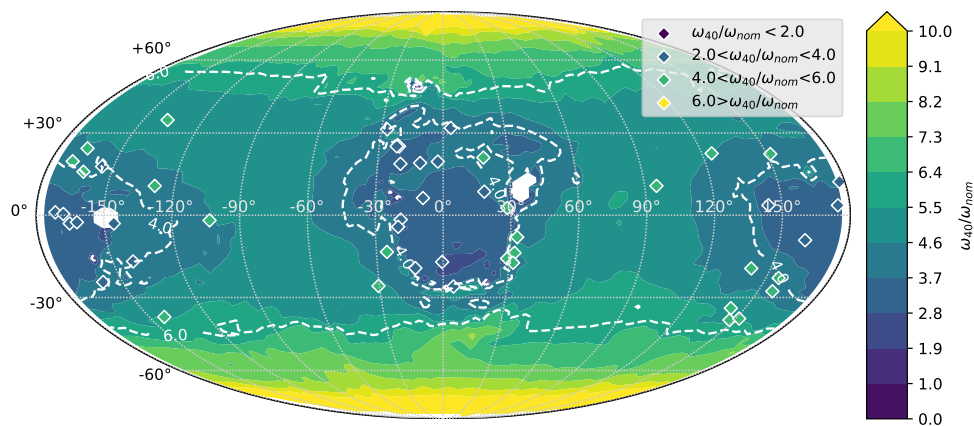


Figure 3.50: Itokawa ~ 3000 facet polyhedron with 50 boulders distributed on its surface



(a) Fission (cohesionless)



(b) Slopes at 40 [deg]

Figure 3.51: Threshold angular velocity compared to Itokawa nominal for boulder motion. The heatmaps indicate surface (facet) properties, and the diamonds indicate boulders placed on the surface.

3.1.3.2 Results

An overview of the boulder motion in the simulation can be seen in Figures 3.52 and 3.53. These figures show very little boulder surface motion which result in five boulders launching to a hyperbolic escape from the modeled asteroid system. An additional four boulders move short distances on the surface before stopping. All boulders that move are situated at the long axis edges, with more motion observed on the edge of the smaller shape node.

The boulder escapes result in an orbital ΔV applied to the modeled asteroid according to Eq. 2.34. Each escaped boulder contribution is presented in Table 3.5. These ΔV magnitudes sum is $0.0133 \text{ mm}\cdot\text{s}^{-1}$, however, once their directions are accounted for the overall ΔV experienced by the model asteroid is only 64% of sum value at $0.00849 \text{ mm}\cdot\text{s}^{-1}$ at the inertial direction of $[0.945 -0.006 -0.325]$. Despite the boulder launch direction varying in the inertial x-y plane, their z-axis distribution is close to the 0 value, keeping the ΔV contribution perpendicular to the angular velocity.

Boulder	ΔV magnitude [$\text{mm}\cdot\text{s}^{-1}$]	ΔV direction (inertial)
19	0.00398	[0.783, -0.618, 0.059]
21	0.00320	[0.855, -0.491, -0.162]
23	0.00109	[0.958, -0.125, -0.255]
47	0.00057	[0.908, 0.416, -0.020]
48	0.0049	[0.133, 0.863, -0.486]

Table 3.5: Itokawa-shaped asteroid model boulder escape ΔV s

Figures 3.54 and 3.55 present inertia tensor element and principal axis element ratio evolution. Figure 3.54 shows the system mass loss in the decrease of the primary inertia tensor elements. The principal axis inertia element ratio shows a decrease in the z to x ratio, but an increase in the z to y ratio. This result represents the loss of mass mainly from the long x-axis as seen in Figure

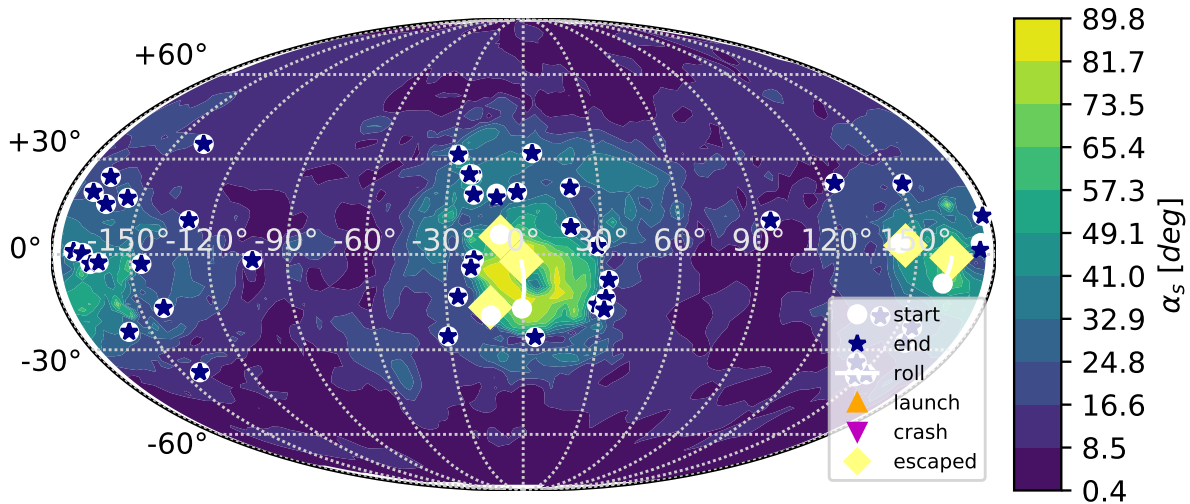


Figure 3.52: Boulder motion surface projection in Itokawa-like multiple boulder simulation. The heatmap indicates surface slopes, boulder initial position indicated by white dot, surface motion indicated by white line, boulder escape indicated by yellow diamonds, and boulder final position indicated by blue star.

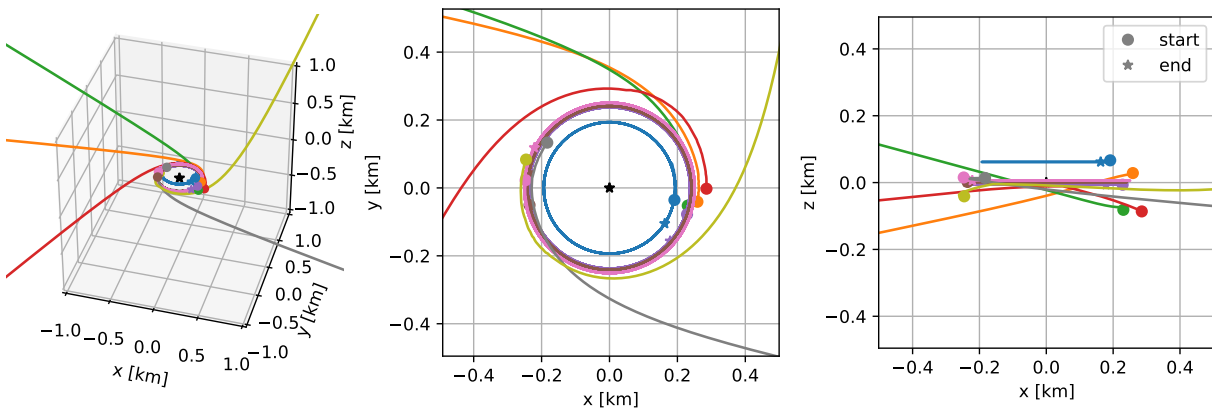


Figure 3.53: Boulder orbit motion in Itokawa-like multiple boulder simulation

3.52.

The evolving angular velocity can be seen in Figures 3.56-3.58. Again, the loss of the PAR characteristic is observed. A decrease in angular velocity magnitude is observed in Figure 3.56, which is equivalent to 0.92 seconds added to the 3.45 hour rotation period. The small magnitude in angular velocity decrease compared to the Bennu shaped asteroid model case can be explained by the limited surface motion that occurs in this simulation, showing again that angular velocity magnitude change is caused by mass redistribution and not by boulder launch (without an external ΔV). The direction of the angular velocity vector with respect to the asteroid body and inertial frames, respectively, in Figures 3.57 and 3.58 shows a complex pattern of motion due to the asymmetries in Itokawa's shape. Both figures also show the center of angular velocity shift due to the boulder launches with no return. Specifically, the body frame angle between original maximum inertia axis and evolving angular velocity shows the superposition of two events: the boulder launches seen by the initial jump in the angle, and the boulder mass loss seen by the precession presented after the first two hours.

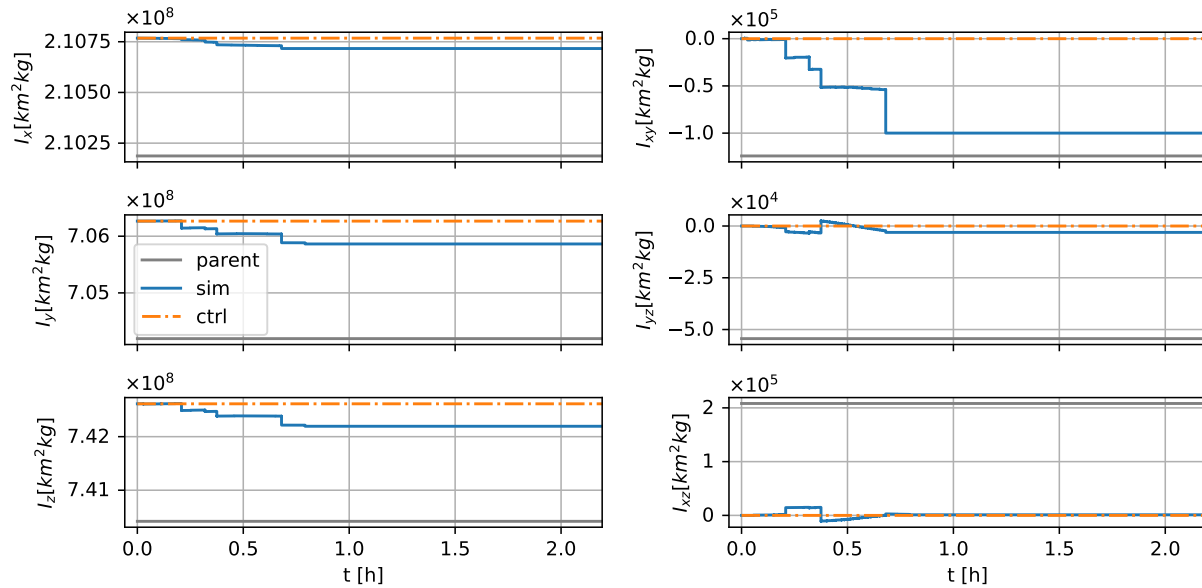


Figure 3.54: Modeled asteroid inertia tensor elements in Itokawa-like multiple boulder simulation. The parameters presented include parent body inertia tensor, asteroid inertia tensor, and control case inertia tensor.

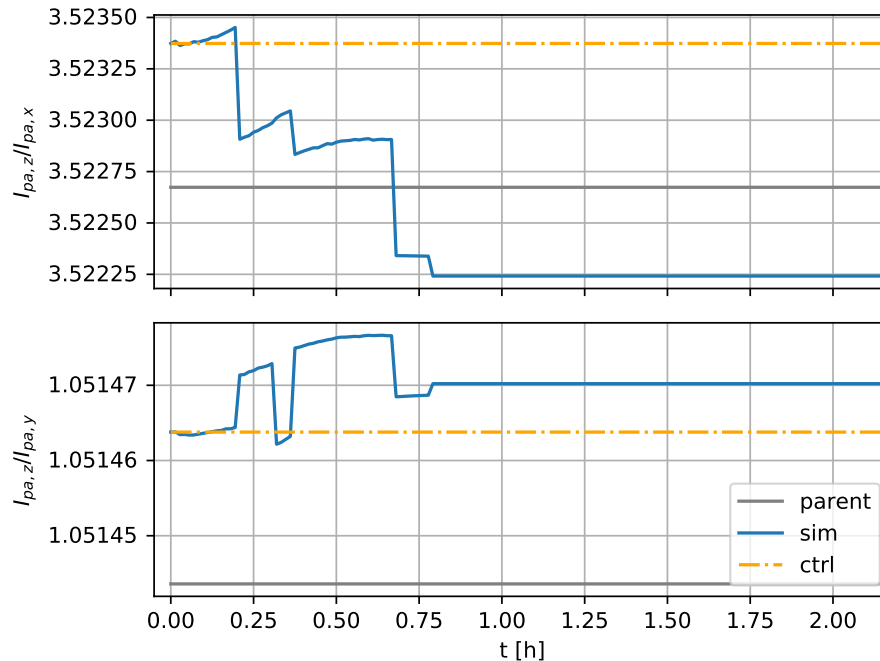


Figure 3.55: Modeled asteroid principal maximum moment of inertia ratio with median and minimum principal moments of inertia in Itokawa-like multiple boulder simulation. The parameters presented include parent body inertia ratio, asteroid inertia ratio, and control case inertia ratio.

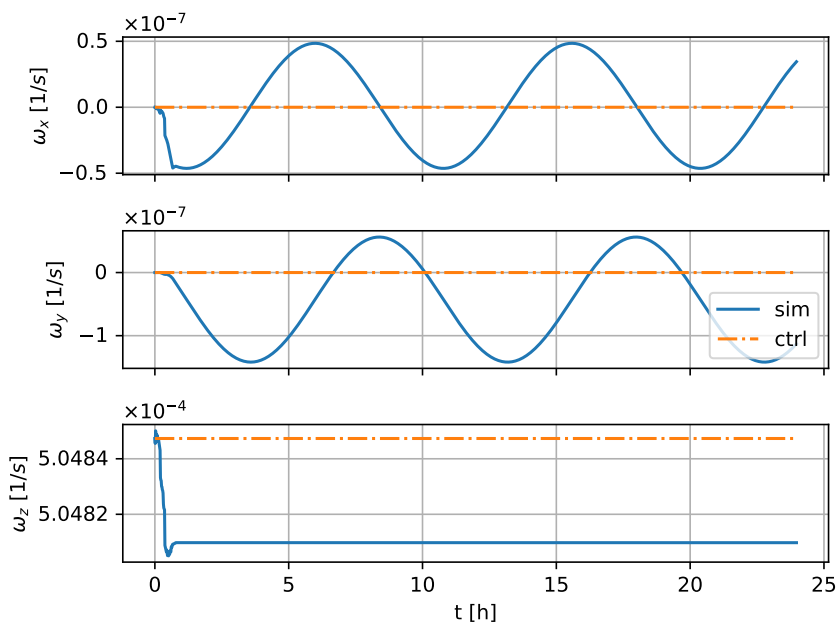


Figure 3.56: Modeled asteroid and control case angular velocity evolution in Itokawa-like multiple boulder simulation (asteroid body frame)

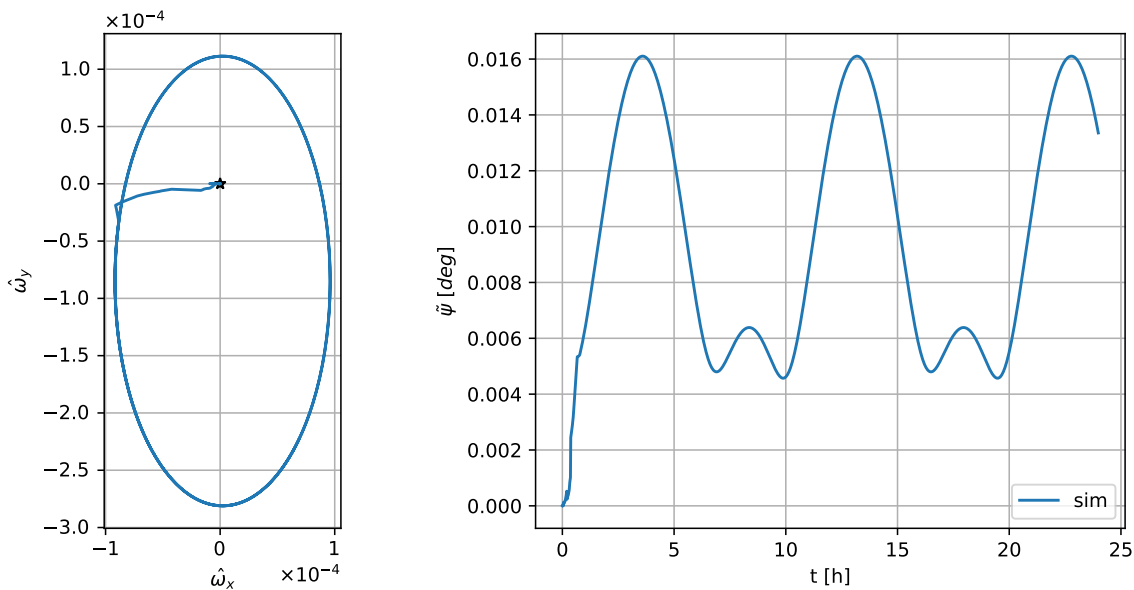


Figure 3.57: Modeled asteroid angular velocity vector projection on the equatorial plane and angle between angular velocity vector and initial axis of maximum inertia in Itokawa-like multiple boulder simulation (asteroid body frame)

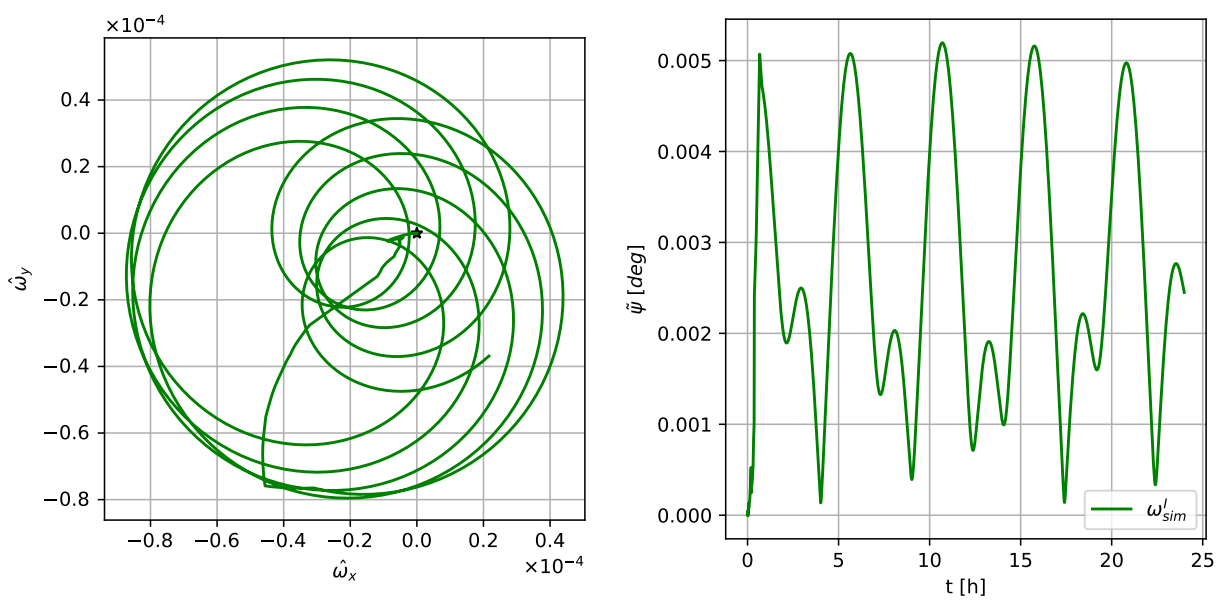


Figure 3.58: Modeled asteroid angular velocity vector projection on inertial x-y plane and angle between angular velocity vector and initial axis of maximum inertia in Itokawa-like multiple boulder simulation (inertial frame)

3.1.4 Trends in fast rotating small bodies

The simulation results presented in this section show several trends that appear to be consistent through all the cases. First, boulder motion always leads to loss of the PAR characteristic and introduction of precession. This precession can center around the original angular velocity direction if material is returned to the surface, or around some other direction when the material is lost to the asteroid or system. Behavior that is seen to exist both in the asteroid body frame as well as in the inertial frame, while their magnitudes and frequencies differ. Dissipation is expected to damp the precession [38] and converge the angular velocity vector around these centers. Which in the cases of a removed center means new, slightly reoriented, inertial frame angular velocity. A mechanism that should be accounted for when discussing angular velocity and momentum direction evolution.

Boulder mass redistribution always leads to a reduction of the angular velocity magnitude, an expected result due to its lower energy state. This redistribution trends consistently towards the modeled asteroid equator, even in complex tumbling motion. When comparing mass loss due to launch and mass migration on the surface it appears that mass loss results in introduction of a higher degree of precession and lower change in angular velocity magnitude, while mass surface migration results a higher in a higher change to angular velocity magnitude and lower degree of precession.

3.2 Particle events and the YORP effect

Since its arrival at the asteroid Bennu in late 2018 NASA’s OSIRIS-REx mission has observed several particle ejection events [130]. The evidence for these events is seen after-the-fact in optical imagery of the near surface environment which show illuminated pixels that are not stars and appear to have trajectories around the asteroid. Trajectories that vary from sub-orbital to orbital to hyperbolic escapes [131]. The dynamic paths of the particles observed originate from several events that occurred on the asteroid surface. Events that seem to lack any preference to location on the surface or geometry with respect to the asteroid orbit or Sun relative position. Currently, two hypotheses have been suggested: thermal fracturing and meteoroid impacts. Both events that introduce energy and angular momentum into the asteroid system, either from “storage” in the surface material, or from external bodies impacting at high velocities. The particle observations are prone to be biased towards slow moving particles due to the imagery cadence of the mission. These particles move at sub $\text{m}\cdot\text{s}^{-1}$ velocities and most remain in the asteroid system. However, if the meteoroid impact theory is correct, and these events are the main cause of the observed particles, a 7000 J event should be expected on average every two weeks when Bennu is near its periapsis.

The following sections present an analysis of three magnitudes of particle events occurring on Bennu’s surface. The particle events are modeled as a single small boulder launching in defined directions with a ΔV added to its orbital velocity at the moment of launch (the $\dot{\mathbf{r}}_{B,j}^{\mathcal{B}A}$ element in Eq. 2.20). The events modeled are: a 7000 J event demonstrating a high energy collision, a 0.5 J event as an example of a low energy event that results in particle ejection from the asteroid system, and a 0.0115 J event showing results for mass redistribution due to a slow particle ejection. Table 3.6 presents Bennu’s and the particles’ physical parameters used for the simulations in the following sections.

The results show that the extent of change in asteroid rotation, both in magnitude and degree of precession, is smaller than the uncertainty bounds of the estimated rotation state of Bennu [132],

Parameter	Values
Rotation period	4.29 [h]
Rotation period uncertainty	0.0072 [s]
Pole direction uncertainty [right ascension, declination]	0.12, 0.09 [deg]
Parent body density	1190 [kg·m ⁻³]
YORP rotational acceleration rate	3.63×10^{-6} [deg·day ⁻²]
Boulder density	2000 [kg·m ⁻³]
7000 J event boulder launch velocity	37.4 [m·s ⁻¹]
7000 J event boulder mass	10 [kg]
0.5 J event boulder launch velocity	1 [m·s ⁻¹]
0.5 J event boulder mass	1 [kg]
0.0115 J event boulder launch velocity	0.1 [m·s ⁻¹]
0.0115 J event boulder mass	2.3 [kg]
Boulder location [lon,lat]	4.3, 24.3 [deg]

Table 3.6: Bennu asteroid model parameters

these values are also presented in Table 3.6. Despite the unobservability of a single event and apparent stochastic distribution with respect to the asteroid structure and angular velocity these events can have a non-zero contribution that should be taken in to account when discussing asteroid shape and, more importantly, rotation evolution.

3.2.1 The effects of a fast particle events

The angular velocity change due to a high energy particle event is presented in Figures 3.59 and 3.60. In this event a 10 kg particle is launched at $37.4 \text{ m}\cdot\text{s}^{-1}$ (7000 J) in a direction normal to the launch surface location in a lower-mid latitude. At this point the discrepancy between surface normal and surface position direction is 23.4 degrees which means a lever arm of ~ 100 meters is applied with respect to the asteroid center of mass. This lever arm is the main cause of the shift in angular velocity direction observed in Figure 3.60. The extent of change in angular velocity magnitude is equivalent to 2.8×10^{-5} seconds added to the instantaneous rotation period at the end of the simulation (two orders of magnitude smaller than the rotation period uncertainty bounds). This change in angular velocity is equivalent to ~ 1 day of the YORP rotational acceleration magnitude. However, the current YORP effect appears to accelerate Bennu, thus, the particle event deceleration of the asteroid's rotation presents a complex trend in the rotation evolution. The maximum angle reached between the angular velocity vector and maximum inertia axis is $\sim 3 \times 10^{-6}$ degrees (four orders of magnitude smaller than the estimation uncertainty). The magnitude of this angle is similar in both the asteroid body and inertial frames (unlike in the previous section) because the source of angular velocity shift is related to the external energy launching the particle and not mass redistribution. The precession in the asteroid body frame remains centered near the original angular velocity direction and will likely dissipate back to the original body frame angular velocity direction. In the inertial frame, however, the center of precession is removed from the original direction of rotation, demonstrating how particle events can cause a small scale random walk migration of an asteroid's angular momentum direction.

Figures 3.61 and 3.62 present the angular velocity evolution due to low energy 1 kg particle at a $1 \text{ m}\cdot\text{s}^{-1}$ launch normal to surface, this ejection constitutes a 0.5 J event. Overall the nature of the event is similar to that of the 7000 J event with change magnitudes substantially lower due to the lower energy. The ejection event leads to 7.3×10^{-8} seconds added to the instantaneous rotation period at the end of the simulation, equivalent to ~ 0.0026 days of the current YORP acceleration rate, and a maximum $\tilde{\psi}$ angle of $\sim 9 \times 10^{-9}$ degrees. Both parameters are, again, well within the estimation uncertainty bounds.

The directionality of a particle event with respect to the asteroid surface cannot be predicted or explained until the cause of such events is found. Using the surface normal direction basically provides a mean value of all possible launches in the hemisphere above a certain surface location. In case the source of the events is external impactors the surface normal direction is a good approximate of the averaged contribution of all ejecta leaving the surface [133]¹. However, if the source of the particles is different, or even in the event an impactor approaches the asteroid surface tangentially some off-normal direction should be expected. Figures 3.63 and 3.64 present the change in angular velocity for both particle event magnitudes if various directions from the lower-mid latitude location presented in Table 3.6. The figures show heatmaps of the resulting changes in a local azimuth local zenith coordinate system. Here the zero zenith angle degrees points at the local normal indicating a particle launch normal to the surface, azimuth and zenith $[0,90]$ degrees point north tangentially to the surface, and azimuth and zenith $[90,270]$ degrees point tangentially east.

Figure 3.63 presents the changes to angular velocity due to a possible high energy 7000 J event. Figure 3.63a presents the change in angular velocity magnitude compared to a nominal day of YORP. Changes in magnitude that can reach over 60 days of the YORP rate when aligned perpendicular to the asteroid's angular velocity vector. This magnitude of change is equivalent to ~ 0.0017 seconds reduced or added to the asteroid's rotation period, still under the estimation uncertainty,

¹ A discussion on surface ejecta due to external impacts is presented in further detail in Chapter 4.

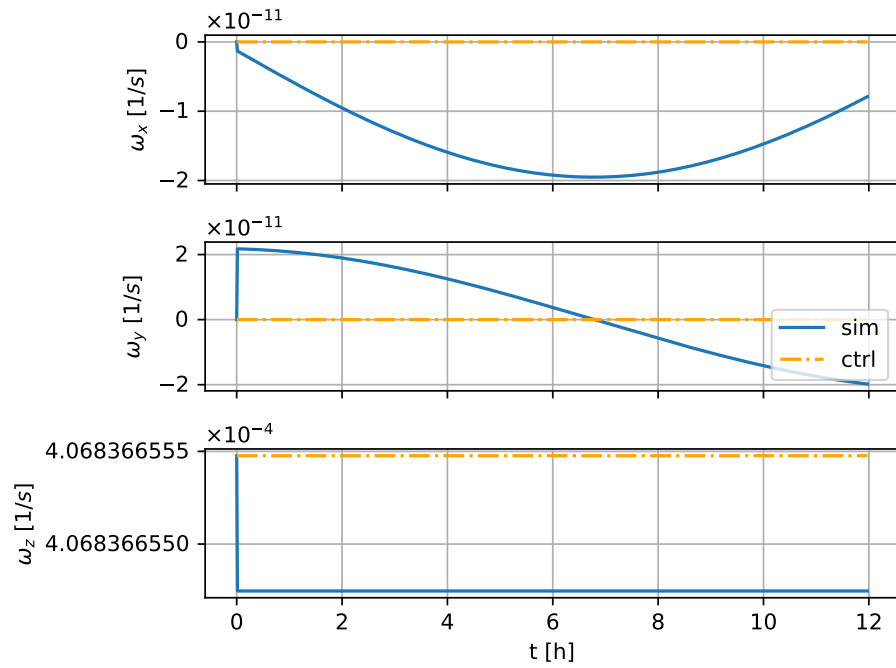
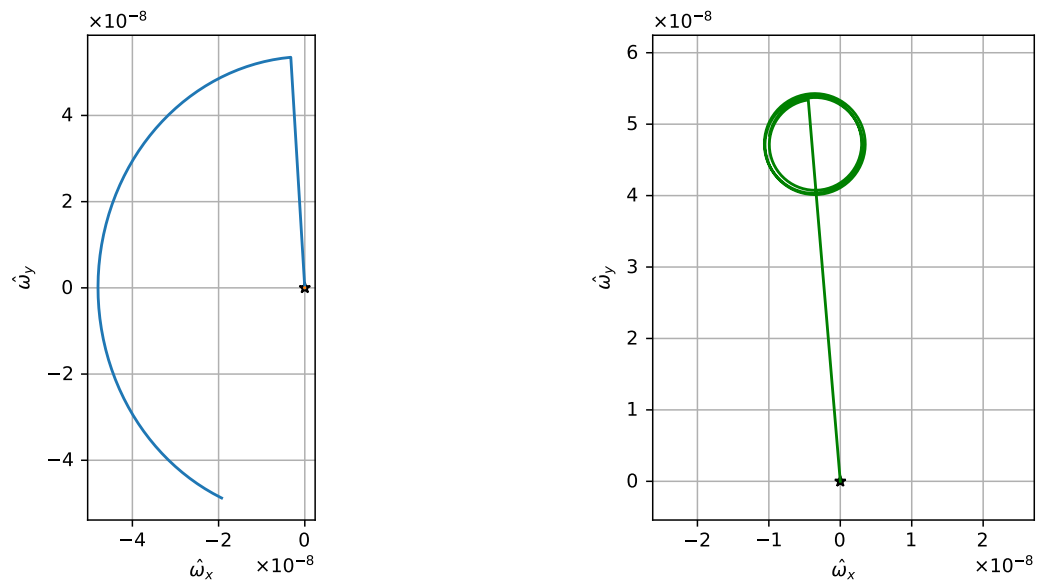


Figure 3.59: Modeled asteroid and control case angular velocity evolution due to 10 kg particle launched at $37.4 \text{ m}\cdot\text{s}^{-1}$ from longitude and latitude $[4.3 \ 24.3]$ degrees (asteroid body frame)



(a) Angular velocity vector projection on the equatorial plane (asteroid body frame) (b) Angular velocity vector projection on the inertial x-y plane (inertial frame)

Figure 3.60: Modeled asteroid angular velocity vector direction change due to 10 kg particle launched at $37.4 \text{ m}\cdot\text{s}^{-1}$ from longitude and latitude $[4.3 \ 24.3]$ degrees

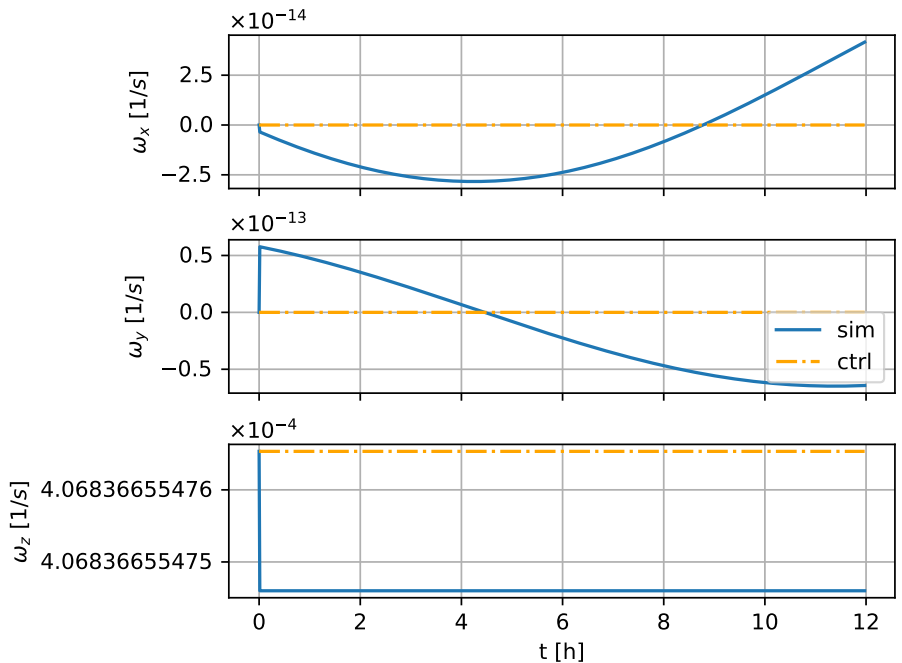
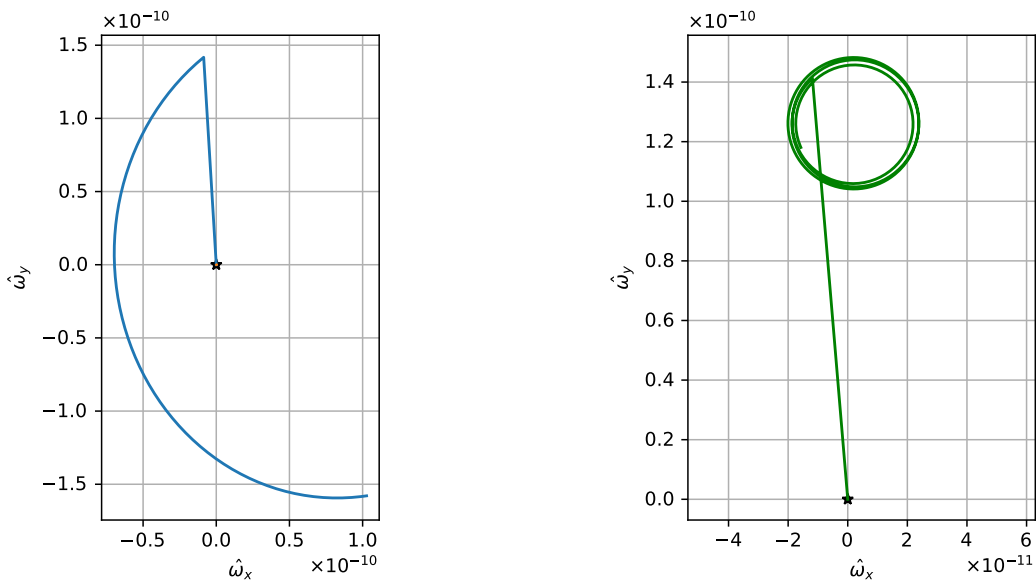
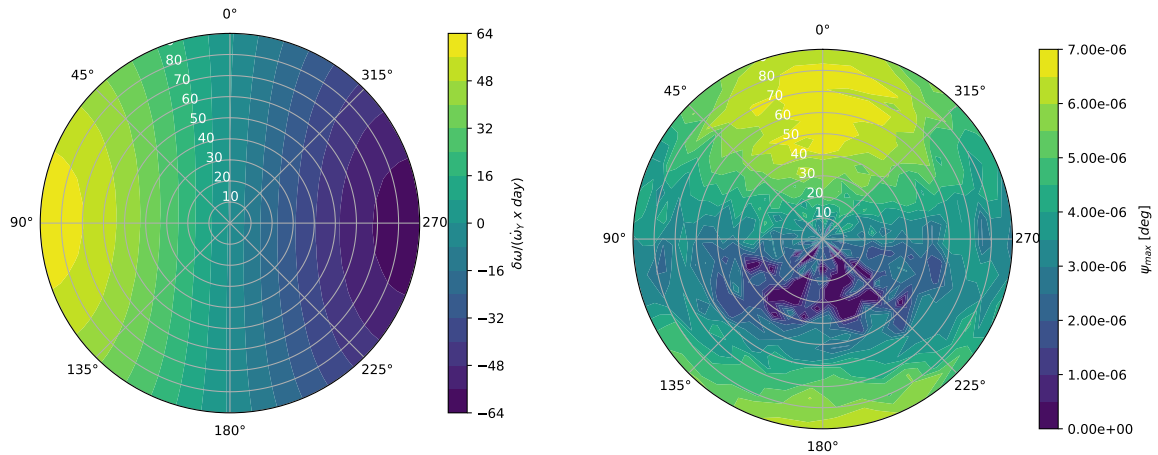


Figure 3.61: Modeled asteroid and control case angular velocity evolution due to 1 kg particle launched at $1 \text{ m}\cdot\text{s}^{-1}$ from longitude and latitude [4.3 24.3] degrees (asteroid body frame)



(a) Angular velocity vector projection on the equatorial plane (asteroid body frame) (b) Angular velocity vector projection on the inertial x-y plane (inertial frame)

Figure 3.62: Modeled asteroid angular velocity vector direction change due to 1 kg particle launched at $1 \text{ m}\cdot\text{s}^{-1}$ from longitude and latitude [4.3 24.3] degrees



(a) Change to angular velocity magnitude compared to nominal YORP acceleration

(b) Maximum precession reached

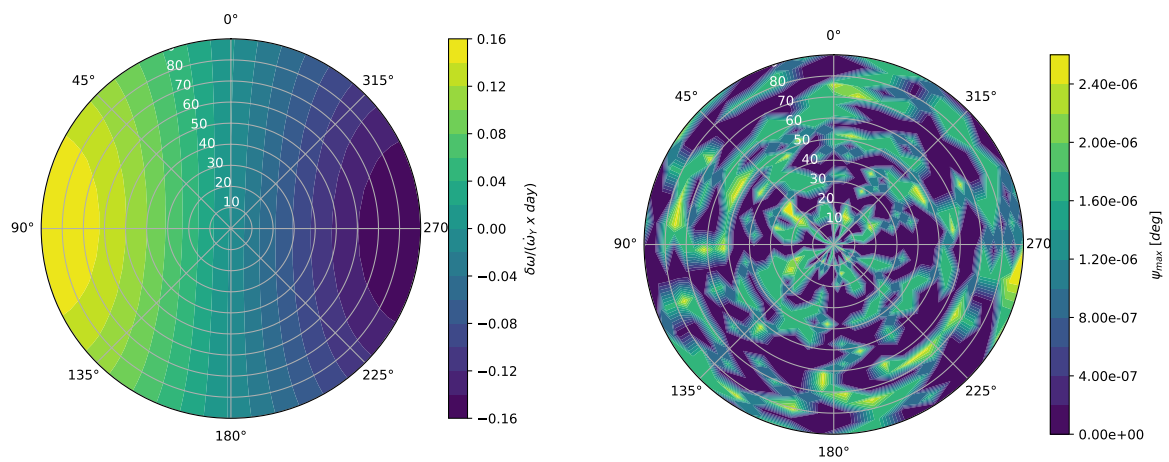
Figure 3.63: Change to angular velocity due to 10 kg particle launched at $37.4 \text{ m}\cdot\text{s}^{-1}$ from longitude and latitude $[4.3 \ 24.3]$ degrees in various directions with respect to surface normal

but comparable in magnitude. Figure 3.63b presents the maximum precession angle that is reached for the different particle event directions². Here the normal direction shows the same result as presented before, some precession, but not a possible maximum. The maximum values appear to result from a northern close to tangential event which maximizes the lever arm with respect to the asteroid CM. The minimal, near-zero, values or precession angle appear in a direction opposite to the launch location latitude, a direction that correlates with the launch location position vector direction, minimizing the lever arm with respect to the CM. The results for different launch directions in the 0.5 J case are presented in Figure 3.64 which show a similar trend for the angular velocity magnitude change as the high energy case with a maximum change equivalent to $\sim 4.4 \times 10^{-06}$ seconds reduced or added to the rotation period. The precession results appear to be inconsistent due to their small numerical values with respect to the asteroid system calculations³.

The results presented above span the possible outcomes for a possible particle event from a single point on Bennu's surface. These results are affected by that point's latitude and angle

² Here the precession angle is computed analytically according to Eq. 2.9.

³ The change to maximum moment of inertia is of magnitude 10^{-16} .

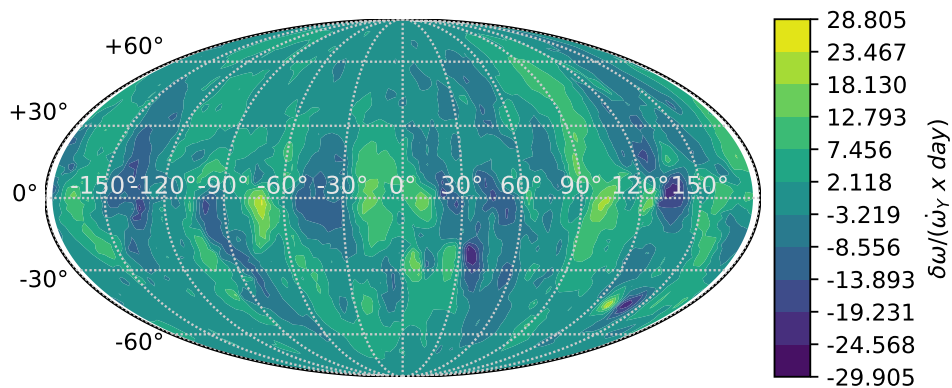


(a) Change to angular velocity magnitude compared to nominal YORP acceleration

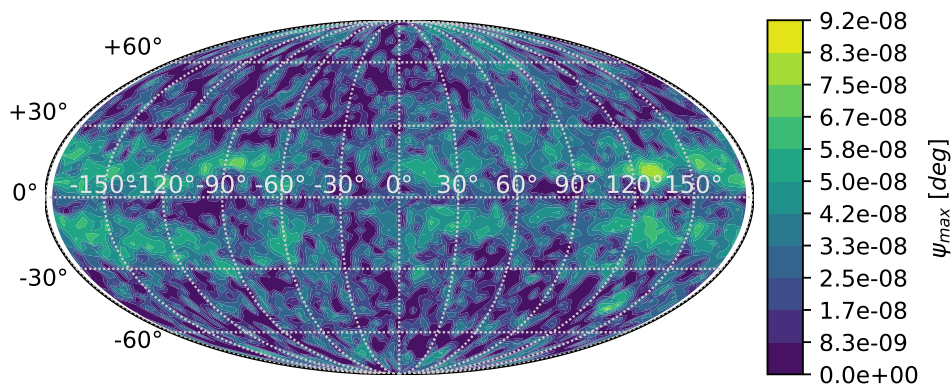
(b) Maximum precession reached

Figure 3.64: Change to angular velocity due to 1 kg particle launched at $1 \text{ m}\cdot\text{s}^{-1}$ from longitude and latitude [4.3 24.3] degrees in various directions with respect to surface normal

between normal and position direction vector, on a north-south axis as well as an east-west axis. For that reason global maps have been produced to present the possible outcomes for any point on the asteroid surface. Figures 3.65 and 3.66 present the change in angular velocity magnitude (compared to a day of YORP) and maximum precession angle for particle ejections normal to the surface of both the high and low energy ejections. The high energy case shows particle events that can equal up to ~ 30 day of YORP accelerations and the low energy case reach up to 0.08 of a YORP day, both 30 times larger than the single location results presented. The high change areas correlate with either western (accelerate) or eastern (decelerate) slopes of the north-south slopes of the asteroid. The precession results for the high energy case show low latitude areas outside of the equator prone to higher maximum precession angles. The low energy case again show small magnitudes of precession that reach the limit of numerical values with respect to the asteroid system.

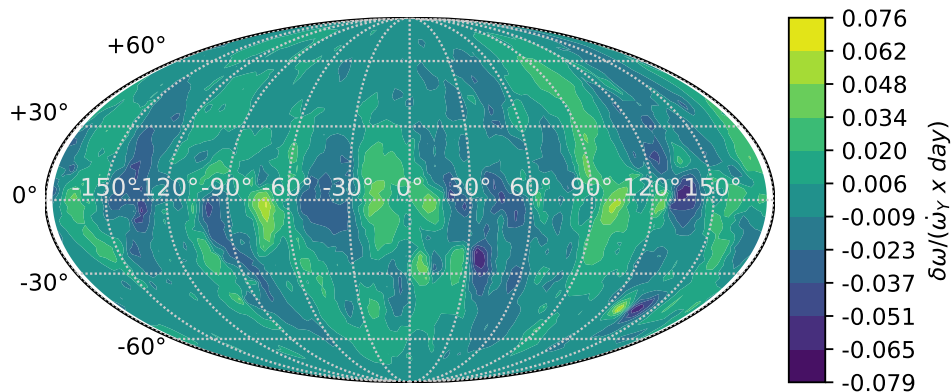


(a) Change to angular velocity magnitude compared to nominal YORP acceleration

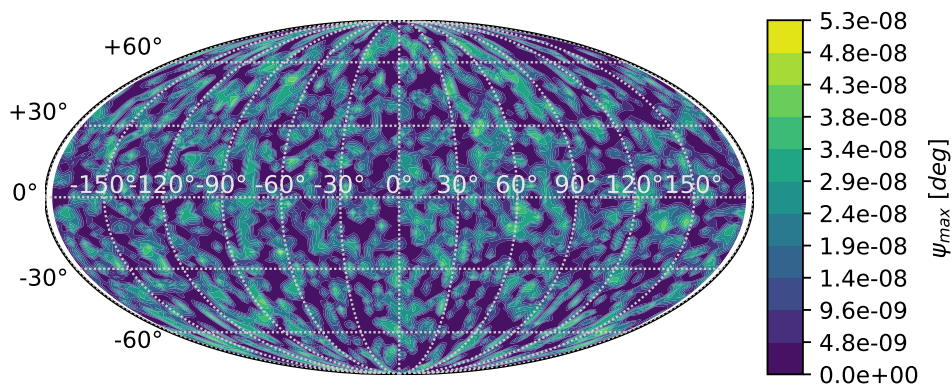


(b) Maximum precession reached

Figure 3.65: Change in angular velocity due 10 kg particle launched at $37.4 \text{ m}\cdot\text{s}^{-1}$ from any point on surface in normal direction



(a) Change to angular velocity magnitude compared to nominal YORP acceleration



(b) Maximum precession reached

Figure 3.66: Change in angular velocity due 1 kg particle launched at $1 \text{ m}\cdot\text{s}^{-1}$ from any point on surface in normal direction

3.2.2 Slow moving particles' fate

Particle surface ejections do not necessarily mean system escapes. The results in this section present a 2.3 kg particle launched from the lower-mid latitude location in a sub surface escape velocity (as seen in Figure 2.5) of $0.1 \text{ m}\cdot\text{s}^{-1}$. These type of particles effect the asteroid by redistributing mass on the surface in addition to the external source of energy and angular momentum they provide.

The results of a low velocity particle event launched normal to the surface are presented in Figures 3.67-3.70. The particle is seen traveling in a short sub-orbital arc towards the equator, crashing on the surface, traveling slightly below it, and bouncing once before stopping. The asteroid angular velocity vector evolution seen in Figure 3.69 shows a slight reduction in angular velocity magnitude due the launch and then an additional reduction due to the crash and surface movement. Overall the change in angular velocity magnitude is equivalent to 3.6×10^{-7} seconds added to the asteroid rotation period. The body frame precession seen in Figure 3.70a shows the center of precession removed from the initial body frame angular velocity direction. This precession is not sufficient to affect the asteroid surface geopotential, but its dissipation will drain energy from the asteroid system. The precession in the inertial frame (Figure 3.70b) shows the precession center move away from the initial rotation direction with the particle launch and then return to be centered around it with the particle crash, demonstrating the overall conservation of angular momentum in the enclosed system.

The launch direction of a single slow particle is can be influenced by multiple variables such as the ejection instigation mechanism, other particles, local slopes, or the particle shape. For that reason a 500 case MC simulation was run to examine possible outcomes of variabilities in ejection geometry. The launch magnitude in all cases is $0.1 \text{ m}\cdot\text{s}^{-1}$ and the launch direction is randomized within a hemisphere centered at the local normal. In addition, the surface motion randomness is enabled in the simulations. Figure 3.71 presents the trajectories of all simulated particles. All

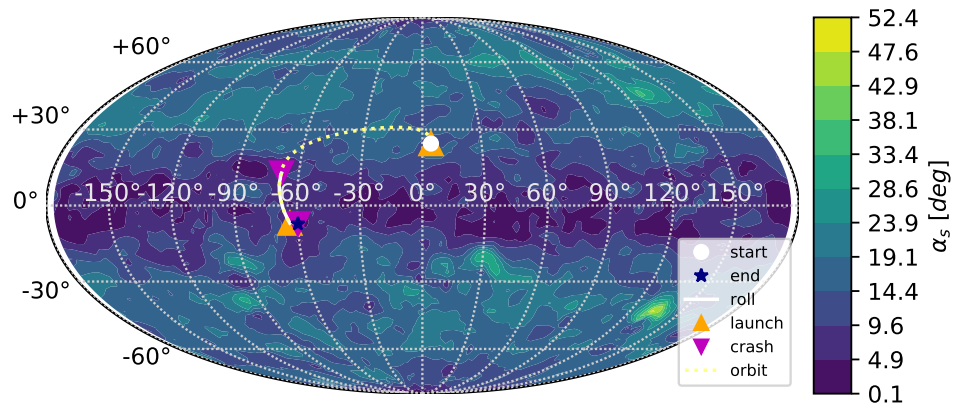


Figure 3.67: Boulder motion surface projection for a 2.3 kg particle launch at $0.1 \text{ m}\cdot\text{s}^{-1}$ launched from longitude and latitude $[4.3 \ 24.3]$ degrees. The heatmap indicates surface slopes, particle initial position indicated by white dot, surface motion indicated by white line, particle launch and crash events indicated by triangles, orbit projection on surface indicated by dashed yellow line, and particle final position indicated by blue star.

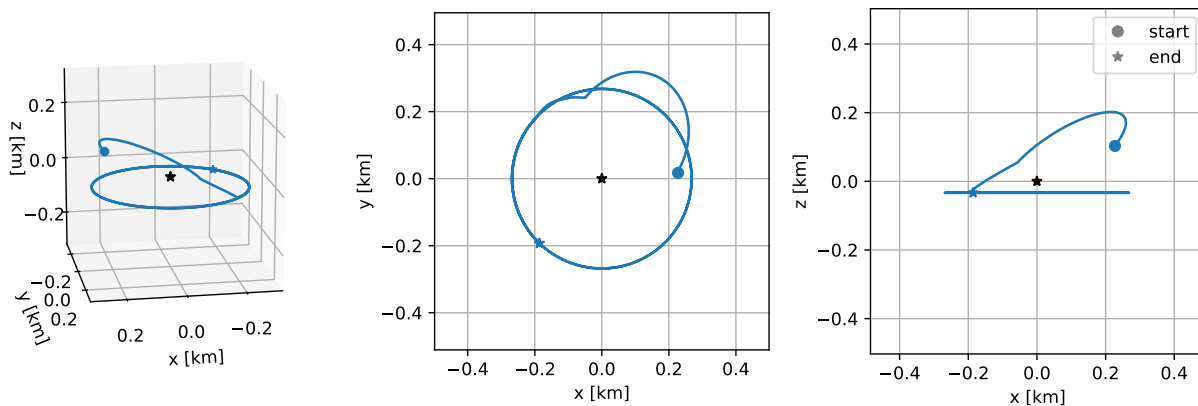


Figure 3.68: Boulder orbit motion for a 2.3 kg particle launch at $0.1 \text{ m}\cdot\text{s}^{-1}$ launched from longitude and latitude $[4.3 \ 24.3]$ degrees

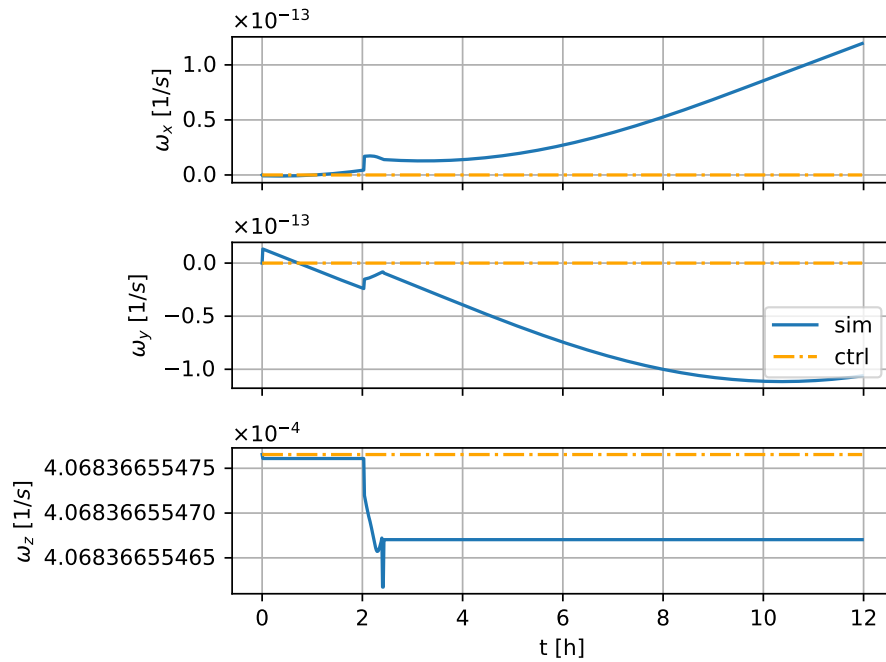
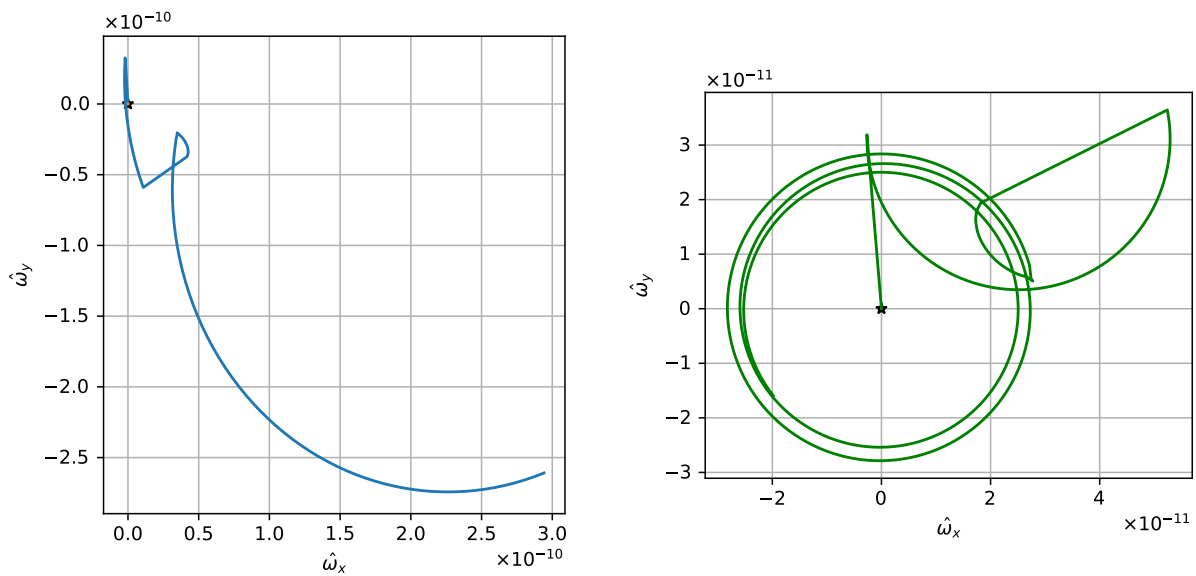


Figure 3.69: Modeled asteroid and control case angular velocity evolution due to 2.3 kg particle launched at $0.1 \text{ m}\cdot\text{s}^{-1}$ from longitude and latitude [4.3 24.3] degrees (asteroid body frame)



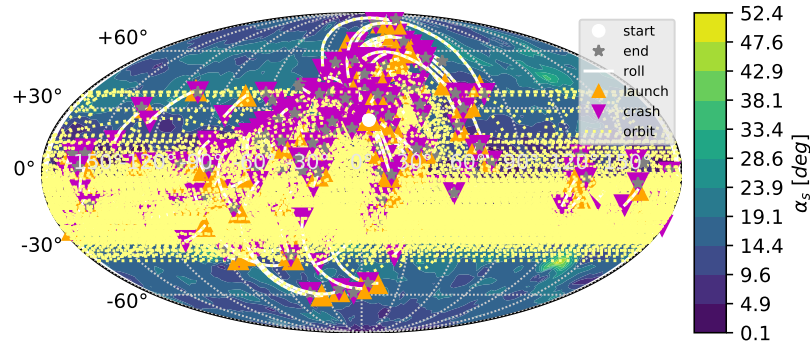
(a) Angular velocity vector projection on the equatorial plane (asteroid body frame) (b) Angular velocity vector projection on the inertial x-y plane (inertial frame)

Figure 3.70: Modeled asteroid angular velocity vector direction change due to 2.3 kg particle launched at $0.1 \text{ m}\cdot\text{s}^{-1}$ from longitude and latitude [4.3 24.3] degrees

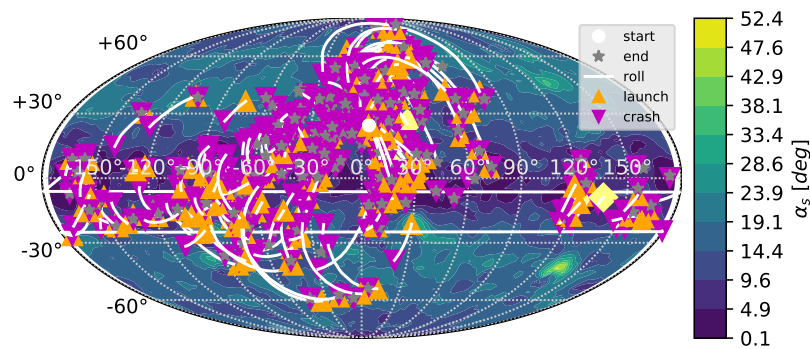
particles are launched from the initial lower-mid latitude at the beginning of the simulations, 431 particles crash back to the surface, out of those 263 move on the surface and 217 launch again into orbit. By the simulations' ends 86 cases present a particle still in orbit and 7 cases present an escaped particle. Figure 3.71c presents the surface distribution of the simulated particles. The largest cluster of particles remain near the initial launch location. Some clustering can be seen on the equator and some can be seen in a sub-equatorial mid latitude due west from the initial launch location. Those particles appear to have traveled a short sub-orbital cross-equatorial arc prior to falling back into the surface as the asteroid rotated underneath.

Figure 3.72 presents the simulations' end angular velocity magnitude change compared to a day of YORP (3.72a) and the center of precession at the end of the simulations in the inertial frame (3.72b). Most cases present little to no change compared to the initial angular velocity values (the majority of rotation centers in Figure 3.72b lay near the initial $[0,0]$ value). Extreme cases do show an increase or decrease in angular velocity magnitude of up to 5% of the daily YORP change. The arc of rotation canters to the right of the initial value is caused by cases in which a particle launched but did not crash by simulation's end.

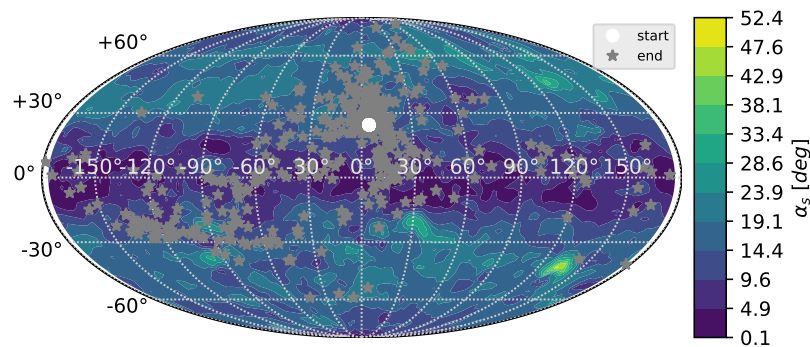
Similar MC simulations for other particle event latitudes were preformed, those are presented in the following figures, which show the results of a mid latitude particle event (Figure 3.73) and an equatorial particle event (Figure 3.74). Overall, the results are very similar regardless in latitude with a distinction in magnitudes reached as the event occurs closer to the equator.



(a) Complete trajectories



(b) Surface motion



(c) Initial and final surface positions

Figure 3.71: Boulder motion 500 case Monte Carlo surface projection for a 2.3 kg particle launch at $0.1 \text{ m}\cdot\text{s}^{-1}$ launched from longitude and latitude [4.3 24.3] degrees. The heatmaps indicate surface slopes, particle initial position indicated by white dot, surface motion indicated by white lines, particle launch and crash events indicated by triangles, orbit projection on surface indicated by dashed yellow lines, particle final positions indicated by gray stars, and yellow diamond indicates escaped particle.

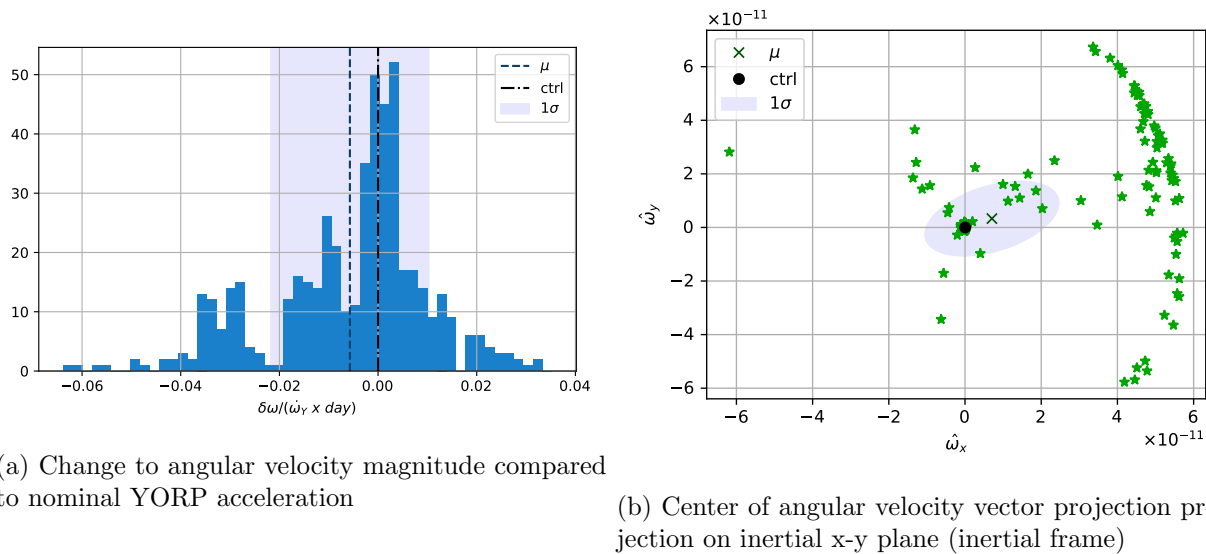


Figure 3.72: Modeled asteroid angular velocity change due to 2.3 kg particle launched at $0.1 \text{ m}\cdot\text{s}^{-1}$ from longitude and latitude $[4.3 \ 24.3]$ degrees. Histograms include distribution means and 1σ bounds as well as control values.

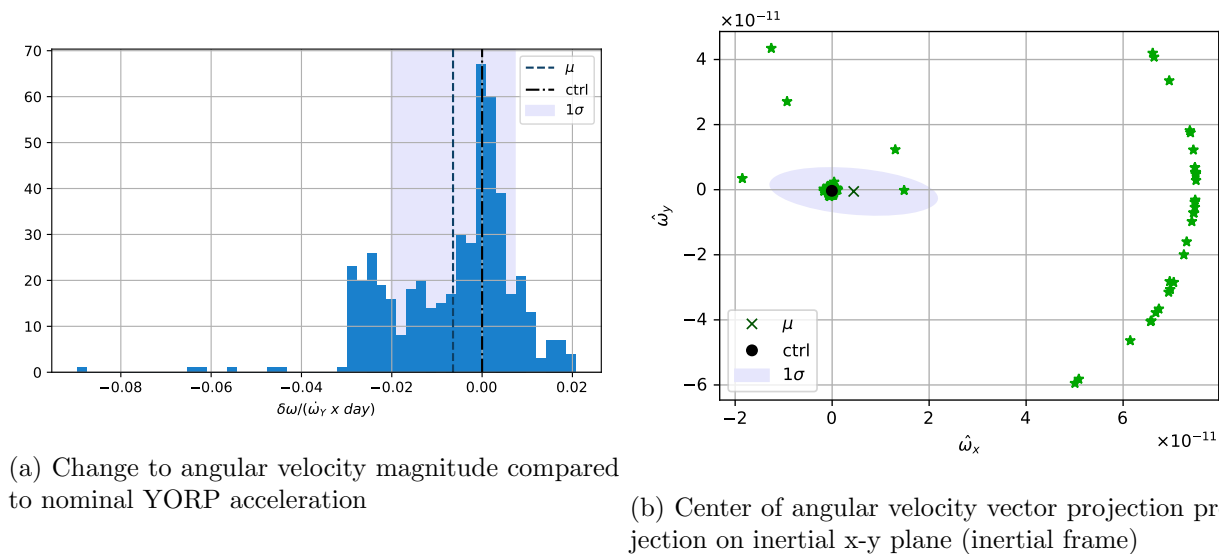


Figure 3.73: Modeled asteroid angular velocity change due to 2.3 kg particle launched at $0.1 \text{ m}\cdot\text{s}^{-1}$ from longitude and latitude $[-4.2 \ 40.1]$ degrees. Histograms include distribution means and 1σ bounds as well as control values.

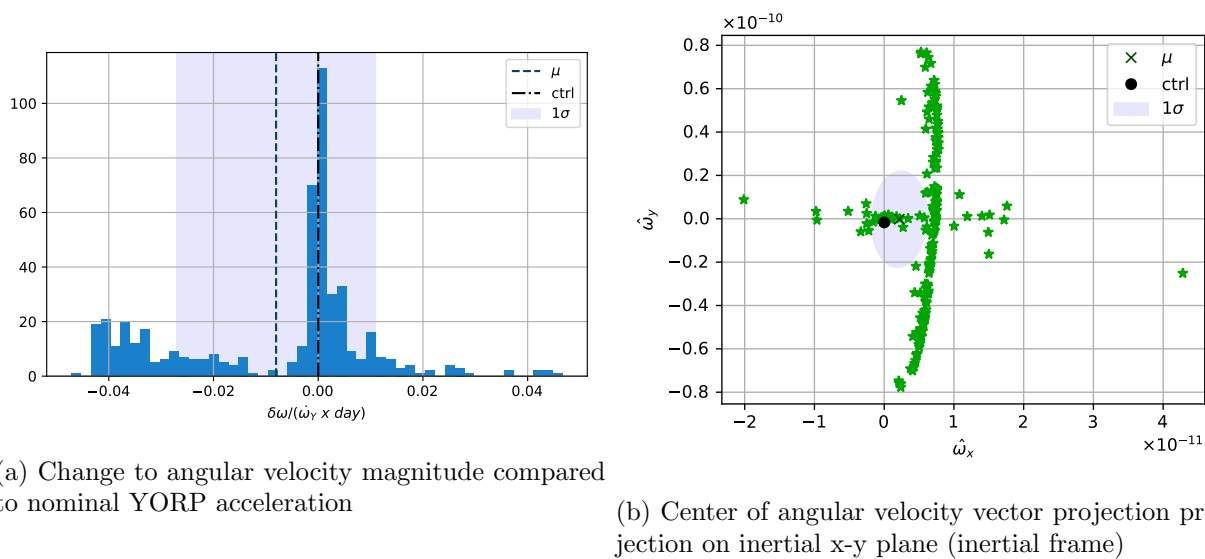


Figure 3.74: Modeled asteroid angular velocity change due to 2.3 kg particle launched at $0.1 \text{ m}\cdot\text{s}^{-1}$ from longitude and latitude $[-2.4 \ 2.6]$ degrees. Histograms include distribution means and 1σ bounds as well as control values.

Chapter 4

Artificial manipulation of small bodies

This chapter discusses the relationship between asteroid rotation and human induced activity on asteroid surfaces, together with considerations of the surface activity on asteroid orbital states.

4.1 Momentum transfer deflection relationship with small body rotation

The effect momentum transfer deflection has on asteroid rotation is presented and discussed in this section. Additionally, the effect asteroid rotation has on deflection efficiency is presented.

4.1.1 Background

The direct momentum transfer methods of nuclear detonation and kinetic interception are currently at the highest technology readiness levels and apply to both asteroids and comets [63]. The Deep Impact mission has shown the capability of accurately hitting a small body, comet Tempel 1, at high relative velocities ($10.3 \text{ km}\cdot\text{s}^{-1}$) in 2005 [134]. The Demonstration of Autonomous Rendezvous Technology (DART) mission is planned to perform a kinetic interception demonstration of the secondary body in the (65803) Didymos binary asteroid system in 2022 [135].

The momentum transfer in these methods is intended to be linear, usually close to the direction of orbital velocity of the PHO [136, 137], affecting the its orbital energy and momentum. However, an almost inevitable byproduct is the introduction of angular momentum to the PHO's rotational state. This torquing side-effect is the result of a lever arm between the body's center of mass and

deflection interface location on the surface and direction with respect to the center of mass. Either due to unintentional targeting discrepancies or due to operational requirements or limitations, such as the required orbital direction of deflection, or the degree of surface illumination. The ejection of material off the surface will also change the body's mass distribution which would, in turn, affect its rotational state.

For both the Deep Impact mission and the DART mission little a-priori knowledge about the shape of the impacted body was, or is expected to be, available. This means that the impact location, impact angle of incidence, and resulting lever arm was, and will be, in the realm of rough estimates. For both missions the operational scheme includes a phase in which accurate imagery is taken and the shape, spin state, and other dynamical and surface parameters estimated post impact. The incidence angle with respect to the local horizon for Deep Impact was estimated at 34 degrees, which was higher than initially planned for maximizing the ejecta plume (a different required operational outcome than deflection) [134, 138, 139]. No change to the comet's rotation or orbit was planned or observed, mostly due to the impactor mass of ~ 400 kg being substantially smaller than required to deflect the $\sim 7.5 \times 5$ km body. For the DART mission, the impact geometry is planned to be slightly skewed with respect to the secondary's orbital velocity in the system, which could potentially lead to a lever arm with respect to the secondary's center of mass. The observations of the dynamical state of the system post impact are planned to be performed real-time in-situ by the nano-satellite Light Italian Cubesat for Imaging of Asteroid (LICIA) mission [140], as well as from Earth and by a post impact in-situ mission, Hera [141]. These observations are expected to resolve the secondary's rotation state, currently assumed to be synchronized with the system's rotation period, as part of the entire binary system dynamical state. However, due to the complexity of the full two-body dynamics in a binary system, separating the initial change in rotation due to impact and mass loss from the complete system state would be difficult if not impossible, thus, not providing a complete analog for the effects of momentum transfer deflection on single small body's rotation.

Past research into momentum transfer deflection has mostly focused its discussion on efficiency in the orbital sense of optimal trajectories, deflection timing, orbit phases, and relative velocity

magnitudes and directions, or in analysis of the impact event, focusing on the expected momentum transfer from different types of surfaces and their resulting ejecta. The majority of this research assumes a spherical PHO or an impact normal to the surface with little to no consideration to the realistic small body shapes. Several studies in the past have incorporated realistic asteroid shapes: Asphaug et al. [142] used an N-body simulated shape of asteroid (4769) Castalia to examine the possible fragmentation outcomes of the rubble-pile asteroid. Scheeres et al. [143] performed an analysis of deflection efficiency variations for an impact on a polyhedral asteroid model along one of its principal axes with some uncertainty. This analysis examined the magnitude of velocity change to the asteroid as well as initial changes to angular velocity when the incoming impactor direction is not aligned with the local normal direction. Following Scheeres et al., Feldhacker et al. [133] further examined the efficiency of asteroid deflection for misaligned impactor-local normal instances with the development and validation of an analytical model. This model was then implemented on entire asteroid surfaces, showing variations in impact efficiency for different areas on different asteroids. Additionally, Delchambre et al. [144, 145], expanded the concept of the momentum enhancement β factor by adding consideration for momentum lost to angular motion. Lastly, McMahon and Scheeres [146] examined the efficiency reduction for beam ablation deflection when asteroid shapes are taken into consideration. This section is a direct continuation of this previous research in examining the effects of momentum transfer deflection on a small body's rotational state. In addition, the evaluations of deflection efficiency presented in [133] are expanded to include consideration of asteroid rotation. This section also addresses, for the first time, the effects that nuclear deflection detonation has on asteroid rotation as well as the effect that small body shapes have on the efficiency of this method.

4.1.2 Dynamics of kinetic interception

The linear momentum change to an asteroid in a kinetic interception scenario is the sum of the momentum introduced from the impactor and the momentum change due to ejecta leaving the

asteroid system [118]

$$P = P_i + P_e \quad (4.1)$$

The momentum introduced from the impactor is the multiplication of the impactor mass and its velocity with respect to the asteroid

$$P_i = M_i V_i \quad (4.2)$$

The momentum change due to ejecta is

$$P_e = \frac{n}{\sqrt{2}(n-1)} (M_e V_{e,min}) \quad (4.3)$$

where n represents the power-law slope of the experimentally derived particle ejection velocity vs ejected mass graph [117], nominally $n = 1.2$ for porous materials and $n = 1.65$ for rocky material, M_e and $V_{e,min}$ are the total mass ejected and the lowest velocity of that ejecta that eventually leaves the asteroid system, respectively. The total ejected mass can be found using the experimentally or numerically derived momentum multiplication factor β , nominally ranging between 1.5 and 3.5,

$$M_e = M_i (\beta - 1) \frac{V_i}{V_{e,min}} \frac{\sqrt{2}(n-1)}{n} \quad (4.4)$$

For the purpose of this research the nominal impactor mass is set to $M_i = 10^4$ kg, which is the upper limit of state-of-the-art launching capability. The nominal impactor relative velocity with respect to the asteroid is $V_i = 10 \text{ km}\cdot\text{s}^{-1}$. The nominal values of n , β , and $V_{e,min}$ of the modeled asteroid are set to 1.2, 2.0, and $0.2 \text{ m}\cdot\text{s}^{-1}$, respectively [133]. These are conservative values that assume a porous asteroid with lower than expected ejecta. The selected value of $V_{e,min}$ is in the range of surface escape velocities for the asteroids evaluated in this paper.

The overall ΔV provided to the asteroid is [133]

$$\Delta \mathbf{V}_A = \frac{M_i}{M_A} (\mathbf{V}_i + (\beta - 1) (\hat{\mathbf{n}} \cdot \mathbf{V}_i) \hat{\mathbf{n}}) \quad (4.5)$$

where $\hat{\mathbf{n}}$ is the surface normal vector at impact location. It is important to note that it is assumed that the ejecta is distributed symmetrically around the surface normal at the impact location, leading the mean ejecta direction to be in the normal direction. Here the asteroid system ΔV vector

is notated as ΔV_A to prevent confusion with other general ΔV mentions. The scenarios presented in this section are those in which ejecta escapes in each launch, thus the asteroid system and the asteroid (parent body and surface boulders) are the same. The notation in the work presented here is in the inertial frame, which is assumed to coincide with the body frame at the moment of impact.

4.1.3 Impact effects on rotating ellipsoids

A rotating ellipsoid is used as a first analog for an asteroid. The ellipsoid has an overall mass M_A , principal semi-axes a , b , and c , and a point mass M_e placed on its surface in location \mathbf{r} . The overall system inertia tensor before impact is

$$[I_0] = [I_{ellipsoid}] + M_e[\tilde{\mathbf{R}}][\tilde{\mathbf{R}}]^T \quad (4.6)$$

Using the inertia matrix eigenvalues and eigenvectors the principal axes are found and the ellipsoid asteroid analog is set to rotate as a PAR about the maximum moment of inertia with fixed angular velocity $\boldsymbol{\omega}_0$. The overall angular momentum at this time is

$$\mathbf{H}_0 = [I_0]\boldsymbol{\omega}_0 \quad (4.7)$$

The impact and mass ejection are modeled as launching of the point mass at an equivalent velocity \mathbf{V}_{eq} . The velocity's magnitude being the overall linear momentum introduced in the event, P , divided by the ejected mass M_e

$$V_{eq} = \frac{P}{M_e} \quad (4.8)$$

For the impact parameters presented above, the impactor mass is four orders of magnitude smaller than the ejecta mass and thus neglected from the moment of impact on. The equivalent velocity direction is the weighted sum of the impactor direction and surface normal at point of impact

$$\hat{\mathbf{V}}_{eq} = \frac{-\hat{\mathbf{V}}_i + (\beta - 1)\hat{\mathbf{n}}}{|-\hat{\mathbf{V}}_i + (\beta - 1)\hat{\mathbf{n}}|} \quad (4.9)$$

In the case of an ellipsoid the surface normal at any point (in the ellipsoid frame) is $\hat{\mathbf{n}} = [\frac{r_x}{a^2}, \frac{r_y}{b^2}, \frac{r_z}{c^2}]$. Due to the ejecta launch the new inertia tensor of the system is only that of the ellipsoid $[I_{ellipsoid}]$.

The angular velocity right after the ejecta launch based on Eq. 2.26 is

$$\boldsymbol{\omega}(t = 0^+) = [I_{\text{ellipsoid}}]^{-1} (\mathbf{H}_0 - M_e \mathbf{R} \times (\mathbf{R} \times \boldsymbol{\omega}_0 + \mathbf{V}_{eq})) \quad (4.10)$$

The combination of the different inertia tensor and new angular velocity no longer guarantees rotation around the maximum moment of inertia, leading to some tumbling/wobbling motion for the ellipsoid. Figure 4.1 presents the maximum precession angle (found using the analytical Eq. 2.9) reached for an impactor at various locations on the eastern hemisphere of an ellipsoid with the mass and mean dimensions of asteroid Bennu. The impact parameters are set to the values presented in the previous section and Bennu's parameters are set to the nominal ones presented in Table 3.6. The impactor approach direction is $\hat{\mathbf{V}}_i = [0, -1, 0]$, providing all of its momentum in the system (ellipsoid and point mass) frame¹ negative y-axis direction, and rendering the longitude and latitude $[0, 90]$ degree coordinate directly parallel to the impactor velocity (indicated in the figure with a white dot). Here it is assumed that the required orbital direction for deflection is the incoming impactor direction. The western hemisphere is not presented as it is obscured by the ellipsoid itself for this impactor direction and thus not possible for collision. The figure shows a maximum precession of 3.5 degrees for high latitude regions at the retreating edge of the hemisphere facing the impactor (high longitudes)². This result is explained by the combination of the impactor providing maximal torque at the hemisphere edges (maximum lever arm) and these areas having the same local linear velocity direction as the incoming impactor. For that reason the approaching edge of the hemisphere (lower longitudes) shows lower maximum precession reached. The equatorial regions of the system show the least precession because of their symmetry with respect to the xy plane, mostly torquing the existing rotation direction and providing less or no torque to the x and y elements of the angular velocity. The expanded low precession area around longitude and latitude $[0, 20]$ degrees can be explained by the offset between applied torque and removed mass, rendering

¹ This is an ellipsoid fixed frame in which the x-axis is set to parallel the long axis, the y-axis is set to parallel the median axis, and the z-axis completes a right-hand system and is parallel to the short axis. The ellipsoid is initiated as a maximum inertia axis PAR, setting the angular velocity vector near the z-axis, but not at it, due to the added point mass.

² Here the terms retreating and approaching edges are with respect to the incoming impactor. The retreating edge moves linearly in the same direction as the impactor, thus moving away from it. The approaching edge moves linearly in the opposite direction from the impactor, towards it

the ellipsoid closer to a PAR. The polar regions show high but not maximal precession because of their radial proximity to the existing axis of rotation.

Figure 4.2 shows the ratio between the angular velocity prior to impact and maximum angular velocity reached after impact. It is important to note that once the ellipsoid is no longer a PAR the angular velocity is not time-constant and thus its magnitude oscillates. The figure shows that equatorial hemisphere edge impacts have the most dramatic change to the angular velocity magnitude of up to $\sim 5\%$, or ~ 800 second change in the case of Bennu's rotation period. A dashed line indicating 1-1 angular velocity ratios can also be observed in the figure, showing where impacts on the surface will not change the Bennu-like ellipsoid's rotation rate.

In Figure 4.3 the ΔV induced by the impact as calculated in Eq. 4.5 is presented. A maximum value of $2.8 \text{ mm}\cdot\text{s}^{-1}$ can be seen for an impact that is parallel to the surface normal. The hemisphere edge impacts provide a ΔV of $1.3 \text{ mm}\cdot\text{s}^{-1}$, showing the amount of momentum lost to torquing the system instead of propelling it.

Figures 4.4-4.6 present the impact results for an impactor hitting the ellipsoid in longitude and latitude [25,25] degrees. The figures show heatmaps of the resulting changes in a local azimuth local zenith coordinate system, the same coordinates as presented in Figures 3.63 and 3.64. The local surface normal is in the center of each plot, the white star in the plots indicates the direction of the local position vector. The discrepancy between the two directions leads to the lever arm that torques the ellipsoid. The lever arm will be discussed further in the next section. Figure 4.4 shows the correlation between local coordinates and the least tumbling impact direction. Due to the offset between applied torque and removed mass the least precessing direction is not observed for the local position vector direction, but for a direction skewed by ~ 40 degrees from it. Figure 4.5 shows the torquing effect that impacts with low incidence angles would have, especially with large lever arms with respect to the existing rotation axis. Here higher correlation between the local position vector and zero change in angular velocity magnitude can be seen. However, the offset due to mass loss can be seen as well in the misalignment of the position vector direction and the zero

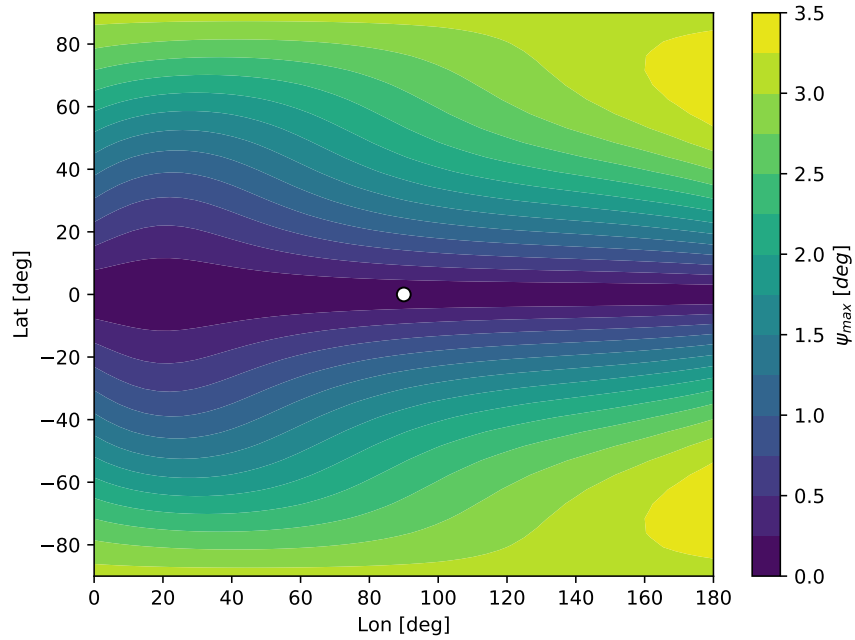


Figure 4.1: Precession reached for impacts on Bennu-like ellipsoid for $\hat{\mathbf{V}}_i = [0, -1, 0]$, the dot indicates the impactor direction parallel to the surface normal

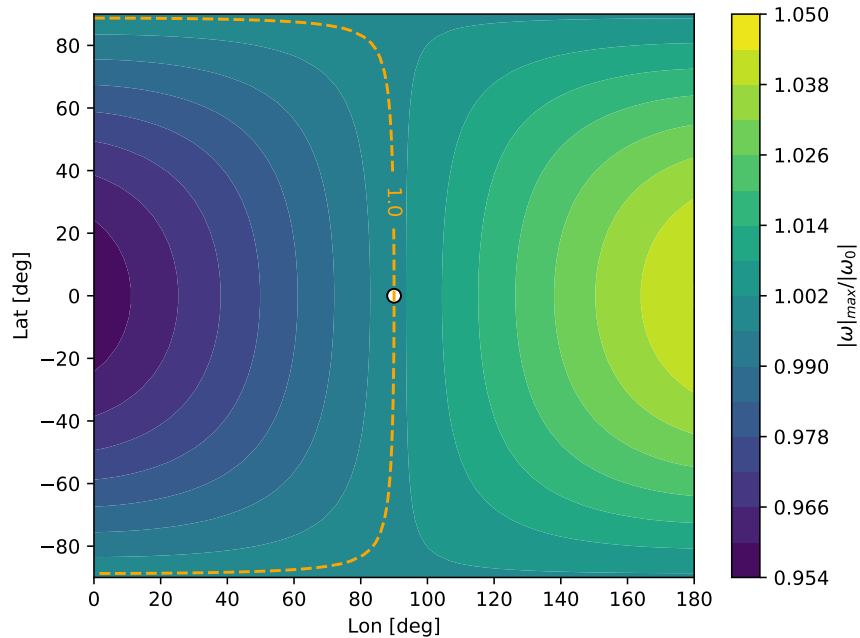


Figure 4.2: Change in angular velocity magnitude reached for impacts on Bennu-like ellipsoid for $\hat{\mathbf{V}}_i = [-1, 0, 0]$, the dot indicates the impactor direction parallel to the surface normal, the dashed line indicates equal values between $|\omega|_{max}$ and $|\omega_0|$

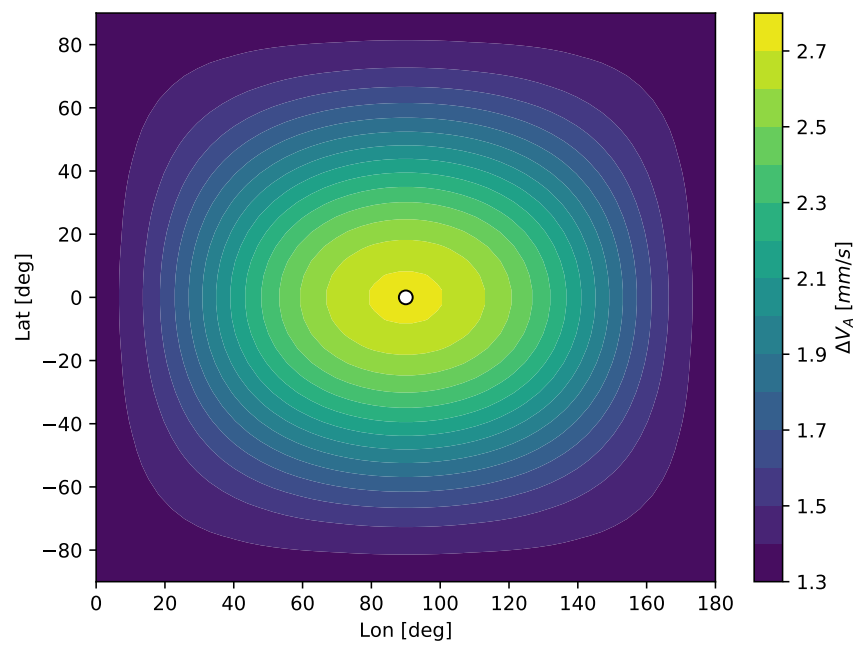


Figure 4.3: ΔV reached for impacts on Bennu-like ellipsoid for $\hat{\mathbf{V}}_i = [0, -1, 0]$, the dot indicates the impactor direction parallel to the surface normal

torque curve³. Figure 4.6 demonstrates again the preference for aligning the surface normal and impactor velocity vector for best deflection performance, assuming the required orbital deflection direction is that of the incoming impactor.

The axis ratio of asteroid Bennu is close to spherical - around 1.1-1.05-1.0 - more elongated asteroids would show a larger span of outcomes for different impact locations. Figures 4.7-4.8 present the precession reached and change in angular velocity magnitude due to impacts on an elongated ellipsoid based on asteroid Itokawa, which has an axes ratio of 2.5-1.5-1.0. Itokawa's mass is about 44% of Bennu's, leading to more substantial effects from the impactor presented above. Similar to the previous figures, the impactor is approaching in the negative y-axis direction, setting the ellipsoid's long axis to be perpendicular to the incoming impactor. Interestingly, Figure 4.7 presents more symmetrical behavior for the elongated ellipsoid with respect the y-axis. The low precession zone is slightly offset west of $[0,90]$. The maximum precession zone is in the approaching hemisphere edge, different from the Bennu-like ellipsoid due to the different ratio between rotation rate and incoming impactor velocity. Figure 4.8 shows similar behavior to the near-spherical case, with some offset from extreme points due to the mass ejection.

³ Marked as the 1-1 ratio dashed line.

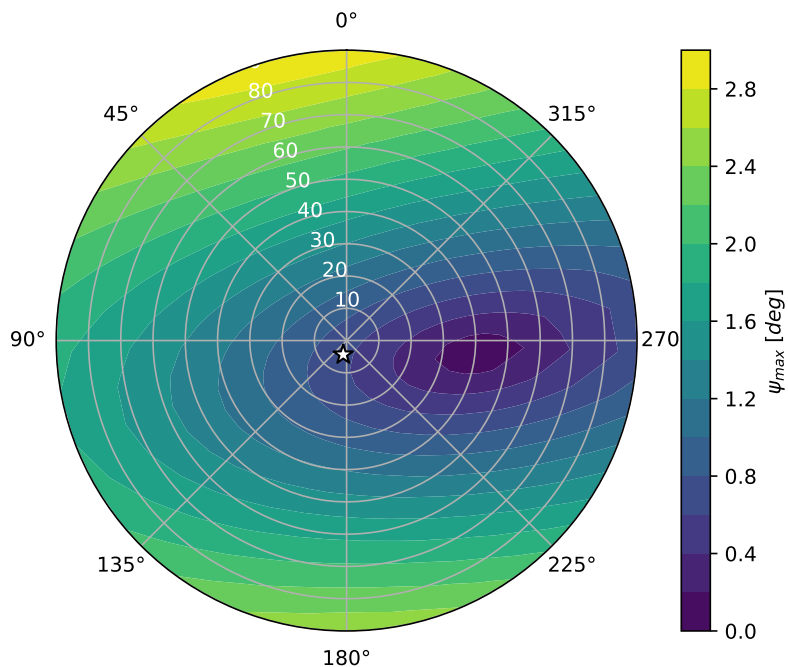


Figure 4.4: Precession reached for impacts located at [25,25] degrees on a Bennu-like ellipsoid, the star indicates the impactor direction parallel to the surface position

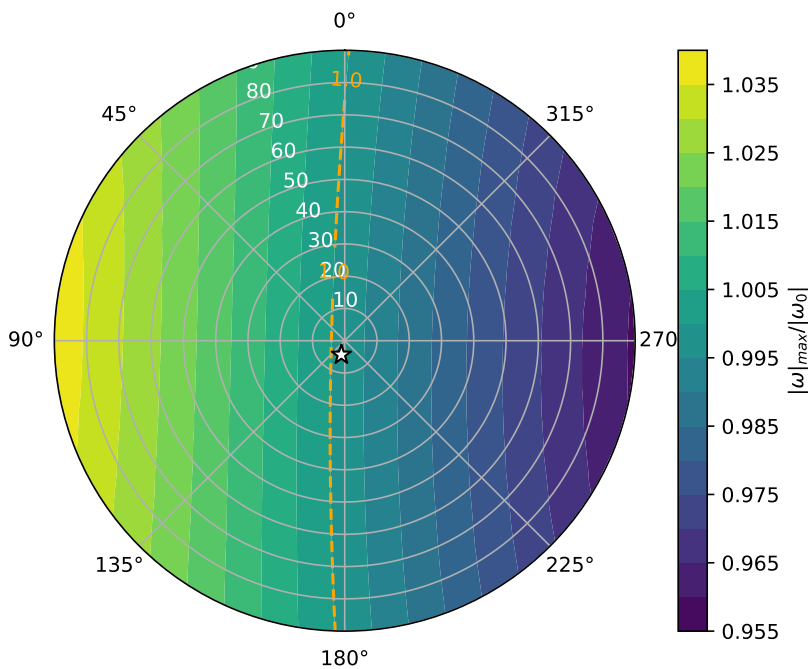


Figure 4.5: Change in angular velocity magnitude reached for impacts located at [25,25] degrees on a Bennu-like ellipsoid, the star indicates the impactor direction parallel to the surface position, the dashed line indicates equal values between $|\omega|_{max}$ and $|\omega_0|$

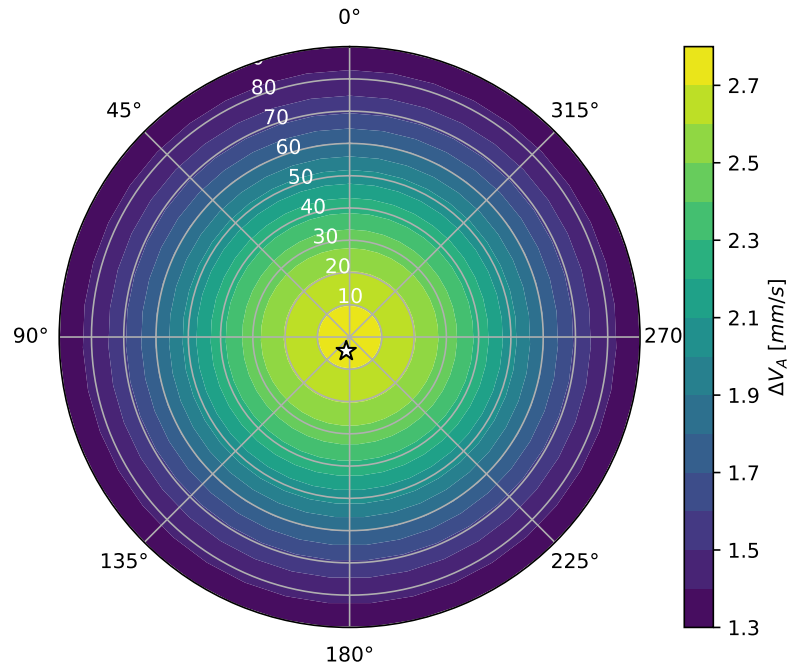


Figure 4.6: ΔV reached for impacts located at $[25,25]$ degrees on a Bennu-like ellipsoid, the star indicates the impactor direction parallel to the surface position

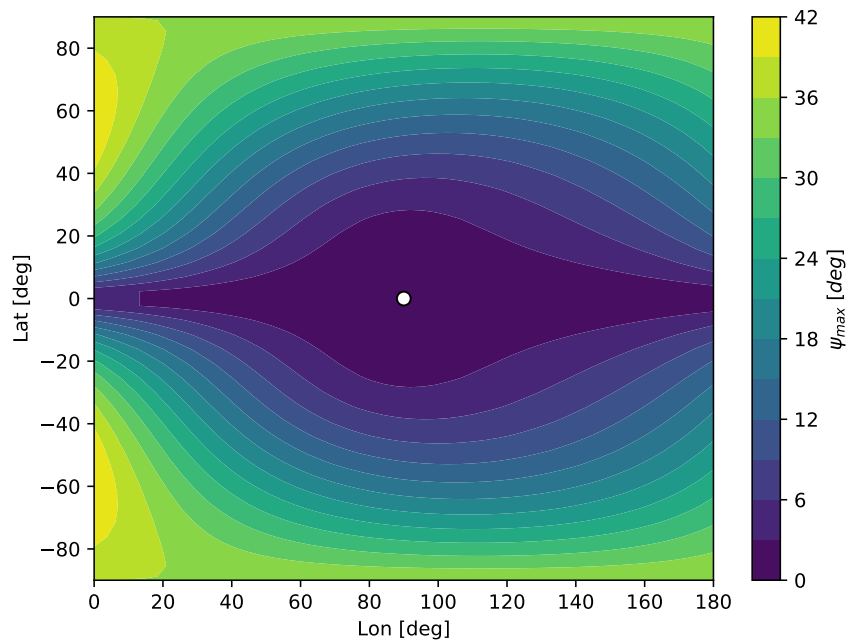


Figure 4.7: Precession reached for impacts on Itokawa-like ellipsoid for $\hat{V}_i = [0, -1, 0]$, the dot indicates the impactor direction parallel to the surface normal

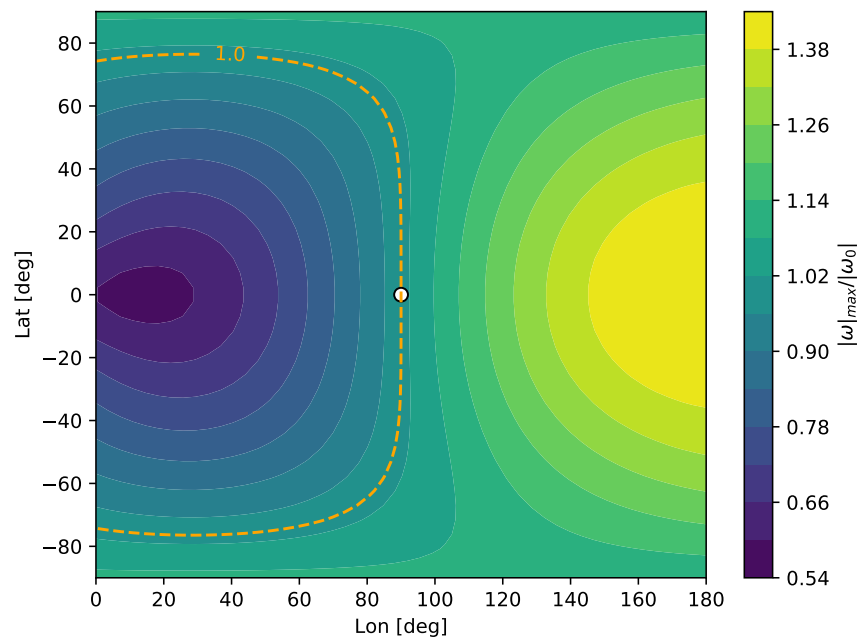


Figure 4.8: Change in angular velocity magnitude reached for impacts on Itokawa-like ellipsoid for $\hat{\mathbf{V}}_i = [0, -1, 0]$, the dot indicates the impactor direction parallel to the surface normal, the dashed line indicates equal values between $|\omega|_{max}$ and $|\omega_0|$

4.1.4 Considerations of asteroid shape

The results presented in the previous section use a simple analytical analysis to demonstrate the importance of aligning the incoming impactor velocity with the impact location surface normal. However, as seen in Figures 4.4-4.6, these results are for simple ellipsoids in which there is a high correlation between position vector and surface normal: for the Bennu-like ellipsoid the maximal angle between surface position and surface normal is 7 degrees and for the Itokawa-like ellipsoid it is somewhat higher at 48 degrees. The correlating lever arm to with respect to the center of mass is defined as $l_M = |\mathbf{r}| \sin(\hat{\mathbf{n}} \cdot \hat{\mathbf{r}})$. Figures 4.9-4.10 present the lever arm magnitudes reached for the Bennu-like and Itokawa-like ellipsoids. These levers would apply torque on the asteroid, wasting linear momentum towards changing the asteroid's rotation (spin up/down of existing direction and/or introducing precession) rather than applying it to the deflection effort. For the most part, the equatorial and polar regions in the figures present the lowest overall lever arm, showing a preference for them as impact location.

When comparing the ellipsoid geometry with the polyhedral geometry of Bennu and Itokawa shown in Figures 4.11-4.12 for the entire asteroid surface (Figures 4.9-4.10 only show one hemisphere) correlation in trends can be found. However, the maximal magnitudes for lever arm are ~ 2 (Itokawa) to ~ 5 (Bennu) times higher for the polyhedrons, and the maximal lever arm area distributions are slightly different: for Bennu these areas are closer to the equator due to the spinning-top shape and for Itokawa these areas are mostly concentrated in the node edge corners due to the asteroid being more rod-like than ellipsoidal, especially near the asteroid's small node. Furthermore, small shape irregularities show higher than nominal lever arm regions, these should be examined further in the future. The following sections implement the impact dynamics on detailed polyhedral shapes, adding the required level of complexity to the deflection success analysis.

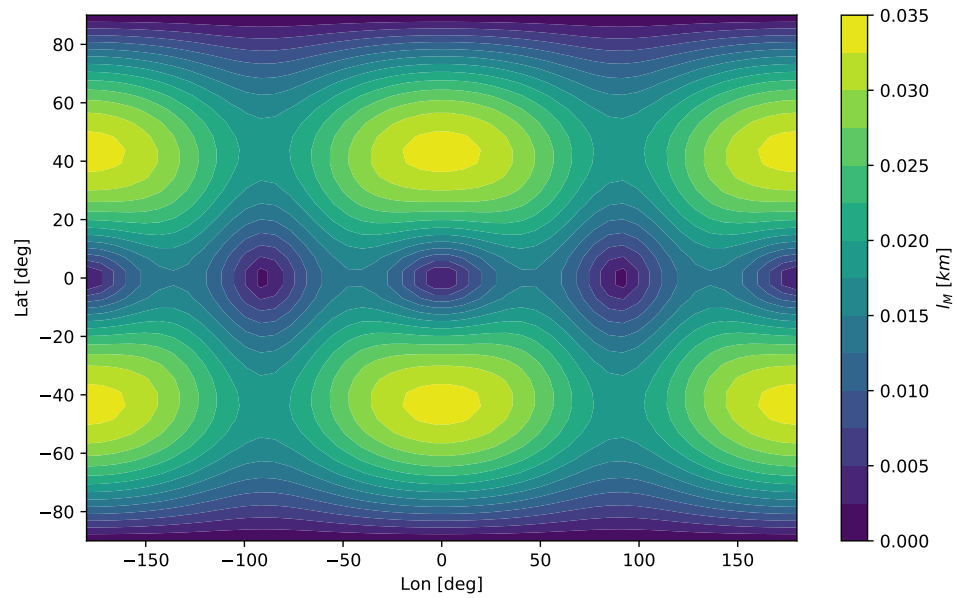


Figure 4.9: Lever arm due to angle between surface position and surface normal for a Bennu-like ellipsoid

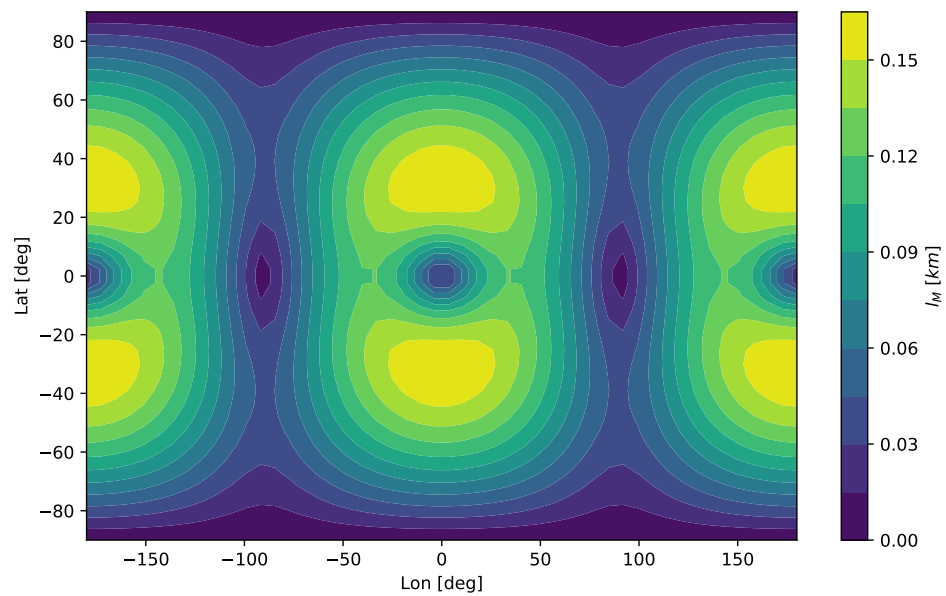


Figure 4.10: Lever arm due to angle between surface position and surface normal for an Itokawa-like ellipsoid

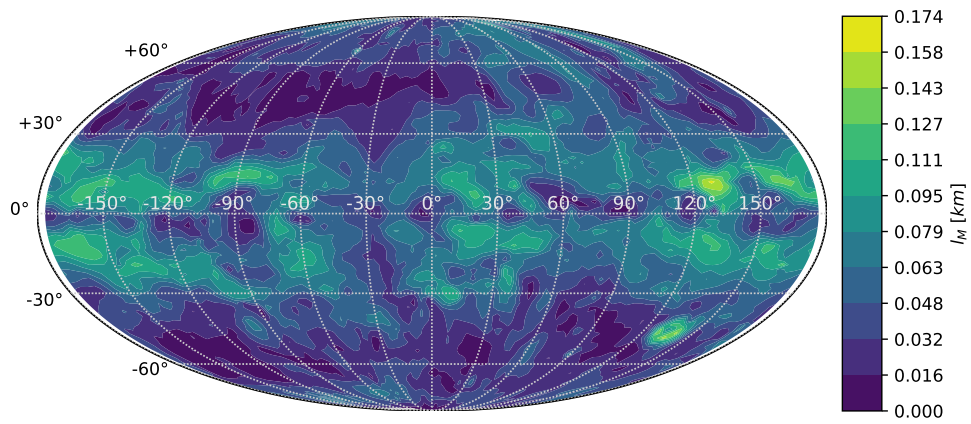


Figure 4.11: Lever arm due to angle between facet position and facet normal for Bennu polyhedral shape

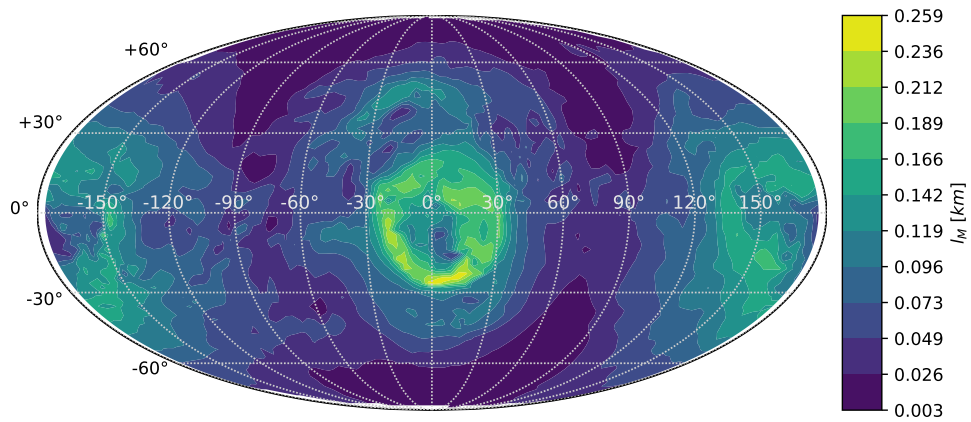


Figure 4.12: Lever arm due to angle between facet position and facet normal for Itokawa polyhedral shape

4.1.5 Nuclear detonation deflection

The dynamics of nuclear detonation deflection entail a more complex and specified view than those of kinetic interception. There are different considerations for a subsurface, surface, or above-surface explosions [62, 147]. For the purpose of this research approximated ejecta mass and ejecta velocities will be derived from Figure 4.13, which is taken from Sanchez et al. [148] and presents the ejecta masses and average velocities due to different radiation types emitted as part of an above-surface deflection effort of a 1.5 kT detonation.

For the purpose of this research the ejected mass will be that created by neutron and x-ray radiation at the maximum performance altitude presented for the detonation. The overall neutron radiation ejecta mass used will be $M_{e,ntrn} = 3 \times 10^6$ kg, ejected at a velocity of $V_{eq,ntrn} = 4$ km·s⁻¹. The x-ray radiation ejecta mass used will be $M_{e,xray} = 3 \times 10^3$ kg, ejected at a velocity of $V_{eq,xray} = 50$ km·s⁻¹. The total ejecta mass is then $M_e = 3.003 \times 10^6$ kg and the equivalent velocity is

$$V_{eq} = \frac{M_{e,ntrn}V_{eq,ntrn} + M_{e,xray}V_{eq,xray}}{M_{e,ntrn} + M_{e,xray}} = 4.45 \text{ km} \cdot \text{s}^{-1} \quad (4.11)$$

This mass estimate is based on a spherical model of asteroid (99942) Apophis and thus is conservative for an asteroid such as Bennu which has seven times more surface area, and will likely produce more ejecta. However, use of these parameters still present a good contrast for comparing ejecta velocities between the kinetic interceptor and nuclear detonation scenarios. Additionally, a nuclear detonation deflection does not require high approach velocities with respect to the asteroid, thus allowing the deflecting spacecraft to optimally align itself and the detonation energy with respect to the asteroid center of mass and required orbital direction.

4.1.6 Deflection effect on rotational dynamics using polyhedrons

As seen in Section 4.1.4, complex asteroid shapes have the potential to further complicate the rotational effect deflection efforts might have on asteroids. In the following sections the fission option of the SEA-RATS model is utilized to simulate deflection ejecta and the rotational dynamics

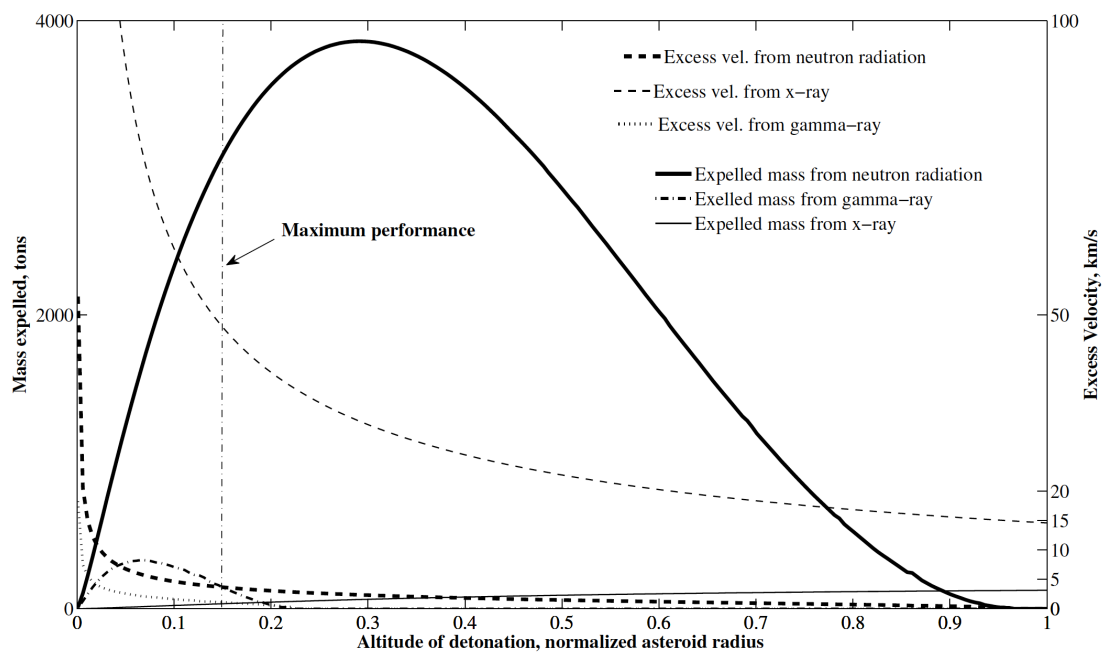


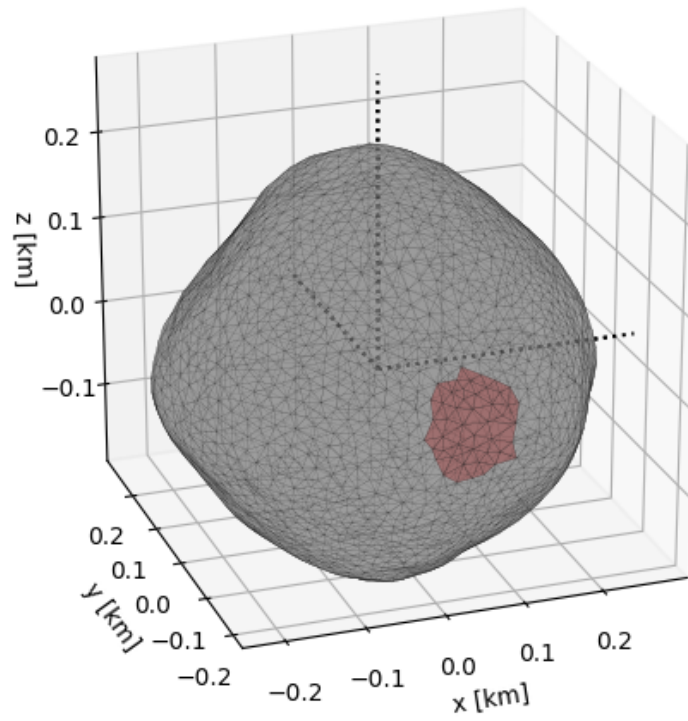
Figure 4.13: Ejecta mass and velocity due to above surface nuclear detonation deflection from Sanchez et al. 2009

that follow. In the simulated breakup process the ejecta mass is defined as fissioned material and then launched at \mathbf{V}_{eq} as defined in Eqs. 4.8, 4.9, and 4.11. The polyhedral shape which represents the ejected mass is found in the iterative process presented in Section 2.5 around the deflection interface location on the polyhedral asteroid surface. The ejected/fissioned material is then treated as a boulder by the SEA RATS model and code.

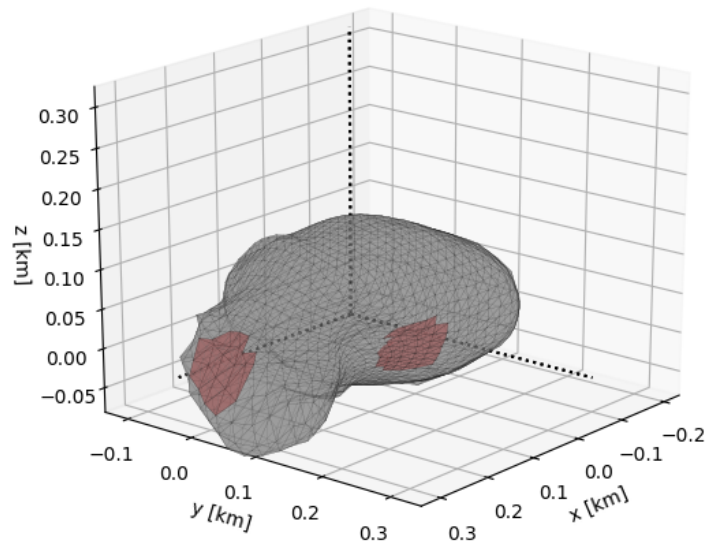
Figure 4.14 presents the Bennu and Itokawa polyhedrons, with the impact ejecta masses indicated on the shapes. For asteroid Bennu a single location is seen in an equatorial region, for asteroid Itokawa two equatorial locations are seen, one on along the asteroid's long x-axis, and another along the asteroid's median y-axis. Section 4.1.6.2 presents the rotational state after kinetic impactor deflection on the presented locations as well as a nuclear detonation deflection on the location presented on asteroid Bennu.

4.1.6.1 Asteroid state effect on asteroid velocity change

Section 2.3.4 presents the the asteroid velocity change due to boulder escape. The direction of the velocity change is opposite to that of the boulder as it escapes the system. In this section an assumption is made that for sufficiently high ejection velocities the initial velocity direction at launch is the parallel to the ejection velocity direction when the ejecta leaves the asteroid system Hill sphere, $\hat{\mathbf{R}}_{\infty} \parallel \hat{\mathbf{R}}_{t_0}$. Validation for this assumption on small bodies can be seen in Figure 4.15, which presents the comparison of ejecta velocity direction at launch and its velocity direction at the Hill radius for various scenarios on asteroids Bennu and (66391) 1999 KW4 Alpha [149]. The velocity directions are compared using the angle between the two vectors. The launch scenarios include 3 launch sites (equatorial, mid-latitude, and polar) and 12 launch directions. The launch sites longitudes and latitudes are presented in each subplot title. The launch direction right ascension and declination values are presented in the plots' legends. Figure 4.15a shows that, for Bennu, all ejecta launch velocity magnitudes, $|\Delta\mathbf{V}_e|$, over $1 \text{ m}\cdot\text{s}^{-1}$ reach a direction error of less than 2 degrees. Asteroid 1999 KW4 Alpha, which is ~ 30 times more massive than Bennu, shows the smaller than 2



(a) Bennu



(b) Itokawa

Figure 4.14: Asteroid polyhedra, impact locations, and ejecta mass

degree error at launch velocity magnitudes over $3 \text{ m}\cdot\text{s}^{-1}$. A 2 degree deviation leads to $\sim 0.06\%$ loss in velocity magnitude in the desired direction. The effect of this deviation on the orbital dynamics of the deflection efforts will be further discussed in a later section.

In addition to deflection momentum lost in torquing an asteroid, some momentum can be added or subtracted from the deflection effort because of the ejecta mass pre-deflection linear velocity due to rotation. Using Eq. 2.20 in terms of the equivalent velocity

$$\dot{\mathbf{R}}_0 = \boldsymbol{\omega} \times \mathbf{R}_0 + \mathbf{V}_{eq} \quad (4.12)$$

where \mathbf{V}_{eq} is the $\mathbf{r}_{B,j}^{\mathfrak{B}_A}$ element in Eq. 2.20, and inputting it into Eq. 2.34 together with the $\hat{\mathbf{R}}_{B,\infty} \parallel \hat{\mathbf{R}}_{B,t_0}$ assumption leads to the asteroid velocity change as a function of the material ejection

$$\Delta \mathbf{V}_A = -\frac{M_e}{M_A} \sqrt{|\boldsymbol{\omega} \times \mathbf{R}_0 + \mathbf{V}_{eq}|^2 - 2 \frac{GM}{|\mathbf{R}_0|} \frac{\boldsymbol{\omega} \times \mathbf{R}_0 + \mathbf{V}_{eq}}{|\boldsymbol{\omega} \times \mathbf{R}_0 + \mathbf{V}_{eq}|}} \quad (4.13)$$

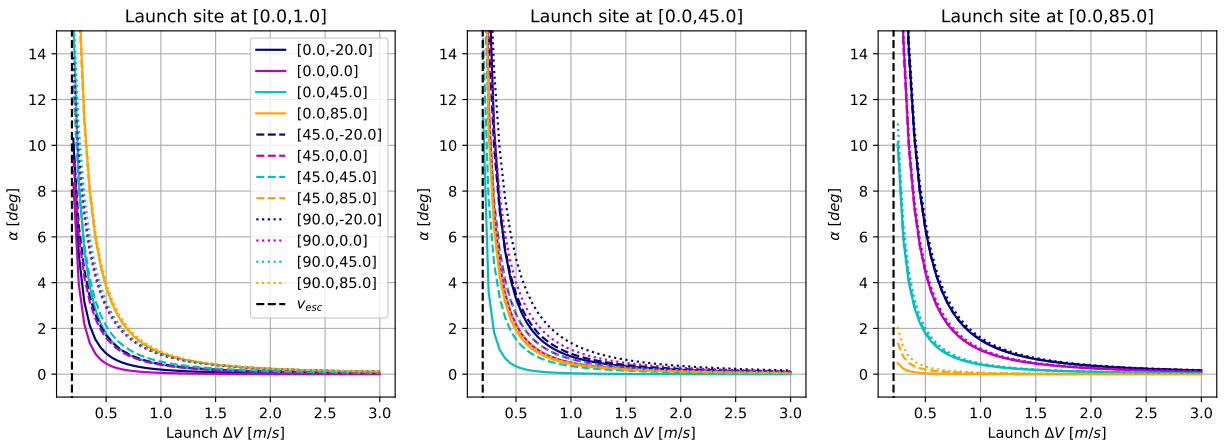
which accounts for the ejecta velocity due to asteroid's rotation. Here, the reduction in ejecta velocity at the Hill radius is accounted for. And, more importantly as Section 4.1.6.3 demonstrates, accounts for the influence of the asteroid's rotation on the deflection direction and effective magnitude.

In deflection scenarios the inertial direction of asteroid velocity change is of importance to the change in orbital elements required for deflection, mainly the velocity change direction should align closely with the asteroid's orbital velocity [136]. For that reason the deflection applicable velocity change is the projection of the velocity change on a required inertial direction $\Delta \hat{\mathbf{V}}^*$. For the purpose of this section $\Delta \hat{\mathbf{V}}^*$ will be defined as the direction of the incoming deflection spacecraft \mathbf{V}_i . Thus, the deflection applicable velocity change is

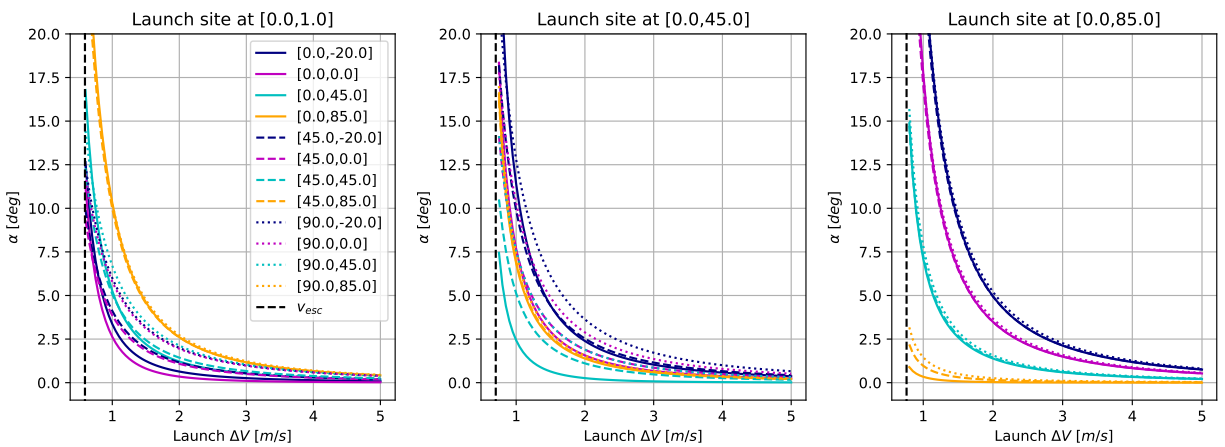
$$\Delta \mathbf{V}_A^* = \left(\Delta \mathbf{V}_A \cdot \hat{\mathbf{V}}_i \right) \hat{\mathbf{V}}_i \quad (4.14)$$

The effective deflection magnitude is then

$$|\Delta \mathbf{V}_A^*| = \Delta \mathbf{V}_A \cdot \hat{\mathbf{V}}_i \quad (4.15)$$



(a) Asteroid Bennu



(b) Asteroid 1999 KW4 Alpha

Figure 4.15: Deviation angle between launch velocity and velocity at Hill radius

4.1.6.2 Rotational state after deflection

Figures 4.16 and 4.17 present the rotation state evolution after a kinetic impactor deflection off the location presented in Figure 4.14a, centered at longitude and latitude [-84.4, 5.9] degrees. The angle between facet normal and facet position in this case is 4.93 degrees, which correlates to a 0.022 km lever arm on the asteroid center of mass. Figure 4.16 shows the asteroids angular velocity vector⁴ between 10 hours prior to impact and 90 hours after it, a time span that allows for several cycles of the angular velocity vector in the body frame. The most important result seen in the figure is loss of the PAR characteristic and introduction of precession to the asteroid system. The increase in the angular velocity magnitude is mostly seen in the z-axis of the angular velocity, this change translates to a decrease of 25.2 seconds in the instantaneous rotation period in the moments after the impact. Despite the angular velocity acceleration, the overall angular momentum decreases from $|\mathbf{H}_0| = 7.88 \times 10^6 \text{ kg}\cdot\text{km}^2\cdot\text{s}^{-1}$ to $|\mathbf{H}^+| = 7.86 \times 10^6 \text{ kg}\cdot\text{km}^2\cdot\text{s}^{-1}$ (about 0.21%), a result that can be explained by more angular momentum being carried away by the ejecta than that introduced by the deflection. Figure 4.17 presents the precession introduced to the system due to the deflection event. Similarly to the results in Section 3.2, but in much larger scale, two phenomena can be observed in $\tilde{\psi}$: first the initial shift in angular velocity as a result of the introduction of momentum to the system, and second the existence of precession due to the misalignment between the new angular velocity and new principal inertia axes. The motion observed in the figures speaks to the evolving geopotential of the asteroid surface environment. Figure 4.18 presents Bennu's surface slopes prior to impact. In the Bennu kinetic impact case presented, the magnitude of rotation change and precession created are not sufficient to alter the geopotential environment, keeping the asteroid surface stable after deflection, and presenting the same surface slopes shown in Figure 4.18.

The required velocity change direction in this case is the incoming impactor direction, set to be parallel to the facet position (local interface location) at the moment of impact. The velocity change to the asteroid in required direction is $\Delta V_A = 2.674 \text{ mm}\cdot\text{s}^{-1}$, which is 99.6% of the overall velocity

⁴ In the asteroid body frame.

change applied on the asteroid.

The impact scenario off Itokawa's long axis is presented in Figures 4.19-4.20, it again shows the loss of the PAR characteristic. The impact interface location, centered at [1.0,-0.9] degrees has a facet position to facet normal angle of 12.6 degrees and a lever arm of 0.063 km. These figures show a substantially higher change in angular velocity and precession reached than the Bennu case and an increase in angular velocity, which is equivalent to 22.05 minutes (1322.7 seconds) reduced from the asteroid's instantaneous rotation period. Due to Itokawa's slow rotation period the substantial increase in angular velocity and introduction of precession are not sufficient to disturb the surface environment and change the surface accelerations or slopes. The overall change to angular momentum shows an increase from $|\mathbf{H}_0| = 1.068 \times 10^6 \text{ kg}\cdot\text{km}^2\cdot\text{s}^{-1}$ to $|\mathbf{H}^+| = 1.086 \times 10^6 \text{ kg}\cdot\text{km}^2\cdot\text{s}^{-1}$ (about 1.67%). The magnitude of velocity change in the required direction to the asteroid in this case is $\Delta V_A = 5.851 \text{ mm}\cdot\text{s}^{-1}$, which is 97.6% efficiency.

The impact off Itokawa's median axis is presented in Figures 4.21-4.22. The impact interface location in this case is centered at [82.4,-11.32] degrees with a facet position to facet normal angle of 9.92 degrees and a lever arm of 0.018 km. The increase in angular velocity in this case leads to a instantaneous rotation period decrease of 18.3 minutes (1097.1 seconds), smaller than the long axis case due to the reduced lever arm of the impact point. The initial angle change to the angular velocity vector is lower than the previous case (~ 4 vs. ~ 7 degrees), but similar in amplitude of precession. Similarly to the previous case the change in rotation regime is not sufficient to affect the surface accelerations and slopes. In this case the overall change to angular momentum shows an increase from the value as the previous case to $|\mathbf{H}^+| = 1.092 \times 10^6 \text{ kg}\cdot\text{km}^2\cdot\text{s}^{-1}$ which is about 2.32%. This increase is a slightly higher change than in the prior case despite a smaller increase in angular velocity, explained, similarly to the Bennu case, by angular momentum being taken away by the ejecta. The magnitude of velocity change in the required direction in this case is $\Delta V_A = 5.537 \text{ mm}\cdot\text{s}^{-1}$, which is 98.6% of the overall velocity change applied. This velocity change is also only 94.6% of that presented for the long axis case. That due to the added linear velocity of the debris from the asteroid rotation and its contribution to deflection.

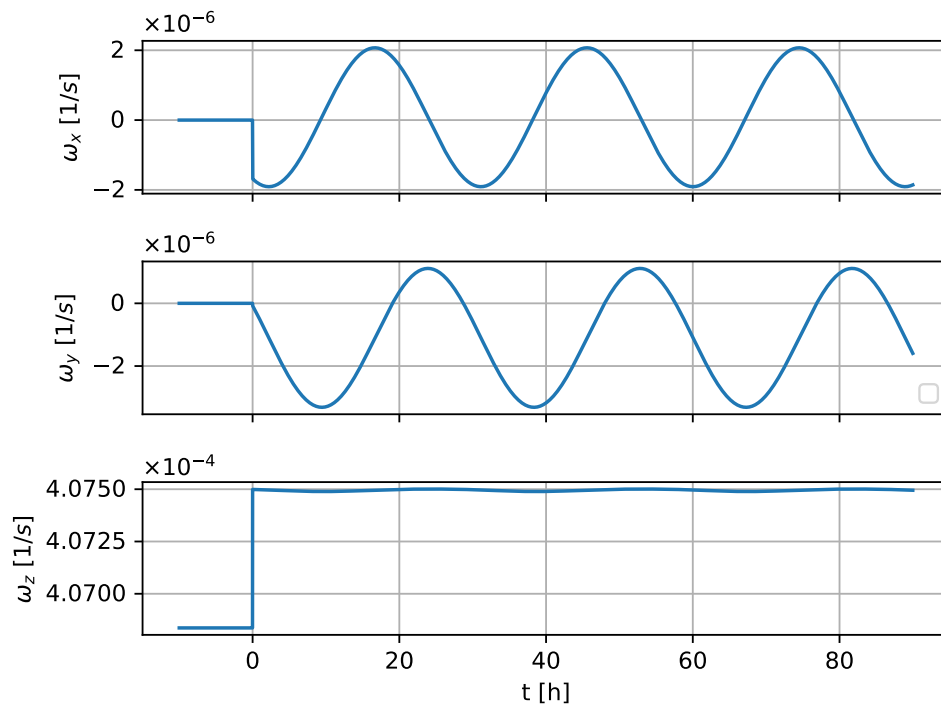


Figure 4.16: Benu angular velocity vector after kinetic interceptor impact

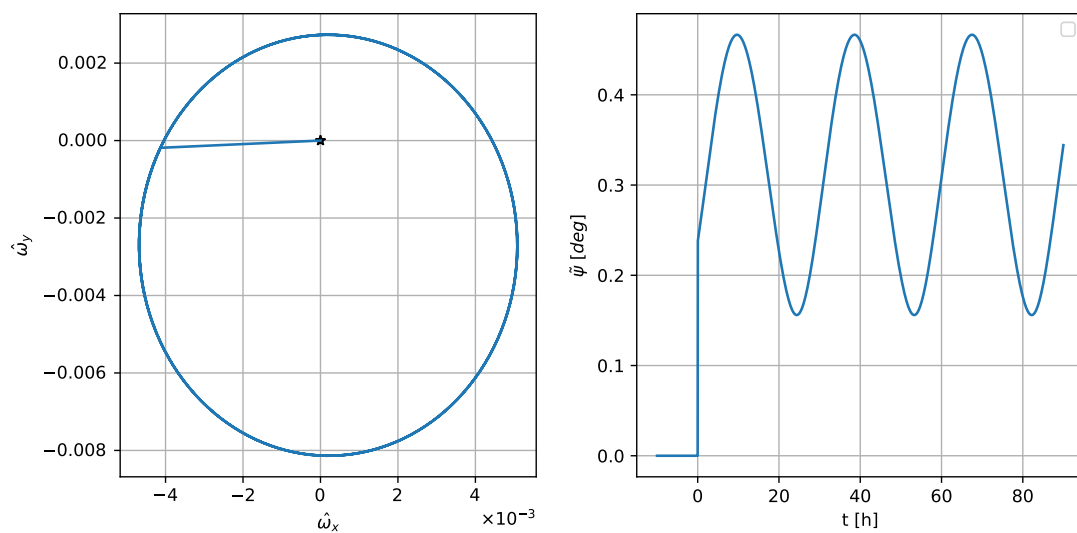


Figure 4.17: Benu angle between angular velocity after kinetic interceptor impact and angular velocity prior to impact

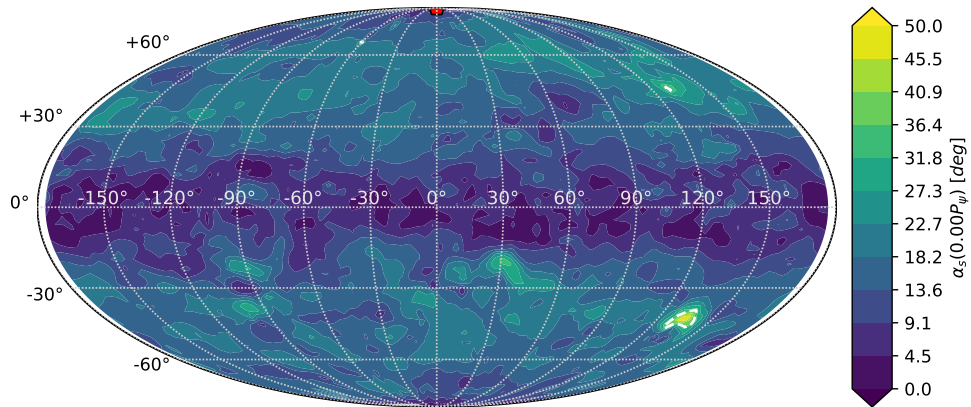


Figure 4.18: Surface slopes on Bennu prior to deflection effort

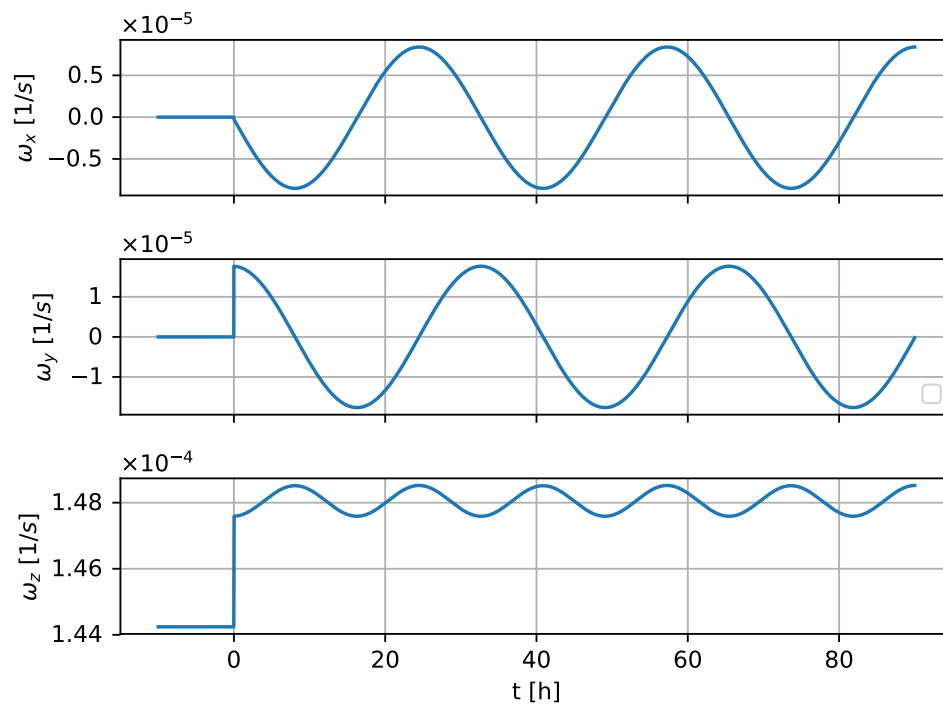


Figure 4.19: Itokawa angular velocity vector after kinetic interceptor impact along x-axis

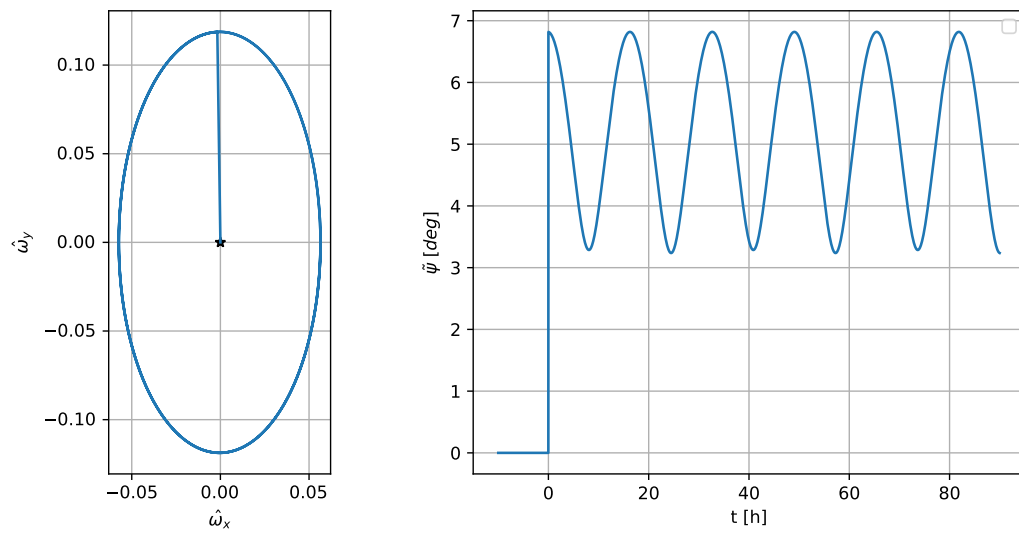


Figure 4.20: Itokawa angle between angular velocity after kinetic interceptor impact along x-axis and angular velocity prior to impact

The case presented in Figures 4.23-4.25 shows the rotational and surface state of the asteroid Bennu after nuclear detonation deflection. A substantial increase in angular velocity is observed in Figure 4.23, together with a large shift in angular velocity direction, and some introduced precession. The shift in angular velocity is equivalent to a reduction of 50.2 minutes (3010.0 seconds) from the instantaneous rotation period, or a speed up of 19.5% of Bennu's nominal rotation rate. This increase, together with the shift in angular velocity direction and introduction of precession lead to an excited surface dynamical environment. Figure 4.25 presents the surface slopes on Bennu through four phases of the precession cycle (notated as P_ψ), showing the evolution of surface slopes after the deflection effort. The pentagon seen in each heatmap indicates the projection of the body frame angular velocity vector on the surface. The dashed lines encompass surface areas with slopes higher than 35 degrees, the lowest threshold above which material motion is thought to be induced [10, 114]. The figure shows extensive areas on the surface reaching this threshold at some time in the rotation cycle, the overall surface percentage reaching these slopes in a cycle is 81.2%. This means that, at a minimum, material is expected to move on and off the surface as a result of the deflection. Furthermore, with this extent of extreme surface slopes it is expected that subsurface accelerations would also lead to a motion of material, motion that would probably lead to a reconfiguration of the asteroid structure or a complete disaggregation of it. The increase in angular momentum is equivalent to 22.47% of the nominal value presented for Bennu in the first case. The required direction velocity change to the asteroid system as a whole is $\Delta V_A = 189.7 \text{ mm}\cdot\text{s}^{-1}$, which is 99.6% of the overall velocity change.

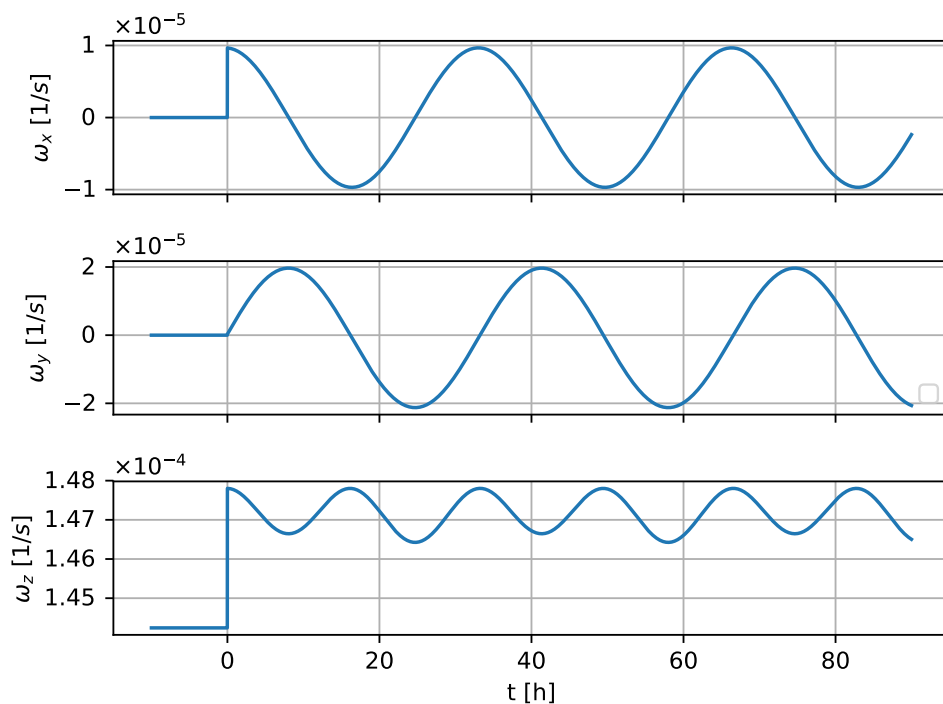


Figure 4.21: Itokawa angular velocity vector after kinetic interceptor impact along y-axis

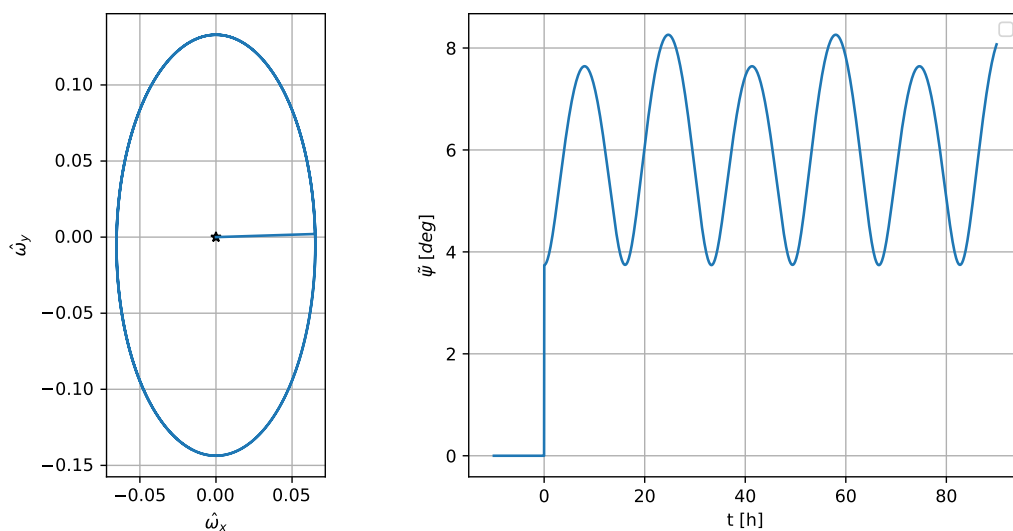


Figure 4.22: Itokawa angle between angular velocity after kinetic interceptor impact along y-axis and angular velocity prior to impact

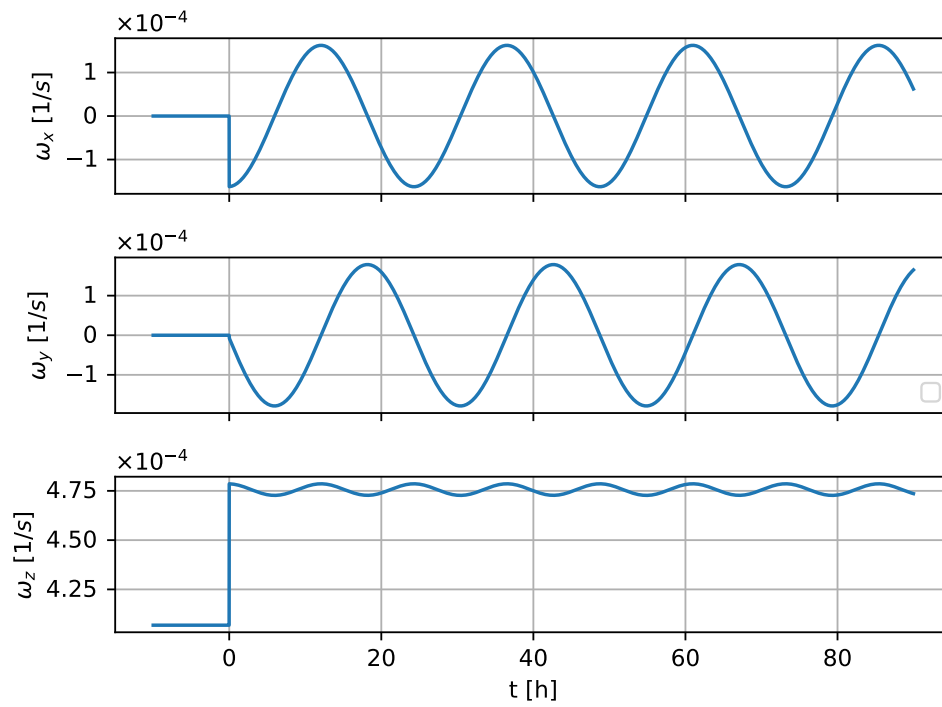


Figure 4.23: Benu angular velocity vector after nuclear detonation

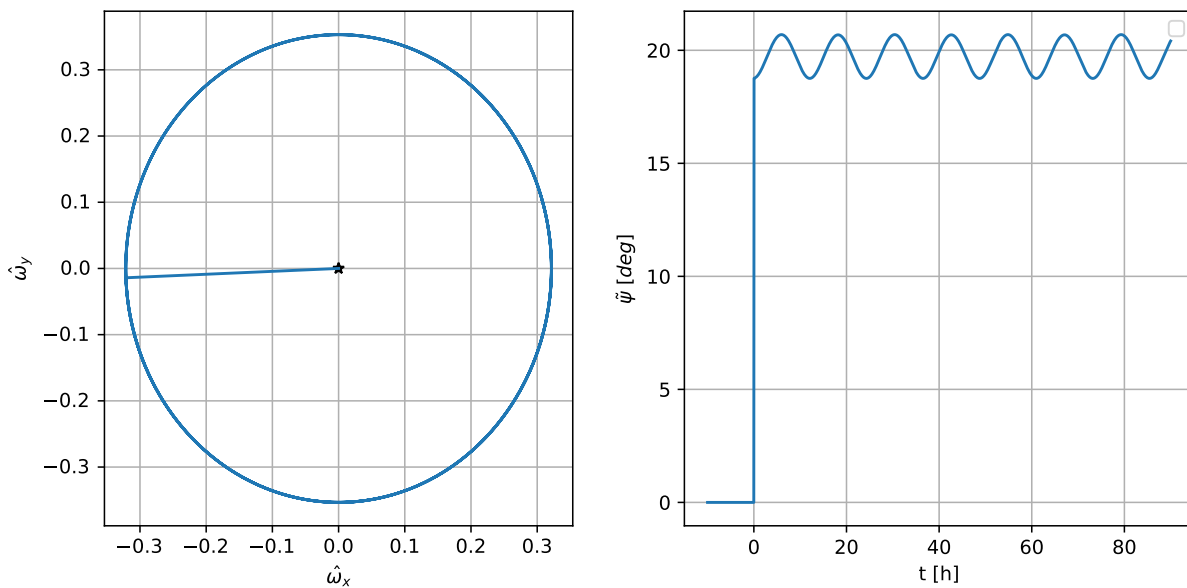


Figure 4.24: Benu angle between angular velocity after nuclear detonation and angular velocity prior to impact

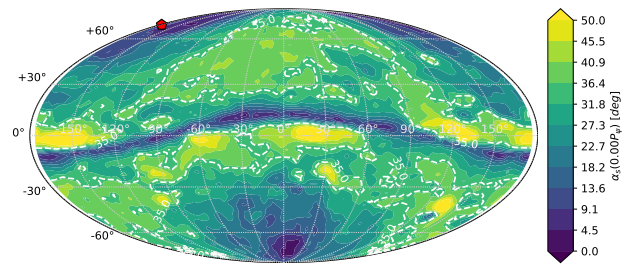
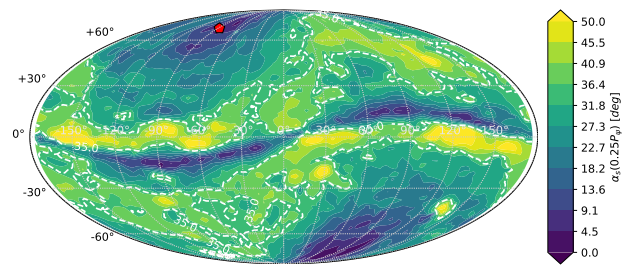
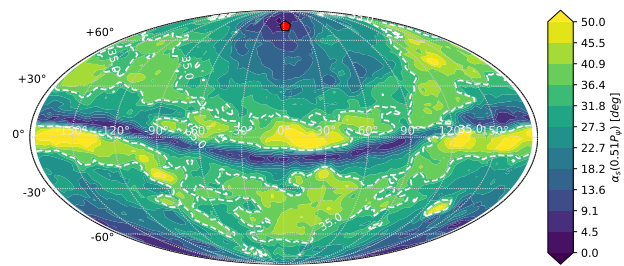
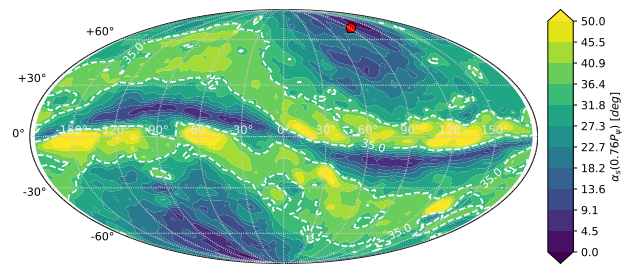
(a) $T = 0$ (b) $T = 0.25P_\psi$ (c) $T = 0.51P_\psi$ (d) $T = 0.76P_\psi$

Figure 4.25: Surface slopes on Bennu in a precession cycle after nuclear detonation

4.1.6.3 Considerations of deflection direction for complex shapes

The incoming deflection direction is examined in the following section, in which, similarly to Figures 4.4-4.6, the deflection outcomes are shown for all possible incoming directions (local zenith and azimuth) for specific locations on the polyhedral model asteroid.

Figures 4.26-4.28 present the deflection results for a kinetic impact on a polyhedral Bennu at longitude and latitude $[-84.4, 5.9]$ degrees, the same location shown in Figure 4.14a. The precession resulting for all deflection directions in Figure 4.26 shows a minimal precession impact direction similar to the facet location direction with a slight offset caused by the lost mass. When the precession map is compared with the angular velocity magnitude change map in Figure 4.27 the direction in which the resulting disturbance to asteroid rotation rate is minimal can be found. Alternatively, a direction that minimizes precession and reduces the asteroid rotation can also be seen. This type of deflection would change the asteroid rotation regime, but do so in such a way that reduces the possibility of rotational instability that could cause fission. Overall, the changes to rotation inflicted by deflection in all directions in the polyhedral Bennu case are minor and will not lead to instability of the asteroid structure or surface. However, when comparing the minimal rotation disturbance directions with the deflection efficiency, defined in Eqs. 4.14-4.15, the directions close to the facet location direction appear to best for maximizing the deflection. The maximum magnitude of efficient deflection is $2.690 \text{ mm}\cdot\text{s}^{-1}$, in zenith and azimuth $[20,270]$ degrees with respect to facet normal, or, due east. The magnitude of effective deflection in the facet normal direction is $2.679 \text{ mm}\cdot\text{s}^{-1}$, and in the facet position direction is $2.674 \text{ mm}\cdot\text{s}^{-1}$, within 0.5% of the maximum. The skewed direction of maximum efficacy is explained by the addition of linear velocity due to rotation, as discussed in Section 4.1.6.1, which for Bennu can add up to $0.1 \text{ m}\cdot\text{s}^{-1}$ to its $\sim 1.65 \text{ m}\cdot\text{s}^{-1}$ maximum equivalent launch velocity magnitude for this case. This result is not represented in the model presented in Eq. 4.5 and thus cannot be observed in Figure 4.6.

By examining the three deflection efficiency parameters presented in Figures 4.26-4.28 together a weighted optimal incoming deflection direction to be defined and further researched.

The results shown in this section for polyhedral shapes are similar in nature to those seen for the ellipsoids in Section 4.1.3 in change of asteroid spin and introduction of precession, however, discrepancies in the outcomes of specific deflection directions can be seen. Figure 4.29 presents the precession reached for kinetic impactor deflection interfaced at longitude and latitude [25,25] degrees, these results for a polyhedron mirror those for an ellipsoid presented in Figure 4.4. When comparing the two heat maps, the direction of minimal precession shifts from an zenith and azimuth [40,260] degrees for the ellipsoid to that of [55,240] in the polyhedral model. The maximum precession reached is also different: 2.9 degrees for an ellipsoid and 3.5 degrees for a polyhedral. These outcomes demonstrate the importance of shape representation of an asteroid when planning a deflection mission.

Figures 4.30-4.31 present the changes to asteroid rotation that result from the different deflection directions on the impact location along the long axis of Itokawa. The trends seen in the figures are similar to the Bennu results presented. However, the magnitudes of change are substantially higher with maximum precession reached at 30 degrees and changes in angular velocity magnitudes of up to 45% of the original value. Some of these changes can be attributed to the lower mass and smaller rotation rate of Itokawa compared to Bennu. But a major contributor to this outcome is Itokawa's elongated shape, which leads to a larger lever arm and applies more torque on the asteroid. Thus when planning deflection efforts of an elongated asteroid, the shorter side should be targeted for impact. The deflection efficiency results are similar in nature to those shown for Bennu, presenting a western skew due to the rotation.

The results of a nuclear detonation deflection off Bennu in the location presented in Figure 4.14a are seen in Figures 4.32-4.27. The precession heatmap in Figure 4.32 reaches values beyond 90 degrees (the nullified areas in the heatmap), meaning the asteroid transitioned from SAM to LAM rotation setting it in a tumble state which would lead to surface and structural instability. The change to angular velocity magnitude is presented in Figure 4.33, here a small region of directions which will keep the angular velocity magnitude at nominal values or lower is observed. However, impact in close to half of the directions in this region would lead to LAM rotation. Similarly to

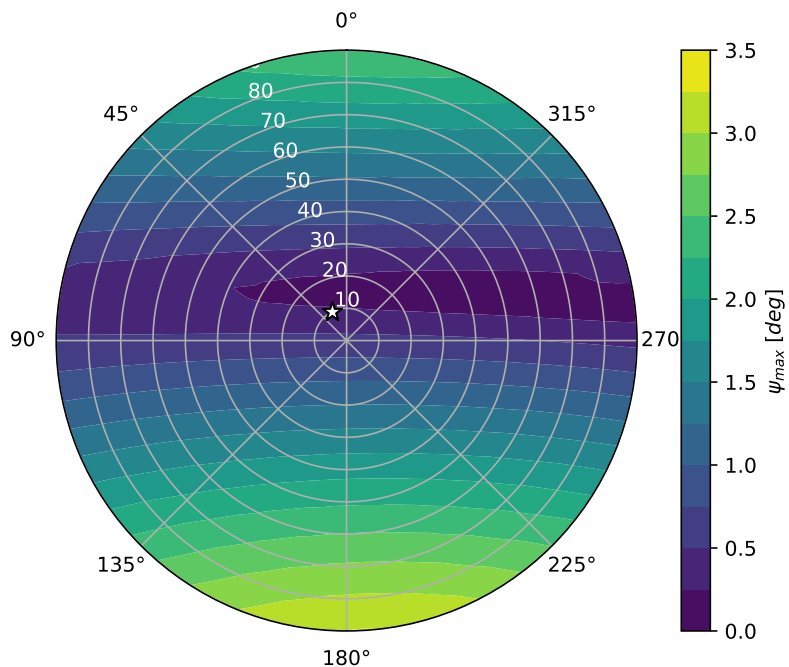


Figure 4.26: Precession reached for impacts located at $[-84.4, 5.9]$ degrees on a polyhedral Bennu, the star indicates the impactor direction parallel to the surface position

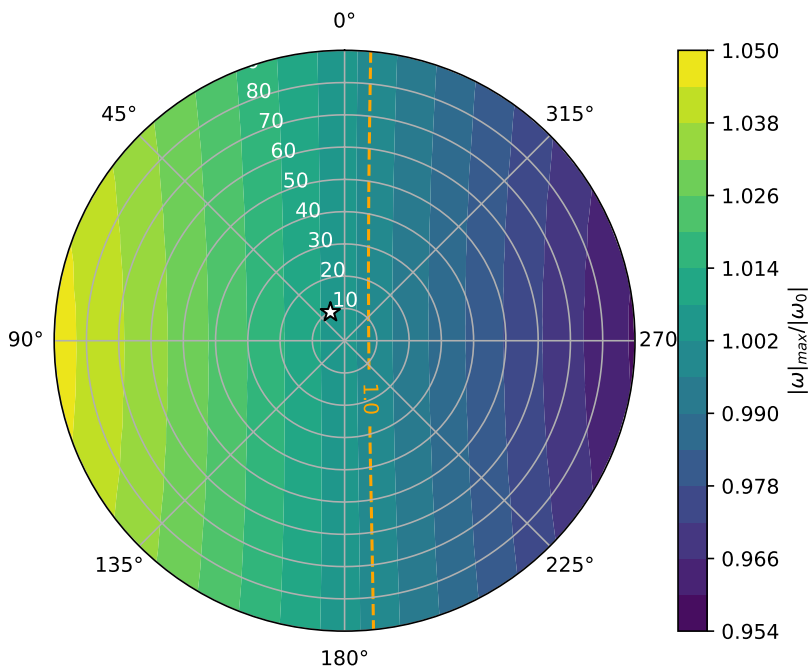


Figure 4.27: Change in angular velocity magnitude reached for impacts located at $[-84.4, 5.9]$ degrees on a polyhedral Bennu, the star indicates the impactor direction parallel to the surface position, the dashed line indicates equal values between $|\omega|_{max}$ and $|\omega_0|$

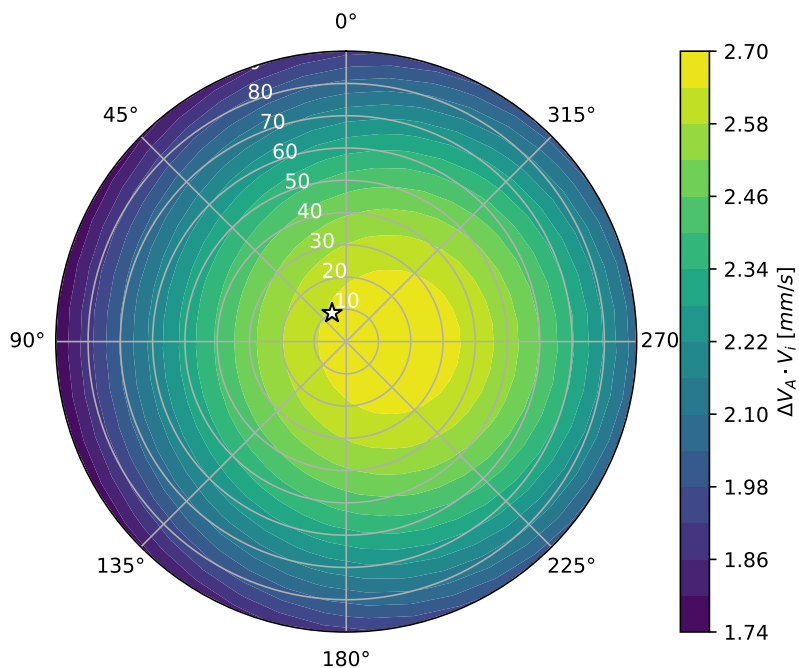


Figure 4.28: Δv reached for impacts located at $[-84.4, 5.9]$ degrees on a polyhedral Bennu, the star indicates the impactor direction parallel to the surface position

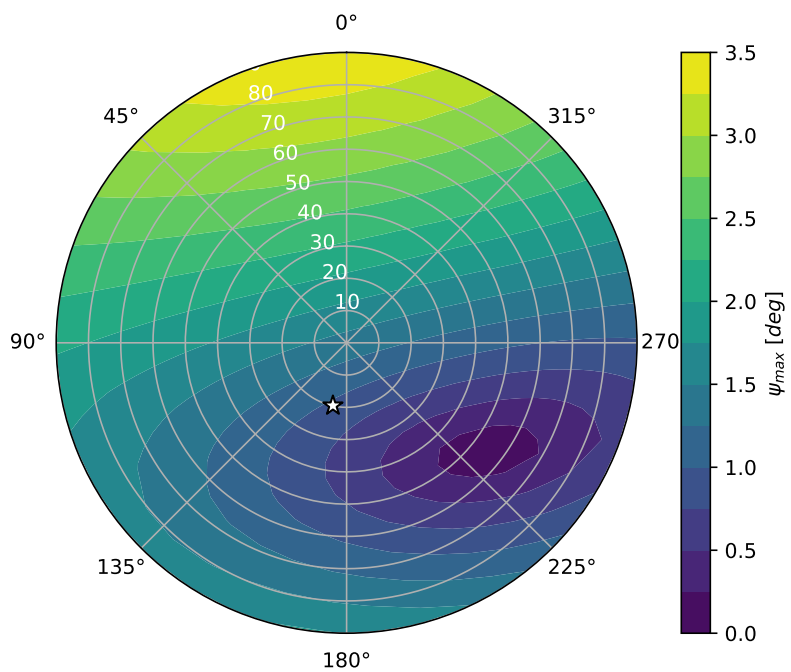


Figure 4.29: Precession reached for impacts located at $[25.0, 25.0]$ degrees on a polyhedral Bennu, the star indicates the impactor direction parallel to the surface position

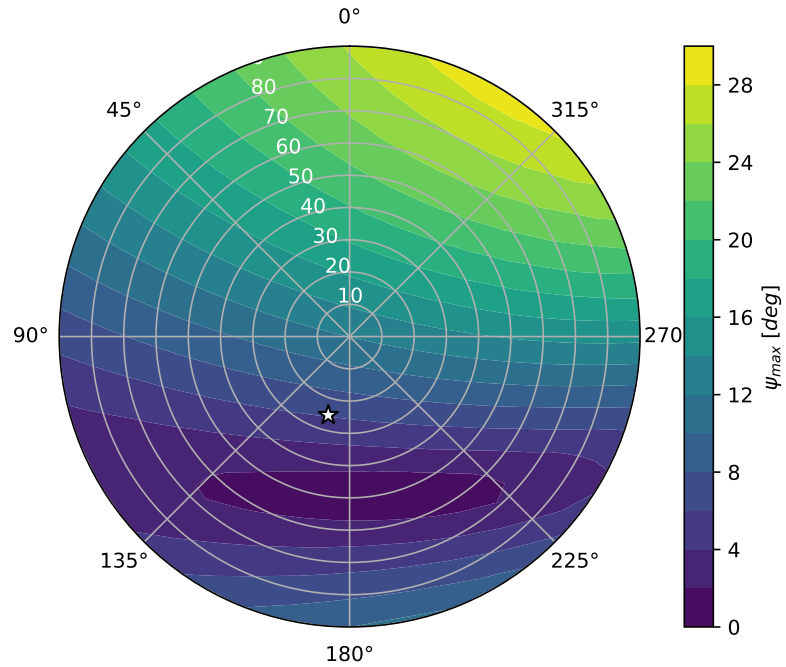


Figure 4.30: Precession reached for impacts located at $[1.0, -0.9]$ degrees on a polyhedral Itokawa, the star indicates the impactor direction parallel to the surface position

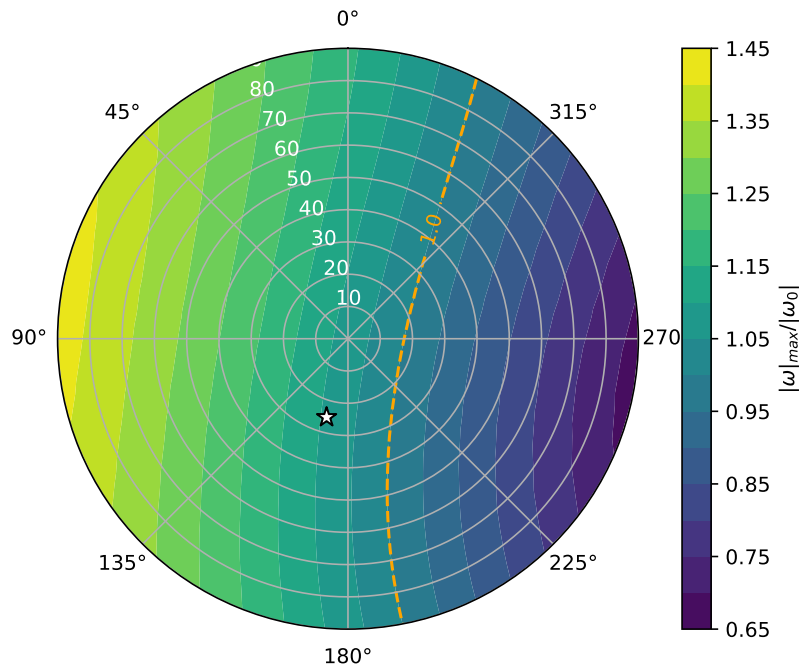


Figure 4.31: Change in angular velocity magnitude reached for impacts located at $[1.0, -0.9]$ degrees on a polyhedral Itokawa, the star indicates the impactor direction parallel to the surface position, the dashed line indicates equal values between $|\omega|_{max}$ and $|\omega_0|$

the previous cases, a direction in which the effects on rotation are minimized can be seen near the interface location position direction. Although, the minimized effect is an order of magnitude larger than in the kinetic impact case. The overall deflection efficiency is presented in Figure 4.34, it shows high correlation with the local normal (no eastern skew) because of the equivalent launch velocity is five orders of magnitude higher than the ejecta linear velocity induced from rotation.

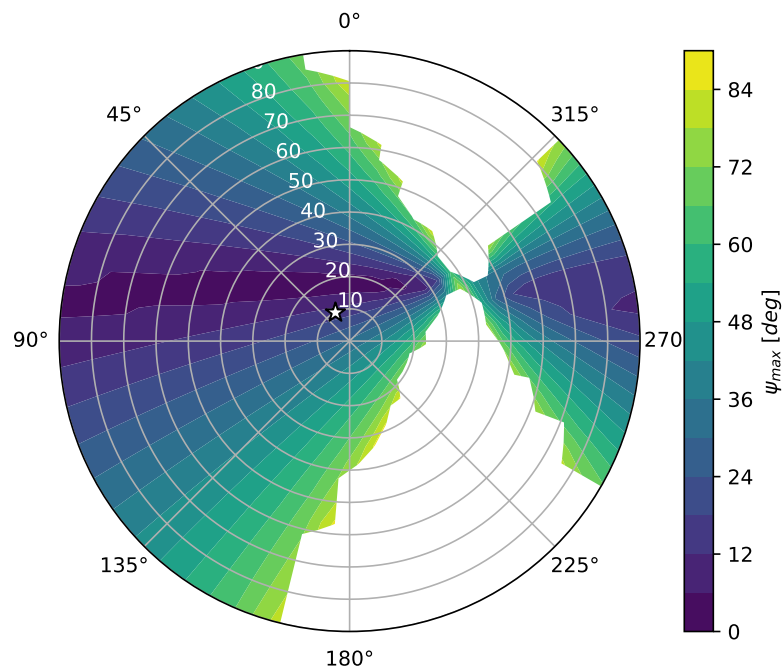


Figure 4.32: Precession reached for nuclear detonations located above $[-84.4, 5.9]$ degrees on a polyhedral Bennu, the star indicates the impactor direction parallel to the surface position, the white areas indicate directions in which the rotation has reached LAM and thus ψ cycles through $[0,360]$ degrees

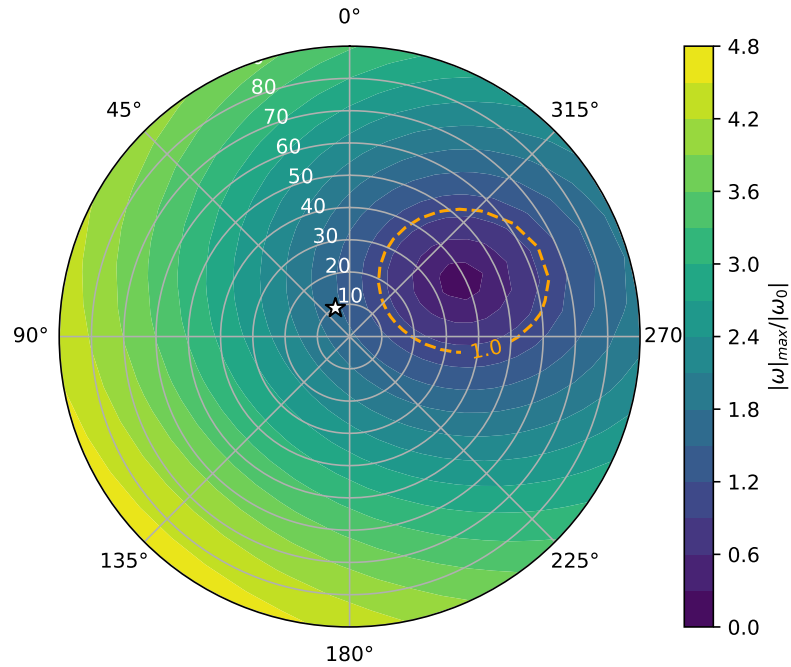


Figure 4.33: Change in angular velocity magnitude reached for nuclear detonations located above $[-84.4, 5.9]$ degrees on a polyhedral Bennu, the star indicates the impactor direction parallel to the surface position, the dashed line indicates equal values between $|\omega|_{max}$ and $|\omega_0|$

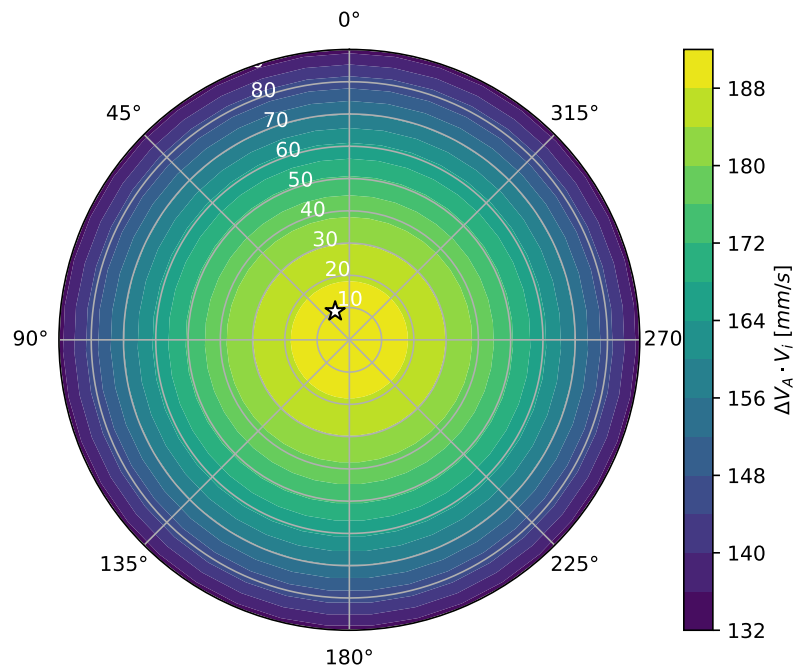


Figure 4.34: Δv reached for nuclear detonations located above $[-84.4, 5.9]$ degrees on a polyhedral Bennu, the star indicates the impactor direction parallel to the surface position

4.1.6.4 Deflection results for entire asteroid surface

The following section presents the deflection results for every facet on the asteroid polyhedral shape models. The deflection interface direction used for each facet is the facet center position vector. This direction is also defined as the required deflection direction, $\Delta\hat{\mathbf{V}}^*$. Figures 4.35-4.37 present these results for the polyhedral Bennu kinetic impactor case. The precession reached for every facet is seen in Figure 4.35. The lowest precession reached occurs for equatorial regions, specifically areas that appear to be large craters on the asteroid's equatorial ridge [132]. Polar region impacts also result in low precession angles. The change in angular velocity magnitude is presented in Figure 4.36. The heatmap shows a correlation between north to south ridge slopes and the magnitude of change to asteroid rotation. Impacts on east facing slopes reduce the asteroid's angular velocity magnitude and on west facing slopes increase it. All results for Bennu's surface (when impacts are in direction of local facet position) appear to be below the threshold to change the surface geopotential or risk the asteroid's structure. Figure 4.37 presents the efficiency of deflection for an impact on each facet of Bennu, here the efficiency is defined as $|\Delta\mathbf{V}_A^*|/|\Delta\mathbf{V}_A|$, which compares the facet specific asteroid velocity change reached with its required direction. The majority of facets present an efficiency of 99.5% or higher, but those that correlate to the maximum precession reached can get as low as 95% efficiency. Overall, the results show that multiple areas can be found on Bennu's surface that would minimize effect on rotation and lead to full deflection efficiency, this due to Bennu's near spherical shape.

The deflection results for every facet on the polyhedral Itokawa are presented in Figures 4.38-4.40. The results in Figure 4.38 show regions on both nodes which lead to precession of 30 degrees or higher, these areas face diagonally with respect to the equatorial plane of the asteroid, applying their lever arm to change the angular velocity vector direction. Similarly to Bennu, areas directly on the equator and near the poles can be found that lead to little precession. Figure 4.39 presents the change in angular velocity magnitude caused by the deflection effort. The figure shows a maximum change in asteroid rotation magnitude (over 20%) for impacting the side of node ends.

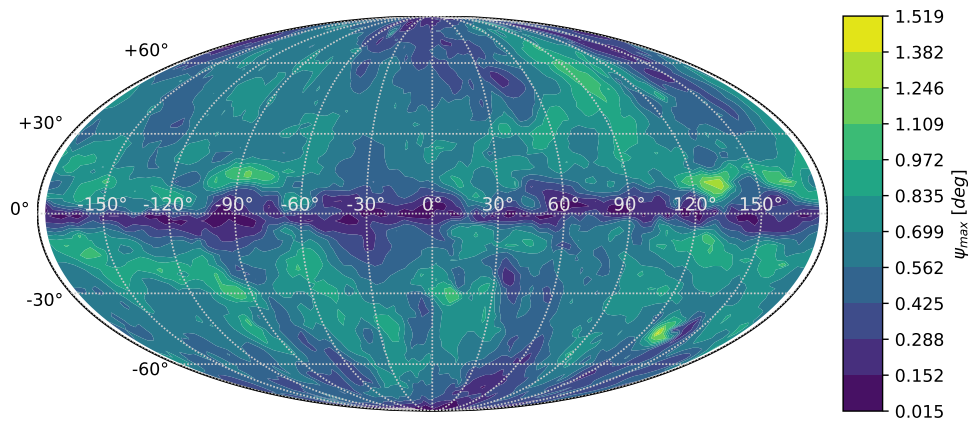


Figure 4.35: Precession reached for impacts in direction of facet position on all surface locations on a polyhedral Benu

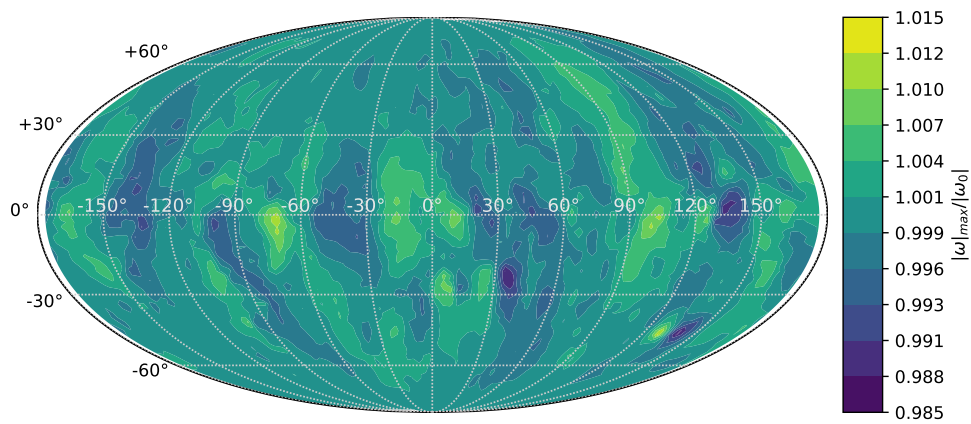


Figure 4.36: Change in angular velocity magnitude reached for impacts in direction of facet position on all surface locations on a polyhedral Benu

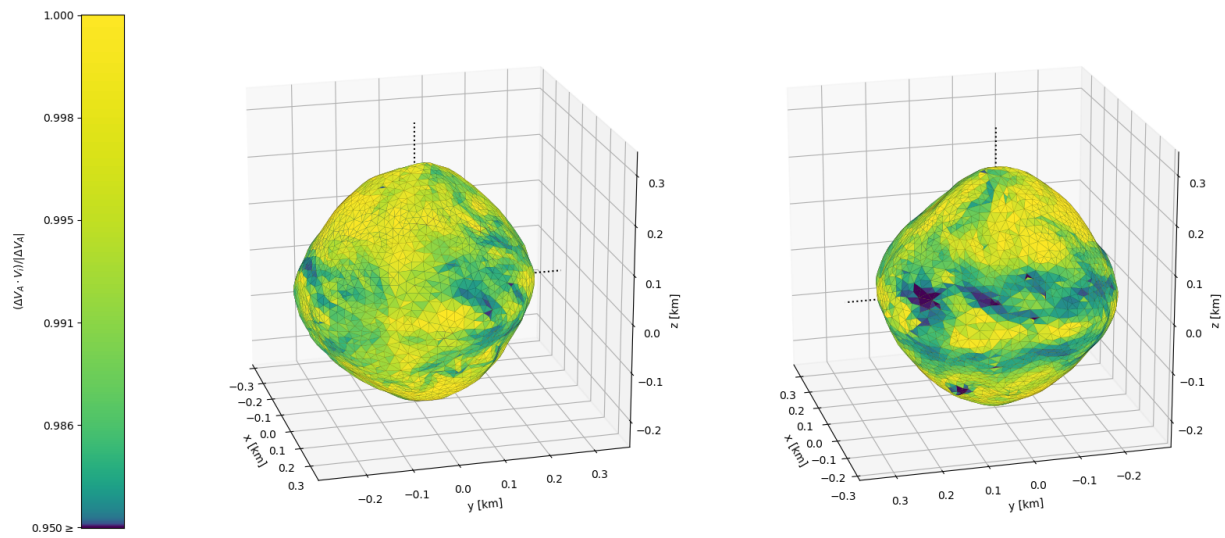


Figure 4.37: Δv efficiency reached for impacts in direction of facet position on all surface locations on a polyhedral Benu

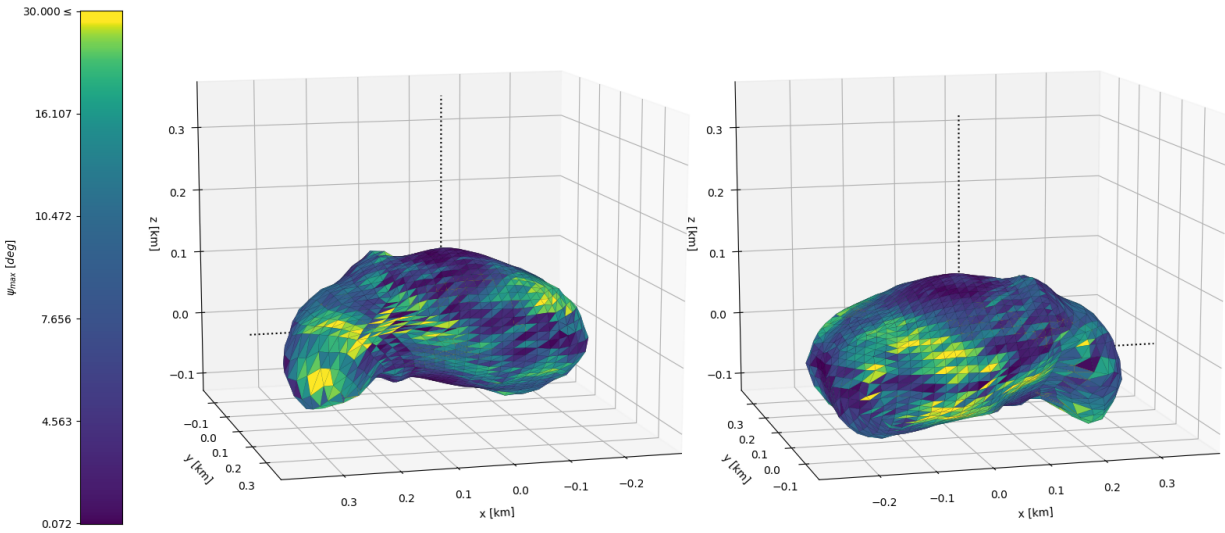


Figure 4.38: Precession reached for impacts in direction of facet position on all surface locations on a polyhedral Itokawa

Here a difference between impacting an east facing, rotation decelerating, node and impacting a west facing, rotation accelerating, node is seen. Figure 4.39 presents the impact deflection efficiency which reaches lower than 90% for node eastern or western impacts. When comparing the effect on rotation and impact efficiency it appears that the best location for deflection is in the middle of the asteroid long axis, in an equatorial or polar region.

Figures 4.41-4.42 present the deflection results for a nuclear detonation near the surface of polyhedral Bennu. Overall, the trends are similar to those seen for the Bennu kinetic impactor case, maximum precession values for impacts near the equator, and maximum spin up/down for west/east facing slopes. However, the change magnitudes are significantly higher, showing some regions that even reach LAM rotation for a detonation pointed in the interface facet position vector direction. The magnitude of change to the asteroid rotation can reach an increase of over 200%, a change that could cause complete rotational breakup of the asteroid [114]. Similarly to the previous cases, locations that provide minimum disturbance to rotation and maximum efficiency to deflection can be found. However, these areas can be near highly perturbing regions and require good accuracy in detonation direction.

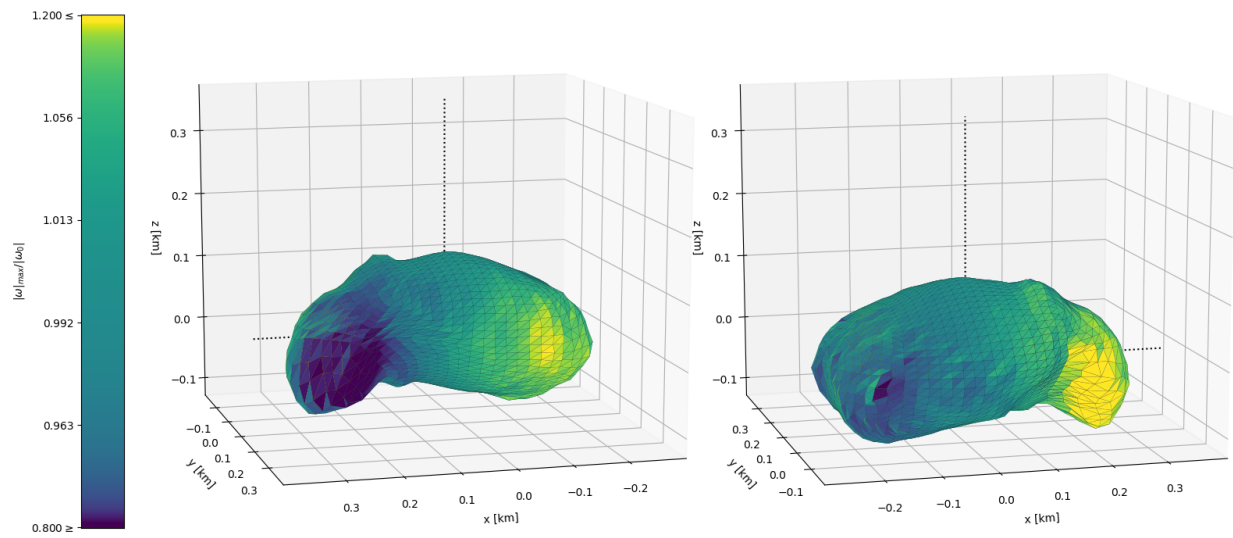


Figure 4.39: Change in angular velocity magnitude reached for impacts in direction of facet position on all surface locations on a polyhedral Itokawa

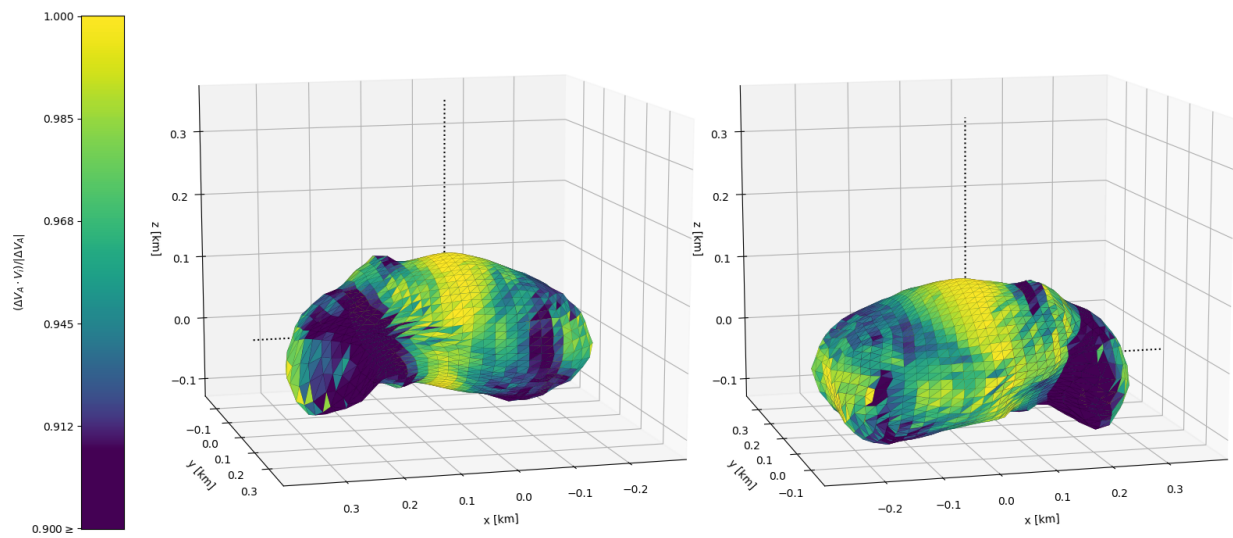


Figure 4.40: Δv efficiency reached for impacts in direction of facet position on all surface locations on a polyhedral Itokawa

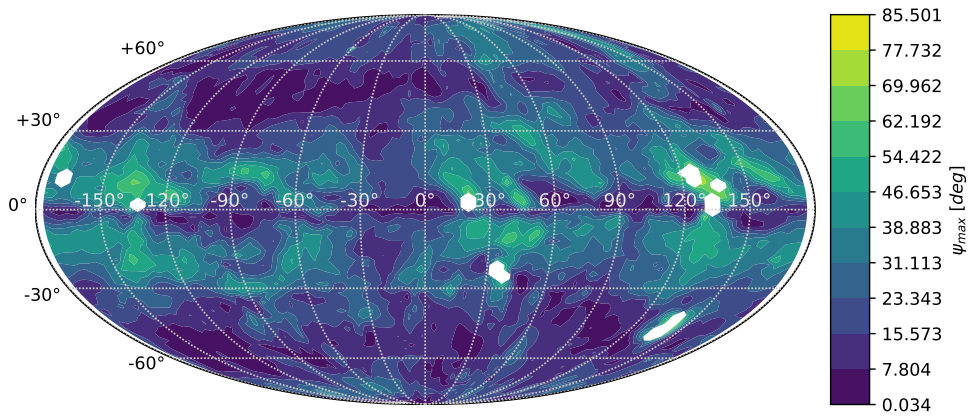


Figure 4.41: Precession reached for nuclear detonations in direction of facet position on all surface locations on a polyhedral Bennu

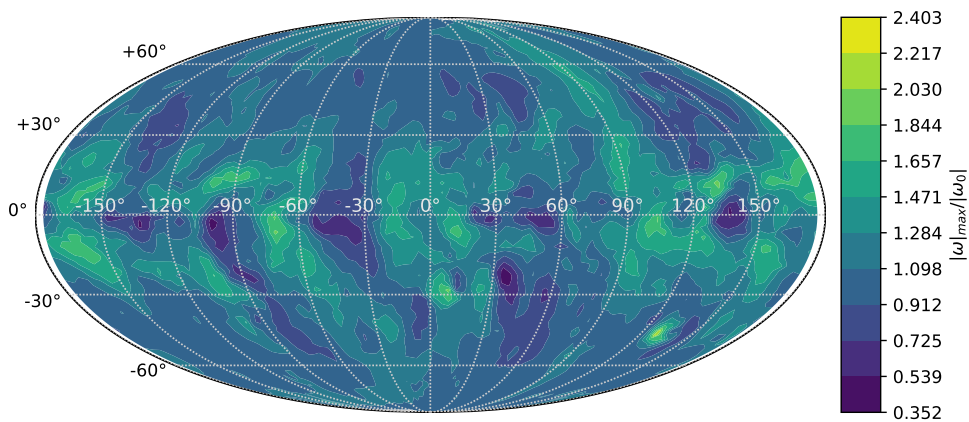


Figure 4.42: Change in angular velocity magnitude reached for nuclear detonations in direction of facet position on all surface locations on a polyhedral Bennu

4.1.7 Implications of the rotation - surface activity relationship on momentum transfer deflection

The work presented here demonstrates the effect deflection efforts would have on PHO rotation. It shows negligible effects in rotation and high efficiency of kinetic impact deflection on near-spherical asteroid shapes, such as Bennu. For elongated asteroids the effects on rotation are non-negligible and has the potential to disturb the asteroid rotation and structure. Additionally, a reduced efficiency is observed for some locations on the surface of the elongated asteroid. This reduced efficiency can be mitigated with proper planned margins or with advanced guidance which is capable of selecting the impact location during the approach phase. The effects on rotation of a nuclear detonation deflection on a near-spherical asteroid have been shown to be dramatic even when the deflection pointing is close to optimal. These effects on rotation have the potential to completely restructure or disaggregate the deflected asteroid and should be taken into consideration when planning such an operation. On the other hand, the deflection efficiency of this type of deflection scheme (nuclear on near-spherical) is high and provides the magnitude of ΔV required for short warning time deflection.

4.2 Mass driver deflection and additional applications

The dynamics of mass launch from PAR asteroid surfaces are derived in this section. These dynamics are then used to examine considerations in mass driver deflection. The section also presents and analyzes an operational orbital scheme for mass driver deflection.

4.2.1 Background

The previous section presented some risks related with single-shot deflection methods, kinetic interception and nuclear detonation, and implied the greatest risk related with these type of methods - an “all the eggs in one basket” approach. These methods provide the maximum deflection as early as possible: maximizing the deflection efficiency with respect to the asteroid time to MOID, but also posing only a single opportunity for deflection. If the deflection fails, an entirely new deflection mission needs to be conducted. Failure of such a mission could come from providing too little momentum, leading to an insufficient ΔV for the asteroid, from providing too much momentum, leading to asteroid fragmentation [150], or, as seen in the previous section, applying the momentum in such a way that provides rotational torque at cost to the asteroid ΔV and at risk of causing wide-scale fission of asteroid fragments. These fragments that could still be on a collision course with Earth, either as multiple threats to the planet, or as a reaggregated asteroid with little change in collision path [115].

The other deflection methods discussed in the introduction take longer to implement, but have the ability for course correction and pose little threat to the asteroid structural stability. In addition to the long implementation times, these spacecraft missions would usually require substantial amounts of fuel to be used in the deflection effort. For example Scheeres and Schwickart [68] proposed concept would use a continuous low thrust system (force lower than 1 Newton) that can deflect an asteroid given reasonable detection time frames (several years). This concept, however, would require de-spinning the asteroid or reorienting its spin in order to align the thrust vector in a specific inertial direction. Furthermore, Izzo [137] showed that by simply using the mass of

a lander-thruster required for deflection as a kinetic impactor counter mass, the deflection success chances are higher, making the added complexity of operating the lander unnecessary. Successive “single event” deflection methods that could bridge the intensity of a nuclear detonation or kinetic interception with the controllability of slower methods have been proposed as well [151].

A different approach to the lander-thruster concept has been suggested. This approach, dubbed as Mass Driver (MD) deflection, proposed by Olds et al. in their NASA Innovative Advanced Concepts (NIAC) report [69], suggests using material from the asteroid itself as kinetic propellant for deflection. This idea, which has been proposed by other advanced concept research studies as well [152, 71], only requires the thrusting mechanism to reach the asteroid surface. Thus, substantially reducing the launched mass of the deflection system and therefore expanding launch opportunities and trajectory design options. In addition, the proposed concepts rely on radioisotopic thermoelectric generators as a power source for in-situ operations, further reducing mass requirements and making these systems robust and flexible to a wide range of environments. Furthermore, the proposed concepts are inherently multi-agent based, providing redundancy to the system and allowing it to keep deflection efforts operational even if segments of the system have failed. Moreover, the discrete nature of MD thrusting detaches the asteroid’s rotation from the deflection problem by timing the mass ejections with the proper asteroid phase in its rotation. Specifically, the new type of robotic lander-rover presented by McMahon [152], the Area-of-Effect Soft (AoES) Robots, is a great example of a surface operations concept for MD deflection. These robots would be adapted for operations on asteroid surfaces, able to maneuver and manipulate objects in the unique micro-gravity environment. The AoES could potentially roam the surface of the deflected asteroid, pick up boulders of varied sizes, or volumes of regolith from various locations and launch them into defined hyperbolic trajectories, providing small ΔV increments to the deflection. These ΔV increments will allow for assessment and correction of the deflection effort.

4.2.2 Small deviations near principal axis rotation

This section will develop the linear approximated solution for torque free rotational motion around a general PAR body. The dynamic manipulations applied to the body in this section and those that follow are assumed to be instantaneous with respect to the body's rotation rate. This assumption is based on rotation periods several hours long and manipulations that are on the scale of several seconds for small bodies or several minute rotation periods and sub-second timeframes manipulations for spacecraft.

The system presented in this section can change its inertia tensor, its angular velocity, or both with small deviations around the nominal PAR state defined as $\boldsymbol{\omega}_N$ and $[I_N]$

$$\boldsymbol{\omega} = \boldsymbol{\omega}_N + \delta\boldsymbol{\omega} \quad (4.16)$$

$$[I] = [I_N] + [\delta I] \quad (4.17)$$

Here, the nominal angular velocity only has a z-axis element, $\boldsymbol{\omega}(t) = [0, 0, \omega_z]^T$, and the nominal inertia tensor is diagonal, $[I_N] = \text{diag}(I_x, I_y, I_z)$. It is important to note that while the angular velocity becomes time dependent in this case ($\delta\boldsymbol{\omega} = \delta\boldsymbol{\omega}(t)$), the inertia tensor remains constant between $[\delta I]$ shifts.

Inputting Eqs. 4.16 and 4.17 to Euler's equation (Eq. 2.6)

$$([I_N] + [\delta I])(\dot{\boldsymbol{\omega}}_N + \delta\dot{\boldsymbol{\omega}}) + (\boldsymbol{\omega}_N + \delta\boldsymbol{\omega}) \times ([I_N] + [\delta I])(\boldsymbol{\omega}_N + \delta\boldsymbol{\omega}) = \mathbf{0} \quad (4.18)$$

For simplicity of presentation the $_N$ notation is removed

$$([I] + [\delta I])(\dot{\boldsymbol{\omega}} + \delta\dot{\boldsymbol{\omega}}) + (\boldsymbol{\omega} + \delta\boldsymbol{\omega}) \times ([I] + [\delta I])(\boldsymbol{\omega} + \delta\boldsymbol{\omega}) = \mathbf{0} \quad (4.19)$$

The Euler equation shows that $\dot{\boldsymbol{\omega}} = \mathbf{0}$, leading to

$$([I] + [\delta I])\delta\dot{\boldsymbol{\omega}} + (\boldsymbol{\omega} + \delta\boldsymbol{\omega}) \times ([I] + [\delta I])(\boldsymbol{\omega} + \delta\boldsymbol{\omega}) = \mathbf{0} \quad (4.20)$$

which can be rewritten as

$$\begin{aligned} [I]\delta\dot{\boldsymbol{\omega}} + [\delta I]\delta\dot{\boldsymbol{\omega}} + \boldsymbol{\omega} \times [I]\boldsymbol{\omega} + \delta\boldsymbol{\omega} \times [I]\boldsymbol{\omega} + \boldsymbol{\omega} \times [\delta I]\boldsymbol{\omega} + \delta\boldsymbol{\omega} \times [\delta I]\boldsymbol{\omega} + \\ \boldsymbol{\omega} \times [I]\delta\boldsymbol{\omega} + \delta\boldsymbol{\omega} \times [I]\delta\boldsymbol{\omega} + \boldsymbol{\omega} \times [\delta I]\delta\boldsymbol{\omega} + \delta\boldsymbol{\omega} \times [\delta I]\delta\boldsymbol{\omega} = \mathbf{0} \end{aligned} \quad (4.21)$$

Under the small perturbations assumption all higher order δ elements are assumed zero

$$[I]\delta\dot{\boldsymbol{\omega}} + \boldsymbol{\omega} \times [I]\boldsymbol{\omega} + \delta\boldsymbol{\omega} \times [I]\boldsymbol{\omega} + \boldsymbol{\omega} \times [\delta I]\boldsymbol{\omega} + \boldsymbol{\omega} \times [I]\delta\boldsymbol{\omega} = \mathbf{0} \quad (4.22)$$

Because of the PAR property the $\boldsymbol{\omega} \times [I]\boldsymbol{\omega}$ element is nullified and the equation can be rewritten as

$$-[I]\delta\dot{\boldsymbol{\omega}} = \delta\boldsymbol{\omega} \times [I]\boldsymbol{\omega} + \boldsymbol{\omega} \times [\delta I]\boldsymbol{\omega} + \boldsymbol{\omega} \times [I]\delta\boldsymbol{\omega} \quad (4.23)$$

This dynamical equation can be used to propagate a rotating body's precession motion. Inputting the PAR nominal angular velocity leads to a system of linearized differential equations

$$\delta\dot{\omega}_x = \frac{\omega_z}{I_x} [(I_y - I_z)\delta\omega_y + \delta I_{yz}\omega_z] \quad (4.24)$$

$$\delta\dot{\omega}_y = \frac{\omega_z}{I_y} [(I_z - I_x)\delta\omega_x - \delta I_{xz}\omega_z] \quad (4.25)$$

$$\delta\dot{\omega}_z = 0 \quad (4.26)$$

For which the solution is

$$\begin{aligned} \delta\omega_x = & \left(\delta\omega_{x,0} - \frac{\delta I_{xz}\omega_z}{I_z - I_x} \right) \cos(\phi(t - t_0)) - \\ & \sqrt{\frac{I_y(I_z - I_y)}{I_x(I_z - I_x)}} \left(\delta\omega_{y,0} - \frac{\delta I_{yz}\omega_z}{I_z - I_y} \right) \sin(\phi(t - t_0)) + \frac{\delta I_{xz}\omega_z}{I_z - I_x} \end{aligned} \quad (4.27)$$

$$\begin{aligned} \delta\omega_y = & \left(\delta\omega_{y,0} - \frac{\delta I_{yz}\omega_z}{I_z - I_y} \right) \cos(\phi(t - t_0)) + \\ & \sqrt{\frac{I_x(I_z - I_x)}{I_y(I_z - I_y)}} \left(\delta\omega_{x,0} - \frac{\delta I_{xz}\omega_z}{I_z - I_x} \right) \sin(\phi(t - t_0)) + \frac{\delta I_{yz}\omega_z}{I_z - I_y} \end{aligned} \quad (4.28)$$

$$\delta\omega_z = \delta\omega_{z,0} \quad (4.29)$$

where

$$\phi = -\sqrt{\frac{\omega_z^2}{I_x I_y} (I_z - I_x)(I_z - I_y)} \quad (4.30)$$

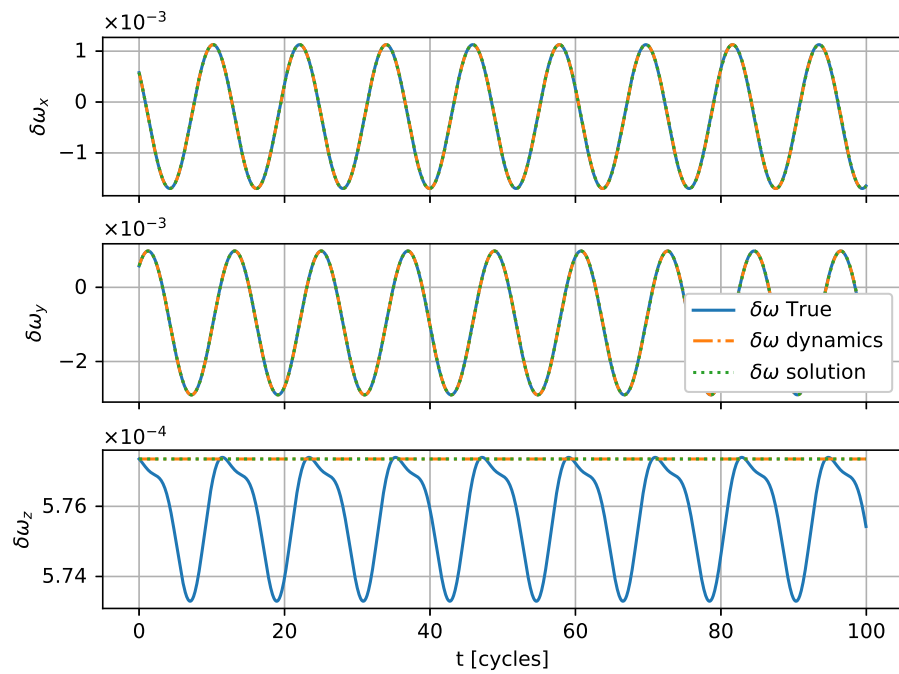
is the angular velocity oscillation frequency and $[\delta\omega_{x,0}, \delta\omega_{y,0}, \delta\omega_{z,0}]$ are initial deviations to the angular velocity at time t_0 .

Figure 4.43a compares the true deviation to the linearized differential equations (Eqs. 4.24-4.26) and the linearized solution (Eqs. 4.27-4.29) for 100 cycles. The state is propagated with a fixed (unitless) nominal angular velocity $\omega_N = [0, 0, 1.0]^T$, a nominal ellipsoidal 5-3-2 ratio mass distribution, and a total (unitless) mass of $M = 10000$. The initial angular velocity deviation is $[\frac{0.001}{\sqrt{3}}, \frac{0.001}{\sqrt{3}}, \frac{0.001}{\sqrt{3}}]^T$ and the inertia tensor deviation is of a point mass located at $[1.5, 1.2, 1.0]^T$ and a value of $dM = 0.0002M$. Figure 4.43b presents the error between the true deviation and the linearized solution defined as

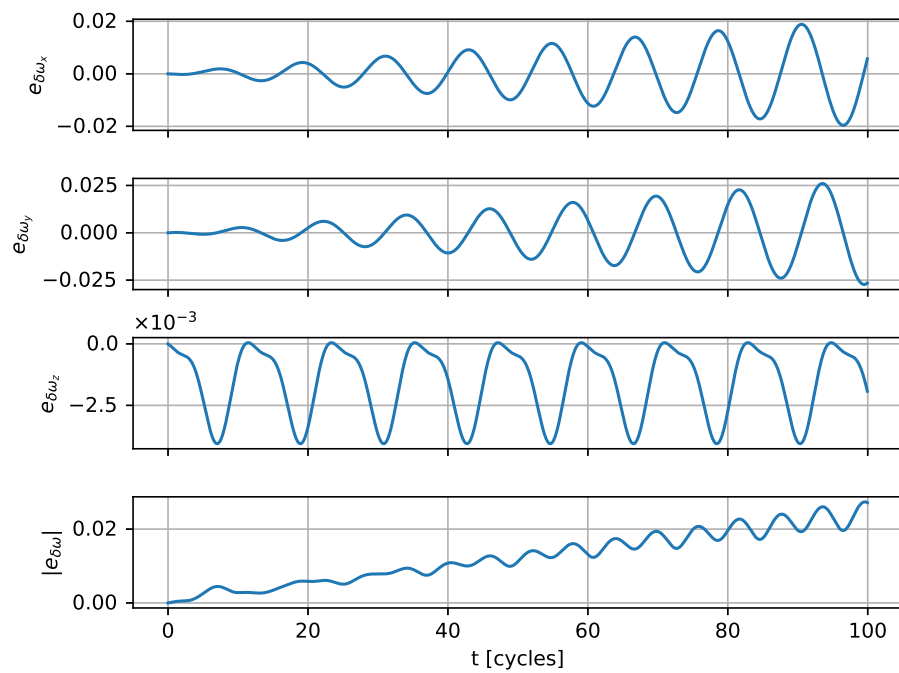
$$e_{\delta\omega} = \frac{\delta\omega_{True} - \delta\omega}{|\delta\omega_0|} \quad (4.31)$$

The figures show a good correlation between the true and linearized solutions, with an error magnitude that remains less than 3% of the initial deviation after 100 cycles. The deviation oscillation in the z-axis is not modeled in the linearized propagation and solution. However, this z-axis deviation is 3 orders of magnitude smaller than the initial deviation.

A more generalized view of the deviation error can be seen in Figure 4.44, which presents maps of the maximum errors reached after 100 cycles. In addition to the ellipsoid presented in Figure 4.44a a near-spherical 1.1-1.05-1.0 ratio body is examined in Figure 4.44b. Both bodies are subject to an initial angular velocity deviation in the $[\frac{1}{\sqrt{3}}, \frac{1}{\sqrt{3}}, \frac{1}{\sqrt{3}}]^T$ direction with magnitudes varying from $|\omega_N|$ to $10^{-8} \times |\omega_N|$. The point mass located at $[1.5, 1.2, 1.0]^T$ varies in value between $10^{-6.5} \times M$ and $0.32M$. The map and all axes in it are presented in a logarithmic scale. The bottom horizontal axis in the figure shows the determinant ratio between the nominal inertia tensor and the deviation tensor. The top horizontal axis correlates to the deviation inertia tensor and shows the ratio between the point mass and nominal shape mass. The vertical axis shows the ratio between the initial deviation magnitude and the nominal angular velocity magnitude. The figures show a region in which the deviation and nominal state ratios lead to small errors between the true and linearized deviations. The largest error regions are seen at small angular velocity deviation but large inertia tensor deviation, an outcome which is explained by the error magnitude reflecting the change from initial deviation. The small error region (less than 5% of initial value) for the near-spherical body



(a) Deviation propagation



(b) Deviation error

Figure 4.43: Propagation comparison of true and linearized states

reaches higher angular velocities than the near spherical error region. However, the ellipsoid reaches smaller errors for smaller initial angular velocity deviations.

When examining the linearized solutions in Eqs. 4.27-4.29 further, the first order precession frequency can be seen to only depend on the nominal principal inertia axes and nominal angular velocity. As seen in Figure 4.43a Eq. 4.29 shows the linearized solution in the z-axis as constant at the initial deviation value. The solutions also show that the first order precession can be nullified with proper adjustment of the off-axis xz and yz inertia tensor deviations.

4.2.2.1 Spacecraft small precession mitigation using inertia tensor adjustment

Using the solution in Eqs. 4.27-4.29 a body's inertia tensor can be adjusted in order of reducing small precession motion. For a spacecraft this mechanism would be similar to the damping mechanism used on spin-stabilized spacecraft [153], but without the energy loss associated with such a mechanism. Such a device could be as simple as a small mass placed on a platform outside of the xy plane with the ability to relocate itself on the x and y axes. A similar concept has been proposed for solar-sail attitude control using two masses moving along rails between the sail segments [154]. For any precession cancellation system the sinusoidal coefficients in Eqs. 4.27-4.29 would need to be nullified

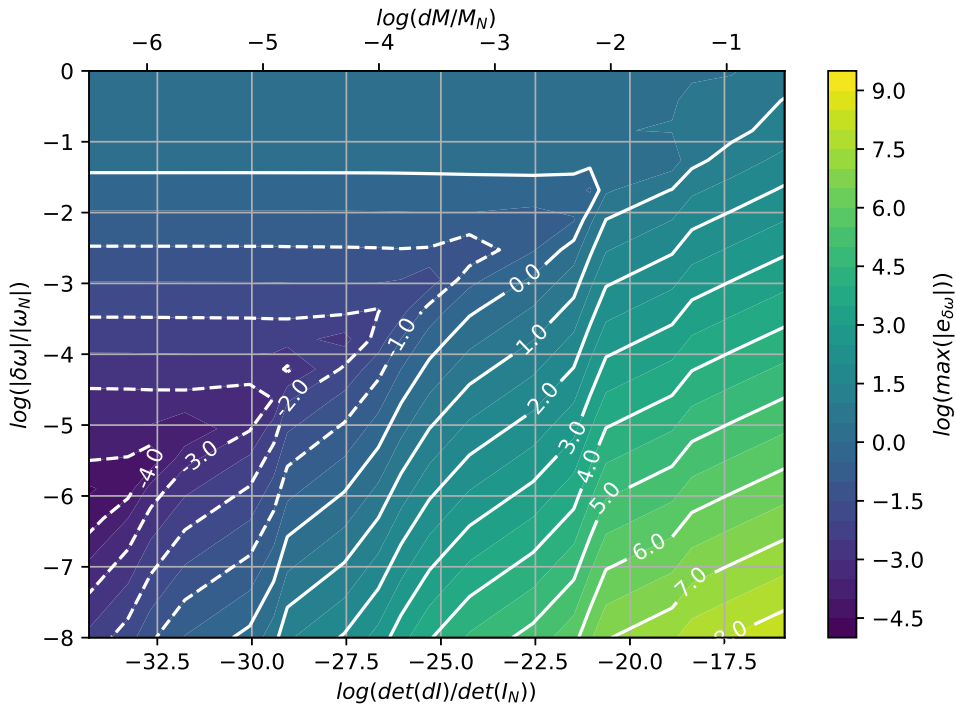
$$\delta\omega_x(t = t_{[\delta I]}) - \frac{\delta I_{xz}\omega_z}{I_z - I_x} = 0 \quad (4.32)$$

$$\delta\omega_y(t = t_{[\delta I]}) - \frac{\delta I_{yz}\omega_z}{I_z - I_y} = 0 \quad (4.33)$$

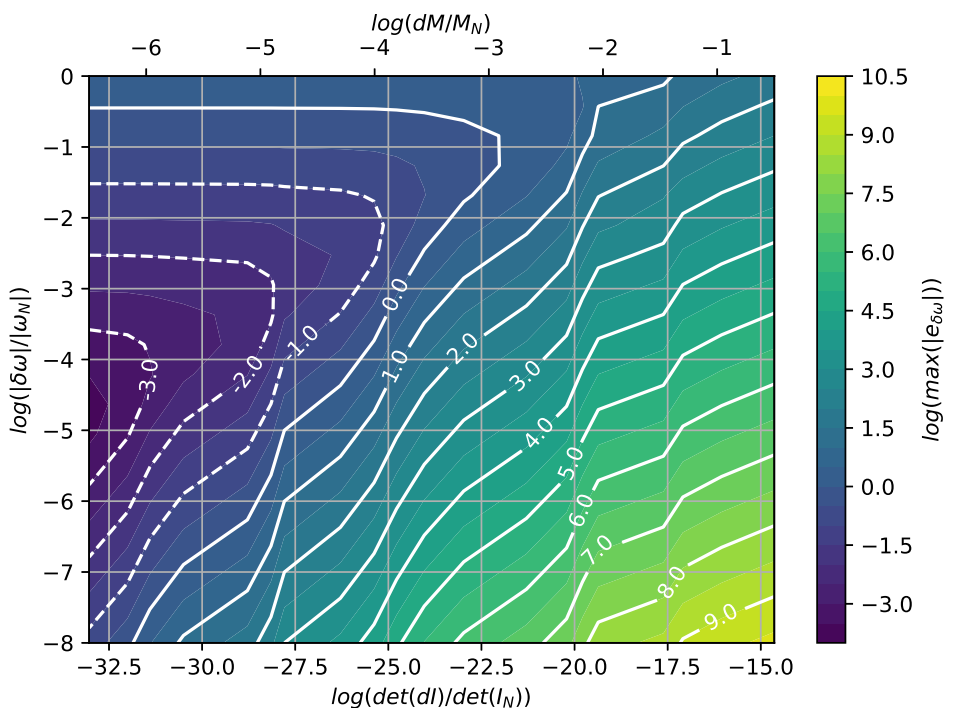
where the $\delta\omega$ values would be at the time of the inertia deviation adjustment. Which values would be

$$\delta I_{xz} = \delta\omega_x(t_{[\delta I]}) \frac{I_z - I_x}{\omega_z} \quad (4.34)$$

$$\delta I_{yz} = \delta\omega_y(t_{[\delta I]}) \frac{I_z - I_y}{\omega_z} \quad (4.35)$$



(a) Ellipsoid



(b) Near spherical

Figure 4.44: Deviation error between propagated and linearized solutions

Using a point mass with a fixed, non-zero, z_{dM} value the location change would be

$$\delta x_{dM} = -\delta\omega_x(t_{[\delta I]}) \frac{I_z - I_x}{\omega_z} \frac{1}{z_{dM} dM} \quad (4.36)$$

$$\delta y_{dM} = -\delta\omega_y(t_{[\delta I]}) \frac{I_z - I_y}{\omega_z} \frac{1}{z_{dM} dM} \quad (4.37)$$

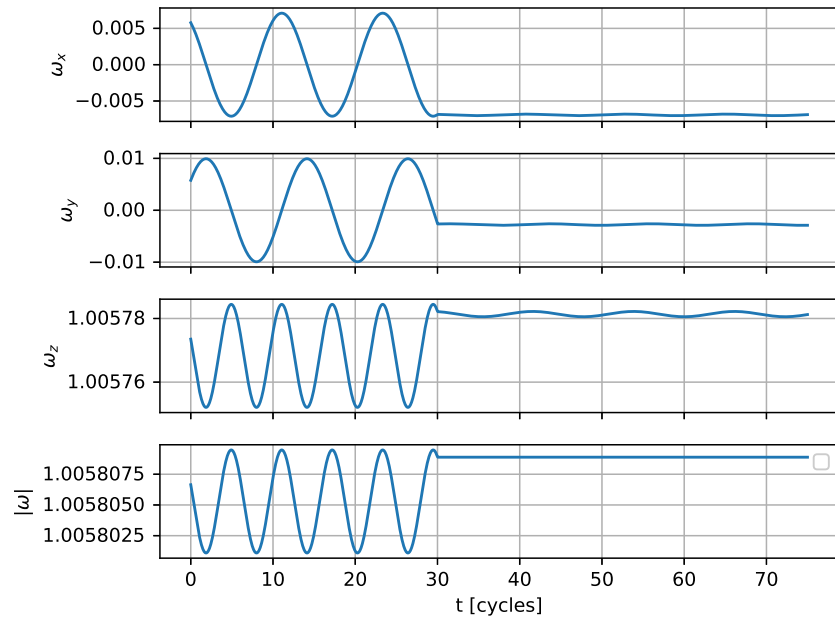
Using a small point mass the ellipsoid presented in the previous section is adjusted to cancel the precession motion. Figure 4.45 presents the precessing ellipsoid with an initial angular velocity deviation of $[\frac{0.01}{\sqrt{3}}, \frac{0.01}{\sqrt{3}}, \frac{0.01}{\sqrt{3}}]^T$ and a point mass of $0.01M$ initially located at $[0, 0, 1.0]^T$. At time 30 cycles the point mass is moved according to Eqs. 4.36 - 4.37 to location $[0.718, 0.066, 1.0]^T$. The resulting change in out-of-nominal motion leads to a deviation $\sim 95\%$ smaller seen in Figure 4.45b. Figure 4.45a also shows that despite the z-axis not being properly modeled in the linearized solution it too is adjusted to reduce fluctuations by 85% .

4.2.3 Asteroid rotation manipulation

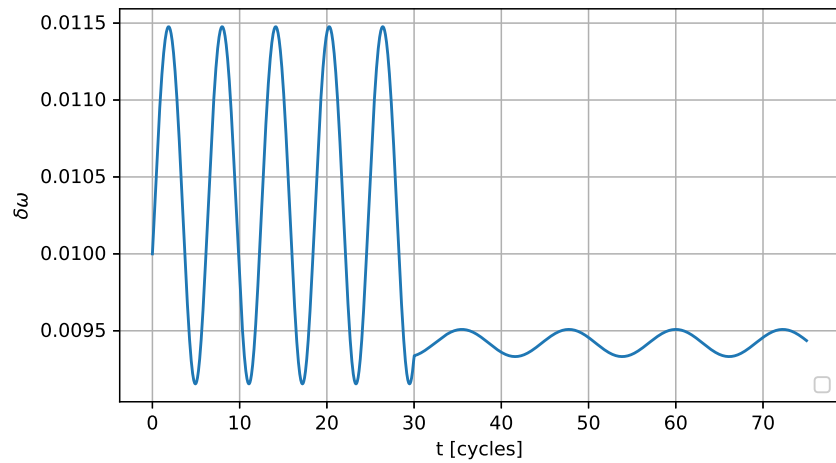
The small deviation solutions derived in the previous section can be applied to scenarios of PAR asteroids and boulders on their surfaces. For example a 5.2 meter mean diameter boulder (122 tons) placed on Bennu's equator has a mass ratio in order of magnitude of 10^{-6} and an inertia tensor determinant ratio in order of magnitude of 10^{-21} . Launching such a boulder off the surface of the asteroid at $1 \text{ m}\cdot\text{s}^{-1}$ would cause a deviation in angular velocity in order of magnitude of 10^{-6} of the original angular velocity magnitude. The following section expands the linearized solution in Eqs. 4.27-4.28 to reflect deviations in angular velocity and inertia tensor in scenarios of boulder launches off asteroids.

Section 2.3.2 shows the state of asteroid model angular velocity at the moment of a boulder launch off the surface. This angular velocity value is reached through the angular momentum equilibrium in Eq. 2.23. Rewriting the angular momentum equilibrium in terms of inertia tensors and body angular velocities in the inertial frame (while minimizing the notation for simplicity) leads to

$$[I^+] \boldsymbol{\omega}^+ = [I^-] \boldsymbol{\omega}^- - [I_B] \boldsymbol{\omega}^- - M_B \mathbf{R}_B \times \dot{\mathbf{R}}_B^+ \quad (4.38)$$



(a) Overall angular velocity



(b) Deviation from principal axis rotation

Figure 4.45: Corrected rotation state of slightly precessing spacecraft

The boulder center of mass velocity can be presented as in Eq. 4.12

$$\dot{\mathbf{R}}_B^+ = \boldsymbol{\omega}^- \times \mathbf{R}_B + \Delta \mathbf{V}_B \quad (4.39)$$

where $\Delta \mathbf{V}_B$ is the launch velocity added to the boulder's rotating frame velocity.

Using the notation convention presented in Eqs. 4.16-4.17, defining $\boldsymbol{\omega}^+ = \boldsymbol{\omega}$ and $[I^+] = [I]$, adding a $_0$ notation to the angular velocity deviation element to account for the equilibrium only existing at the moment of launch, removing the $_N$ notation for simplicity, and inputting Eqs. 4.16,4.17, and 4.39 as well as the relationship between $[\delta I]$, $[I_B]$ and \mathbf{R}_B as $[\delta I] = -[I_B] + M_B[\tilde{\mathbf{R}}_B][\tilde{\mathbf{R}}_B]^T$ into Eq. 4.38, and removing elements which cancel each other leads to

$$[I]\delta\boldsymbol{\omega}_0 - [I_B]\delta\boldsymbol{\omega}_0 + M_B[\tilde{\mathbf{R}}_B][\tilde{\mathbf{R}}_B]^T\delta\boldsymbol{\omega}_0 = -M_B\mathbf{R}_B \times \Delta \mathbf{V}_B \quad (4.40)$$

Using the set of PAR small perturbation assumptions the $[I_B]\delta\boldsymbol{\omega}_0$ and $M_B[\tilde{\mathbf{R}}_B][\tilde{\mathbf{R}}_B]^T\delta\boldsymbol{\omega}_0$ elements are nullified and Eq. 4.40 becomes

$$[I]\delta\boldsymbol{\omega}_0 = -M_B\mathbf{R}_B \times \Delta \mathbf{V}_B \quad (4.41)$$

Eq. 4.41 can be expanded to a set of equations in the principal-axis body frame

$$\delta\omega_{x,0} = \frac{M_B}{I_x} [-r_{B_y}\Delta v_{B_z} + r_{B_z}\Delta v_{B_y}] \quad (4.42)$$

$$\delta\omega_{y,0} = \frac{M_B}{I_y} [-r_{B_z}\Delta v_{B_x} + r_{B_x}\Delta v_{B_z}] \quad (4.43)$$

$$\delta\omega_{z,0} = \frac{M_B}{I_z} [-r_{B_x}\Delta v_{B_y} + r_{B_y}\Delta v_{B_x}] \quad (4.44)$$

Here, and throughout the rest of Section 4.2, lower-case vectors represent the principal-axis body frame and upper-case vectors represent the inertial frame. Inputting the inertia tensor deviation $[\delta I] = -[I_B] + M_B\mathbf{r}_B \times \mathbf{r}_B \times$ into the linearized solution in Eqs. 4.27-4.29 leads to

$$\begin{aligned} \delta\omega_x = & \left(\delta\omega_{x,0} + \frac{(I_{B,xz} - M_B r_{B,x} r_{B,z})\omega_z}{I_z - I_x} \right) \cos(\phi(t - t_0)) - \\ & \sqrt{\frac{I_y(I_z - I_y)}{I_x(I_z - I_x)}} \left(\delta\omega_{y,0} + \frac{(I_{B,yz} - M_B r_{B,y} r_{B,z})\omega_z}{I_z - I_y} \right) \sin(\phi(t - t_0)) - \frac{(I_{B,xz} - M_B r_{B,x} r_{B,z})\omega_z}{I_z - I_x} \end{aligned} \quad (4.45)$$

$$\delta\omega_y = \left(\delta\omega_{y,0} + \frac{(I_{B,yz} - M_B r_{B,y} r_{B,z})\omega_z}{I_z - I_y} \right) \cos(\phi(t - t_0)) + \sqrt{\frac{I_x(I_z - I_x)}{I_y(I_z - I_y)}} \left(\delta\omega_{x,0} + \frac{(I_{B,xz} - M_B r_{B,x} r_{B,z})\omega_z}{I_z - I_x} \right) \sin(\phi(t - t_0)) - \frac{(I_{B,yz} - M_B r_{B,y} r_{B,z})\omega_z}{I_z - I_y} \quad (4.46)$$

$$\delta\omega_z = \delta\omega_{z,0} \quad (4.47)$$

Combining Eqs. 4.42-4.44 and 4.45-4.47 can lead to a variety of boulder launch outcomes. As presented in the following sections.

4.2.4 Boulder removal without precession

A boulder launch scenario can be designed such that the angular velocity is slightly shifted from the original direction, but the PAR characteristic is kept. Such a scenario could be important in close proximity asteroid mining operations, where boulders are lifted to orbit using spacecraft, or in an MD scenario in which boulders are launched to hyperbolic trajectories, while seeking to minimize disturbances to the asteroid's rotation. In a recursive removal process keeping the PAR characteristic could mean the difference between a safe, successful mission and mission failure due to the introduction of complex dynamics in the asteroid's rotation.

Examining the sinusoidal element coefficients in Eqs. 4.45-4.46 together with the relationships in Eqs. 4.42-4.43 leads to the conclusion that the non-precessing solution can be reached by nullifying the coefficients using the following launch directions

$$\Delta v_{B,x} = \beta_y + \alpha_x \Delta v_{B,z} \quad (4.48)$$

$$\Delta v_{B,y} = -\beta_x + \alpha_y \Delta v_{B,z} \quad (4.49)$$

where the α coefficients are the launch direction ratios and the β coefficients are the launch direction offset

$$\alpha_x = \frac{r_{B,x}}{r_{B,z}} \quad (4.50)$$

$$\alpha_y = \frac{r_{B,y}}{r_{B,z}} \quad (4.51)$$

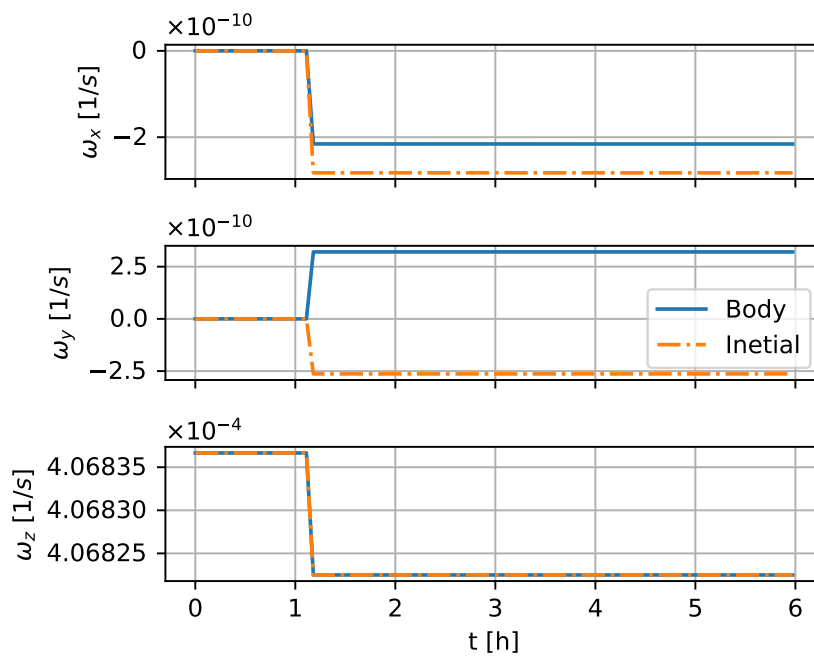
$$\beta_x = \frac{\omega_z I_x (I_{B,xz} - M_B r_{B,x} r_{B,z})}{M_B r_{B,z} (I_z - I_x)} \quad (4.52)$$

$$\beta_y = \frac{\omega_z I_y (I_{B,yz} - M_B r_{B,y} r_{B,z})}{M_B r_{B,z} (I_z - I_y)} \quad (4.53)$$

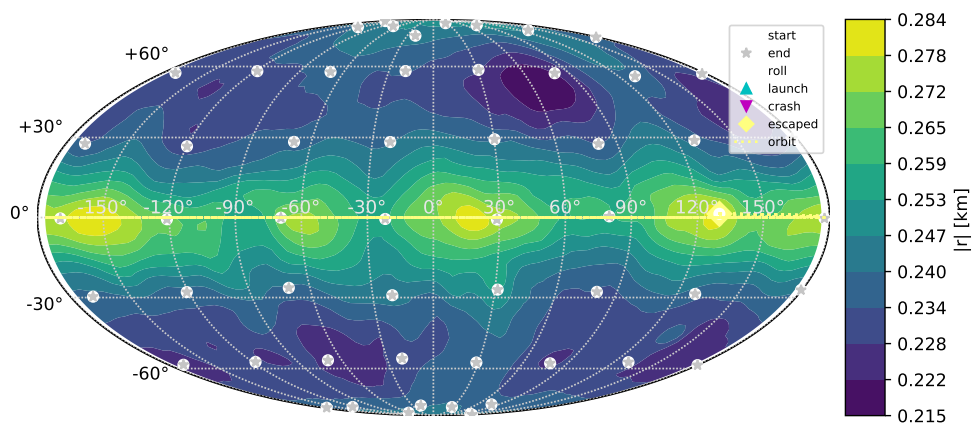
Here the $\Delta v_{B,z}$ element is a degree of freedom that can be defined according to additional operational requirements. Figure 4.46 presents a launch scenario of a single boulder from the surface of Bennu (rotating at its nominal 4.3 hour period). The $\Delta v_{B,z}$ component is set to zero, for example in a scenario which seeks not to disturb the asteroid's out-of-equatorial plane orbital motion. Figure 4.46b presents a field of fifty-six identical 5.2 meter average diameter boulders, with a mass of 122 tons each, evenly distributed on the surface. The boulder which provides the largest $\delta\omega_0$ is selected for launch. Its location is on the equator at the largest surface radius available (longitude ~ 130 degrees). The boulder's launch velocity is $|\Delta \mathbf{v}_B| = 0.797 \text{ m}\cdot\text{s}^{-1}$ and the overall change in angular velocity magnitude is $\delta\omega_0 = 1.416 \times 10^{-8} \text{ s}^{-1}$ which amounts to 0.53 seconds added to the rotation period. This change to angular velocity magnitude is equivalent to 52.9 years of the YORP effect rate presented in Table 3.6. Figure 4.46a shows the asteroid angular velocity in both the body and inertial frames. The shift from one fixed position of the vector to another is seen in the figure in both frames, showing that the asteroid remains a PAR after the boulder is removed and launched. The boulder launch velocity magnitude is high enough to launch it in a hyperbolic trajectory, causing it to leave the asteroid's gravity well.

The launch magnitude in the Figure 4.46 case is derived from the zero $\Delta v_{B,z}$ and Eqs. 4.48-4.49 constraints. A scenario in which a boulder's launch velocity could exceed the technical feasibility of the hardware removing the boulder. For that reason a launch velocity constraint can be imposed on the launch scenario. Assuming a set Δv_B magnitude for a given boulder

$$|\Delta \mathbf{v}_B|^2 = \Delta v_{B,x}^2 + \Delta v_{B,y}^2 + \Delta v_{B,z}^2 \quad (4.54)$$



(a) Angular velocity change



(b) Boulder surface location and trajectory projection

Figure 4.46: Single boulder launch results

and inputing Eqs. 4.48-4.49 into the equation leads to

$$|\Delta \mathbf{v}_B|^2 = (\beta_y + \alpha_x \Delta v_{B,z})^2 + (-\beta_x + \alpha_y \Delta v_{B,z})^2 + \Delta v_{B,z}^2 \quad (4.55)$$

The equation's solution for $\Delta v_{B,z}$ is

$$\Delta v_{B,z} = \frac{\alpha_y \beta_x - \alpha_x \beta_y \pm \sqrt{-(\alpha_x \beta_x + \alpha_y \beta_y)^2 + |\Delta \mathbf{v}_B|^2 (1 + \alpha_x^2 + \alpha_y^2) - \beta_x^2 - \beta_y^2}}{\alpha_x^2 + \alpha_y^2 + 1} \quad (4.56)$$

This solution leads to two boulder launch directions, one of which can be set into the asteroid itself. By imposing that $\Delta \mathbf{v}_B \cdot \mathbf{r}_B > 0$ the outward launch direction can be selected. The square-root phrase in Eq. 4.56 shows that in order of reaching a physical solution for $\Delta v_{B,z}$ there is minimum required boulder launch magnitude. This Δv is also the minimum value needed to keep the asteroid as a PAR

$$|\Delta \mathbf{v}_{min}| = \sqrt{[(\alpha_x \beta_x + \alpha_y \beta_y)^2 + \beta_x^2 + \beta_y^2] [1 + \alpha_x^2 + \alpha_y^2]^{-1}} \quad (4.57)$$

Table 4.1 presents the minimum launch velocities required to keep the asteroid as a PAR for several of the identical boulders seen in Figure 4.46b. The table also shows the change in asteroid angular velocity for each boulder launch at the minimum value. The boulder launched in Figure 4.46 is numbered 4 in the table, with a minimum launch velocity magnitude being 99.3% of the value reached in the $\Delta V_{B,z} = 0$ scenario. Interestingly, the reached change in angular velocity is 0.06% higher when $\Delta V_{B,z}$ is given the freedom to be defined by minimum launch velocity. As expected, a high correlation is seen between the launch velocity and the change in angular velocity. The table also shows that a boulder's latitude is the best indicator of the launch velocity needed to keep the PAR characteristic. In the comparison of boulders 4 and 6, both on the equator, the small difference in launch velocities stems from the added 25 meters in altitude boulder 4 has.

Using the indicators presented in Table 4.1 and expanding on them can produce preference tables to rank boulder launches according to desired outcomes. Such outcomes as maximum tilt of the angular velocity vector in a certain direction, maximum change to the z component of the angular velocity, or lowest ΔV required to launch a boulder while keeping the asteroid as a PAR. In a real operational scenario, where boulders are not identical, a boulder's mass and the ability to launch it

Boulder	Longitude [deg]	Latitude [deg]	Radius [km]	ΔV_{min} [m·s ⁻¹]	$\delta\omega_0$ [s ⁻¹]	YORP years
1	132.6	80.1	0.246	0.118	-0.21×10^{-8}	7.9
2	130.7	55.5	0.239	0.379	-0.63×10^{-8}	23.6
3	128.7	28.9	0.238	0.588	-0.92×10^{-8}	34.2
4	130.0	1.4	0.283	0.792	-1.417×10^{-8}	52.95
5	-20.2	-55.3	0.231	0.326	-0.53×10^{-8}	19.8
6	-21.9	-0.5	0.258	0.64	-1.05×10^{-8}	39.0

Table 4.1: Minimum launch velocities for boulders in different locations

will also need to be considered in the ranking. For a given boulder the launch velocity magnitude is a function of the boulder mass, the launch thrust T and the thrusting time t_b (assuming constant and infinitesimally short thrust)

$$|\Delta \mathbf{v}_B| = \frac{T t_b}{M_B} \quad (4.58)$$

For a defined thrust boulders can also be ranked by the ΔV their masses allow to reach. For example, for a 100 kN engine thrusting for 10 second would lead to a $\Delta V_B = 8.2 \text{ m}\cdot\text{s}^{-1}$ for the boulder presented in Figure 4.46.

When observing the relationship between Eqs. 4.48-4.49, 4.50-4.53, and 4.56 together with results of boulders seen in Table 4.1 and Figure 4.46b the overall change observed in angular velocity is always negative. This means that a boulder launch while keeping the PAR characteristic for a given launch capability has a decelerating effect on an asteroid's angular velocity.

A scenario in which boulders are launched to maximize angular velocity deceleration is presented in Figure 4.47. This scenario could be useful for in-situ operations when seeking to reduce the rotation rate, increase the surface geopotential, and prevent particles or equipment from launching to orbit. Thirty boulders, with mean diameters ranging from 2.2 to 9.5 meters (5.3 to 467 tons) are randomly placed on the surface of Bennu. The boulders are ranked by their contribution to the total $\delta\omega$ with a thrusting magnitude of 100 kN for 10 seconds. The highest ranking ten boulders are launched at 10000 second intervals sequentially. This scenario is not probable in near future asteroid operations, but it demonstrates the achievable changes of advanced operations of asteroid surfaces. The overall change in angular velocity magnitude is $\delta\omega = 16.5 \times 10^{-8} \text{ 1}\cdot\text{s}^{-1}$ which amounts to 6.16 seconds

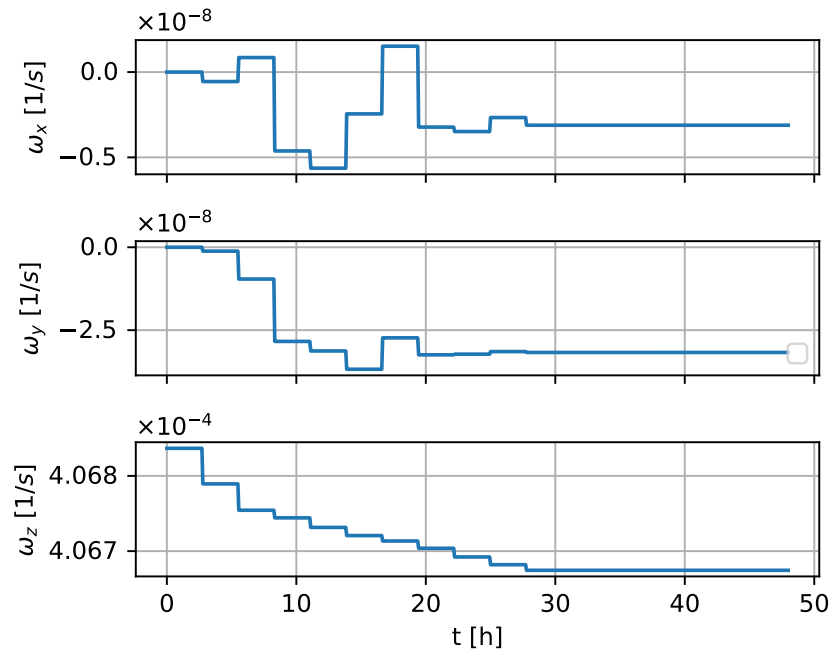
added to the rotation period. A change in angular velocity magnitude that is equivalent to 605 years of the YORP effect on Bennu. Figure 4.47a shows the body frame angular velocity evolution, the change in the x and y elements is erratic, but the change in the z direction is consistent in its decelerating trend. Figure 4.47b presents all 30 boulders on the surface, with relative magnitudes and contribution to angular velocity magnitude change. The figure shows some preference for boulder size over boulder location. However, given similar boulder sizes, generally boulders closer to the equator contribute more to the angular velocity change.

4.2.4.1 Tumbling an asteroid with boulder removal

An operational scenario can exist which requires disruption of an asteroid's rotation; for example in order of destabilizing the surface environment of the asteroid as part of an asteroid deflection or mining efforts. Two changes to the angular velocity can assist in reaching disruption: precession and acceleration. As described in Section 2.4.1 precession would lead to a time varying surface environment, that would include a varying acceleration regime on surface material, possibly to the extent of loosening it so it independently launches to space. Accelerating an asteroid's rotation would lead some areas to have an outward pointing surface acceleration, causing material from that region to launch off of the surface. Examining Eqs. 4.42-4.47 again shows that in order of reaching maximum acceleration the x and y components of the launch vector need to be perpendicular to the boulder's xy plane position vector. Assuming the entire launch vector is in the xy plane with a given magnitude of $|\Delta\mathbf{v}_B|$ the launch velocity vector is

$$\Delta v_{B,x} = \frac{r_{B,y}}{\sqrt{r_{B,x}^2 + r_{B,y}^2}} |\Delta\mathbf{v}_B| \quad (4.59)$$

$$\Delta v_{B,y} = -\frac{r_{B,x}}{\sqrt{r_{B,x}^2 + r_{B,y}^2}} |\Delta\mathbf{v}_B| \quad (4.60)$$



(a) Angular velocity change

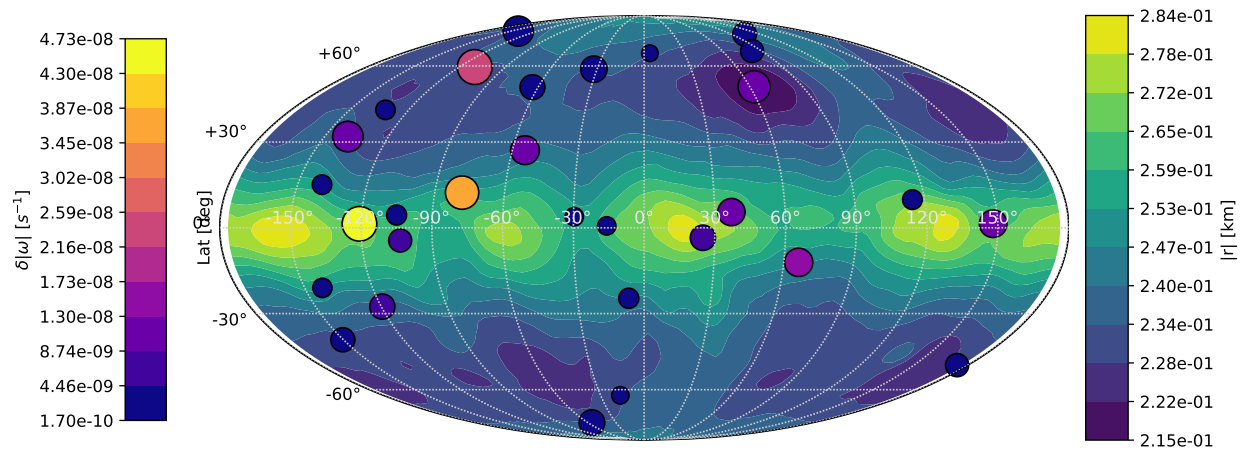
(b) Boulder surface location, size, and contribution to $\delta\omega$

Figure 4.47: Multiple boulder launch results

A z-axis launch velocity element can be introduced by adding some factor κ for the x and y elements

$$\Delta v_{B,x} = \kappa \frac{r_{B,y}}{\sqrt{r_{B,x}^2 + r_{B,y}^2}} |\Delta \mathbf{v}_B| \quad (4.61)$$

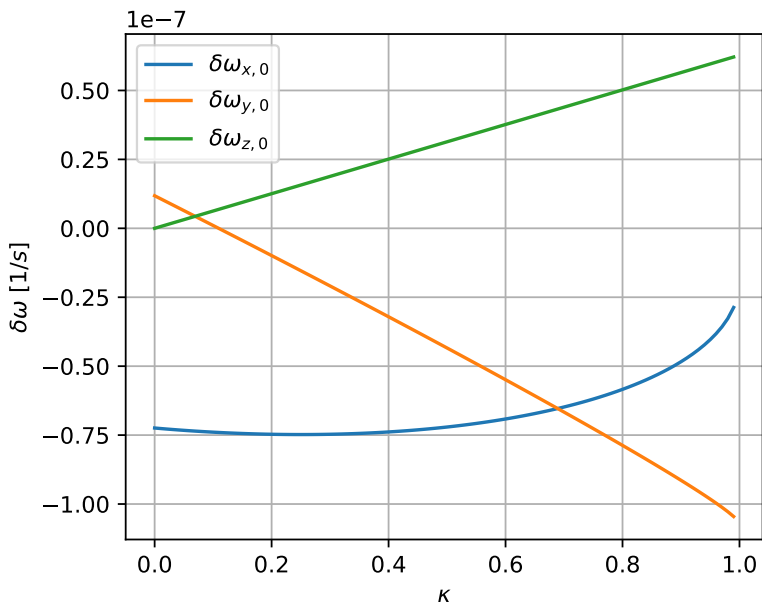
$$\Delta v_{B,y} = -\kappa \frac{r_{B,x}}{\sqrt{r_{B,x}^2 + r_{B,y}^2}} |\Delta \mathbf{v}_B| \quad (4.62)$$

$$\Delta v_{B,z} = \pm \sqrt{1 - \kappa^2} |\Delta \mathbf{v}_B| \quad (4.63)$$

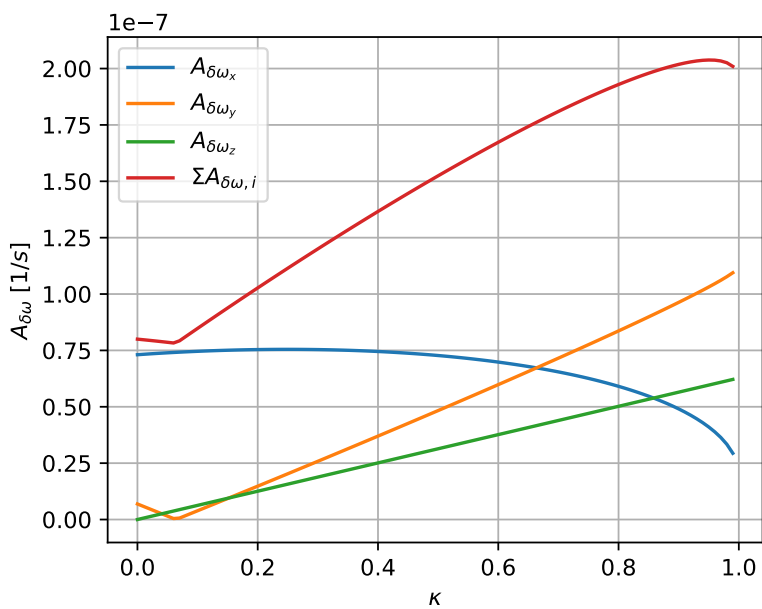
where the z-axis launch velocity sign is set outwards, in the direction of the boulder's z-axis position. Figure 4.48 presents the changes in $\delta\omega$ values as a function of the κ ratio in a tumbling scenario for a boulder from the field presented in Figure 4.46. This boulder is ranked highest in the overall $\delta\omega$ it provides to the asteroid. Figure 4.48a shows the $\delta\omega_0$ values, with a linear increase in $\delta\omega_{0,z}$, a non-linear increase in $\delta\omega_{0,x}$ and a near-linear decrease in the $\delta\omega_{0,y}$ as κ approaches 1. Recalling that the actual $\delta\omega$ solution is a function of the boulder geometry as well, the amplitudes of the cosine coefficients in Eqs. 4.45 and 4.46 are plotted in Figure 4.48b, together with the time constant value of $\delta\omega_{0,z}$ and the sum of all three elements. A maximum point can be seen at $\kappa = 0.95$ with an amplitude sum of $\Sigma A_{\delta\omega} = 20.4 \times 10^{-8} \text{ s}^{-1}$.

Figure 4.49 presents the results of the boulder launch at maximum disturbance $|\Delta \mathbf{v}_B|$. The angular velocity deviation magnitude at the end of the simulation $\delta\omega = 12.2 \times 10^{-8} \text{ s}^{-1}$, which is equivalent to 2.6 seconds reduced from the instantaneous rotation period (at simulation end), or ~ 220 years of YORP. Figure 4.49a shows the angular velocity precessing both in the body and inertial frames. The boulder launch southward direction seen in Figure 4.49b demonstrates the substantial z-axis element for the tumbling case. It is interesting to point out that the boulder is located in the lowest radial position in found in the field, placing it closest to the asteroid's center of mass.

It is impotent to note that in a tumbling scenario the linearized PAR dynamics will quickly break down and the launch directions derived from these dynamics will not necessarily be optimal for tumbling. Further investigation into how best to tumble an asteroid should be conducted to expand all possibilities of this application.

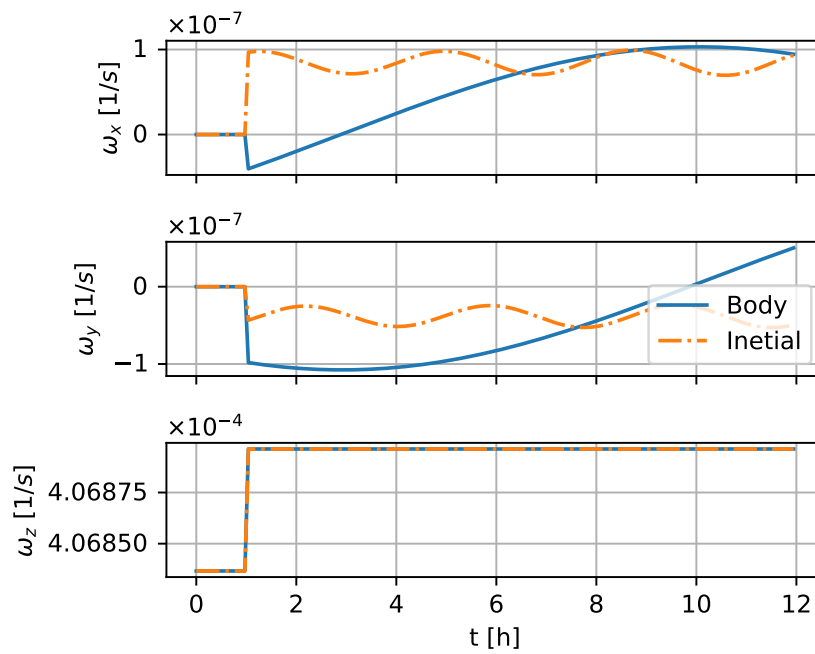


(a) Angular velocity change

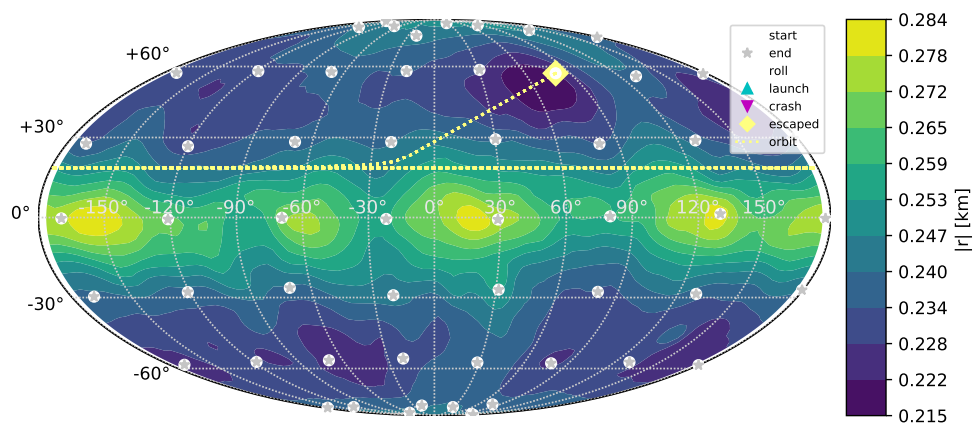


(b) Angular velocity function amplitude

Figure 4.48: Tumble angular velocity change for different κ ratios



(a) Angular velocity evolution



(b) Boulder surface location and trajectory projection

Figure 4.49: Single boulder tumble launch results

4.2.5 Boulder launch to affect asteroid orbits

Using Eq. 4.39 together with the $\hat{\mathbf{R}}_{B,\infty} \parallel \hat{\mathbf{R}}_{B,t_0}$ assumption in Eq. 4.13 leads to the asteroid velocity change as a function of the launch $\Delta\mathbf{V}_B$

$$\Delta\mathbf{V}_A = -\frac{M_B}{M^+} \sqrt{|\boldsymbol{\omega} \times \mathbf{R}_B + \Delta\mathbf{V}_B|^2 - 2\frac{GM^+}{|\mathbf{R}_B|} \frac{\boldsymbol{\omega} \times \mathbf{R}_B + \Delta\mathbf{V}_B}{|\boldsymbol{\omega} \times \mathbf{R}_B + \Delta\mathbf{V}_B|}} \quad (4.64)$$

Similarly to the previous section, asteroid system ΔV vector is notated as $\Delta\mathbf{V}_A$ to prevent confusion with other general ΔV mentions, and because the scenarios presented are those in which boulders escape in each launch, thus the asteroid system and the asteroid (parent body and surface boulders) are the same. It is important to note that Eq. 4.64 is presented in the inertial frame, meaning the boulder inertial position vector is constantly changing and the required launch direction changes in the body frame. Keeping with the PAR asteroid assumption, the inertial and body z axes are set to be aligned. This arrangement sets the angular velocity vector as constant in both frames. The boulder velocity can be presented using an Euler rotation matrix around the z

$$\dot{\mathbf{R}}_B = [R_z(\theta(t))](\boldsymbol{\omega} \times \mathbf{r}_B + \Delta\mathbf{v}_B) = \begin{bmatrix} C_\theta & -S_\theta & 0 \\ S_\theta & C_\theta & 0 \\ 0 & 0 & 1 \end{bmatrix} \begin{bmatrix} -\omega_z r_{B,y} + \Delta v_{B,x} \\ \omega_z r_{B,x} + \Delta v_{B,y} \\ \Delta v_{B,z} \end{bmatrix} = \begin{bmatrix} C_\theta(-\omega_z r_{B,y} + \Delta v_{B,x}) - S_\theta(\omega_z r_{B,x} + \Delta v_{B,y}) \\ S_\theta(-\omega_z r_{B,y} + \Delta v_{B,x}) + C_\theta(\omega_z r_{B,x} + \Delta v_{B,y}) \\ \Delta v_{B,z} \end{bmatrix} \quad (4.65)$$

where $\theta(t) = \omega_z t + \theta_0$. It should be noted that the z-axis element is fixed for all θ angles.

For the goal of asteroid deflection a desired asteroid velocity change direction $\Delta\hat{\mathbf{V}}^*$ is defined based on the orbital requirements that will be described in a later section. The next subsection will present optimized planning schemes for boulder launch. First by optimizing the launch timing in the asteroid's rotation for a boulder when the $\Delta\mathbf{V}_B$ values are fixed in the body frame. And then by examining a change in $\Delta\mathbf{V}_B$ values together with the launch phase in the asteroid's rotation.

4.2.5.1 Optimized boulder launch

The requirement in an optimized boulder launch is to maximize the alignment of $\Delta \mathbf{V}_A$ with $\Delta \hat{\mathbf{V}}^*$. This alignment can be represented as the projection of $\Delta \mathbf{V}_A$ on $\Delta \hat{\mathbf{V}}^*$

$$\Delta \mathbf{V}_{A,p*} = (\Delta \mathbf{V}_A \cdot \Delta \hat{\mathbf{V}}^*) \Delta \hat{\mathbf{V}}^* \quad (4.66)$$

The fixed values of $\Delta \mathbf{v}_B$ in the body frame mean that the magnitude elements of $\Delta \mathbf{V}_A$ are fixed for any launch direction. Thus, in order of maximizing $\Delta \mathbf{V}_A$ with respect to $\Delta \hat{\mathbf{V}}^*$ the dot product $\Delta \hat{\mathbf{V}}_A \cdot \Delta \hat{\mathbf{V}}^*$ needs to be maximized. The z element in Eq. 4.65 is fixed and thus the projection can only be maximized in the xy plane. A cost function is defined as the xy plane dot product of the boulder inertial velocity and the required asteroid velocity change direction

$$J = S_\theta \left((-\omega_z r_{B,x} - \Delta v_{B,y}) \Delta V_x^* + (-\omega_z r_{B,y} + \Delta v_{B,x}) \Delta V_y^* \right) + \\ C_\theta \left((-\omega_z r_{B,y} + \Delta v_{B,x}) \Delta V_x^* + (\omega_z r_{B,x} + \Delta v_{B,y}) \Delta V_y^* \right) \quad (4.67)$$

Here $S_\theta = \sin(\theta(t))$ and $C_\theta = \cos(\theta(t))$ are the rotation matrix elements.

Finding the extrema of this cost function would provide the boulder escape direction that is aligned most with the required asteroid velocity change. The minimum solution would launch the boulder in the direction of desired asteroid velocity change, propelling it opposite to the desired direction. The maximum solution would maximize the thrust provided to the asteroid's deflection measure.

Differentiating the cost function by the angle θ and setting to zero ($\frac{\partial J}{\partial \theta} = 0$) leads to

$$\theta^* = \pi + \arctan \left(\frac{(-\omega_z r_{B,x} - \Delta v_{B,y}) \Delta V_x^* + (-\omega_z r_{B,y} + \Delta v_{B,x}) \Delta V_y^*}{(-\omega_z r_{B,y} + \Delta v_{B,x}) \Delta V_x^* + (\omega_z r_{B,x} + \Delta v_{B,y}) \Delta V_y^*} \right) \quad (4.68)$$

Thus, the optimized time in the asteroid's rotation for boulder launch is

$$t^* = \frac{1}{\omega_z} (\theta^* + \theta_0 + 2n\pi) \quad (4.69)$$

where n is an integer.

When not fixing the value of $\Delta v_{B,z}$ a second degree of freedom becomes available. In this case the boulder launch velocity in the body frame is as presented in Eqs. 4.48-4.49. And the absolute value

of $\Delta v_{B,z}$ is bound between its maximum value derived from the overall maximum launch velocity magnitude $|\Delta \mathbf{v}_B|$ as presented in Eq. 4.56 and the minimum launch velocity magnitude derived from the surface escape velocity. Inserting $\Delta \mathbf{v}_B$ to the boulder inertial velocity term leads to

$$\dot{\mathbf{R}}_B = [R_z(\theta)](\boldsymbol{\omega} \times \mathbf{r}_B + \Delta \mathbf{v}_B) = \begin{bmatrix} -C_\theta(-\omega_z r_{B,y} + \beta_y) - S_\theta(\omega_z r_{B,x} - \beta_x) + (C_\theta \alpha_x - S_\theta \alpha_y) \Delta v_{B,z} \\ -S_\theta(-\omega_z r_{B,y} + \beta_y) + C_\theta(\omega_z r_{B,x} - \beta_x) + (S_\theta \alpha_x + C_\theta \alpha_y) \Delta v_{B,z} \\ \Delta v_{B,z} \end{bmatrix} \quad (4.70)$$

Observing Eq. 4.64 with 4.65 and 4.70

$$\Delta \mathbf{V}_A = -\frac{M_B}{M^+} \sqrt{|\boldsymbol{\omega} \times \mathbf{r}_B + \Delta \mathbf{v}_B|^2 - 2 \frac{GM^+}{|\mathbf{R}_B|} \frac{\dot{\mathbf{R}}_B}{|\boldsymbol{\omega} \times \mathbf{r}_B + \Delta \mathbf{v}_B|}} = -\frac{M_B}{M^+} \sqrt{1 - \frac{2GM^+}{|\mathbf{R}_B| [(-\omega_z r_{B,y} + \beta_y + \alpha_x \Delta v_{B,z})^2 + (\omega_z r_{B,x} - \beta_x + \alpha_y \Delta v_{B,z})^2 + \Delta v_{B,z}^2]}} \dot{\mathbf{R}}_B \quad (4.71)$$

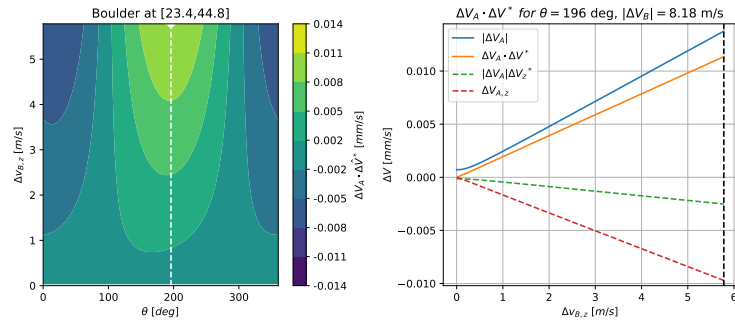
The cost function now takes the magnitude of $\Delta \mathbf{V}_A$ into account

$$J(\Delta v_{B,z}, \theta) = \Delta \mathbf{V}_A(\Delta v_{B,z}, \theta) \cdot \Delta \hat{\mathbf{V}}^* \quad (4.72)$$

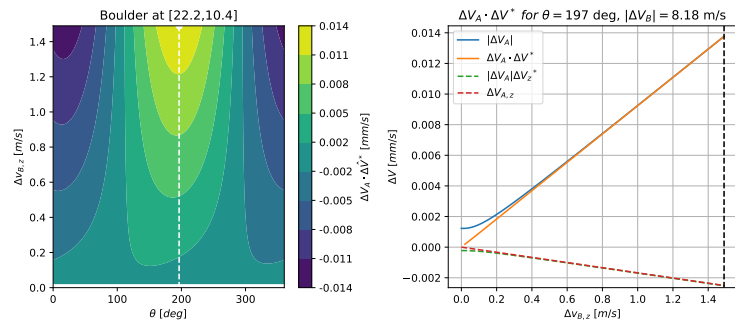
Due to the complexity of differentiating J with respect to $\Delta v_{B,z}$ and the limited domain in which the maximum value of J is bound in (for rotation angle θ and $\Delta v_{B,z}$ with a given maximum thrust) a solution for $\nabla J = 0$ can be found numerically. Figure 4.50 presents the $\Delta \mathbf{V}_A$ performance of four boulders identical to the those presented in Figure 4.46 placed on the surface of the asteroid Bennu. The maximum value of boulder launch velocity provided to each boulder, $\Delta V_B = 8.18 \text{ m}\cdot\text{s}^{-1}$, is based on a launch thrusting scheme presented in the previous section. This maximum value is used to determine the range of possible $\Delta v_{B,z}$ values to be examined, a value range that changes with the boulder's location. The required inertial $\Delta \hat{\mathbf{V}}^*$ direction in this scenario is $[0.707, 0.683, -0.183]$ which represents a cone (in the body frame) with a half-angle of 10.54 degrees due south. Each sub-figure in Figure 4.50 shows a heatmap of the magnitude of $\Delta \mathbf{V}_A$'s projection on $\Delta \hat{\mathbf{V}}^*$ as a function of the asteroid's rotation angle θ and the z-axis boulder launch velocity $\Delta v_{B,z}$. Each sub-figure also presents the magnitude of various asteroid velocity change components as a function

of $\Delta v_{B,z}$. The maximum point in each heatmaps is marked by a white dot, and the analytical θ^* solution is presented as a dashed line. The asteroid velocity change components' plots show the total velocity change magnitude ($|\Delta \mathbf{V}_A|$), the magnitude of velocity change projection on required direction ($\Delta \mathbf{V}_A \cdot \hat{\mathbf{V}}^*$), the velocity change magnitude multiplied by the z-axis value of the required direction ($|\Delta \mathbf{V}_A| \Delta \hat{\mathbf{V}}_z^*$), and the actual velocity change z-axis value ($\Delta V_{A,z}$), all as a function of $\Delta v_{B,z}$ for the selected maximum θ^* . The numerically found value of $\Delta v_{B,z}$ is also marked on the plots as a vertical dashed line. The physical interpretation of maximizing the cost function in Eq. 4.72 is to best align $\Delta \mathbf{V}_A$ with $\Delta \hat{\mathbf{V}}^*$. The variation in performance in the plots in Figure 4.50 shows how the alignment correlates with the magnitude of $\Delta \mathbf{V}_A \cdot \Delta \hat{\mathbf{V}}^*$ reached. The heatmaps in Figures 4.50a-4.50c show the cost function maximized at the maximum magnitude of $\Delta v_{B,z}$ (the sign varies with location with respect to the equator). This means that despite the 'waste' in ΔV due to the misalignment between $\Delta \mathbf{V}_A$ and $\Delta \hat{\mathbf{V}}^*$ the maximized magnitude of $\Delta \mathbf{V}_A$ has a more substantial contribution to the deflection effort. The three cases in Figures 4.50a-4.50c represent the majority of cases on the asteroid surface. The use of the maximum $\Delta v_{B,z}$ also means the analytical θ^* solution in Eq. 4.68 is valid for most cases. Figure 4.50d presents a maximized cost function at the smallest possible $\Delta v_{B,z}$, which correlates with the surface escape velocity, for a boulder near the south pole. This behavior is the result of the body frame geometry for launching such a boulder with the requirement of keeping the asteroid a PAR. In this case the analytical solution for θ does not maximize the cost function. The launch results seen in Figure 4.50b show the z-axis launch direction matching the required direction, which leads to full efficiency in the boulder launch. It should be remembered that the boulder launch direction is the opposite of the asteroid velocity change, such that a boulder launched north leads to an velocity change south (as seen in the figure). Figure 4.50a shows that despite the z-axis element being in the wrong direction the overall $\Delta \mathbf{V}_A$ still provides about 90% efficiency in the launch.

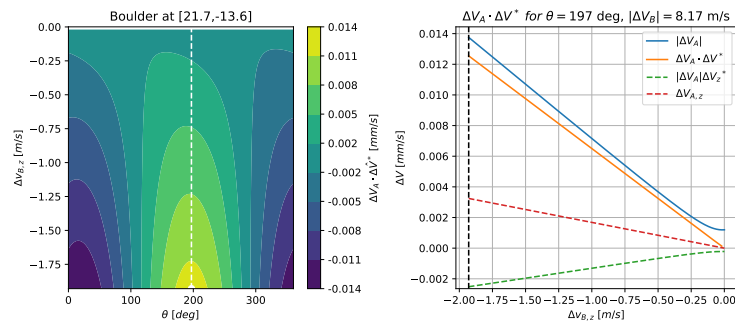
The maximum results presented in Figure 4.50 are expanded to a global overview in Figure 4.51, which presents the maximized $\Delta \mathbf{V}_A \cdot \Delta \hat{\mathbf{V}}^*$ for 200 boulders placed on the surface of Bennu. The boulder performance is presented in a scatter plot, overlaid on a heatmap of the surface escape



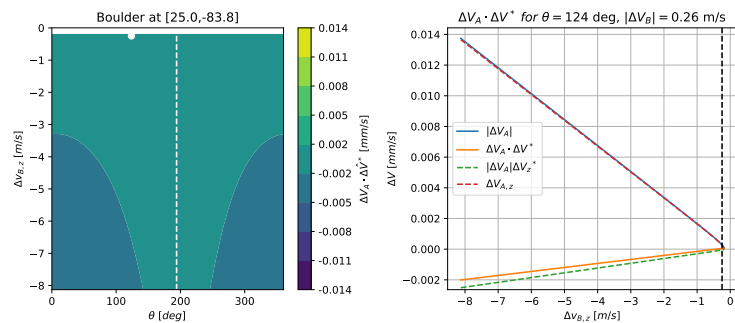
(a) Boulder at [23.4, 44.8]



(b) Boulder at [22.2, 10.4]



(c) Boulder at [21.7, -13.6]



(d) Boulder at [25.0, -83.8]

Figure 4.50: Boulder launch performance for launch direction and $\Delta v_{B,z}$ magnitude

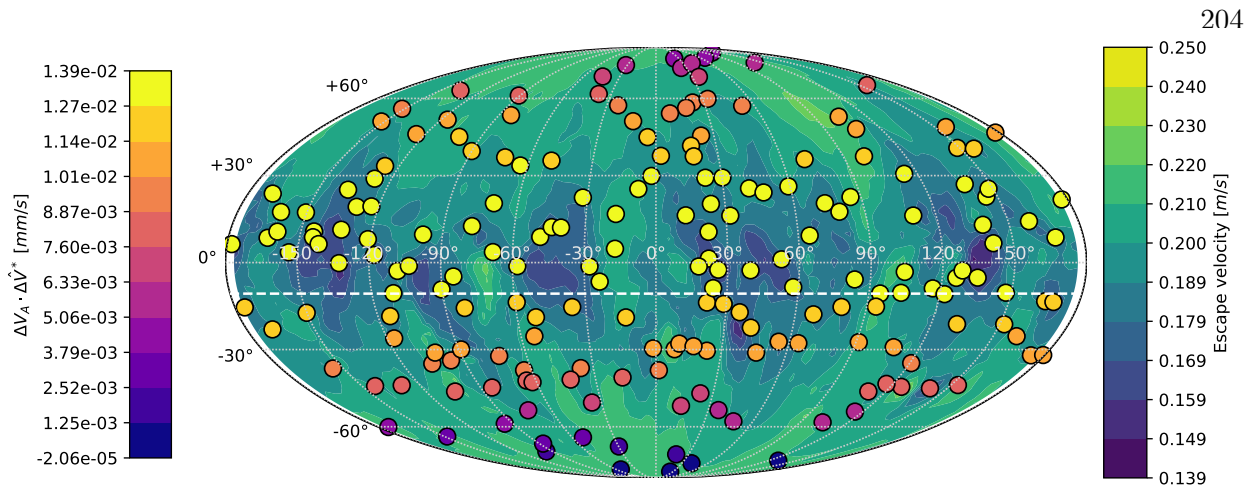


Figure 4.51: Boulder launch performance for the asteroid Bennu

velocity. The latitude of the required $\Delta\hat{\mathbf{V}}^*$ z-axis direction is presented in the figure as a white dashed line. The figure shows the best performance in equatorial and near-equatorial boulders opposite to the required z direction. The poorest performance is seen for boulders in the south pole. The deviation in surface escape velocity of the equatorial boulders shows little effect on the desired asteroid velocity change, in part due to the overall ΔV_B velocities which are two orders of magnitude larger than the escape velocities. As seen in Figure 4.50b boulders slightly north of the equator are perfectly situated to contribute all the $\Delta\mathbf{v}_B$ provided to them to the deflection effort.

When looking at the effect every boulder launch has on the asteroid rotation it is useful to look at the change in angular velocity magnitude. Figure 4.52 shows the percent reduction each boulder has on the asteroid angular velocity magnitude. Here, the equatorial boulders reduce the asteroid's rotation rate at most with an addition of ~ 0.5 seconds to the rotation period. The effect on rotation rate does not appear to 'favor' any side of the equator. It should be noted that while these launches do not perturb the asteroid's PAR characteristic, they do change the direction of the angular momentum (and angular velocity) as seen in Figure 4.53, which presents the angles between the original angular and new velocity vectors. The maximum change in angular velocity direction is seen for mid-latitude boulders, and the minimum change in direction is seen for equatorial boulders, showing a preference for equatorial or near-equatorial boulders in addition to the

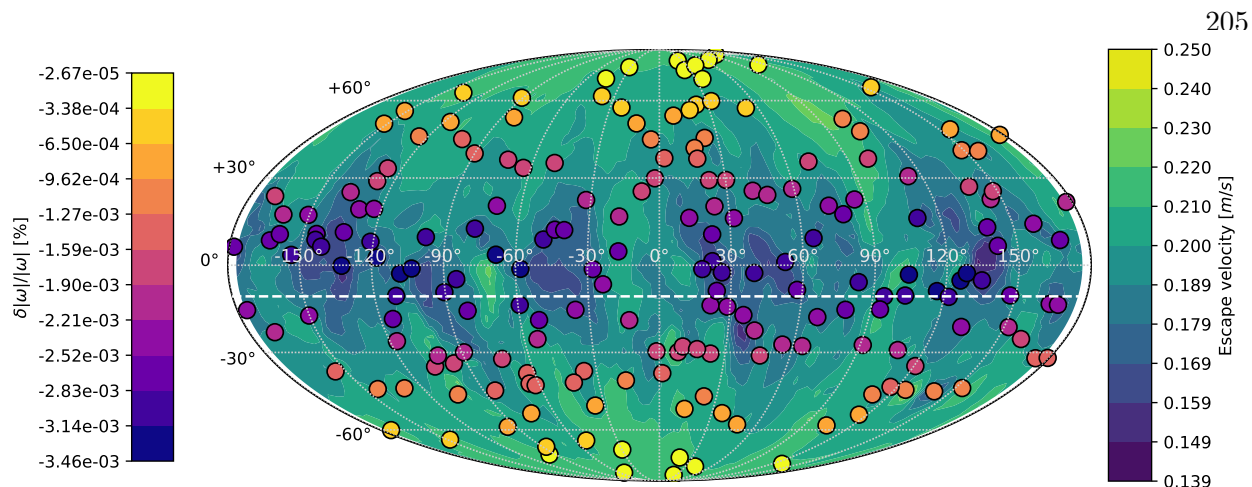


Figure 4.52: Benu change in rotation rate due to boulder launch

required launch direction performance.

The need for a designated PAR keeping launch is demonstrated in Figure 4.54 which shows the maximum precession angle reached in case of a launch in the required direction without consideration of the PAR characteristic. In this case $\Delta\mathbf{V}_A$ is always set to parallel $\Delta\hat{\mathbf{V}}^*$ and there is 100% deflection efficiency in the launch. The figure shows a maximum precession angle of ~ 0.02 degrees for polar launches. In a deflection scenario, which would require multiple boulder launches, this precession can grow with every launch and lead to a perturbed asteroid rotation that could affect the boulder launching scheme or the asteroid's orbital behavior in unpredictable ways. As expected, the boulders slightly north of the equator do not disturb the PAR characteristic because of their location alignment with the optimized PAR launch direction.

The favored boulders to launch for a polar launch direction are seen in Figure 4.55, in which the required $\Delta\hat{\mathbf{V}}^*$ vector is $[0.099, 0.257, -0.961]$. The figure shows the northern most boulders providing the maximum ΔV to the asteroid in this scenario, expanding on the north-south behavior difference seen in Figure 4.51.

Benu, the example asteroid used in Figures 4.50-4.55, is a spinning-top shaped asteroid with a close-to-axisymmetric geometry with respect to the maximum inertia axis (and the angular velocity vector). This shape naturally leads to similar behavior for the boulders on the same latitudes. Fig-

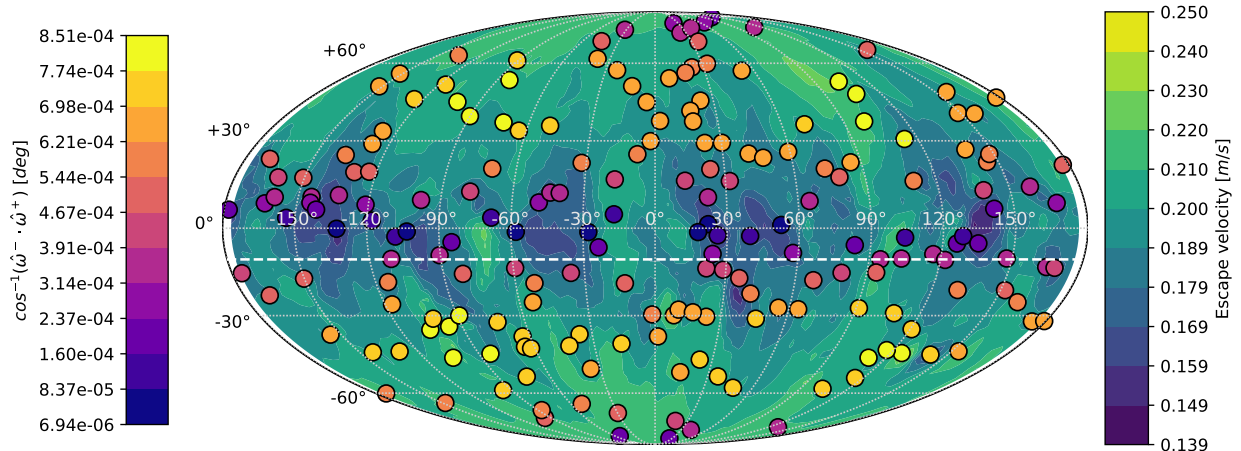


Figure 4.53: Bennu change in rotation rate due to boulder launch

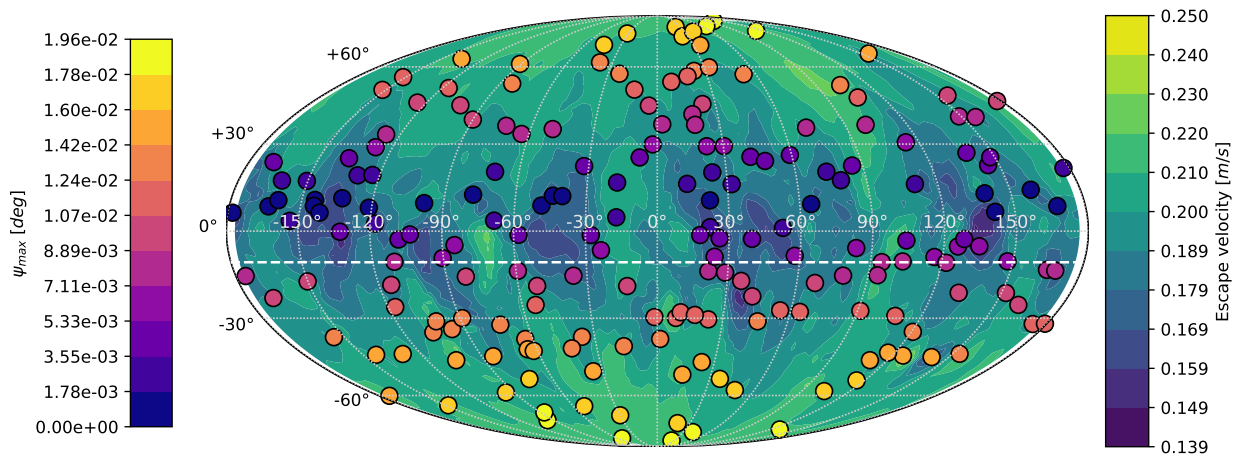


Figure 4.54: Bennu precession angle caused by directed boulder launch

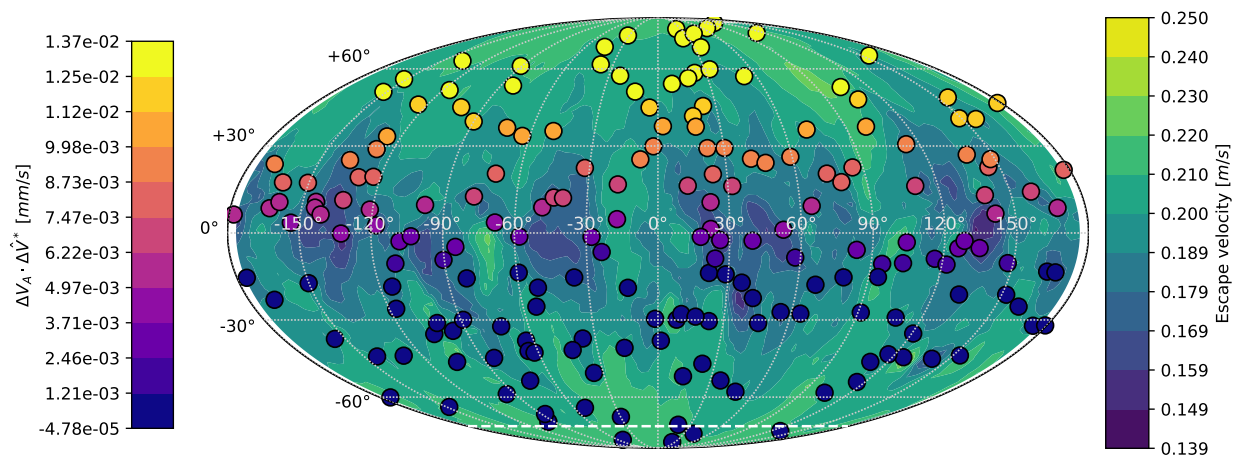


Figure 4.55: Boulder launch performance for the asteroid Bennu for polar launch

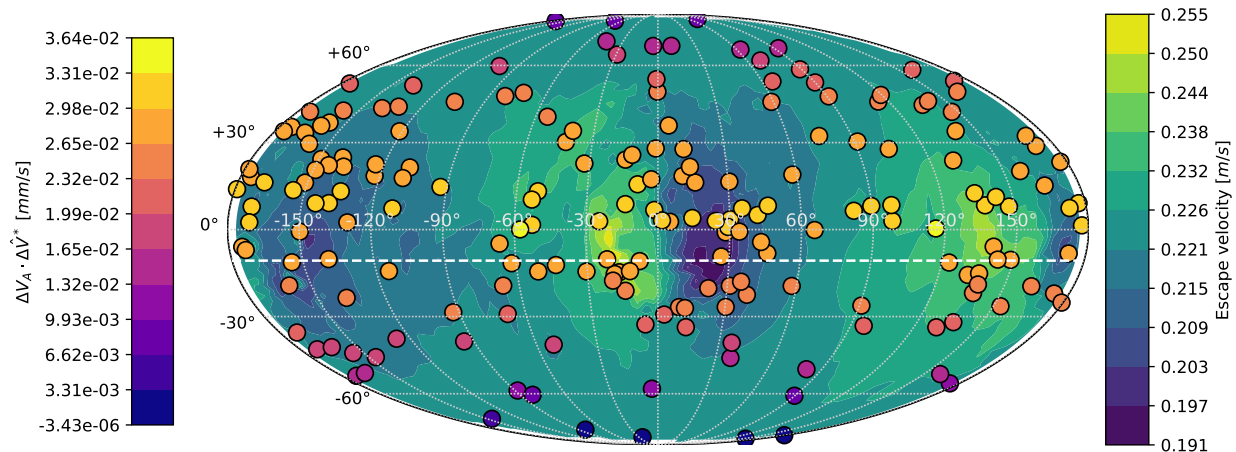


Figure 4.56: Boulder launch performance for the asteroid Itokawa

Figure 4.56 presents the launch performance of 200 boulders (identical in shape and mass to previous analysis) launched off the surface of asteroid Itokawa. The figure shows that, similarly to asteroid Bennu, the most relevant factor in boulder launch performance is its latitudinal placement. This, despite the difference in radial distance from the z-axis which ranges from ~ 150 to ~ 250 meters on the equator. This result indicates that the most substantial factor in boulder launch behavior is its location on the z-axis, and not its z-axis radial distance.

The main conclusion from the results presented in Figures 4.51-4.56 is that for any launch scenario a region can be found which optimizes the body frame launch direction while keeping the asteroid a PAR. When looking at a specific region it is important to understand if there are preferences to specific types of boulders, mainly, specific size. Figure 4.57 presents the launch performance of 100 boulders placed in a near equatorial region of Bennu's surface. The boulders range in mean diameter between ~ 2 and ~ 8 meters and in mass between ~ 12 and ~ 540 tons. The figure indicates the boulder size by the size of the representing dot in the scatter plot. The results in the figure show that there are little differences in performance between boulder sizes, as all boulders provide 96-100% efficiency in deflection effort. This result is explained by the fixed thrusting force and time which provides the same momentum change to all boulders regardless of their size. This result also provides flexibility in launch mechanism design and boulder selection, allowing use mechanisms

that prefer one size of boulder over the other. In addition, this result means that errors in a-priori estimate of a boulder's mass will have small effects on the launch efficiency as the Δv_B is mostly determined by a boulder's location.

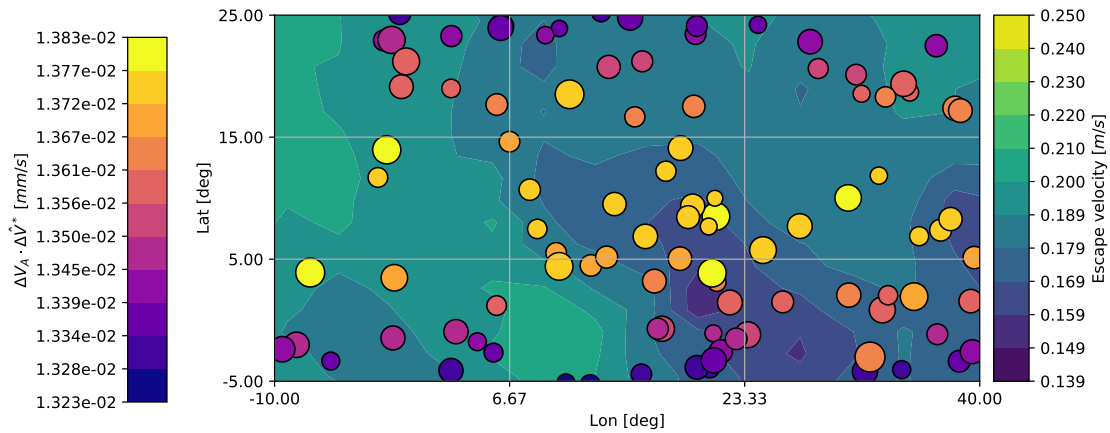


Figure 4.57: Boulder launch performance on asteroid Bennu equatorial region

When looking at the effect launching boulders of different sizes have on the asteroid's rotation Figure 4.58 presents the percent decrease in rotation rate for boulders of different sizes. Here a preference to smaller boulders can be seen, as they disrupt the asteroid's rotation less, both in the reduction of rotation rate, and in the change in angular velocity direction.

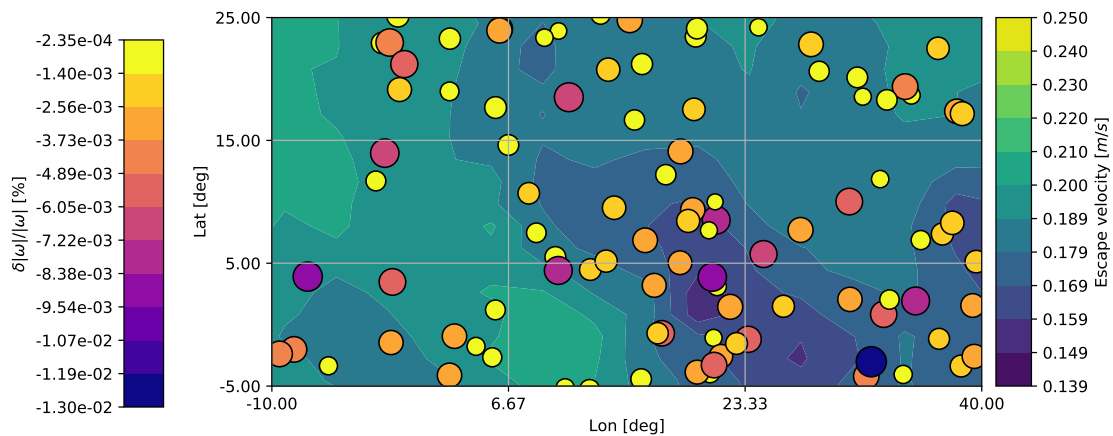


Figure 4.58: Bennu change in rotation rate due to boulder launch from equatorial region

4.2.6 Mass driver deflection launch campaign

In terms of boulder launch design in the inertial frame, a single boulder launch event can be thought of as a miniature kinetic impactor interception. Several studies have examined maximizing the deflection results of a kinetic interception by thrusting the asteroid in an optimized direction [155, 137, 156, 61, 136, 157]. For the purpose of this section a collision scenario between Earth and a Bennu-like asteroid has been designed. Figure 4.59 presents the distance between the Earth and the asteroid from 10 years prior to MOID until 50 days after MOID. The bodies' positions are propagated using Keplerian dynamics. The Earth's and asteroid's orbital elements at MOID are presented in Table 4.2. The minimum distance of both bodies' CMs at MOID is $\Delta s \sim 54$ km, well inside the Earth's radius, which means a collision between the two objects.

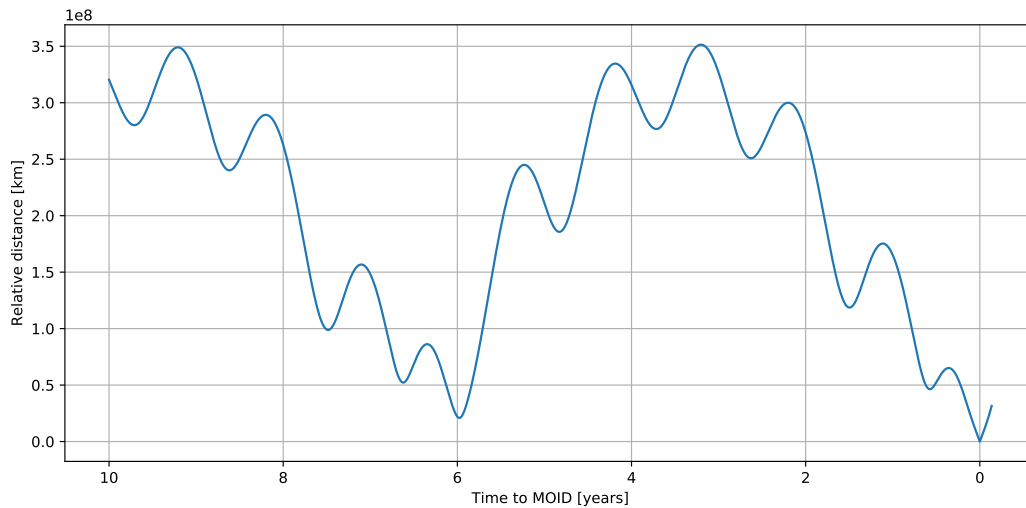


Figure 4.59: Earth-Asteroid distance in 10 years prior to MOID

	a [AU]	e []	i [deg]	Ω [deg]	ω [deg]	ν [deg]
Earth	1.0	0.0167	1.5786	174.9	102.19	195.0
Asteroid	1.1264	0.20375	6.035	125.5048	274.3911	72.1309

Table 4.2: MOID orbital states

The deflected distance presented by Vasile and Colombo [136] in the Satellite Radial (RSW) [127] frame is

$$\delta s_R = \frac{r}{a} \delta a + \frac{ae \sin(\nu_M)}{\sqrt{1-e^2}} \delta M - a \cos(\nu_M) \delta e \quad (4.73)$$

$$\delta s_S = \frac{r}{(1-e^2)^{\frac{3}{2}}} (1 + e \cos(\nu_M))^2 \delta M + r \delta \omega + \frac{r \sin(\nu_M)}{1-e^2} (2 + e \cos(\nu_M)) \delta e - r \cos(i) \delta \Omega \quad (4.74)$$

$$\delta s_W = r(\sin(\nu_M + \omega) \delta i - \cos(\nu_M + \omega) \sin(i) \delta \Omega) \quad (4.75)$$

where the changes to orbital elements, computed through the Gauss planetary equations, are

$$\delta a = \frac{2a^2 V}{\mu} \Delta V_T \quad (4.76)$$

$$\delta e = \frac{1}{V} \left[-\frac{r}{a} \sin(\nu_d) \Delta V_N + 2(e + \cos(\nu_d)) \Delta V_T \right] \quad (4.77)$$

$$\delta i = \frac{r \cos(\nu_d + \omega)}{\sqrt{\mu a (1-e^2)}} \Delta V_W \quad (4.78)$$

$$\delta \Omega = \frac{r \sin(\nu_d + \omega)}{\sqrt{\mu a (1-e^2)} \sin(i)} \Delta V_W \quad (4.79)$$

$$\delta \omega = \frac{1}{eV} \left[\left(2e + \frac{r \cos(\nu_d)}{a} \right) \Delta V_N + 2 \sin(\nu_d) \Delta V_T \right] - \frac{r \sin(\nu_d + \omega)}{\sqrt{\mu a (1-e^2)}} \frac{\cos(i)}{\sin(i)} \Delta V_W \quad (4.80)$$

$$\begin{aligned} \delta M &= \delta M_0 + \delta n \Delta T = \\ &= -\frac{\sqrt{1-e^2}}{eV} \left[\frac{r \cos(\nu_d)}{a} \Delta V_N + 2 \left(1 + \frac{e^2 r}{a(1-e^2)} \right) \sin(\nu_d) \Delta V_T \right] + \left(\sqrt{\frac{\mu}{a^3}} - \sqrt{\frac{\mu}{(a+\delta a)^3}} \right) \Delta T \end{aligned} \quad (4.81)$$

where ν_M and ν_d are the true anomaly at MOID and time of deflection, respectively. The elements of $\Delta \mathbf{V} = [\Delta V_N, \Delta V_T, \Delta V_W]$ are the in-plane normal to velocity, velocity, and out-of-plane directions.

The transformation matrix between the NTW frame and the inertial frame is [127]

$$[T]_{NTW}^3 = \begin{bmatrix} C_\phi C_\Omega C_u - S_\Omega C_i S_u - S_\phi C_\Omega S_u + S_\Omega C_i C_u & C_\phi S_\Omega C_u + C_\Omega C_i S_u - S_\phi S_\Omega S_u - C_\Omega C_i C_u & C_\phi S_i S_u + S_\phi S_i C_u \\ -C_\phi C_\Omega S_u + S_\Omega C_i C_u - S_\phi C_\Omega C_u - S_\Omega C_i S_u & -C_\phi S_\Omega S_u - C_\Omega C_i C_u - S_\phi S_\Omega C_u + C_\Omega C_i S_u & C_\phi S_i C_u - S_\phi S_i S_u \\ S_\Omega S_i & -C_\Omega S_i & C_i \end{bmatrix} \quad (4.82)$$

where $u = \nu + \omega$, and ϕ is the flight path angle of the body.

It is important to note that the change to mean anomaly is the combination of the momentary

change (δM_0) and change to orbit frequency derived from change to semi-major axis ($\delta n \Delta T$). The optimized direction for deflection is found by solving the eigenvalues of $T^T T$ where $T = A_M G_d$ is the transition matrix between $\Delta \mathbf{V}$ at time of deflection and $\delta \mathbf{s}$ at MOID. The components of the T transition matrix are:

$$A_M^T = \begin{bmatrix} \frac{r_M}{a} - \frac{3}{2} \frac{e \sin(\nu_M)}{\sqrt{1-e^2}} \frac{\sqrt{\mu}}{a^{\frac{3}{2}}} \Delta t & -\frac{3}{2} \frac{r_M}{(1-e^2)^{\frac{3}{2}}} (1 + e \cos(\nu_M))^2 \frac{\sqrt{\mu}}{a^{\frac{3}{2}}} \Delta t & 0 \\ -a \cos(\nu_M) & \frac{r_M \sin(\nu_M)}{1-e^2} (2 + e \cos(\nu_M)) & 0 \\ 0 & 0 & r_M \sin(\nu_M + \omega) \\ 0 & r_M \cos(i) & -r_M \cos(\nu_M + \omega) \sin(i) \\ 0 & r_M & 0 \\ \frac{ae \sin(\nu_M)}{\sqrt{1-e^2}} & \frac{r_M}{(1-e^2)^{\frac{3}{2}}} (1 + e \cos(\nu_M))^2 & 0 \end{bmatrix} \quad (4.83)$$

$$G_d = \begin{bmatrix} \frac{2a^2 V_d}{\mu} & 0 & 0 \\ \frac{2(e + \sin(\nu_d))}{V_d} & -\frac{r_d}{a V_d} \sin(\nu_d) & 0 \\ 0 & 0 & \frac{r_d \cos(\nu_d + \omega)}{\sqrt{\mu a (1-e^2)}} \\ 0 & 0 & \frac{r_d \sin(\nu_d + \omega)}{\sqrt{\mu a (1-e^2)} \sin(i)} \\ \frac{2 \sin(\nu_d)}{e V_d} & \frac{2e + (r_d/a) \cos(\nu_d)}{e V_d} & -\frac{r_d \sin(\nu_d + \omega) \cos(i)}{\sqrt{\mu a (1-e^2)} \sin(i)} \\ -\frac{2\sqrt{1-e^2}}{eV} \left(1 + \frac{e^2 r_d}{a(1-e^2)}\right) \sin(\nu_d) & -\frac{\sqrt{1-e^2}}{eV} \frac{r_d}{a} \cos(\nu_d) & 0 \end{bmatrix} \quad (4.84)$$

The eigenvector which corresponds to the largest eigenvalue of $T^T T$ is the optimized direction of $\Delta \mathbf{V}$ for deflection. Applying the maximum possible ΔV in that direction provides the maximum deflected distance at MOID, δs . Figure 4.60 presents the deflected distance reached for the scenario presented in Table 4.2 with 10 years to MOID and a single $0.02 \text{ mm}\cdot\text{s}^{-1}$ ΔV_A in the optimized direction. The deflection results are presented both as a function of time (4.60a) and as a function of true anomaly (4.60b). In addition to the computed δs the figures show the square-root of the largest eigenvalue of $T^T T$, some correlation can be seen between this value and the magnitude of deflection. A local minimum can be seen around apoapsis passage, but the overall trend of reduced deflection leads to this minimum value within less than half a revolution. The applied ΔV_A is

orders of magnitude smaller than the $\text{cm}\cdot\text{s}^{-1}$ magnitude ΔV required for full kinetic deflection in a single event. As a result, the deflection reached is substantially smaller than the Earth's radius. However, by accumulating these incremental thrusts full deflection can be reached.

Figure 4.61 presents the deflection results for a 10 years to MOID deflection scenario. The boulders are launched once a day in the maximum $T^T T$ eigenvalue direction. The one day interval simulates the time period needed by the lander-thruster system or systems to prepare for boulder launch.

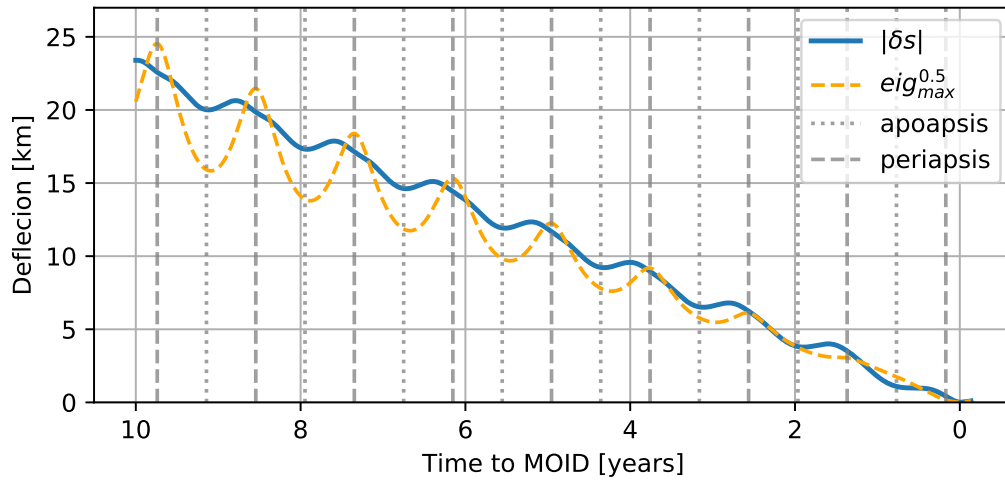
Deflection success is defined as

$$|\delta \mathbf{s}| > \gamma f_\infty R_E, \quad f_\infty = \sqrt{1 + 2\mu_E / (R_E V_{rel,M}^2)} \quad (4.85)$$

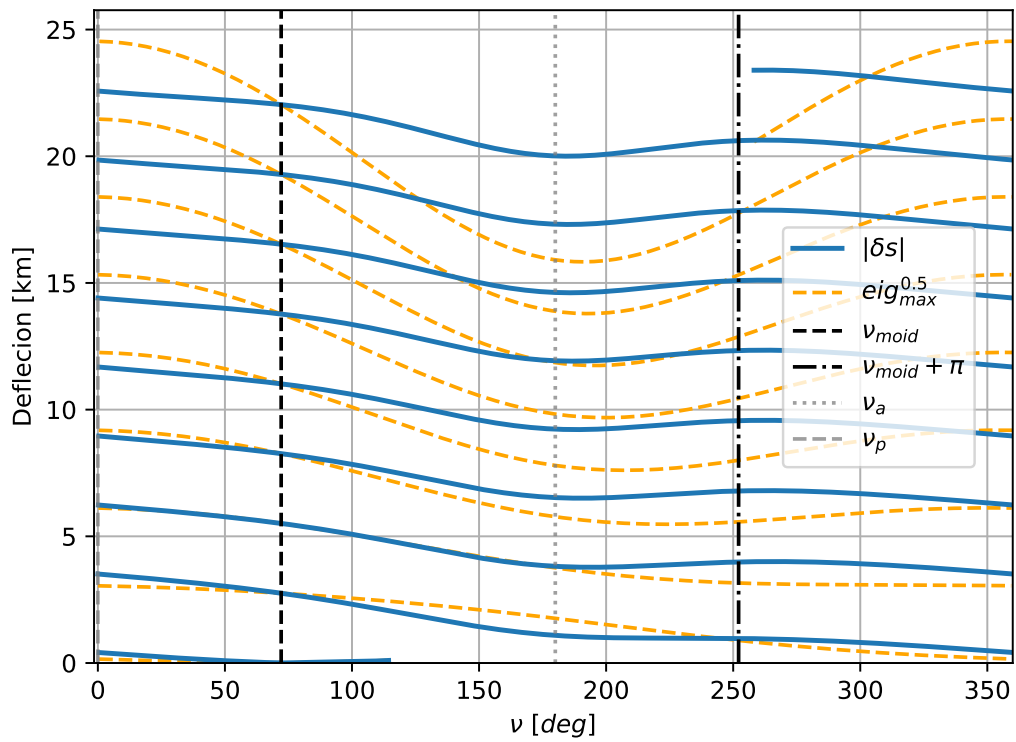
where R_E is the Earth's radius at 6378 km, f_∞ is the gravitational focusing factor [68], $\gamma = 1.25$ is an additional safety factor, and $V_{rel,M}$ is the magnitude of Earth-asteroid relative velocity at MOID. The required deflection value in this case is 16058 km at the time of first deflection, this value changes as semi-major axis and momentary mean anomaly change with every deflection effort. In the case presented here, a ΔV_A in direction of velocity reduces f_∞ with every deflection effort and a ΔV_A in the direction opposite to the deflection direction increases it. However, for the case presented in Figure 4.61 the relative velocity at MOID increases from $6.393 \text{ km}\cdot\text{s}^{-1}$ to $6.396 \text{ km}\cdot\text{s}^{-1}$, leading to a decrease in f_∞ from 2.014 to 2.013 and in the final required deflection distance to be 16053 km, a 5 km change, which is significantly smaller than the overall deflection needed. The other cases presented in this paper show the same magnitude of changes for the required deflection distance.

In single effort kinetic interception, both ΔV_A in and opposite the asteroid's velocity direction reach the same deflection result. In a multiple deflection scheme there is importance in consistency of the deflection result. The scheme presented here calculates both δs possibilities and selects the ΔV_A that continues the trend of overall Δs . Thus, no deflection effort disrupts the deflection reached thus far.

Row iii in Table 4.3 presents the overall results for the deflection seen in Figure 4.61. The time to deflection represents the time from initial deflection to time of deflected distance reaching the



(a) Time to MOID



(b) By true anomaly

Figure 4.60: Deflection reached for single launch

required magnitude. This result includes the changes to f_∞ . In addition to the number of deflection efforts applied, the table includes the overall deflection velocity change, $\Sigma|\Delta V_A|$, which is the sum of all single deflection efforts, the equivalent single deflection reached, $|\delta s_{eq}|$, which represents the deflection that would have been achieved if $\Sigma|\Delta V_A|$ was applied at the time of first deflection (time to MOID), the total change to asteroid angular velocity, $\Sigma\delta\omega$, based on a value of $\delta\omega = 10^{-8} \text{ s}^{-1}$ ⁵, and the total change to rotation period. For the case seen in Figure 4.61 and in Table 4.3 row iii 948 boulders were launched over the span of 2.6 years. Giving over 7 years for deflection corrections if needed. Figure 4.62 presents the evolution of orbital elements throughout the deflection effort. The semi-major axis and momentary mean anomaly are most affected by the deflection effort. The out-of-orbital plane elements do not change at all, demonstrating that the ΔV_A applied is completely in the orbital plane.

Table 4.3 presents results for similar cases, identical in all parameter except time to MOID (rows i-v). These results show an exponential increase in number of launches needed to reach deflection within the given time frame. For the cases of 5 and 3 years to MOID the frequency of launches had to be increased in order of reaching deflection before MOID.

Row vi in Table 4.3 presents the deflection results when ΔV_A is applied opposite to the asteroid velocity. The results are similar to the nominal case (iii), with slightly poorer performance, mostly due to the initial Δs being in the opposite direction of deflection, and due to the increase, rather than reduction, in f_∞ .

The performance of different launch intervals is presented in Figures 4.63-4.64 and in Table 4.3 rows vii-viii. As expected, more frequent launches reach deflection substantially faster and with less overall launch intervals required. An interesting phenomena can be observed for the 2 day launch interval case: a plateau can be observed around 5 years to MOID. This is the result of the added δs efforts contributing less to the overall deflection until the direction of ΔV_A flips with respect to the asteroid's velocity. This flip can be seen in the semi-major axis, eccentricity, and

⁵ The results in the previous section show a single 5.6 meter boulder launched from the surface of Bennu reduces the rotation rate of the asteroid at about 0.5×10^{-8} to $1.5 \times 10^{-8} \text{ s}^{-1}$.

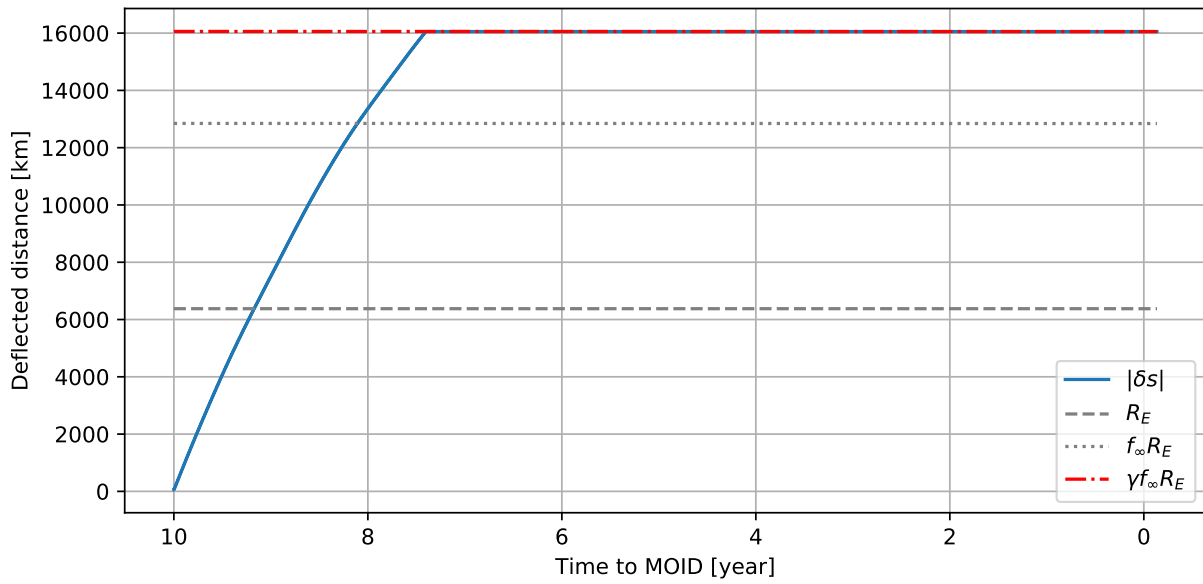


Figure 4.61: Reached deflection in 10 year scenario

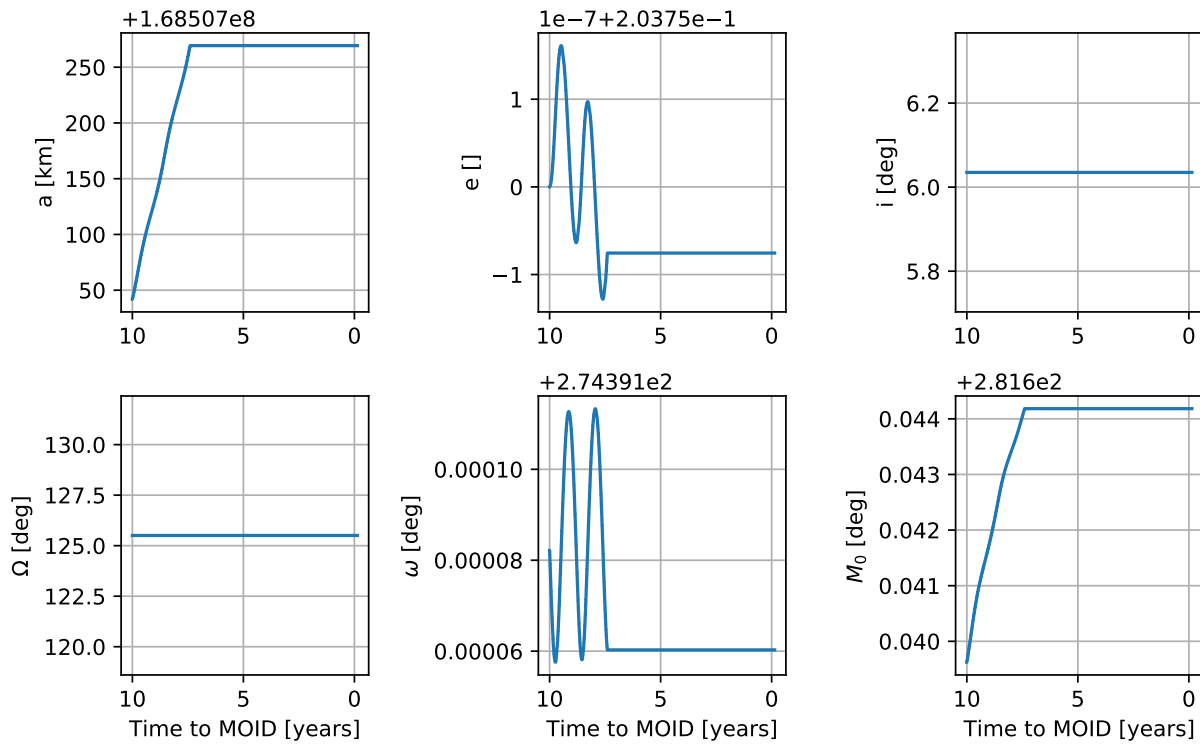


Figure 4.62: Orbit element evolution in 10 year scenario

argument of periapsis of the 2 day launch interval in Figure 4.64. This type of behavior is also seen in the 5 and 3 years to MOID cases and in the lower ΔV_A magnitude case in row x. The deflection reached for different ΔV_A magnitudes is presented in Figures 4.65-4.66 and in rows ix and x. Due to the similar double and half ratios from nominal, the changed interval and changed ΔV_A results show the same ratios with the nominal case. Which demonstrates possible design trade-offs between launch ability and number of launches or launchers needed for deflection.

The launch direction analysis in Figure 4.15 shows a possible $\Delta \mathbf{V}_A$ direction error of several degrees compared to the required $\Delta \hat{\mathbf{V}}^*$ direction. Figure 4.67 presents the deflection results for the nominal 10 years to MOID case with a 5 degree error in the $\Delta \mathbf{V}_A$ direction. Two cases are examined, an in-plane bias and an out-of-plane bias, both consistent between intervals with respect to the calculated eigenvector direction. The correlating results also appear in Table 4.3 rows xi-xii. The deflection results with errors show an additional $\sim 1\%$ launches needed to reach deflection, with the out-of-plane error performing slightly better than in-plane error. The launch error cases' orbital element evolution seen in Figure 4.68 show similar results to the nominal case with negligible out-of-plane changes in the out-of-plane case.

Figures 4.69-4.70 present the results of 10 years to MOID deflection of an eccentric orbit Bennu-like asteroid. Its orbital elements at MOID presented in Table 4.4 (the Earth's state remains the same as in previous cases). The required deflection distance of 12006 km is reached in 260 launches ($\Delta V_A=0.02$ mm/s, launch once a day), or 0.715 years, demonstrating that deflection of an eccentric orbit PHO requires less overall ΔV for success.

In Figure 4.60 local minima in deflection results can be observed, these local minimum deflection basins are presented in Figure 4.71. A maximum efficiency launch scheme is examined and presented in Figures 4.72-4.73 and Table 4.3 row xiii. This launch scheme does not permit launching boulders when the deflection reached is a local minima. The minimum one day interval between launches is still implemented. The 'efficient launch' results reach deflection with 71% more launches and 5 years after the nominal case. This result shows the importance of an early launch vs a locally optimal launch, meaning that the lander-thruster system or systems should have the ability to

	Time to MOID [y]	Launch interval [d]	$ \Delta V_A $ [mm·s ⁻¹]	Time to deflection [y]	Number of launches	$\Sigma \Delta V_A $ [mm·s ⁻¹]	$ \delta s_{eq} $ [km]	$\Sigma\delta\omega$ [s ⁻¹]	δP [s]
i	20	1	0.02	1.01	369	7.38	16430	-3.69×10^{-6}	141.9
ii	15	1	0.02	1.42	517	10.34	17412	-5.17×10^{-6}	199.6
iii	10	1	0.02	2.60	948	18.96	22153	-9.48×10^{-6}	369.9
iv	5	0.5	0.02	4.35	3177	63.54	37687	-31.77×10^{-6}	1313
v	3	0.125	0.02	1.97	5756	115.12	37928	-57.56×10^{-6}	2555.7
vi	10	1	0.02 in - \hat{V}	2.62	957	19.14	22363	-9.57×10^{-6}	373.5
vii	10	2	0.02	8.69	1585	31.70	37081	-15.85×10^{-6}	628.6
viii	10	0.5	0.02	1.08	790	15.80	18482	-7.90×10^{-6}	307.0
ix	10	1	0.04	1.08	395	15.80	18456	-3.95×10^{-6}	152.0
x	10	1	0.01	8.69	3170	31.7	37081	-31.70×10^{-6}	1310.3
xi	10	1	0.02 in-plane err	2.62	957	19.14	22389	-9.57×10^{-6}	373.5
xii	10	1	0.02 out-of-plane err	2.63	958	19.16	22412	-9.58×10^{-6}	373.9
xiii	10	1 launch eff	0.02	7.51	1622	32.44	37947	-16.22×10^{-6}	643.9

Table 4.3: Launch scenario deflection results

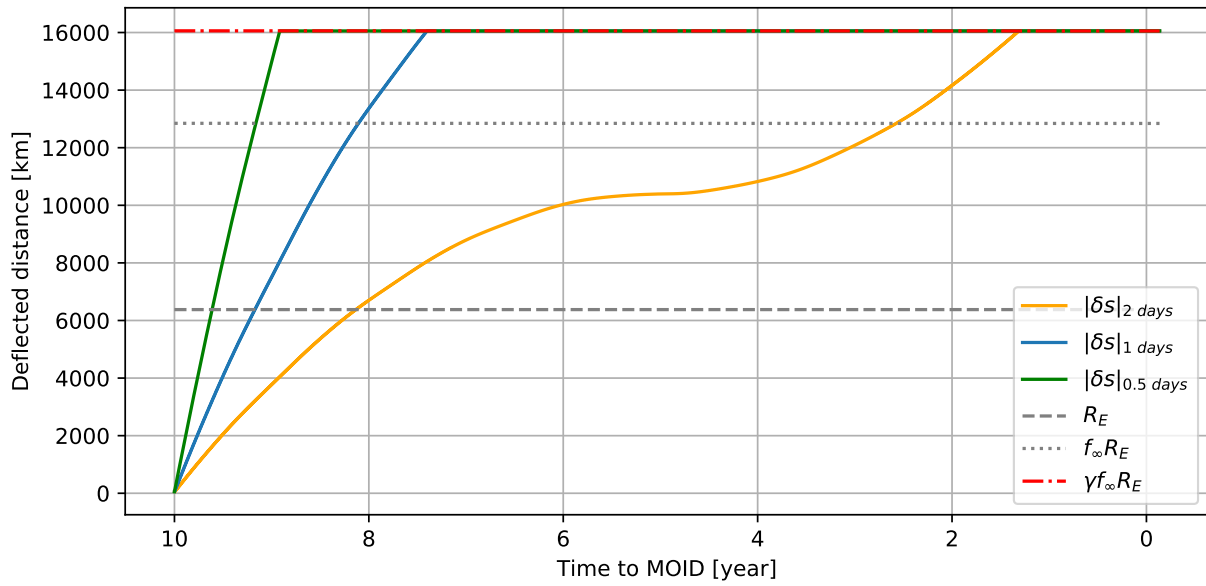


Figure 4.63: Reached deflection in 10 year scenario with varying launch intervals

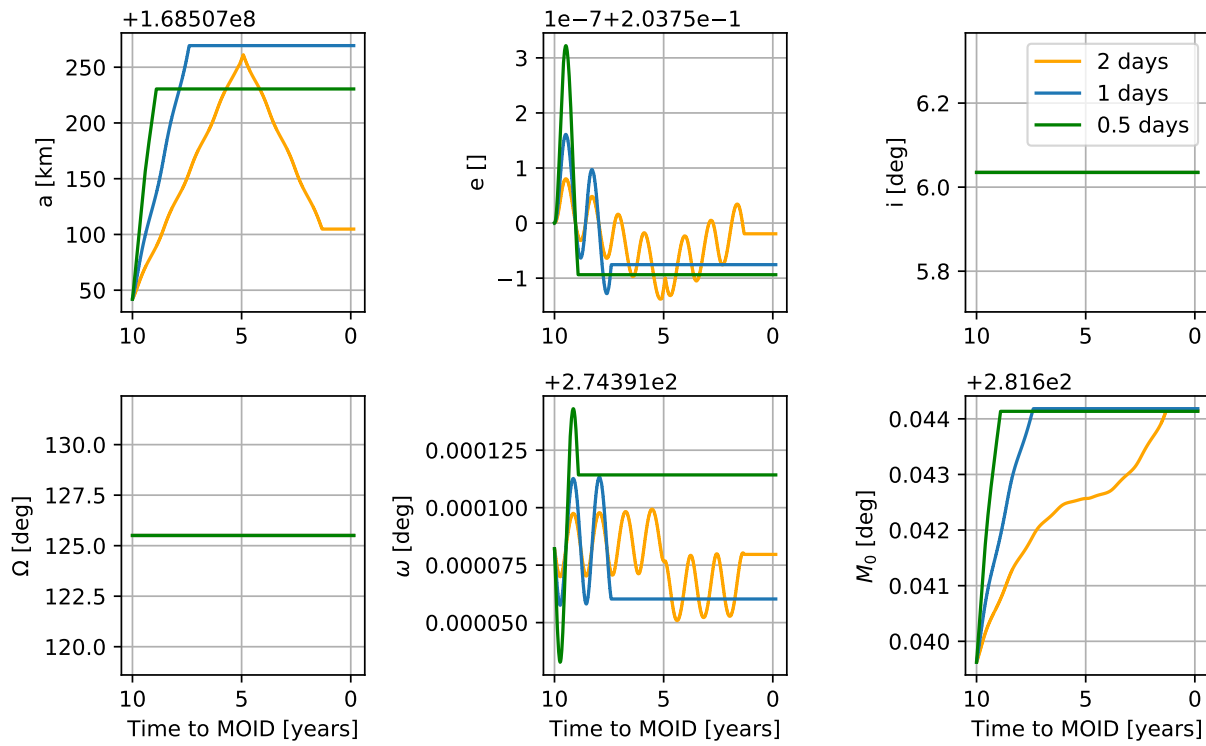


Figure 4.64: Orbit element evolution in 10 year scenario with varying launch intervals

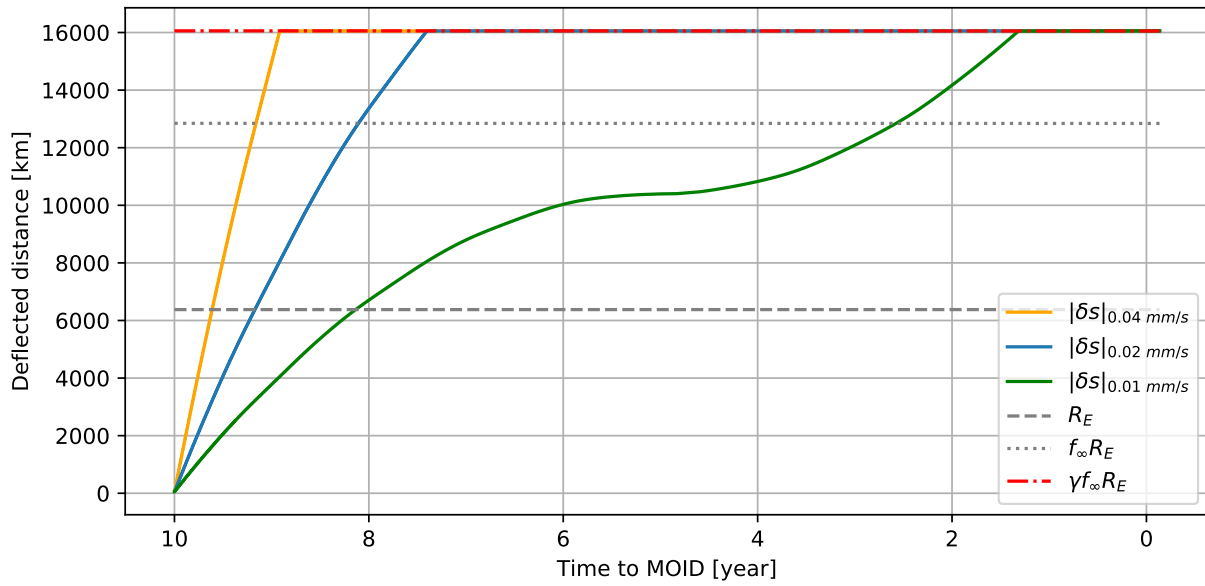


Figure 4.65: Reached deflection in 10 year scenario with varying launch ΔV s

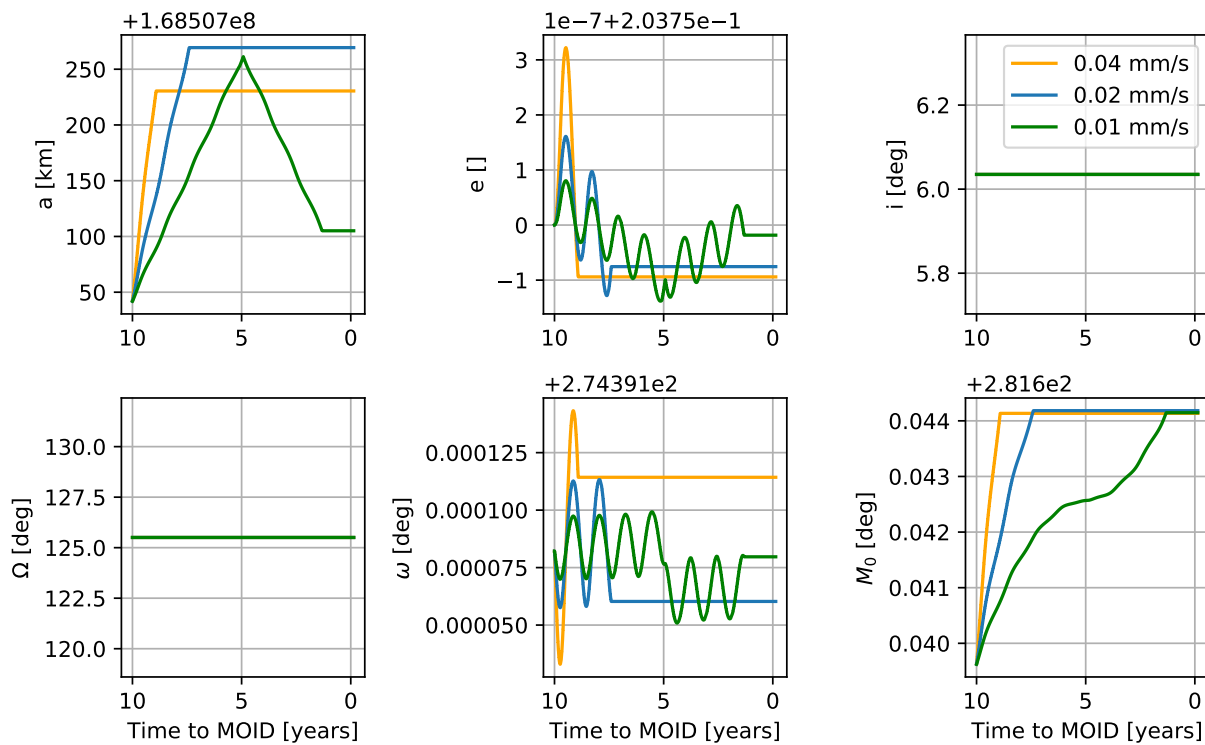


Figure 4.66: Orbit element evolution in 10 year scenario with varying launch ΔV s

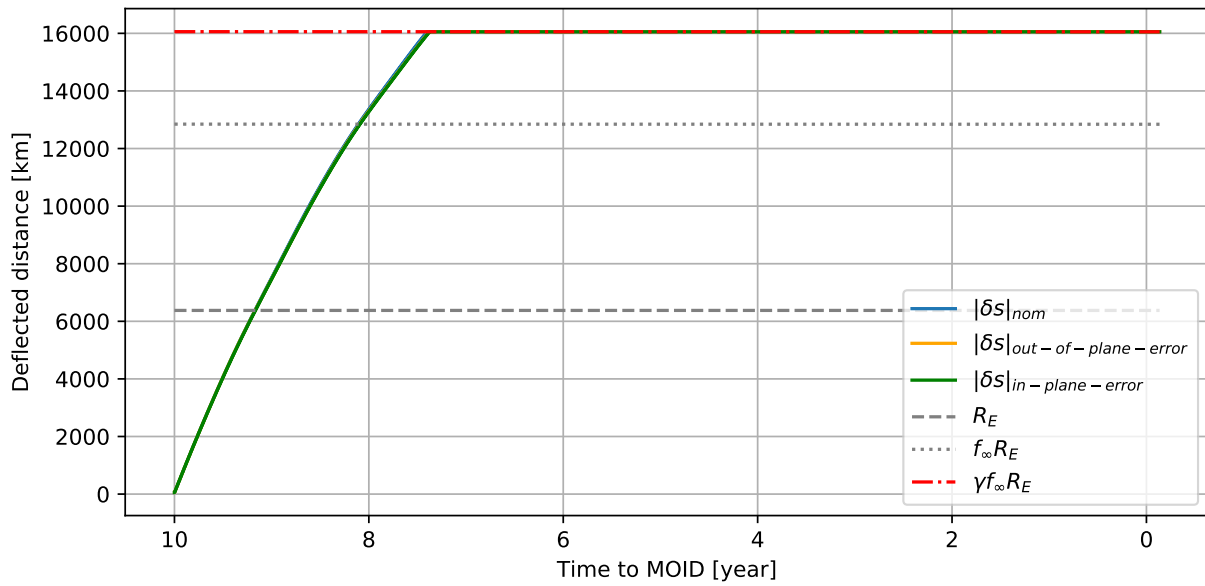


Figure 4.67: Reached deflection in 10 year scenario with 5 degree $\Delta\hat{V}$ bias

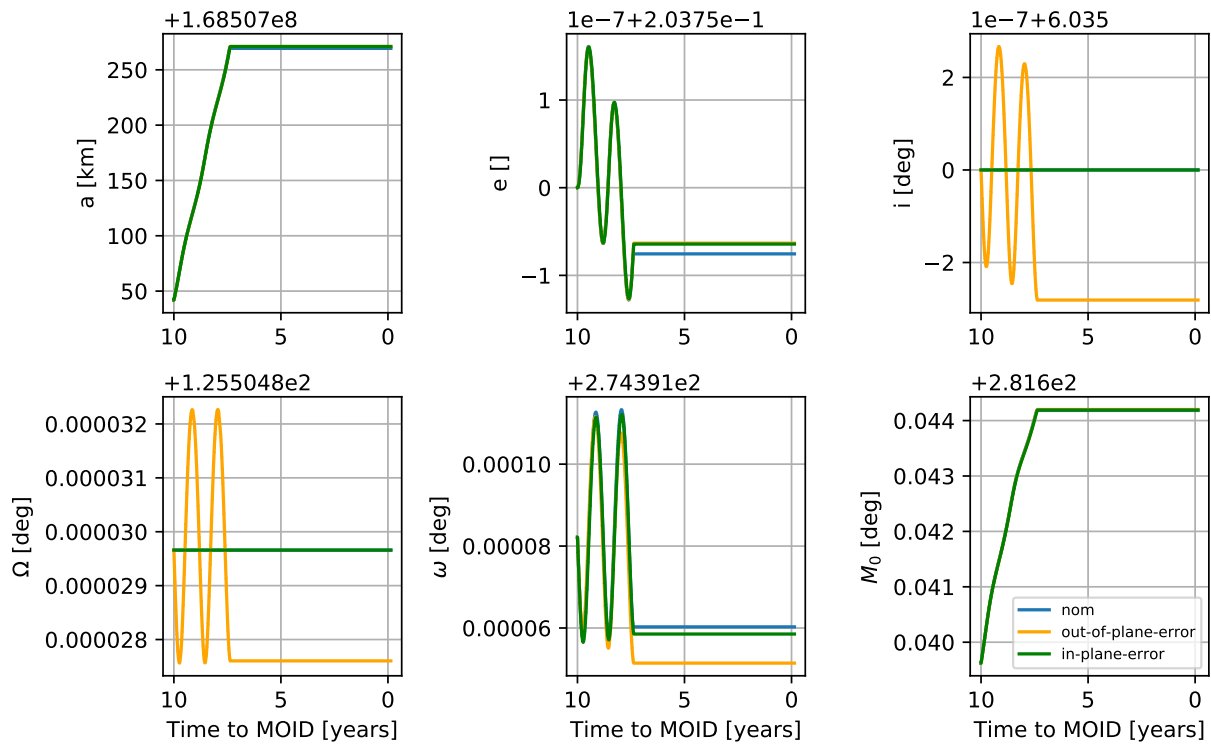


Figure 4.68: Orbit element evolution in 10 year scenario with 5 degree $\Delta\hat{V}$ bias

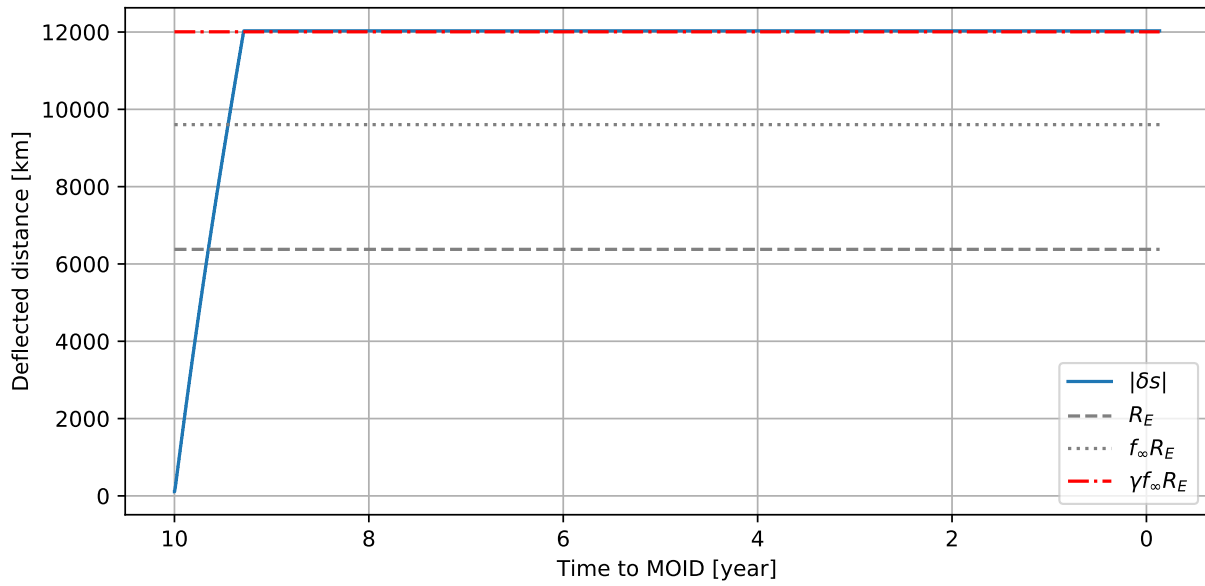


Figure 4.69: Reached deflection in 10 year scenario of eccentric orbit

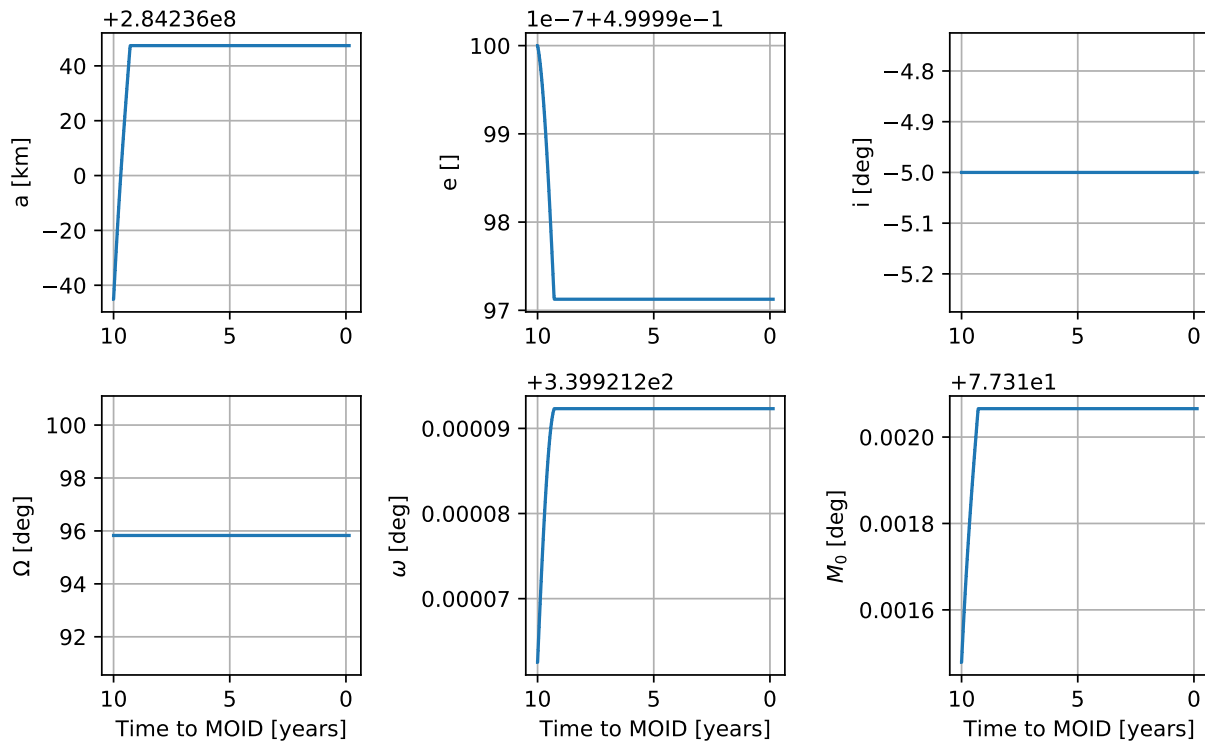


Figure 4.70: Orbit element evolution in 10 year scenario of eccentric orbit

	a [AU]	e []	i [deg]	Ω [deg]	ω [deg]	ν [deg]
Asteroid	1.9	0.5	-5.0	95.8282	339.9212	36.4082

Table 4.4: MOID orbital state for eccentric asteroid

launch as soon as possible.

4.2.7 Mass driver deflection effects on Yarkovsky and YORP

A concern that might arise from the MD deflection efforts is a drastic change in the PHO's natural state evolution drivers, mainly the orbital Yarkovsky and YORP effects. When looking at asteroids like Bennu, which spin axis is almost parallel to its orbit plane at an obliquity of 178 degrees [1] the diurnal effect contributes the majority of change to orbital semi-major axis. For asteroid Bennu's current state [158, 1] the diurnal Yarkovsky semi-major axis rate change (as presented by Vokrouhlicky [24]) is $-0.4297 \text{ km}\cdot\text{year}^{-1}$. When looking at the nominal case presented in Table 4.3 row iii the change to Yarkovsky rate after applying all deflection efforts is $-0.4311 \text{ km}\cdot\text{year}^{-1}$, an added $1.30 \text{ m}\cdot\text{year}^{-1}$ to the semi-major axis change rate. For the most extreme case, presented in Table 4.3 row v, the change to Yarkovsky rate is $-0.4378 \text{ km}\cdot\text{year}^{-1}$, with an added $8.02 \text{ m}\cdot\text{year}^{-1}$ to the semi-major axis reduction rate. These Yarkovsky driven changes are 7 orders of magnitude smaller than the overall deflection distance reached and 6 orders of magnitude smaller than the change to semi-major axis observed. Thus, it is safe to assume that in the time scales discussed in this paper the effect on the Yarkovsky effect for a typical PHO is negligible compared to the deflection itself.

The observed YORP change rate for Bennu's presented in Table 3.6 is equivalent to $7.3407 \times 10^{-13} \text{ s}^{-1}$ per day in the accelerating direction [1]. Thus, a single launch event, at $\delta\omega = -10^{-8} \text{ s}^{-1}$ is equal to 37.3 years of YORP in the decelerating direction. The nominal case presented in Table 4.3 row iii is equivalent to 35381 years of decelerating YORP, and the 3 years to MOID case (row v) is equivalent to 214826 years of decelerating YORP. It is important to note that the YORP change

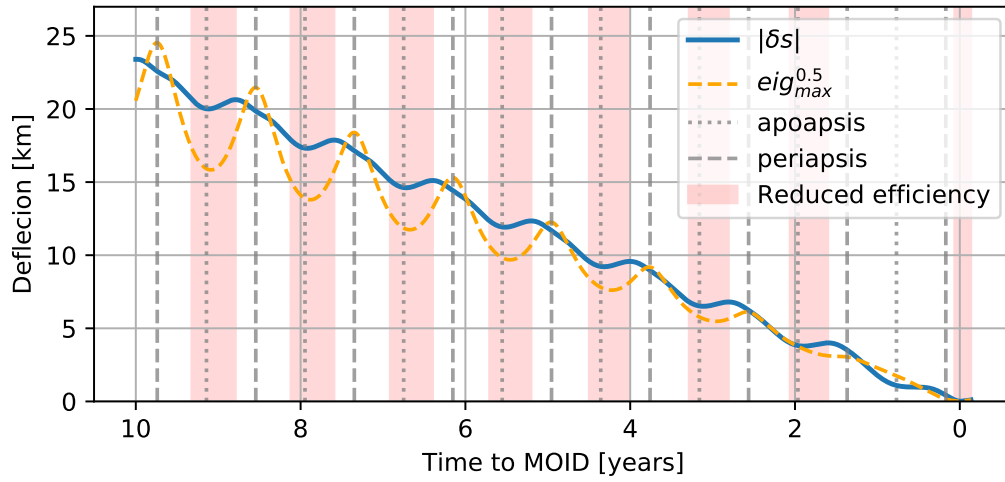


Figure 4.71: Deflection reached for single launch with local minima presented

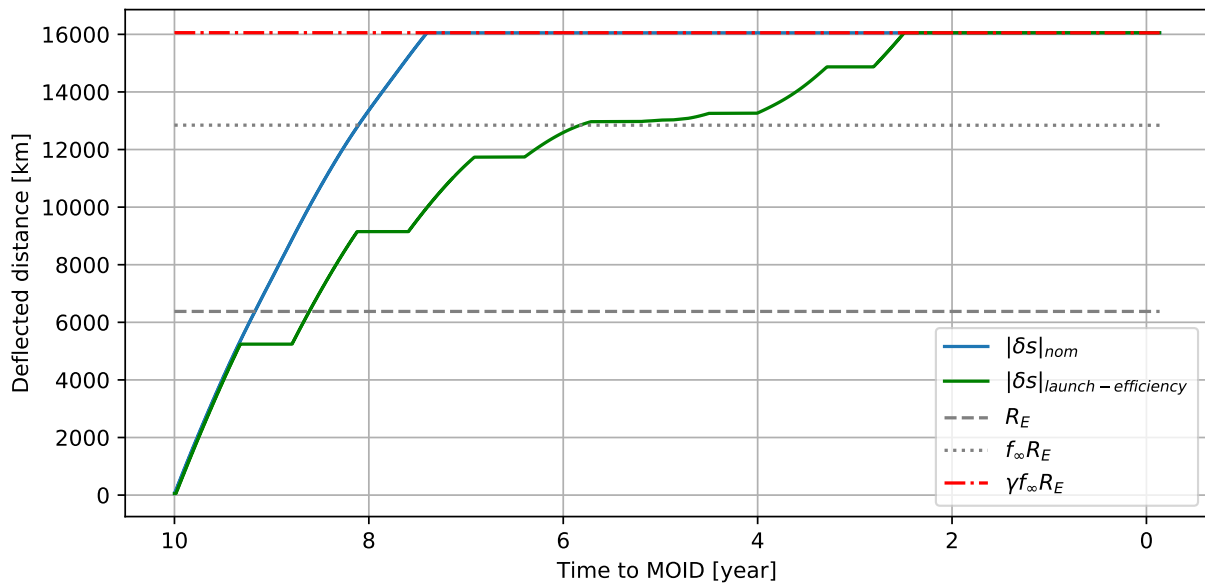


Figure 4.72: Reached deflection in 10 year scenario with maximum efficiency launch scheme

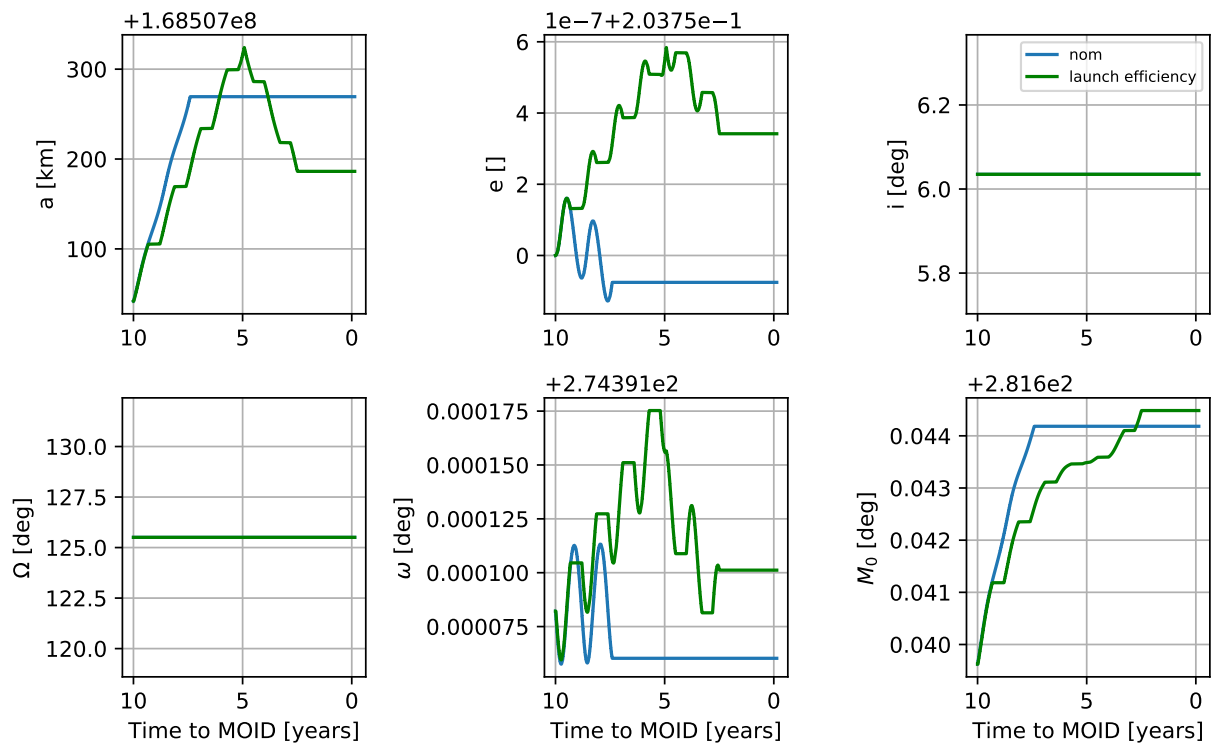


Figure 4.73: Orbit element evolution in 10 year scenario with maximum efficiency launch scheme

rate itself is a function of the rotation rate, and thus these calculations are only approximate. These changes are not negligible and might cause unexpected changes to the asteroid's structure. However, given that the deflection effort rotation rate change is always decelerating the asteroid it can be assumed that no catastrophic event, such as rotational fission would occur.

4.2.8 Insights into engineering mass driver deflection

The work presented here develops a linearized model for small deviations in angular velocity and inertia tensor for a PAR. Which is then applied for boulder launches off asteroids for different rotation manipulation purposes. Boulders can be launched in a variety of directions and thrust magnitudes while keeping the asteroids PAR characteristic. A desired outcome in multiple launch operational schemes in which any disturbance to the asteroid's rotation could mean a failed mission or catastrophic change in the asteroid state. Launch events can also be designed to maximize asteroid tumbling.

The linear model to boulder launching is then examined for asteroid deflection purposes with criteria for boulder selection identified. The work shows that while launching boulders for MD deflection it is preferable to maximize the launch velocity, even at the expense of optimizing launch direction. However, surface areas that geometrically optimize launch direction and thus maximize contribution of the launch to deflection can be identified. The optimized contribution to deflection is geographical, and not by boulder type, thus allowing a wide variety of boulders to be used for the deflection. The effect each launch has on the asteroid's rotation rate is not negligible, but with proper selection of boulder size, location and launch direction it can be minimized. The change in rotation rate provided by the boulder launch is decelerating in nature, thus, reducing the risk of a catastrophic structural change to the asteroid. A complete PHO MD deflection campaign presented in this section seeks to optimize the MD deflection's launches. It shows that, with current state of the art detection and action time frames, deflection is possible using MD. The variety of launching schemes examined show a flexibility in this method, allowing for course corrections and additional

deflection efforts if needed. Small pointing errors in launches show to have little effect on the overall deflection effort. The results also show that an 'early as possible' and highest frequency approach is best for MD deflection as it require less launch intervals for success. This indicates that while using the MD deflection a degree of autonomy should be given to the launching system or systems to launch boulders as soon as possible.

Chapter 5

Future work

This chapter presents possible expansion for the work presented in this dissertation.

5.1 The SEA RATS model

5.1.1 Modeling landslides and regolith motion

Currently, the manipulations that the SEA RATS model can perform in the asteroid model polyhedral parent body only enable a fission event to occur. Enabling other manipulations of the polyhedral shape such as local surface reshaping or small scale complete axis ratio change would allow modeling events such as landslides or the slow creep of material due to seismic shaking. This ability expansion requires monitoring the geopotential of test points inside the parent body polyhedral shape for motion conditions. Additionally, a polyhedral reshaping algorithm is required to adhere to conservation of mass, perhaps through conservation of volume.

5.1.2 Modeling long term processes

The events modeled in this dissertation are very fast in asteroid lifetime scales, hours and days. Expanding the model to simulate processes that occur in many year time scales would allow an examination of the shape's interaction with the YORP and Yarkovsky effects. In order of adding this ability some kind of averaged rotation dynamics would have to be incorporated into the model. These dynamics would connect well with the polyhedral reshaping

capabilities. Additionally, the evolving shape and rotation state should be connected to evolving YORP coefficients, modeling the feedback loop between rotation and shape in long time scales.

5.1.3 Expanding analysis tools

The analysis parameters used in this dissertation rely mostly on the state of the asteroid angular velocity vector, its mass distribution, and its surface slopes. These parameters do not observe the change in dynamical environment above the asteroid surface. Adding an ability to plot the orbital equilibrium points around the asteroid and asteroid Roche Lobe as they change with the angular velocity evolution could provide insights into the fate of material that is ejected from the surface.

5.2 Further investigations of momentum transfer deflection

The work presented in this dissertation only examined one set of kinetic impactor deflection characteristics and one set of nuclear deflection characteristics. Many deflecting spacecraft variables, such as impactor size and relative velocity, or nuclear detonation magnitude, as well as PHO variables such as specific interface location martial composition, density, and grain-size have not been fully examined and require further research. Additional PHO shapes, sizes, shape model resolutions, internal structures, and momentum enhancement β factors should be examined to make work presented here more complete. Specifically an analysis of existing craters should be preformed as crater formation processes might provide the characteristics required for successful deflection. The type of analysis presented should also be expanded to the orbital geometry of asteroid deflection, linking the incoming deflection spacecraft direction with the required ΔV direction, and asteroid rotational state.

Additionally, once available, an investigation of the results of the DART mission into the initial change in rotation should be attempted to further expand the discussion on the relationship be-

tween PHO deflection and PHO rotational state.

5.3 Expanding the orbital dynamics guidance of mass driver deflection

The guidance law used for finding launch directions in the MD deflection case was designed to be optimal for one time kinetic interception deflection. An attempt to expand to optimization for MD deflection based on local minima has proven unsuccessful in this dissertation. Further investigations into MD deflection orbital dynamics should be performed in order of optimizing the capability of deflecting an asteroid with small discrete thrusts.

Bibliography

- [1] DS Lauretta, DN DellaGiustina, CA Bennett, DR Golish, KJ Becker, SS Balram-Knutson, OS Barnouin, TL Becker, WF Bottke, WV Boynton, et al. The unexpected surface of asteroid (101955) bennu. Nature, 568(7750):55, 2019.
- [2] Seiichiro Watanabe, M Hirabayashi, N Hirata, Na Hirata, R Noguchi, Y Shimaki, H Ikeda, E Tatsumi, M Yoshikawa, S Kikuchi, et al. Hayabusa2 arrives at the carbonaceous asteroid 162173 ryugu - a spinning top-shaped rubble pile. Science, 364(6437):268–272, 2019.
- [3] Thomas G. Muller, Josef Durech, Masateru Ishiguro, Michael Mueller, Thomas Kruhler, Hao Yang, Myung-Jin Kim, Laurence O’Rourke, Fumihiko Usui, Casba Kiss, et al. Hayabusa-2 mission target asteroid 162173 ryugu (1999 ju3): Searching for the object’s spin-axis orientation. Astronomy & Astrophysics, 599:A103, 2017.
- [4] Hideaki Miyamoto, Hajime Yano, Daniel J. Scheeres, Shinsuke Abe, Olivier Barnouin-Jha, Andrew F. Cheng, Hirohide Demura, Robert W. Gaskell, Naru Hirata, Masateru Ishiguro, et al. Regolith migration and sorting on asteroid itokawa. Science, 316(5827):1011–1014, 2007.
- [5] NASA and University of Arizona. Osiris-rex mission website, 2019.
- [6] Jaxa hayabusa2 mission update.
- [7] Daniel J. Scheeres. Rotational fission of contact binary asteroids. Icarus, 189(2):370–385, 2007.
- [8] Clark R. Chapman. Asteroid collisions, craters, regoliths, and lifetimes. 1978.
- [9] Derek C. Richardson, Zoe M. Leinhardt, H.J ay Melosh, William F. Bottke, and Erik Asphaug. Gravitational aggregates: evidence and evolution. Asteroids III, 1:501–515, 2002.
- [10] Alan W. Harris, Eugene G. Fahnestock, and Petr Pravec. On the shapes and spins of rubble pile asteroids. Icarus, 199(2):310–318, 2009.
- [11] Emilien Azéma, Paul Sánchez, and Daniel J Scheeres. Scaling behavior of cohesive self-gravitating aggregates. Physical Review E, 98(3):030901, 2018.
- [12] Alan W. Harris. On the slow rotation of asteroids. Icarus, 156(1):184–190, 2002.
- [13] Paul Sanchez and Daniel J. Scheeres. The strength of regolith and rubble pile asteroids. Meteoritics & Planetary Science, 49(5):788–811, 2014.

- [14] Ben Rozitis, Eric MacLennan, and Joshua P Emery. Cohesive forces prevent the rotational breakup of rubble-pile asteroid (29075) 1950 da. *Nature*, 512(7513):174, 2014.
- [15] Daniel J. Scheeres, Christine M. Hartzell, Paul Sanchez, and Michael J. Swift. Scaling forces to asteroid surfaces: The role of cohesion. *Icarus*, 210(2):968 – 984, 2010.
- [16] Keith A Holsapple. Spin limits of solar system bodies: From the small fast-rotators to 2003 el61. *Icarus*, 187(2):500–509, 2007.
- [17] DJ Scheeres, JW McMahon, AS French, DN Brack, SR Chesley, D Farnocchia, Y Takahashi, JM Leonard, J Geeraert, B Page, et al. The dynamic geophysical environment of (101955) bennu based on osiris-rex measurements. *Nature Astronomy*, page 1, 2019.
- [18] Daniel J. Scheeres. Minimum energy asteroid reconfigurations and catastrophic disruptions. *Planetary and Space Science*, 57(2):154 – 164, 2009. Catastrophic Disruption in the Solar System.
- [19] Daniel J. Scheeres. Landslides and mass shedding on spinning spheroidal asteroids. *Icarus*, 247:1 – 17, 2015.
- [20] Petr Pravec, Alan W. Harris, and Tadeusz Michalowski. Asteroid rotations. *Asteroids III*, 1:113–122, 2002.
- [21] Petr Pravec, Alan W. Harris, P. Scheirich, Peter Kusnirak, L. Sarounova, C.W. Hergenrother, S. Mottola, M.D. Hicks, G. Masi, Yu.N. Krugly, V.G. Shevchenko, M.C. Nolan, E.S. Howell, M. Kaasalainen, A. Galad, P. Brown, D.R. DeGraff, J.V. Lambert, W.R. Cooney, and S. Foglia. Tumbling asteroids. *Icarus*, 173(1):108 – 131, 2005. Hapke Symposium.
- [22] Alan Harris. Tumbling asteroids 1993.
- [23] Daniel J Scheeres, Steven J Ostro, RS Hudson, and Robert A Werner. Orbits close to asteroid 4769 castalia. *Icarus*, 121(1):67–87, 1996.
- [24] David Vokrouhlicky, William F. Bottke, Steven R. Chesley, Daniel J. Scheeres, and Thomas S. Statler. The yarkovsky and yorp effects. *Asteroids IV*, 1:509–531, 2015.
- [25] David P. Rubincam. Radiative spin-up and spin-down of small asteroids. *Icarus*, 148(1):2 – 11, 2000.
- [26] Daniel J. Scheeres. The dynamical evolution of uniformly rotating asteroids subject to yorp. *Icarus*, 188(2):430 – 450, 2007.
- [27] Daniel J. Scheeres and Sepidehsadat Mirrahimi. Rotational dynamics of a solar system body under solar radiation torques. *Celestial Mechanics and Dynamical Astronomy*, 101(1):69–103, May 2008.
- [28] William F. Bottke, David Vokrouhlicky, David P. Rubincam, and David Nesvorny. The yarkovsky and yorp effects: Implications for asteroid dynamics. *Annu. Rev. Earth Planet. Sci.*, 34:157–191, 2006.
- [29] William F. Bottke, Miroslav Broz, David P. O’Brien, Adriano Campo Bagatin, Alessandro Morbidelli, and Simon Marchi. The collisional evolution of the main asteroid belt. *Asteroids IV*, 1:701–724, 2015.

- [30] Andrew F. Cheng, Noam Izenberg, Clark R. Chapman, and Maria T. Zuber. Pondered deposits on asteroid 433 eros. *Meteoritics & Planetary Science*, 37(8):1095–1105, 2002.
- [31] James E Richardson, H Jay Melosh, and Richard Greenberg. Impact-induced seismic activity on asteroid 433 eros: A surface modification process. *science*, 306(5701):1526–1529, 2004.
- [32] Anthony R Dobrovolskis and Joseph A Burns. Angular momentum drain: A mechanism for despinning asteroids. *Icarus*, 57(3):464–476, 1984.
- [33] Daniel J. Scheeres, Francesco Marzari, and Alessandro Rossi. Evolution of neo rotation rates due to close encounters with earth and venus. *Icarus*, 170(2):312 – 323, 2004.
- [34] Daniel J. Scheeres, Steven J. Ostro, Robert A. Werner, Erik Asphaug, and R.Scott Hudson. Effects of gravitational interactions on asteroid spin states. *Icarus*, 147(1):106 – 118, 2000.
- [35] Kevin J. Walsh and Derek C. Richardson. Binary near-earth asteroid formation: Rubble pile model of tidal disruptions. *Icarus*, 180(1):201 – 216, 2006.
- [36] Yang Yu, Derek C Richardson, Patrick Michel, Stephen R Schwartz, and Ronald-Louis Balouz. Numerical predictions of surface effects during the 2029 close approach of asteroid 99942 apophis. *Icarus*, 242:82–96, 2014.
- [37] Joseph V DeMartini, Derek C Richardson, Olivier S Barnouin, Nicholas C Schmerr, Jeffrey B Plescia, Petr Scheirich, and Petr Pravec. Using a discrete element method to investigate seismic response and spin change of 99942 apophis during its 2029 tidal encounter with earth. *Icarus*, 328:93–103, 2019.
- [38] Joseph A. Burns, V. S. Safronov, and T. Gold. Asteroid nutation angles. *Monthly Notices of the Royal Astronomical Society*, 165(4):403–411, 1973.
- [39] David Jewitt, Henry Hsieh, and Jessica Agarwal. Asteroids iv, the active asteroids, 2015.
- [40] David Jewitt. The active asteroids. *Astronomical Journal*, 2012.
- [41] Man-To Hui and David Jewitt. Non-gravitational acceleration of the active asteroids. *The Astronomical Journal*, 153(2):80, 2017.
- [42] David Jewitt, Harold Weaver, Max Mutchler, Jing Li, Jessica Agarwal, and Stephen Larson. The nucleus of active asteroid 311p/(2013 p5) panstarrs. *The Astronomical Journal*, 155(6):231, 2018.
- [43] David Jewitt, Jessica Agarwal, Harold Weaver, Max Mutchler, and Stephen Larson. Episodic ejection from active asteroid 311p/panstarrs. *The Astrophysical Journal*, 798(2):109, 2015.
- [44] Kavan Hazeli, Charles El Mir, Stefanos Papanikolaou, Marco Delbo, and K.T. Ramesh. The origins of asteroidal rock disaggregation: Interplay of thermal fatigue and microstructure. *Icarus*, 304:172 – 182, 2018. Asteroids and Space Debris.
- [45] David Jewitt, Jessica Agarwal, Jing Li, Harold Weaver, Max Mutchler, and Stephen Larson. Anatomy of an asteroid breakup: The case of p/2013 r3. *The Astronomical Journal*, 153(5):223, 2017.

- [46] Naomi Murdoch, Paul Sanchez, Stephen R. Schwartz, and Hideaki Miyamoto. Asteroids iv, asteroid surface geophysics, 2015.
- [47] Masatoshi Hirabayashi, Eri Tatsumi, Hideaki Miyamoto, Goro Komatsu, Seiji Sugita, Seichiro Watanabe, Daniel J Scheeres, Olivier S Barnouin, Patrick Michel, Chikatoshi Honda, et al. The western bulge of 162173 ryugu formed as a result of a rotationally driven deformation process. The Astrophysical Journal Letters, 874(1):L10, 2019.
- [48] Louise Prockter, Peter Thomas, Mark Robinson, Jonathan Joseph, Ashley Milne, Ben Bussey, Joseph Veverka, and Andrew Cheng. Surface expressions of structural features on eros. Icarus, 155(1):75–93, 2002.
- [49] MS Robinson, PC Thomas, J Veverka, S Murchie, and B Carcich. The nature of ponded deposits on eros. Nature, 413(6854):396, 2001.
- [50] MS Robinson, PC Thomas, J Veverka, SL Murchie, and BB Wilcox. The geology of 433 eros. Meteoritics & Planetary Science, 37(12):1651–1684, 2002.
- [51] Andrew J Dombard, Olivier S Barnouin, Louise M Prockter, and Peter C Thomas. Boulders and ponds on the asteroid 433 eros. Icarus, 210(2):713–721, 2010.
- [52] KJ Walsh, ER Jawin, R-L Ballouz, OS Barnouin, EB Bierhaus, HC Connolly, JL Molaro, TJ McCoy, M Delbo, CM Hartzell, et al. Craters, boulders and regolith of (101955) bennu indicative of an old and dynamic surface. Nature Geoscience, page 1, 2019.
- [53] S Sugita, R Honda, T Morota, S Kameda, H Sawada, E Tatsumi, M Yamada, C Honda, Y Yokota, T Kouyama, et al. The geomorphology, color, and thermal properties of ryugu: Implications for parent-body processes. Science, page eaaw0422, 2019.
- [54] AM Nakamura, T Michikami, N Hirata, Akira Fujiwara, R Nakamura, M Ishiguro, H Miyamoto, H Demura, K Hiraoka, T Honda, et al. Impact process of boulders on the surface of asteroid 25143 itokawa - fragments from collisional disruption. Earth, planets and space, 60(1):7–12, 2008.
- [55] Gonzalo Tancredi, Santiago Roland, and Sebastián Bruzzone. Distribution of boulders and the gravity potential on asteroid itokawa. Icarus, 247:279–290, 2015.
- [56] Michael Küppers, Richard Moissl, Jean-Baptiste Vincent, Sebastien Besse, Stubbe F Hviid, Benoît Carry, Björn Grieger, Holger Sierks, Horst Uwe Keller, Simone Marchi, et al. Boulders on lutetia. Planetary and Space Science, 66(1):71–78, 2012.
- [57] Ronald-Louis Ballouz, Nicola Baresi, Sarah T Crites, Yasuhiro Kawakatsu, and Masaki Fujimoto. Surface refreshing of martian moon phobos by orbital eccentricity-driven grain motion. Nature Geoscience, page 1, 2019.
- [58] Garrett Serviss. Edison’s Conquest of Mars. 1898.
- [59] Daniel D. Mazanek, Raymond G. Merrill, John R. Brophy, and Robert P. Mueller. Asteroid redirect mission concept: a bold approach for utilizing space resources. Acta Astronautica, 117:163–171, 2015.

- [60] Alan W Harris and Germano D’Abramo. The population of near-earth asteroids. Icarus, 257:302–312, 2015.
- [61] Bong Wie. Astrodynamics fundamentals for deflecting hazardous near-earth objects. Paper No. IAC-09-C1, 3:12–16, 2009.
- [62] Thomas J Ahrens and Alan W Harris. Deflection and fragmentation of near-earth asteroids. Nature, 360(6403):429, 1992.
- [63] Alan Harris. Deflection techniques: What makes sense. In 2004 Planetary Defense Conference: Protecting Earth from Asteroids, page 1451, 2004.
- [64] JP Sanchez and Camilla Colombo. Impact hazard protection efficiency by a small kinetic impactor. Journal of Spacecraft and Rockets, 50(2):380–393, 2013.
- [65] Bong Wie. Dynamics and control of gravity tractor spacecraft for asteroid deflection. Journal of guidance, control, and dynamics, 31(5):1413–1423, 2008.
- [66] Claudio Bombardelli and Jesus Peláez. Ion beam shepherd for asteroid deflection. Journal of Guidance, Control, and Dynamics, 34(4):1270–1272, 2011.
- [67] Massimiliano Vasile, Alison Gibbings, Ian Watson, and John-Mark Hopkins. Improved laser ablation model for asteroid deflection. Acta Astronautica, 103:382–394, 2014.
- [68] Daniel J. Scheeres and Russell Schweickart. The mechanics of moving asteroids. In 2004 Planetary Defense Conference: Protecting Earth from Asteroids, page 1446, 2004.
- [69] J. Olds, A. Charania, M. Graham, and J. Wallace. The league of extraordinary machines: A rapid and scalable approach to planetary defense against asteroid impactors. NASA NIAC report, 2004.
- [70] Russell L Schweickart, Edward T Lu, Piet Hut, and Clark R Chapman. The asteroid tugboat. Scientific American, 289(5):54–61, 2003.
- [71] Jason Dunn, Max Fagin, Michael Snyder, and Eric Joyce. Project rama: Reconstructing asteroids into mechanical automata. 2017.
- [72] Jay McMahan. Dismantling rubble pile asteroids with aoes (area-of-effect soft-bots). NASA NIAC report, 2018.
- [73] Arthur M. Dula and Zhang Zhenjun. Space mineral resources: A global assessment of the challenges and opportunities. Space Mineral Resources: A Global Assessment of the Challenges and Opportunities. Study conducted under the auspices of the International Academy of Astronautics (IAA)., 2015.
- [74] Daniel J Scheeres. Minimum energy asteroid reconfigurations and catastrophic disruptions. Planetary and Space Science, 57(2):154–164, 2009.
- [75] Seth A Jacobson and Daniel J Scheeres. Dynamics of rotationally fissioned asteroids: Source of observed small asteroid systems. Icarus, 214(1):161–178, 2011.

- [76] Seth A Jacobson, Francesco Marzari, Alessandro Rossi, and Daniel J Scheeres. Matching asteroid population characteristics with a model constructed from the yorp-induced rotational fission hypothesis. Icarus, 277:381–394, 2016.
- [77] Daniel J. Scheeres. Disaggregation of small, cohesive rubble pile asteroids due to YORP. Icarus, 2017.
- [78] V Guibout and Daniel J. Scheeres. Stability of surface motion on a rotating ellipsoid. Celestial Mechanics and Dynamical Astronomy, 87(3):263–290, 2003.
- [79] XiaoDong Liu, HeXi Baoyin, and XingRui Ma. Dynamics of surface motion on a rotating massive homogeneous body. Science China Physics, Mechanics and Astronomy, 56(4):818–829, 2013.
- [80] Fabio Ferrari, Alessandro Tasora, Pierangelo Masarati, and Michele Lavagna. N-body gravitational and contact dynamics for asteroid aggregation. Multibody System Dynamics, 39(1-2):3–20, 2017.
- [81] Adriano Campo Bagatin, Rafael A. Aleman, Paula G. Benavidez, and Derek C. Richardson. Internal structure of asteroid gravitational aggregates. Icarus, 302:343–359, 2018.
- [82] Patrick Michel, Paolo Tanga, Willy Benz, and Derek C Richardson. Formation of asteroid families by catastrophic disruption: Simulations with fragmentation and gravitational reaccumulation. Icarus, 160(1):10–23, 2002.
- [83] Petr Pravec, Petr Fatka, David Vokrouhlicky, Daniel J. Scheeres, Peter Kusnirak, Kamil Hornoch, Adrian Galad, Jan Vrastil, Donald P. Pray, Yu N. Krugly, et al. Asteroid clusters similar to asteroid pairs. Icarus, 2017.
- [84] Keisuke Sugiura, Hiroshi Kobayashi, and Shu-ichiro Inutsuka. Toward understanding the origin of asteroid geometries-variety in shapes produced by equal-mass impacts. Astronomy & Astrophysics, 620:A167, 2018.
- [85] Derek C Richardson, William F Bottke Jr, and Stanley G Love. Tidal distortion and disruption of earth-crossing asteroids. Icarus, 134(1):47–76, 1998.
- [86] Derek C. Richardson, Pradeep Elankumaran, and Robyn E. Sanderson. Numerical experiments with rubble piles: equilibrium shapes and spins. Icarus, 173(2):349 – 361, 2005.
- [87] Kevin J. Walsh, Derek C. Richardson, and Patrick Michel. Rotational breakup as the origin of small binary asteroids. Nature, 454(7201):188–191, 2008.
- [88] Masatoshi Hirabayashi, Diego Paul Sánchez, and Daniel J Scheeres. Internal structure of asteroids having surface shedding due to rotational instability. The Astrophysical Journal, 808(1):63, 2015.
- [89] DC Richardson, P Michel, KJ Walsh, and KW Flynn. Numerical simulations of asteroids modelled as gravitational aggregates with cohesion. Planetary and Space Science, 57(2):183–192, 2009.
- [90] Paul Sánchez and Daniel J Scheeres. Simulating asteroid rubble piles with a self-gravitating soft-sphere distinct element method model. The Astrophysical Journal, 727(2):120, 2011.

- [91] Paul Sánchez. Asteroid evolution: role of geotechnical properties. Proceedings of the International Astronomical Union, 10(S318):111–121, 2015.
- [92] Anton V Kulchitsky, Jerome B Johnson, and David M Reeves. Resistance forces during boulder extraction from an asteroid. Acta Astronautica, 127:424–437, 2016.
- [93] Yun Zhang, Derek C. Richardson, Olivier S. Barnouin, Patrick Michel, Stephen R. Schwartz, and Ronald-Louis Ballouz. Rotational failure of rubble-pile bodies: Influences of shear and cohesive strengths. The Astrophysical Journal, 857(1):15, 2018.
- [94] Daniel J. Scheeres and Paul Sanchez. Implications of cohesive strength in asteroid interiors and surfaces and its measurement. Progress in Earth and Planetary Science, 5(1):25, May 2018.
- [95] Paul Sánchez and Daniel J Scheeres. Cohesive regolith on fast rotating asteroids. arXiv preprint arXiv:1909.11270, 2019.
- [96] Florian Thuillet, Patrick Michel, Clara Maurel, Ronald-Louis Ballouz, Yun Zhang, Derek C Richardson, Jens Biele, Eri Tatsumi, and Seiji Sugita. Numerical modeling of lander interaction with a low-gravity asteroid regolith surface. 2018.
- [97] James K Miller, AS Konopliv, PG Antreasian, JJ Bordi, S Chesley, CE Helfrich, WM Owen, TC Wang, BG Williams, DK Yeomans, et al. Determination of shape, gravity, and rotational state of asteroid 433 eros. Icarus, 155(1):3–17, 2002.
- [98] Stefaan Van Wal and Daniel J. Scheeres. Lift-off velocity on solar-system small bodies. Journal of Guidance, Control, and Dynamics, pages 1–16, 2017.
- [99] Yu Takahashi, Daniel Jay Scheeres, and Robert A Werner. Surface gravity fields for asteroids and comets. Journal of guidance, control, and dynamics, 36(2):362–374, 2013.
- [100] Robert A. Werner and Daniel J. Scheeres. Exterior gravitation of a polyhedron derived and compared with harmonic and mascon gravitation representations of asteroid 4769 castalia. Celestial Mechanics and Dynamical Astronomy, 65(3):313–344, 1996.
- [101] Daniel J. Scheeres, Siamak G. Hesar, Simon Tardivel, Hirabayashi Hirabayashi, Davide Farnocchia, Jay W. McMahon, Steven R. Chesley, Olivier Barnouin, Richard P. Binzel, William F. Bottke, et al. The geophysical environment of bennu. Icarus, 276:116–140, 2016.
- [102] Michael W Busch, Jon D Giorgini, Steven J Ostro, Lance AM Benner, Raymond F Jurgens, Randy Rose, Michael D Hicks, Petr Pravec, Peter Kusnirak, Michael J Ireland, et al. Physical modeling of near-earth asteroid (29075) 1950 da. Icarus, 190(2):608–621, 2007.
- [103] Anthony R Dobrovolskis and DG Korycansky. Internal gravity, self-energy, and disruption of comets and asteroids. Icarus, 303:234–250, 2018.
- [104] Simon Tardivel, Daniel J. Scheeres, Patrick Michel, Stefaan Van wal, and Paul Sanchez. Contact motion on surface of asteroid. Journal of Spacecraft and Rockets, 51(6):1857–1871, 2014.
- [105] Stefaan Van Wal, Simon Tardivel, and Daniel J. Scheeres. Parametric study of ballistic lander deployment to small bodies. Journal of Spacecraft and Rockets, 54(6):1330–1355, 2017.

- [106] Stefaan Van Wal, Yuichi Tsuda, Kent Yoshikawa, Akira Miura, Satoshi Tanaka, and Daniel J. Scheeres. Prearrival deployment analysis of rovers on hayabusa2 asteroid explorer. Journal of Spacecraft and Rockets, pages 1–21, 2018.
- [107] Simon Tardivel, Paul Sanchez, and Daniel J. Scheeres. Equatorial cavities on asteroids, an evidence of fission events. Icarus, 304:192 – 208, 2018. Asteroids and Space Debris.
- [108] Yu Takahashi and DJ Scheeres. Morphology driven density distribution estimation for small bodies. Icarus, 233:179–193, 2014.
- [109] Keith A Holsapple. Equilibrium figures of spinning bodies with self-gravity. Icarus, 172(1):272–303, 2004.
- [110] Keith A Holsapple. On yorp-induced spin deformations of asteroids. Icarus, 205(2):430–442, 2010.
- [111] Masatoshi Hirabayashi, Daniel J Scheeres, Steven R Chesley, Simone Marchi, Jay W McMahon, Jordan Steckloff, Stefano Mottola, Shantanu P Naidu, and Timothy Bowling. Fission and reconfiguration of bilobate comets as revealed by 67p/churyumov–gerasimenko. Nature, 534(7607):352, 2016.
- [112] David Polishook, Nicolas A. Moskovitz, Richard P. Binzel, Brian J. Burt, Francesca E. DeMeo, Mary L. Hinkle, Matthew Lockhart, Michael Mommert, Michael Person, Audrey Thirouin, Cristina A. Thomas, David Trilling, Mark Willman, and Oded Aharonson. A 2 km-size asteroid challenging the rubble-pile spin barrier? a case for cohesion. Icarus, 267:243 – 254, 2016.
- [113] Masatoshi Hirabayashi and Daniel J. Scheeres. Stress and failure analysis of rapidly rotating asteroid 29075-1950da. The Astrophysical Journal Letters, 798(1):L8, 2015.
- [114] Masatoshi Hirabayashi and Daniel J Scheeres. Rotationally induced failure of irregularly shaped asteroids. Icarus, 317:354–364, 2019.
- [115] Charles El Mir, KT Ramesh, and Derek C Richardson. A new hybrid framework for simulating hypervelocity asteroid impacts and gravitational reaccumulation. Icarus, 321:1013–1025, 2019.
- [116] Kevin R Housen and Keith A Holsapple. Impact cratering on porous asteroids. Icarus, 163(1):102–119, 2003.
- [117] Kevin R Housen and Keith A Holsapple. Ejecta from impact craters. Icarus, 211(1):856–875, 2011.
- [118] Keith A Holsapple and Kevin R Housen. Momentum transfer in asteroid impacts. i. theory and scaling. Icarus, 221(2):875–887, 2012.
- [119] Nalin H Samarasinha and Michael F A’Hearn. Observational and dynamical constraints on the rotation of comet p/halley. Icarus, 93(2):194–225, 1991.
- [120] Daniel J. Scheeres. Orbital motion in strongly perturbed environments: applications to asteroid, comet and planetary satellite orbiters. Springer, 2016.

- [121] NASA and University of Arizona. Benu shape model files, 2019.
- [122] Daniel J Scheeres, Steven J Ostro, R Scott Hudson, Eric M DeJong, and Shigeru Suzuki. Dynamics of orbits close to asteroid 4179 toutatis. Icarus, 132(1):53–79, 1998.
- [123] Stefaan Van Wal, Simon Tardivel, Paul Sánchez, Darius Djafari-Rouhani, Daniel Scheeres, et al. Rolling resistance of a spherical pod on a granular bed. Granular Matter, 19(1):17, 2017.
- [124] Kendall E Atkinson. An introduction to numerical analysis. John Wiley & Sons, 2008.
- [125] PJ Valent. Coefficients of friction between calcareous sands and some building materials, and their significance. Technical report, CIVIL ENGINEERING LAB (NAVY) PORT HUENEME CALIF, 1979.
- [126] A Azzoni and MH De Freitas. Experimentally gained parameters, decisive for rock fall analysis. Rock mechanics and rock engineering, 28(2):111–124, 1995.
- [127] David A Vallado. Fundamentals of astrodynamics and applications, volume 12. Springer Science & Business Media, 2001.
- [128] CW Hergenrother, CK Maleszewski, MC Nolan, J-Y Li, CY Drouet d’Aubigny, FC Shelly, ES Howell, TR Kareta, MRM Izawa, MA Barucci, et al. The operational environment and rotational acceleration of asteroid (101955) benu from osiris-rex observations. Nature communications, 10(1):1291, 2019.
- [129] Akira Fujiwara, J Kawaguchi, DK Yeomans, M Abe, T Mukai, T Okada, J Saito, H Yano, M Yoshikawa, DJ Scheeres, et al. The rubble-pile asteroid itokawa as observed by hayabusa. Science, 312(5778):1330–1334, 2006.
- [130] C. W. Hergenrother P. Michel S. Schwartz D. Vokrouhlicky K. Walsh D. S. Lauretta W. F. Bottke, A. Moorhead. Meteoroid impacts as the source of benu’s particle ejection events. In Asteroid Science in the Age of Hayabusa2 and OSIRIS-REx meeting, 2019.
- [131] French A. S. Jacobson R. A. Brozovi M. Farnocchia D. Hergenrother C. W. Rozitis B. Selznick S. Takahashi Y. Vokrouhlicky D. Adam C. Antreasian P. G. Bos B. J. Boynton W. V. Carcich B. T. Emery J. P. Leonard J. M. Lessac-Chenen E. Liounis A. J. McMahon J. W. Moreau M. C. Nolan M. C. Owen W. M. Jr. Park R. S. Pelgrift J. Y. Scheeres D. J. Lauretta D. S. Chesley S. R., Davis A. B. Trajectories of ejected particles in benu’s environment. In Asteroid Science in the Age of Hayabusa2 and OSIRIS-REx meeting, 2019.
- [132] OS Barnouin, MG Daly, EE Palmer, RW Gaskell, JR Weirich, CL Johnson, MM Al Asad, JH Roberts, ME Perry, HCM Susorney, et al. Shape of (101955) benu indicative of a rubble pile with internal stiffness. Nature geoscience, 12(4):247, 2019.
- [133] Juliana D Feldhacker, Megan Bruck Syal, Brandon A Jones, Alireza Doostan, Jay McMahon, and Daniel J Scheeres. Shape dependence of the kinetic deflection of asteroids. Journal of Guidance, Control, and Dynamics, 40(10):2417–2431, 2017.
- [134] Michael F A’Hearn, MJS Belton, WA Delamere, J Kissel, KPea Klaasen, LA McFadden, KJ Meech, HJ Melosh, PH Schultz, JM Sunshine, et al. Deep impact: excavating comet tempel 1. science, 310(5746):258–264, 2005.

- [135] Andrew F Cheng, Andrew S Rivkin, Patrick Michel, Justin Atchison, Olivier Barnouin, Lance Benner, Nancy L Chabot, Carolyn Ernst, Eugene G Fahnestock, Michael Kueppers, et al. Aida dart asteroid deflection test: Planetary defense and science objectives. Planetary and Space Science, 157:104–115, 2018.
- [136] Massimiliano Vasile and Camilla Colombo. Optimal impact strategies for asteroid deflection. Journal of guidance, control, and dynamics, 31(4):858–872, 2008.
- [137] Dario Izzo. Optimization of interplanetary trajectories for impulsive and continuous asteroid deflection. Journal of guidance, control, and dynamics, 30(2):401–408, 2007.
- [138] Raymond B Frauenholz, Ramachandra S Bhat, Steven R Chesley, Nickolaos Mastrodemos, William M Owen Jr, and Mark S Ryne. Deep impact navigation system performance. Journal of Spacecraft and Rockets, 45(1):39–56, 2008.
- [139] Peter H Schultz, Clara A Eberhardy, Carolyn M Ernst, Michael F A’Hearn, Jessica M Sunshine, and Carey M Lisse. The deep impact oblique impact cratering experiment. Icarus, 191(2):84–122, 2007.
- [140] E Fahnestock, Y Yu, and AF Cheng. Dart impact ejecta simulation and visualization for fly-along cubesat operational planning. In AGU Fall Meeting Abstracts, 2018.
- [141] Masatoshi Hirabayashi, Alex B Davis, Eugene G Fahnestock, Derek C Richardson, Patrick Michel, Andrew F Cheng, Andrew S Rivkin, Daniel J Scheeres, Steven R Chesley, Yang Yu, et al. Assessing possible mutual orbit period change by shape deformation of didymos after a kinetic impact in the nasa-led double asteroid redirection test. Advances in Space Research, 63(8):2515–2534, 2019.
- [142] Erik Asphaug, Steven J Ostro, RS Hudson, Daniel J Scheeres, and W Benz. Disruption of kilometre-sized asteroids by energetic collisions. Nature, 393(6684):437, 1998.
- [143] Daniel J Scheeres, Jay W McMahon, Brandon A Jones, and Alireza Doostan. Variation of delivered impulse as a function of asteroid shape. In 2015 IEEE Aerospace Conference, pages 1–7. IEEE, 2015.
- [144] Simon Delchambre, Tobias Ziegler, Albert Falke, Ulrich Johann, Georg Willich, and Klaus Janschek. Measurement strategy of the momentum enhancement beta-factor for near earth object mitigation missions. In 2017 IEEE Aerospace Conference, pages 1–9. IEEE, 2017.
- [145] Simon Delchambre, Tobias Ziegler, Albert Falke, Ulrich Johann, Georg Willich, Klaus Janschek, Cristina Piedad, and Diego Trigueros. Influences of enhancement factor measurement technique on the kinetic impactor mission design. In 2018 IEEE Aerospace Conference, pages 1–9. IEEE, 2018.
- [146] Jay W McMahon and Daniel J Scheeres. The effect of asteroid topography on surface ablation deflection. Advances in Space Research, 59(4):1144–1155, 2017.
- [147] B Wie. Hypervelocity nuclear interceptors for asteroid disruption. Acta Astronautica, 90(1):146–155, 2013.

- [148] Pau Sanchez, Camilla Colombo, Massimiliano Vasile, and Gianmarco Radice. Multicriteria comparison among several mitigation strategies for dangerous near-earth objects. Journal of Guidance, Control, and Dynamics, 32(1):121–142, 2009.
- [149] Steven J Ostro, Jean-Luc Margot, Lance AM Benner, Jon D Giorgini, Daniel J Scheeres, Eugene G Fahnestock, Stephen B Broschart, Julie Bellerose, Michael C Nolan, Christopher Magri, et al. Radar imaging of binary near-earth asteroid (66391) 1999 kw4. Science, 314(5803):1276–1280, 2006.
- [150] JP Sanchez, Massimiliano Vasile, and Gianmarco Radice. Consequences of asteroid fragmentation during impact hazard mitigation. Journal of guidance, control, and dynamics, 33(1):126–146, 2010.
- [151] Massimiliano Vasile and Nicolas Thiry. Nuclear cyclers: An incremental approach to the deflection of asteroids. Advances in Space Research, 57(8):1805–1819, 2016.
- [152] Jay McMahon, Shane K Mitchell, Kenshiro Oguri, Nicholas Kellaris, Donald Kuettel, Christoph Keplinger, and Benjamin Bercovici. Area-of-effect softbots (aoes) for asteroid proximity operations. In 2019 IEEE Aerospace Conference, pages 1–16. IEEE, 2019.
- [153] JE Cochran Jr and JA Thompson. Nutation dampers vs precession dampers for asymmetric spacecraft. Journal of Guidance, Control, and Dynamics, 3(1):22–28, 1980.
- [154] Bong Wie and David Murphy. Solar-sail attitude control design for a flight validation mission. Journal of Spacecraft and Rockets, 44(4):809–821, 2007.
- [155] Bruce A Conway. Near-optimal deflection of earth-approaching asteroids. Journal of Guidance, Control, and Dynamics, 24(5):1035–1037, 2001.
- [156] D Izzo, J Olympio, and C Yam. Asteroid deflection theory: fundamentals of orbital mechanics and optimal control. In 1st IAA Planetary Defense Conference, 2009.
- [157] Sonia Hernandez and Brent W Barbee. Design of spacecraft missions to test kinetic impact for asteroid deflection. 2011.
- [158] DN DellaGiustina, JP Emery, DR Golish, Benjamin Rozitis, CA Bennett, KN Burke, R-L Ballouz, KJ Becker, PR Christensen, CY Drouet d’Aubigny, et al. Properties of rubble-pile asteroid (101955) bennu from osiris-rex imaging and thermal analysis. Nature Astronomy, 3(4):341, 2019.